PROJECT BS-1: INTERPRETATION AND CONTROL OF HELICAL PERTURBATIONS IN TOKAMAKS

Project Leader: Calin Atanasiu

Task Force-Integrated Tokamak Modelling (ITM-09-IMP2-T4), Topical Groups-MHD (WP09-MHD-05-01)

C.V. Atanasiu, A. Moraru

National Institute for Lasers, Plasma and Radiation Physics, Bucharest, Romania

During the period July-December 2009, the common research between the **Mathematical Modelling for Fusion Plasmas Group** of **the National Institute for Lasers, Plasma and Radiation Physics (NILPRP),** Magurele - Bucharest, Romania with the **Max-Planck - Institut für Plasmaphysik (IPP)**, Garching, Germany has been focalized on the following objective:

3 Development of concept improvements and advances in fundamental understanding of fusion plasmas. 3.4 Theory and modelling

Specific Objective: Identification of whether some form of plasma dissipation is always required for RWMs stabilisation

The objective of this research made in common with IPP Garching, Tokamakphysics Department, under the frame of ITM and TG-MHD task forces, is to advance the physics understanding of RWMs stability, including the dependence on plasma rotation, wall/plasma distance, and active feedback control, with the ultimate goal of achieving sustained operation at beta values close to the ideal-wall beta limit through passive and active stabilization of the RWMs.

We have continued our research on RWMs made in 2008, in the frame of the following *milestone*:

- **M1.b** *Continuation of the investigation with our semi-analytical RWM model and code of different edge dissipation mechanisms: (1) due to the anomalous plasma viscosity (2)*

due to charge-exchange with cold neutrals, (3) due to neoclassical flow-damping, (4) due to sound-wave damping. TG-MHD (WP09-MHD-05-01)

For this task, we have continued to consider the seminal Fitzpatrick plasma model [1], with the standard large-aspect ratio, low β, circular cross-section tokamak plasma [2, 3, 4], we have drawn the linearized ideal MHD equations, by considering the following perturbed quantities: magnetic field, current density, plasma velocity, plasma pressure, plasma parallel stress tensor, polarization current and the neoclassical current [5, 6]. The perturbed quantities have to be in the frame of the standard assumptions in single-mode neoclassical theory. For the sake of simplicity, the plasma equilibrium has been considered as force-free (i.e., zero pressure gradient and zero diamagnetic current)

$$\vec{J} = \varepsilon_0 \frac{g}{B} \vec{B}, \; \varepsilon_0 = a / R_0, \; g(r) = \frac{1}{r} \frac{d}{dr} \left(\frac{r^2}{q} \right)$$

the magnetic field is expressed in second order approximation of the aspect ratio and as safety profile the well known Wesson profile [7] has been used. Even if really, the ideal external kink modes are driven by plasma pressure gradients, in this model, for sake of simplicity, these modes will be considered driven by current gradients.

The following set of linearized ideal MHD equations have been used

$$\gamma' \tilde{\vec{b}} = \nabla \times (\tilde{\vec{v}} \times \vec{B}), (\gamma' + \upsilon) \rho \tilde{\vec{v}} = -\nabla \tilde{p} - \nabla \cdot \tilde{\vec{\Pi}}_{\|} + \tilde{\vec{j}} \times \vec{B} + \vec{J} \times \tilde{\vec{b}},$$

$$\gamma' \tilde{p} = -\rho c_s^2 \nabla \cdot \tilde{\vec{v}}.$$

($\tilde{\vec{\Pi}}_{\|}$ is the perturbed plasma parallel stress tensor, $\gamma' = \gamma + in\Omega_\phi$ is the mode growth rate in the plasma frame, with n the toroidal wave number and Ω_ϕ the toroidal angular plasma velocity, $c_s(r)$ the plasma sound speed, $\upsilon(r)$ a plasma flow damping rate).

The stability parameter considered in the following will be

$$\kappa = \frac{\beta_c - \beta_{nw}}{\beta_{pw} - \beta_{nw}}$$ where β_{nw} is the no-wall beta limit, β_{pw} is the perfect wall beta limit, while β_c is the current beta. (if κ=1, then the RWM is stabilized, if κ=0 the RWM is not stabilized).

In Fig. 1, the RWMs stability boundaries in function of the toroidal plasma rotation for different plasma flow damping rates (due to charge exchange with neutrals) are given,

while in Fig. 2 the RWMs stability boundaries in function of the toroidal plasma rotation for different plasma neoclassical flow damping parameters are presented.

The dissipation due to the sound wave damping (at the edge) is negligible as stabilization effect.

The RWMs stability boundaries in function of the toroidal plasma rotation for different plasma edge perpendicular viscosities are reported in Fig. 3.
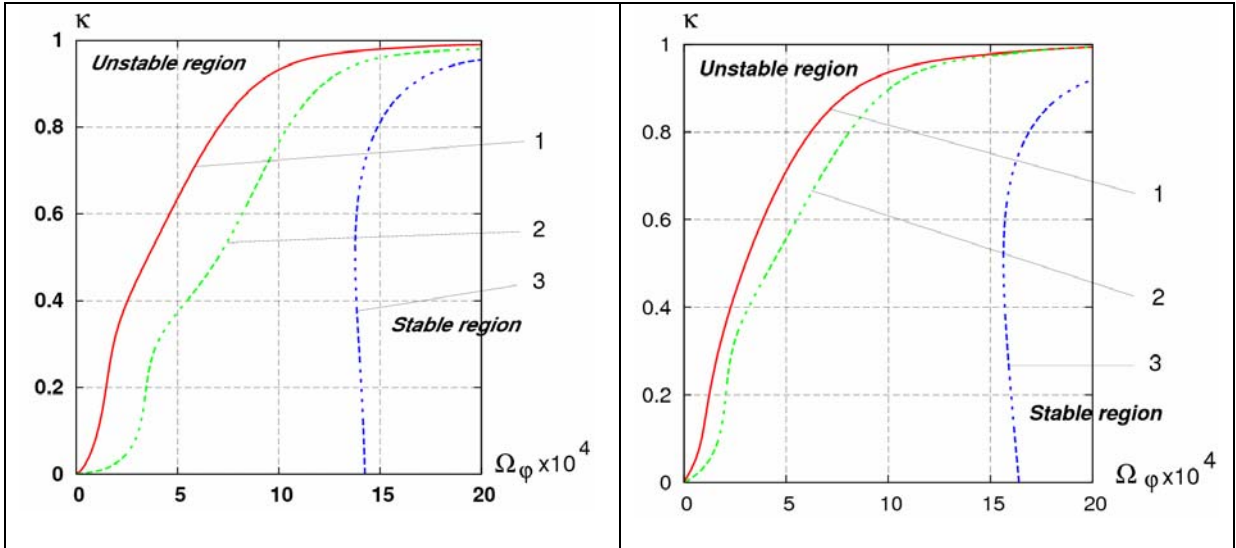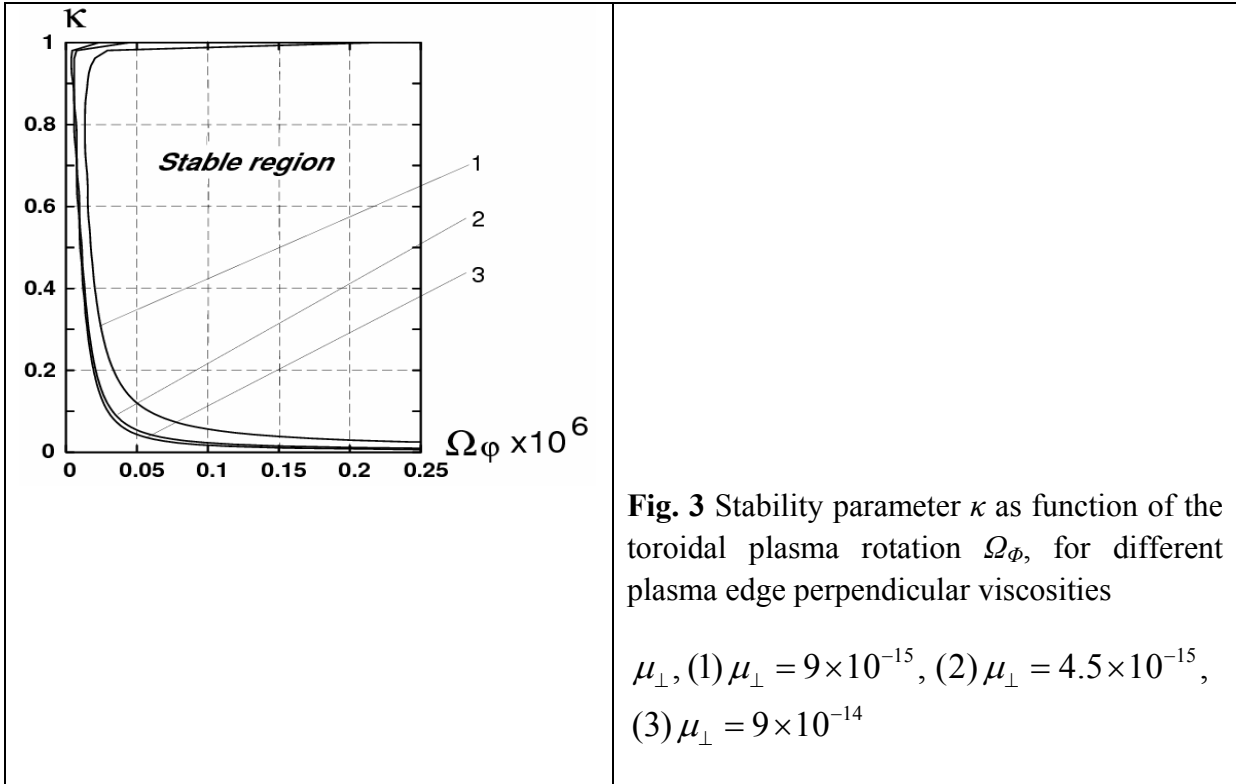
Fig. 1 Stability parameter κ as function of the toroidal plasma rotation Ω_Φ, for different plasma flow damping rates υ due to charge exchange with neutrals: (1) $\upsilon = 7 \times 10^4$, (2) $\upsilon = 4 \times 10^4$, (3) $\upsilon = 1.7 \times 10^3$, m/n=3/1, q(a)=3. $\upsilon \square\, v_i n_n \sigma_x$, $v_i = \sqrt{T_i / m_p}$ is the ion thermic velocity, n_n is the neutral density, σ_x is the charge exchange cross-section.	**Fig. 2** Stability parameter κ as function of the toroidal plasma rotation Ω_Φ, for different neoclassical flow damping parameters $\mu_\perp$, (1) $\mu_\perp = 9 \times 10^{-15}$, (2) $\mu_\perp = 4.5 \times 10^{-15}$, (3) $\mu_\perp = 9 \times 10^{-14}$, with ρ the plasma density (mass) and η_0 the parallel ion viscosity.

Fig. 3 Stability parameter κ as function of the toroidal plasma rotation Ω_Φ, for different plasma edge perpendicular viscosities

$\mu_\perp, (1)\,\mu_\perp = 9\times10^{-15}, (2)\,\mu_\perp = 4.5\times10^{-15},$
$(3)\,\mu_\perp = 9\times10^{-14}$

Conclusions:

- *by using a model with phenomenological damping parameters, there is no evident what kind of dissipation mechanism really is taking place. A numerical simulation will be necessary* [8-10]*;*
- *after running scenarios for different dissipation mechanisms and with a very large scale of plasma parameters, we have to accept that the results obtained with our model, based on Fitzpatrick's model do not correspond to experimentally realistic timescales and plasma rotation values (O(1%) Ω_A) even if it offers some useful information on the plasma rotation influence on mode growth rate. Presently, this seems to be a general opinion. With this in view, we intend to start the developing of a new more realistic analytical model with a resonant resistive-visco-inertial layer inside of the plasma.*

References :

[1] Fitzpatrick R., Aydemir A.Y., Nuclear Fusion, **36**, 11 (1996).

[2] Atanasiu C.V., *"Resistive wall modes stabilization in diverted tokamak configurations »*, invited paper, Hungarian Plasma Physics and Fusion Technology Workshop, 26-28 March 2008, Györ, Hungary.

[3] Atanasiu C.V., Miron I.G., *"An analytical model for resistive wall modes stabilization"*, 11th European   Fusion Theory Conference, 26-28 September 2005, Aix-en-Provence, France.

[4] Atanasiu C.V., Miron I.G., "*A model for resistive wall mode control*", EPS30, 7-11 July 2003, Sankt Petersburg, Russia.

[5] Bondeson A., Ward, Phys D.J., Rev. Lett. **72**, 2709 (1994).

[6] Hammett G.W., Perkins F.W., Phys. Rev. Lett. **64**, 3019 (1990).

[7] Wesson J.A., *Tokamaks*, (Oxford University Press, Oxford, UK, 2004).

[8] H. Zohm, J. Adamek, C. Angioni, G. Antar, C.V. Atanasiu, et. al,   Nuclear Fusion **49** 104009 (9pp) (2009).

[9] C.V. Atanasiu, A. Moraru, L.E. Zakharov, "*Response of a resistive wall with holes to an external kink mode in a tokamak*", 21st International Conference on Numerical Simulation of Plasmas, Lisbon, Portugal, 6-9 October 2009.

[10] C.V. Atanasiu, A. Moraru, L.E. Zakharov, "*Influence of a Nonuniform Resistive Wall on the RWM Stability in a Tokamak*", American Physical Society Plasma Meeting, Atlanta, USA, 2-6 November 2009.

PROJECT BS-2: STABLE ORGANIZED MOTION, COHERENT STRUCTURES AND TURBULENCE IN TOKAMAK PLASMAS

Project Leader: F. Spineanu

EFDA 2008-2009 Work Programme, Task Agreement TGS-02: WP08-TGS-02-02 (V-1-2)
Physics of rotation in plasmas.

Florin SPINEANU

Plasma Theory Group, National Institute for Laser, Plasma and Radiation Physics
EFDA 2008-2009 Work Programme Task Agreement TG-MHD WP08-MHD-04-01:

Dynamics of the vorticity under variational constraints, natural rotation profiles and filamentation events in the high confinement regimes

Introduction

Acting on plasma by Neutral Beams and/or by Ion Cyclotron Resonance Heating injects energy and torque. The effect is increase in the energy content but also rotation of the plasma in the poloidal direction. The generated vorticity is added to the one already existing and takes an evolution that is dictated by the extremum of a functional of the plasma flows. The configurations that are selected hava been described in our previous work by a field theory formalism and have been shown to obey a differential equation with strong nonlinearity. One of the possible solutions of that equation consists of a layer of plasma with strong poloidal rotation, which we have associated with the H-mode regime in the tokamak.

In the present stage of this investigation we look for the stability of this layer of sheared rotation. It is shown that beyond a certain limit of shear, the layer becomes unstable to generation of vortices inside it. The nucleation of vortices is simply the redistribution of the vorticity in the volume, in a way which is more convenient energetically.

However, more interesting from the point of view of the comparison with the experiments is the evolution of the nucleated vortices towards filaments. We have proven in the previous works that the filamentation covers the three most important aspects: vorticity, particle density, current density.

In the first part we review this demonstration.

In the second part we develop an old model (Bulanov and Sasorov, 1987) to show that the speed of breaking up of the current layer is of the order of the Alfven velocity.

The tearing of the density distribution in a layer of current

The current sheets are unstable to the tearing instability and they can be torn apart into strip of current. The geometry adopted by Trubnikov is adequate for studying the tearing of the density distribution in the layer. The width is initially L_0 and it evolves to a profile L which is variable along the direction x of the layer. The coordinate y is perpendicular on the layer in the equilibrium position. **NOTE**. This means that y is *radial* and x is *poloidal*. The magnetic field has a shear $B = B_x(y) = -B_0 \tanh\left(\frac{y}{L}\right)$. The current density is

$$j_z = en(v_{iz} - v_{ez})$$

Then

$$v_{iz} - v_{ez} = \frac{cB_0}{2\pi enL(t,x)} = \frac{const}{nL}$$

Introduce a normalized density of plasma $\rho(t,x) = \frac{nL(t,x)}{n_0 L_0}$ and we have the usual density conservation

$$\frac{\partial \rho}{\partial t} + \frac{\partial}{\partial x}(\rho v) = 0$$

Under the assumption $v_{e,th} \circleddash v_{ez}$ we have the equation of motion

$$\frac{\partial v}{\partial t} + v\frac{\partial v}{\partial x} = \frac{1}{nm_i c}\left(-j_z B_y\right) = \frac{e}{m_i c}\left(v_{iz} - v_{ez}\right)\frac{\partial A}{\partial x}$$

We consider that the system is invariant along the z direction which means that the generalized momenta of the electrons and of ions are conserved

$$m_i v_{iz} + \frac{e}{c}A = const$$

$$m_e v_{ez} - \frac{e}{c}A = const'$$

The equation of motion becomes

$$\frac{\partial v}{\partial t} + v\frac{\partial v}{\partial x} = \frac{e}{m_i c}\left(v_{iz} - v_{ez}\right)\frac{\partial A}{\partial x} = c_0^2 \frac{1}{\rho^3}\frac{\partial \rho}{\partial x}$$
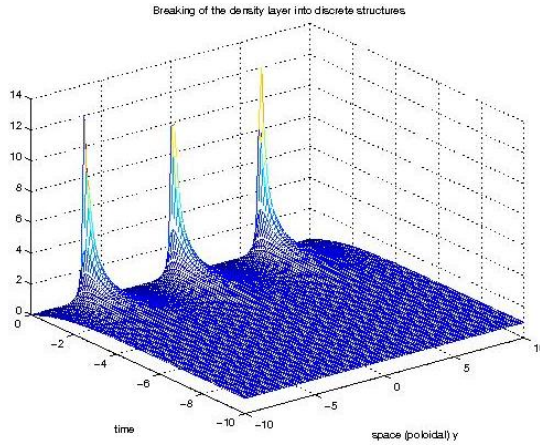
The constant is $c_0^2 = \frac{cm_e}{(m_e + m_i)}\left(\frac{cB_0}{2\pi n_0 L_0}\right)^2$. We note that the condition $c_0 \circleddash v_A$. The two equations

$$\frac{\partial \rho}{\partial t} + \frac{\partial}{\partial x}(\rho v) = 0$$

$$\frac{\partial v}{\partial t} + v \frac{\partial v}{\partial x} = c_0^2 \frac{1}{\rho^3} \frac{\partial \rho}{\partial x}$$

are solved using a *hodograph* transformation.

The picture below shows the filamentation of a layer of density as results from the solution derived by Trubnikov.

Breaking of the density layer into discrete structures

Tearing of the current density layer

It is a study of the *nonlinear* stage of the tearing instability which is made according to the method developed by **Bulanov Sasorov**. The initial state: a plane plasma sheet lying in the $y = 0$ plane with a sheared poloidal (on x) magnetic field. The current flows in the sheet along the z direction. It is assumed that the most important variation of all the quantities in the equilibrium, *unperturbed* state, takes place in the y direction, *i.e.* transversal to the sheet.

For slow motion like in the tearing mode, the plasma is assumed neutral and $v_{ex} = v_{ix} = v$ the velocity along the layer, poloidal. The z current is dominated by the electrons, v_{ez}, and this is connected with the initial state by the conservation equation

$$v_{ez} - \frac{e}{m_e c} A = v_{ez}^{(0)}$$

This is actually the conservation of the *generalized electron momentum* along the symmetry direction, z.

The equations are

$$\frac{\partial v}{\partial t} + v\frac{\partial v}{\partial x} = -\frac{e}{m_i c}\left(V_z^{(0)} + \frac{e}{m_e c}A\right)\frac{\partial A}{\partial x}$$

$$\frac{\partial n}{\partial t} + \frac{\partial}{\partial x}(nv) = 0$$

$$\frac{\partial^2 A}{\partial x^2} + \frac{\partial^2 A}{\partial y^2} = \frac{4\pi e L}{c}\delta(y)n\left(V_z^{(0)} + \frac{e}{m_e c}A\right)$$

where

$$V_z^{(0)} \equiv v_{ez}^{(0)} - v_{iz}^{(0)}$$

We need boundary conditions for the z component of the magnetic potential, A. These consists of assuming that at large distances in the transversal direction to the layer, on y, the poloidally oriented magnetic field becomes constant (this is like the Harris profile)

$$B_0 = \frac{2\pi}{c}en_0 L V_z^{(0)}$$

Then

$$A(x,y)\big|_{y\to\pm\infty} = B_0|y| + O\left(\frac{1}{y}\right)$$

Integrating the last (for A) equation over the transversal direction, close to the layer, $y \approx 0$, we obtain

$$\frac{\partial A}{\partial y}\bigg|_{y=0} = \frac{\pi e L}{e}n\left(V_z^{(0)} + \frac{e}{m_e c}A\big|_{y=0}\right)$$

The following new variables are introduced

$$D \equiv \frac{e}{V_z^{(0)}\sqrt{m_e m_i}}\left(A - B_0|y|\right)$$

$$N = \frac{n}{n_0}$$

$$W = \frac{v}{V_z^{(0)}}$$

and a redefinition of the variables $\frac{x}{l} \to x$, $\frac{y}{l} \to y$, $\frac{V_z^{(0)}t}{l} \to t$. Here l is the inhomogeneity scale in the initial perturbation.

9

The equations become

$$\frac{\partial W}{\partial t} + W\frac{\partial W}{\partial x} = -\frac{1}{2}\frac{\partial}{\partial x}(1+D)^2$$

$$\frac{\partial N}{\partial t} + \frac{\partial(NW)}{\partial x} = 0$$

$$\frac{\partial^2 D}{\partial x^2} + \frac{\partial^2 D}{\partial y^2} = 0 \ \text{ for } \ y > 0$$

with the boundary conditions

$$D\big|_{y\to\infty} = O\left(\frac{1}{y}\right)$$

$$\varepsilon\frac{\partial D}{\partial y} = N\left(1 + D\big|_{y=0}\right) - 1$$

The solution is determined as a series in powers of the small parameter ε

$$f(t,x,y,\varepsilon) = f^{(0)}(t,x,y) + \varepsilon f^{(1)}(t,x,y) + \varepsilon^2 f^{(2)}(t,x,y) + \dots$$

In the zeroth order it is derived the relationship between the potential $D^{(0)}$ and the density $N^{(0)}$ in the sheet

$$D^{(0)}(x, y = 0) = -1 + \frac{1}{N^{(0)}(x)}$$

Using this zeroth order relationship we return to the equations: of motion (for W) and of density conservation (for N),

$$\frac{\partial W}{\partial t} + W\frac{\partial W}{\partial x} = -\frac{1}{N^{(0)}}\frac{\partial}{\partial x}\frac{1}{N^{(0)}}$$

$$\frac{\partial N^{(0)}}{\partial t} + \frac{\partial}{\partial x}\left[N^{(0)}W\right] = 0$$

These are drop-on-ceil instability of a system similar to a Chaplygin gas with negative polytropic.

A change of variables from the Eulerian variables (t,x) to the Lagrangian variables (t,ξ),

$$x = \xi + \Theta(\xi,t)$$

$$W = \frac{\partial\Theta}{\partial t}\bigg|_{\xi=\xi(t,x)}$$

The plasma density is

$$N = \frac{1}{1 + \partial\Theta / \partial\xi}$$

It is assumed that at the initial time $t = 0$,

$$\Theta(t = 0, \xi) = 0$$
$$N(t = 0, \xi) = 1$$

The change of variables from Eulerian to Lagrangian variables leads to

$$\frac{\partial W}{\partial t} + W \frac{\partial W}{\partial x}\bigg|_{Euler} = \frac{\partial W}{\partial t}\bigg|_{Lagrange} = \frac{\partial^2\Theta}{\partial t^2}$$

and

$$\frac{1}{N}\frac{\partial}{\partial x}\frac{1}{N}\bigg|_{Euler} = \frac{\partial}{\partial\xi}\left(1 + \frac{\partial\Theta}{\partial\xi}\right)\bigg|_{Lagrange} = \frac{\partial^2\Theta}{\partial\xi^2}$$

This transforms the equation of motion in Eulerian variables into the equation

$$\frac{\partial^2\Theta}{\partial t^2} + \frac{\partial^2\Theta}{\partial x^2} = 0$$

The complex variable is introduced $s = \xi + it$ and it is seen that the variables

$$\frac{\partial\Theta}{\partial t} = W$$

$$\frac{\partial\Theta}{\partial\xi} = \frac{1}{N} - 1$$

are harmonic conjugate, which means that also W and $\frac{1}{N}$ are *harmonic conjugate.*

The solution to the differential equation for the function Θ in the complex plane is

$$\Theta(\xi,t) = \text{Re}\left[\int_0^{\xi+it} w(s)ds\right]$$

where the function $w(s)$ is *analytic* and is governed by the condition at the boundary on the *real axis*.

$$w(\xi + it)\big|_{t=0} = -\frac{\overline{n}(\xi)}{1 + \overline{n}(\xi)} + i\overline{v}(\xi)$$

Using the connection between Θ and N and W, and the solution for the harmonic function Θ, one finds

$$N(\xi,t) = \frac{1}{1 + \text{Re}[w(s)]}$$

$$W(\xi,t) = \text{Im}[w(s)]$$

The solution describes the evolution for $t > 0$ up to the moment when

$$1 + \text{Re}[w(s)] = \begin{cases} 0 & \text{or} \\ \infty \end{cases}$$

The meaning is: when $\text{Re}[w(s)] = -1$ one has the case that the plasma density becomes *infinite* since the trajectory intersects itself. The other singular situation is $\text{Re}[w(s)] = \infty$ which means that the density *vanishes*, and the plasma sheet is torn. It is mentioned by Bulanov and Sasorov that the situation of one or the other of singularity arises in finite time t .

The solution shows:

1) the sheet is torn apart after a finite time interval
2) the density vanishes over a finite interval on x .

PROJECT BS-3: ANOMALOUS TRANSPORT IN PLASMA

Project Leader: N. Pometescu

Plasma Theory Group: N. Pometescu, Gy. Steinbrecher, D. Constantinescu, M. Negrea, I. Petrisor

Universitatea din Craiova

- **General Objectives**

The scope of the project is to explain some features of the anomalous transport and develop analytical and numerical skills to evaluate correctly the transport in fusion device like ITER. The project aims also to deep insight the physics of plasma turbulence.

Among the objectives there is the analyses of some interesting features of the fusion plasma transport, as long-range correlations, intermittency in plasma edge turbulence, edge transport barriers, core impurity transport with different dominant core turbulence and different radio-frequency heating scheme.

Both analytical and numerical methods are used to achieve the objectives. Stochastic models will be adapted to the study of long-range correlations, self-similarity and intermittency. Gyrokinetic semi-Lagrangean codes with collision term will be adapted to the study of the particle transport in tokamak.

The test particle diffusion in an electromagnetic stochastic field is studied in the framework of the decorrelation trajectory method (DCT). In this kind of stochastic field we must determine the mean square displacements and the radial and poloidal diffusivities using the numerical method and the decorrelation trajectory method. The comparison of the results obtained by these two methods might then allow us to confirm the DCT approach results. These results are important for "Validation of physics-based transport models" and "Plasma edge characterization and modeling", objectives for ITER.

Some characteristics of the anomalous transport of magnetic field lines and charged particles, features that cannot be described in the context of the standard diffusion paradigm, will be explained using the memory effects. The long memory effects will be studied using fractional models and limited (short) memory effects will be studied using delay systems or hysteresis systems.

The results obtained in this project will be applied to existing large plasma devices but oriented specially to be applied to plasma in ITER device.

For the year 2009 the objectives are:

1. Characterization of the intermittent events, long range correlations and particle transport on the plasma boundary.

2. Studies of core impurity transport in tokamak plasmas with different dominant core turbulence. Influence of the collisions in the gyrokinetic simulations on the impurity transport.

3. Impurity transport driven by instabilities in plasma with radio-frequency heating.

    3a. Determine the analytical expression for power density deposition profile of ICRH.

    3b. Study of variation of the density profile for different impurity species

4. Numerical simulation of test particle transport and comparison with theoretical models

5. The construction of a fractional diffusion equation in velocity and position space

6. Studies of transport and of saw-tooth crash phenomena based on mapping models

    6a. Study of the saw-tooth crash phenomena using mapping models

    6b. Study of the test particles' dynamics using mapping models

- **Specific Objectives**

In this stage of the project, July-December 2009 we have attained the following specific objectives from the previous mentioned objectives:

1. Characterization of long-range correlations and multi-scale physics in L-mode plasmas and during edge improved confinement regimes.

2. Influence of the collisions in the gyrokinetic simulations on the particle transport.

3. Impurity transport driven by instabilities in plasma with radio-frequency heating.

    3b. Study of variation of the density profile for different impurity species

4. Numerical simulation of test particle transport and comparison with theoretical models

5. The construction of a fractional diffusion equation in velocity and position space

6. Studies of transport and of saw-tooth crash phenomena based on mapping models

  6b. Study of the test particles' dynamics using mapping models

- **Resume of the stage**

1. *Characterization of long-range correlations and multi-scale physics in L-mode plasmas and during edge improved confinement regimes.*

a) *The effect of the long-range spatial correlations of the stochastic electric field on the impurity transport. Particle transport in the frozen turbulence with long-range correlations.*
 The trapping effect in the cross-field transport, in constant magnetic field and static random electric field was studied. The random electric field that produces the particle transport was modeled by a Gaussian random potential surface with long-range correlation. Rigorous bounds, in the framework of this model on the fraction of the trapped particle in a given domain were obtained, in term of the correlation function. It was proven that in the limit of frozen turbulence the fraction of the trapped particles is independent from the intensity of fluctuations.
 b) *Stochastic models of the long-range correlations, self-similarity, multi-scale physics, intermittency, in the plasma edge plasma turbulence.*

 New class of stochastic models of the edge plasma turbulence was elaborated.
 The first class of the models are derived from our previous one dimensional models of the intermittency. The main feature of this new model is the possibility to explain the L-H transition by pure stochastic mechanism. This model explains in term of a stochastic mathematical model the increase of the intermittency with the increase of the mean pressure gradient.
 The second class of models is derived from a higher dimensional version of the stochastic instability study. This new model provides a stochastic mechanism that explains the inverse cascade.

2. *Studies of the core impurity transport in plasmas with different dominant core turbulence.*

Milestone: *Influence of the collisions in the gyrokinetic simulations on the particle transport.*

Particle transport was studied by using the statistical properties of the random electric field extracted from numerical simulations. Models that explains the regularities of the statistical properties o the random fields, like self-similarity, were elaborated. These models were used to obtain numerical algorithm for the study of particle transport. Self-similar models modelled the effect of the collisions on impurity transport.

3. *Impurity transport driven by instabilities in plasma with radio-frequency heating.*

Milestone 3b: *Study of variation of the density profile for different impurity species*

The dispersion equation for the ITG instability was obtained from the electro-neutrality condition. This equation which contains the dependence of the electrical charge of ion species, the characteristics of ITG instability and those of the RF wave externally launched was studied and compared with similar equations obtained in fluid description. The significant importance of the resonant interaction in the regions where the gradient of the density of an ion species is important was revealed. This region is near to the edge of plasma for some of the ion species, but for other species this can be more inside of the plasma. We emphasize that for this later species the impact of coupled action rf wave – ITG instability can produce a significant modification in their densities. The parameters specific to ITER has been considered in numerical evaluations and the conclusions refer to the installations like ITER.

4. *Numerical simulation of test particle transport and comparison with theoretical models*

We determine the mean square displacement and diffusivities as functions of different plasma parameters in electromagnetic stochastic field. The results obtained using this method are compared with the results yielded by the decorrelation trajectory method (DCT method) for the same environments and determine its range of applicability. In particular, the study of the behavior of impurities (general transport behavior, effects of trapping and impurity accumulation).We use the DCT method and test particle simulations to study impurity transport, as well as runaway electrons, in electromagnetic field environments that consist of an equilibrium magnetic field, in large aspect ratio and also in toroidal geometry, onto which stochastic perturbations of the magnetic and the electric field are superimposed. The study is performed for different degrees of anisotropy of the stochastic fields, as well as for different levels of stochasticity by varying different Kubo numbers.

5. *The construction of a fractional diffusion equation in velocity and position space*

We used this equation for the calculation of the particle and heat diffusivities or pinch velocities specific to the characterization of the transport processes. The fractional diffusion

equation was used in order to describe a nonlocal type of transport: the fluid limit of "microscopic" kinetic transport processes without characteristic spatio-temporal scales. These transport processes, that are known as Continuous Time Random Walk, generalize the standard Brownian motion by allowing trapping events and large displacements known as Levy flights.

6. Studies of transport and of saw-tooth crash phenomena based on mapping models
6b. *Study of the test particles' dynamics using mapping models*

Using the Hamiltonian description and the mapping technique it was proved that a magnetic internal transport barrier exists in the low shear region even for monotonous safety factors. It was shown that the reversed magnetic shear is not compulsory for the formation of the transport barrier. This result confirms the experimental observations and the previous intuitive explanations. The influence of the minimum value of the unperturbed safety profile in the low shear region on the robustness of the transport barriers was also studied. It was proved that, for small and moderate perturbations, a transport barrier is formed when q_0 is a little bit smaller than the main integer values $q_0=1$, $q_0=2$, $q_0=3$, which also confirm the experimental data. These results are important for describing the dynamics of the passing particles.

The particles internal transport barriers in the low shear magnetic regions, even in the absence of the reversed shear were studied using the adapted global drift wave map (Horton W et al, Physics of Plasmas 5, no.10, 3910-3917 (1998)). Two different measures of a global transport (the running diffusion coefficient and the exit time diffusion coefficient) were computed and compared. The relation between these two measures of transport and the formation of a transport barrier was pointed out: the formation of a transport barrier is associated with a drop of these quantities. The milestone will continue in 2010.

- **Scientific description**

Specific Objective 1

Characterization of the intermittent events, long range correlations and particle transport on the plasma boundary.

EFDA Work Programme 2008 and 2009 - V-1/3 and WP08-TGS-02-03 (V-1-3)

Coordinator: Prof. Dr. Gy. Steinbrecher

Milestone 1b: *Characterization of long-range correlations and multi-scale physics in L-mode plasmas and during edge improved confinement regimes.*

a) *The effect of the long-range spatial correlations of the stochastic electric field on the impurity transport. Particle transport in the frozen turbulence with long-range correlations.*

The problem of transversal particle transport in constant magnetic field and random electric field was studied, with special focus on the evaluation of the fraction of permanently trapped particles. The correlation function of the electric field in this model was supposed isotropic, homogenous and with long-range spatial correlations: power law decay at infinity with exponent less or equal 2. By suitable Hilbert formalism rigorous bounds on the fraction of trapped particles was obtained [1]. In this way the extensive Monte-Carlo type simulations, that are necessary to solve numerically this class of problems is replaced by a deterministic problem: numerical minimization of a class of analytic functions of many variables. The frozen turbulence hypothesis modeled the extreme case of long range time correlations We proved that in the limit of frozen turbulence, in the framework of this model, the fraction of the trapped particles is independent on the amplitude of the fluctuations. It is completely determined by the mean value and correlation function of the random field, which can be rescaled by an arbitrary constant factor. By extrapolating to the more realistic case of time dependent random electric field, we conjecture that a reduction of the particle loss can be achieved not by reduction of the turbulence amplitude but by increasing the time correlations. A specific version of the Fletcher-Reeves method was adapted and a C++ code was tested.

b) *Stochastic models of the long-range correlations, self-similarity, multi-scale physics, intermittency, in the plasma edge plasma turbulence.*

Previous stochastic linear low-dimensional models of the edge plasma turbulence from refs. [2-5] was used for the elaboration of a new mechanism of the L-H transitions, based purely on stochasticity. This new model from ref. [6] with minimal assumptions, give a mathematical explanation for the occurrence of the intermittent ELMs in the H mode plasmas. The main shortcoming of this class of the models is the reduced number of components.

Consequently we begin the study of a new class of stochastic models [7-8]: Discrete Random Linear Partial Differential Equations (DRLPDE). These models appear in the stochastic version of the linear instability studies. This category of DRLPDE also describes the effect of the small spatial and temporal scale turbulence to the large-scale evolution of the physical system. In order to be able to study higher dimensional stochastic models by analytic methods, we used in [7] some new results from the theory of Anderson localization [9]. This higher dimensional Discrete Random Linear Partial Differential Equations are interesting also because they relate the local, disordered random fluctuations to the global statistical

characteristics of the physical system, they models the multi scale physics. We studied a simplified model: classical Hamiltonian linear hyperbolic equations with random potential term (Klein-Gordon Equation with random "mass" term). The main motivation was that exactly the Hamiltonian systems in higher dimensions are most exposed to destabilization by random perturbation. The main results are:

1. For a stochastic system with N components, it is possible to obtain a closed set of soluble linear deterministic differential equations for the moments of order p.

2. The k=0 mode is always destabilized

3. In dimension 1 and 2 all of the modes are destabilized, but the modes with high k has a smaller positive Liapunov exponent

4. In 3 dimensions, for low noise intensity, the modes with sufficient high k remain stable. This is a mechanism for the occurrence of the long-range spatial correlations, generated by a completely disordered noise. It is an interesting multi-scale physics effect. This is also an interesting linear stochastic model that gives a qualitative description of the inverse cascade.

This class of models of the generation of the long –range spatial correlations, spatial structures from the parametric amplification of a completely disordered random field characterized by temporal and spatial white noise, give a new, analytic method for the explanation of the main qualitative features of the anomalous particle transport in large tokamaks.

Specific Objective 2

Studies of the core impurity transport in plasmas with different dominant core turbulence.

Coordinator: Prof. Dr. György Steinbrecher.

EFDA Work Programme 2008 and 2009 - III-5 Task 1 and WP08-TGS-01-06 (III-5)

Milestone: *Influence of the collisions in the gyrokinetic simulations on the particle transport.*

This objective is continued from 2008. In the previous stage, the statistical properties of the stochastic electrostatic field were studied. In this period it was found that it is possible to approximate the stochastic electrostatic field by a 3 dimensional generalization of the classical one-dimensional self–similar processes with stationary and independent increments.

The mathematical foundations of the numerical approximation of the particle transport in electrostatic field having the properties of generalized self-similar processes were studied. New models for the explanation of the generation of the random field with the characteristics of this new class of self-similar random field were elaborated. These models predict that by a modification of the collision terms, the statistical properties of the random field are only slightly changed. In the first class of models the random field is locally generated by a special case of the stochastic processes exposed in ref. [2]. In the second class by the use of the generalized Central Limit Theorem the stable random field is generated by a superposition of more general class of processes, studied in refs [3-5]. From the first class of models an algorithm to generate this random fled numerically was derived. The particle transport was studied numerically by using the random field generated by this algorithm. The inclusion of the collision terms breaks this self-similarity, but within the statistical errors has no effect on the impurity transport. In this class of models, the simplified model without collision term case give an accurate description of the impurity transport.

Further analysis of the time evolution of the instabilities and their localised structure will be performed in order to discriminate among the previous coarse-grained models.

The elaboration of the mathematical methods for the interpretation of the first principle gyrokinetic simulations is important for the optimisation of the strategy of the time consuming first principle simulations, necessary for the optimisation of the large tokamaks, like ITER and DEMO.

Specific Objective 3

Impurity transport driven by instabilities in plasma with radio-frequency heating.

Coordinator: Lect. Dr. Nicolae Pometescu

EFDA WP08-TGS-02-03 (V-1-3)

Milestone 3b: *Study of variation of the density profile for different impurity species*

In the present study were assumed the following conditions:

   - Radio-frequency waves are in Ion Cyclotron Range. We are interested in effects of both heating and ponderomotive force;

   - The equilibrium magnetic field is described by the axisymmetric model for a large aspect ratio tokamak with circular concentric magnetic surfaces

- The ITER-like plasma is multi-species plasma. The species are electrons, Deuterium, Tritium, alpha particles and one other impurity species (like Argon).

- We are interested in the impact of Ion Temperature Gradient (ITG) modes on ion density profile in tokamak.

The influence of radio frequency ponderomotive force on anomalous impurity transport in tokamak was studied recently – see ref. [11] in fluid formalism with trace impurity approximation where the normalized impurity density peaking factor is almost constant relative to ponderomotive force term. The result of the balance between convective and diffusive processes disagrees with experimental observation but agree with other fluid or kinetic studies. Consequently we decide to study the influence of radio frequency waves on anomalous impurity transport in tokamak for multi-species plasma using the kinetic formalism. The ensemble averaged distribution function is assumed as the summation between a Maxwellian part and the deviation from Maxwellian where the last depends on both turbulence and particles - RF wave interaction.

The fluctuating part of the distribution function is linearly approximated as a summation between the solution of kinetic equation for turbulence in absence of RF waves and the solution of the kinetic equation in presence of RF-waves but in absence of turbulence.

We used for the ITG-instability a description similar with references [14, 15] but adding more ion species and also the interaction with RF waves. For electrons was assumed an adiabatic response and for ion species both adiabatic and non-adiabatic response was evaluated using the ballooning transform of the perturbed distribution function. The ion density perturbation profile due to ITG in plasma with ICRH was obtained [16].

In our model we have obtained from the electro-neutrality condition the dispersion equation for the frequency. This equation which contains the dependence of the electrical charge of ion species, the characteristics of ITG instability and those of the RF wave externally launched was studied and compared with similar equations obtained in fluid description. The significant importance of the resonant interaction in the regions where the gradient of the density profile of an ion species is important was revealed. This region is near to the edge for some species but for other species this can be more inside of the plasma. We emphasize that for this later species the impact of coupled action RF wave – ITG instability can produce a significant modification in their densities.

The parameters specific to ITER has been considered in numerical evaluations and the conclusions refer to the installations like ITER.

The present work was partially done at Chalmers University of Technology, Gothenburg, Sweden and will continue in 2010.

Specific Objective 4

Numerical simulation of test particle transport and comparison with theoretical models
Coordinators: Lect. Dr. Negrea Marian and Lect. Dr. Iulian Petrisor

EFDA Work Programme 2008 and 2009 - V-1/3] and WP08-TGS-02-03 (V-1-3)

4a. *Test-particle simulations of ion drift in stochastic magnetic fields*

We have studied the influence of stochastic magnetic fields on ion diffusion, using a drift approximation in slab geometry, and applying a stationary stochastic magnetic field on top of a uniform background field. The stochastic magnetic field follows a Gaussian in its distribution function and obeys a prescribed auto-correlation function with given correlation length. The running diffusion coefficients of the ions are determined with the use of test particle simulations in the three dimensional environment, for different levels of turbulence (varying the drift Kubo number and with a fixed magnetic Kubo number). The results of the test-particle simulations were compared to the results obtained for the same physical system by the semi-analytical decorrelation trajectory method (DCT). By construction, the magnetic field is periodic in all three directions, and particles leaving the simulation box are re-injected at the plane opposite to the one through which they leave. The stochastic magnetic field (figure 1) is generated on a grid with 643 grid-points, with a grid-spacing such that the grid-size equals 9 correlation lengths in each direction. In conclusion we find that diffusion is of normal nature (see e.g. the radial running diffusion coefficient in figure 2 and a typical trajectory in figure 3). The diffusive process slows down with both, increasing strength of the magnetic perturbation, and increasing mass of the ions considered, respectively [18, 19, 21, 23, 26]. The values of the diffusion coefficients practically coincide with the results yielded by the DCT we find though a different scaling of the diffusion coefficient with the drift Kubo number. Work was done by M. Negrea and I. Petrisor in collaboration with Dr. B. Weyssow from Universite Libre de Bruxelles and H. Isliker, A. Vogiannou and L. Vlahos from University of Thessaloniki, Greece.
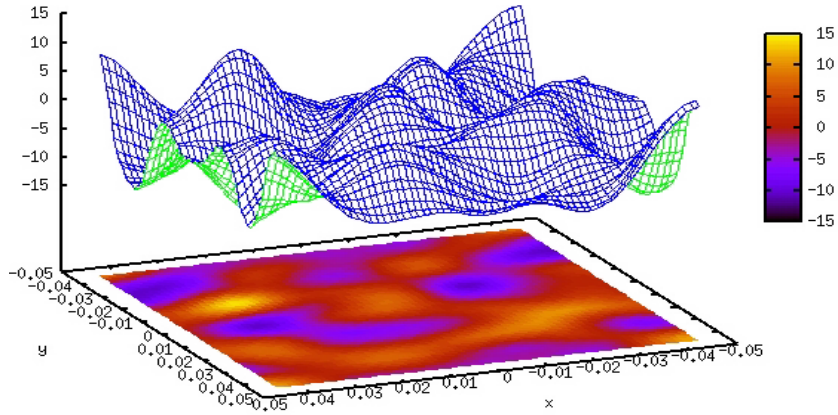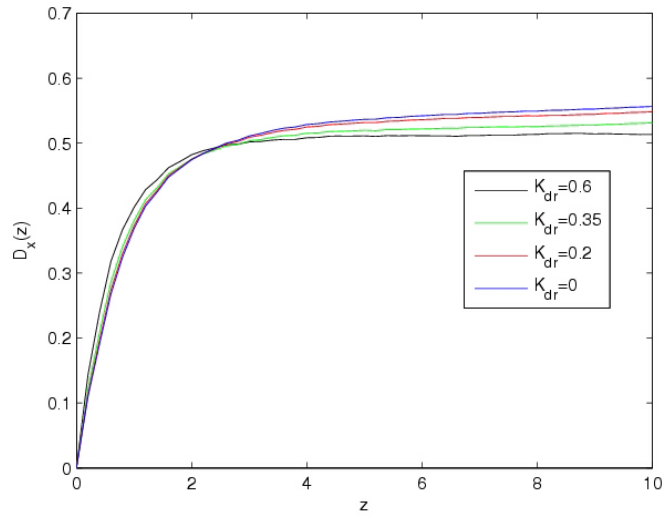
Figure 1: The stochastic magnetic field

Figure 2: Radial diffusion coefficient for different values of the drift Kubo number and for the magnetic Kubo number equal to unity
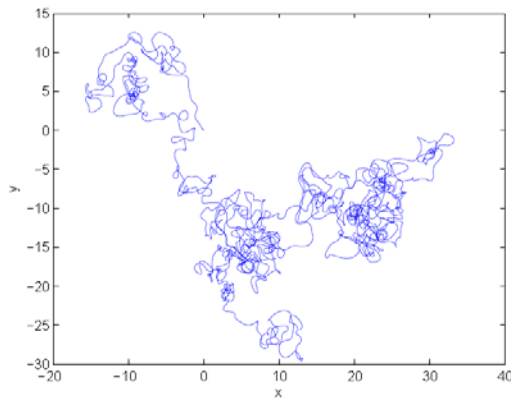

Figure 3: Typical trajectory for the test particle

Specific Objective 5

The construction of a fractional diffusion equation in velocity and position space

Coordinators: Lect. Dr. Negrea Marian and Lect. Dr. Iulian Petrisor

We started our study from the already developed Continuous Time Random Walk equations. In a continuous time random walk model, combined in position and velocity space, we determined the fluid limit of the equations and we derived and analyzed a fractional diffusion equation for the model. We used this equation for the calculation of the particle and heat diffusivities or pinch velocities specific to the characterization of the transport processes. As a second activity, the fractional diffusion equation in position and velocity space will be applied to the electromagnetic environment described in the milestone described above "Numerical simulation of test particle transport and comparison with theoretical models", in order to model the results of the test particle simulations. The fractional diffusion equation was used in order to describe a nonlocal type of transport: the fluid limit of "microscopic" kinetic transport processes without characteristic spatio-temporal scales. These transport processes, that are known as Continuous Time Random Walk, generalize the standard Brownian motion by allowing trapping events and large displacements known as Levy flights. The fractional diffusion models depend on the usual parameters α and β determine the order of the fractional derivatives in space and time, respectively. In our study these parameters were varied in order to take into account the non-Markovian memory effects (when $\beta \neq 1$) and spatial anomalous effect (when $\alpha \notin \{1,2\}$). This objective will be continued in 2010 in collaboration with H. Isliker, A. Vogiannou and L. Vlahos from University of Thessaloniki, Greece.

Specific objective 6

Studies of transport and of saw tooth crash phenomena based on mapping models.

EFDA Work Programme 2008 and 2009 - III-2-b, Related to WP08-MHD-03-01

Coordinator: Conf. Dr. Dana Constantinescu

6b. *The study of the test particles' dynamics using mapping models*

In the present work it was proved that a magnetic internal transport barrier exists in the low shear region even for monotonous safety factors. This result confirms the experimental observations and the previous intuitive explanations. It was shown that the reversed magnetic

shear is not compulsory for the formation of the transport barrier. However, in the reversed shear configuration the transport barrier is more robust, due to the specific topology of the magnetic field involved in the reconnection process. The effect of the amount of flatness of the safety profile in the vicinity of its zero shear point was also studied using the flatness coefficient. The beneficial effect of the vanishing of the shear profile was shown to be increased if the radial extent of the low-shear region is increased due to a flatter q-profile.

The minimum value of the unperturbed safety profile in the low shear region, q_0, also influences the robustness of the transport barriers. The case when it is an integer number is extremely important because it can be correlated with experimental observations.

General results can not be obtained because the system strongly depends on the perturbations. However, it was proved that, for small and moderate perturbations, a transport barrier is formed when q_0 is a little bit smaller than the main integer values $q_0=1$, $q_0=2$, $q_0=3$, which also confirm the experimental data [20, 22, 24, 25].

In order to study the motion of charged particles in the same magnetic configurations, the global drift wave map (Horton W. et al, Physics of Plasmas 5, no.10, 3910-3917 (1998)), was adapted. The aim of the work was to study the particles internal transport barriers in the low shear magnetic regions, even in the absence of the reversed shear. Specific safety factors and magnetic perturbations were considered in the general model. Two different measures of a global transport (the running diffusion coefficient and the exit time diffusion coefficient) were computed and compared. The relation between these two measures of transport and the formation of a transport barrier was pointed out: the formation of a transport barrier is associated with a drop of these quantities. The milestone will continue in 2010.

- **Conclusions**

1 *Characterization of the intermittent events, long-range correlations and particle transport on the plasma boundary.*

a. The effect of the long-range spatial correlations of the stochastic electric field on the impurity transport. Particle transport in the frozen turbulence with long-range correlations.
New, rigorous bounds for the trapping effect in a model of particle transport was obtained, by Hilbert space methods. These results allow a more rapid estimation of the trapping effect, compared to direct integration methods. The computation of the particle trapping in large tokamaks is essential for the optimal planning of the future experiment on ITER. This study will be continued.

b. Stochastic models of the long-range correlations, self-similarity, multi-scale physics, intermittency, in the plasma edge plasma turbulence.

Models of the edge plasma turbulence were elaborated. The first model correlates the L-H transition with increased intermittency. The second class of models is a stochastic linear model that explains the inverse cascade. These models help a better processing of the simulation data of the large tokamaks.

2. *Influence of the collisions in the gyrokinetic simulations on the particle transport.*

The study was performed in two stages: determining the statistical properties of the random electric field and studying the particle transport in this random field separately. Despite the inclusion of the collision term modified the scaling symmetry of the fluctuations, no effect was observed on the impurity transport. Decreasing the statistical error will continue this study. The elaboration of reliable method for the study of the particle transport is essential for the first principle simulation of the large tokamaks, like ITER

3. Impurity transport driven by instabilities in plasma with radio-frequency heating.

3b: *Study of variation of the density profile for different impurity species*

The dispersion equation for the ITG instability was obtained from the electro-neutrality condition. This equation permits to reveal the region where the resonant interaction is important. This region is near to the edge of plasma for some of the ion species, but for other species this can be more inside of the plasma. We emphasize that for this later species the impact of coupled action between ICRH wave and ITG instability can produce a significant modification in their densities. The parameters specific to ITER has been considered in numerical evaluations and the conclusions refer to the installations like ITER. Supplementary detailed studies of the dispersion equation are necessary; these will be accomplished in 2010.

4. *Numerical simulation of test particle transport and comparison with theoretical models*

4a. *Test-particle simulations of ion drift in stochastic magnetic fields*

The radial and poloidal diffusion coefficients of the ions are determined by numerical simulations in the guiding centre approximation taking into account for the stochastic drift. Different levels of the stochastic drift Kubo number and a fixed magnetic Kubo number were used for the analysis. The results of the numerical simulations were compared to the results obtained for the same physical system by the semi-analytical decorrelation trajectory method

(DCT). The values of the diffusion coefficients coincide within 20% with the results yielded by the DCT we find though a different scaling of the diffusion coefficient with the drift Kubo number.

5. *The construction of a fractional diffusion equation in velocity and position space*

In a Continuous Time Random Walk model, combined in position and velocity space, we determined the fluid limit of the equations and we derived and analyzed a fractional diffusion equation for the model. These transport processes, that are known as Continuous Time Random Walk, generalize the standard Brownian motion by allowing trapping events and large displacements known as Levy flights. The fractional diffusion models depend on the usual parameters α and β determine the order of the fractional derivatives in space and time, respectively. In our study these parameters were varied in order to take into account the non-Markovian memory effects (when $\beta \neq 1$) and spatial anomalous effect (when $\alpha \notin \{1,2\}$). This objective will be continued in 2010.

6b. *Study of the test particles' dynamics using mapping models*

The motion of charged particles in magnetic configurations specific to Tore Supra and ASDEX-Upgrade tokamak, was studied using the adapted global drift wave map. The aim of the work was to study the particles internal transport barriers in the low shear magnetic regions, even in the absence of the reversed shear. The relation between the running diffusion coefficient, the exit time diffusion and the formation of a transport barrier was pointed out. Qualitatively, the formation of a transport barrier is associated with a drop of these quantities. The results are important for understanding the mechanisms of the anomalous transport in the neighborhood of the internal transport barriers.

- **Bibliografy**

[1] G. Steinbrecher, B. Weyssow "Generalized robustness of abstract dynamical systems", Physics AUC vol. 18 (part 1), 130-141.

[2] G. Steinbrecher, W. T. Shaw "Quantile Mechanics", European Journal of Applied Mathematics, 19, 87, (2008);
http://functions.wolfram.com/GammaBetaErf/InverseErf/06/01/02/0004/

http://en.wikipedia.org/wiki/Quantile_function

http://wapedia.mobi/en/Quantile_function

http://en.wikipedia.org/wiki/Inverse_transform_sampling.

[3] G. Steinbrecher, B. Weyssow, "Generalized Randomly Amplified Linear System Driven by Gaussian Noise: Extreme Heavy Tail and Algebraic Correlation Decay in the Plasma Turbulence", Phys. Rev. Lett. 92, 125003-1, 2004.

[4] G. Steinbrecher, X. Garbet, B. Weyssow, "Stochastic version of the linear instability analysis", Annals of the Univ. Craiova "Physics AUC", 19, 107-123, (2009). http://cis01.central.ucv.ro/pauc/

[5] G. Steinbrecher, X. Garbet, B. Weyssow, "Weak Convergence to Stationary Distributions in Heavy Tail Models", sent to Journal of Differential Equations.

[6] X. Garbet, G. Steinbrecher, "On-Off Intermittency of Bifurcating Systems and Heavy Tail Exponent in Random Multiplicative Processes.", sent to publication

[7] G. Steinbrecher, X. Garbet, "Stochastic Linear Instability Analysis", International Workshop on "Hamiltonian Approaches to ITER Physics", CIRM, Marseille, 2-6 November 2009;

http://www.cirm.univ mrs.fr/web.ang/liste_rencontre/programmes/AbstractsProgRenc395.pdf

[8] G. Steinbrecher, X. Garbet, "Stochastic Linear Instability Analysis of the Hamiltonian Systems" to be published

[9] V. N. Kuzovkov, W. von Niessen, V. Kascheyevs, O. Hein, J. Phys. Condens. Matter 14, 1377 (2002).

[10] T. Johnson, T. Hellsten and L.-G. Eriksson, Nucl. Fusion 46, S433 (2006)

[11] H. Nordman, R. Singh, T. Fülop, L.-G. Eriksson, R. Dumont, J. Anderson, P. Kaw, P. Strand, M. Tokar and J. Weiland, Phys. Plasmas 15, 042316 (2008)

[12] R. Koch, Phys. Letters A, 157 (6,7), p.399 (1991)

[13] N. Pometescu, *Power deposition profile in tokamak plasma with ICRH*, Annals of the University of Craiova, (*Physics AUC*), vol.**19**, pg 73-78, 2009

[14] F. Romanelli, *Ion temperature-gradient-driven modes and anomalous ion transport in tokamaks*, Phys. Fluids B1, 1018 (1988)

[15] J. Q. Dong, W. Horton, and J. Y. Kim, *Toroidal kinetic η_{i}-mode study in high-temperature plasmas*, Phys. Fluids B4, 1867 (1992)

[16] N. Pometescu, B. Weyssow, Ion density perturbation profile due to ITG in plasma with ICRH, 13th European Fusion Theory Conference, 12-15 October 2009, Riga, Latvia

[17] N. Pometescu, *Dispersion equation for ITG instability in plasma with ICRH,* `presented at` International workshop on "Transport in Fusion Plasma", University of Craiova, November 9-10, 2009.

[18] H. Isliker, A. Vogiannou, L. Vlahos, M. Negrea, I. Petrisor and B. Weyssow, *Test-particle simulations of ion drift in stochastic magnetic fields*, poster session at 36th EPS Conference on Plasma Physics, June 29 - July 3, 2009, Sofia, Bulgaria.

[19] M. Negrea, I. Petrisor, Dana Constantinescu, H. Isliker, A. Vogiannou and L. Vlahos, *Aspects of the Diffusion of Ions in Tokamak Plasma*, poster session at 13th European Fusion Theory Conference, October 12 -15, 2009, Riga (Latvia).

[20] Dana Constantinescu, M-C Firpo, M. Negrea, I. Petrisor, *The study of the sawtooth oscillations in tokamaks using mapping models,* poster session at 13th European Fusion Theory Conference, October 12 -15, 2009, Riga (Latvia).

[21] M. Negrea, I. Petrisor and Dana Constantinescu, *Aspects of the Diffusion of Ions in Tokamak Plasma,* `presented at` International workshop on "Transport in Fusion Plasma", University of Craiova, November 9-10, 2009.

[22] Dana Constantinescu, M. Negrea and I. Petrisor, *Stochastic and regular dynamics in some models proposed for the study of the sawtooth phenomena in tokamaks,* `presented at` International workshop on "Transport in Fusion Plasma", University of Craiova, November 9-10, 2009.

[23] I. Petrisor , M. Negrea and Dana Constantinescu, *The zonal flow in anisotropic weak turbulence,* `presented at` International workshop on "Transport in Fusion Plasma", University of Craiova, November 9-10, 2009.

[24] Dana Constantinescu, O. Dumbrajs, V. Igochine, K. Lackner, R. Meyer-Spasche, H. Zohm, *A low-dimensional model system for non-linear plasma behaviour (ELMs, Sawteeth, etc.)*, poster session at 13th European Fusion Theory Conference, October 12 -15, 2009, Riga (Latvia).

[25] Dana Constantinescu, M.-C. Firpo and L. Nasi, *Influence of the q value in the low shear region on the robustness of the internal transport barrier*, poster session at 13th European Fusion Theory Conference, October 12 -15, 2009, Riga (Latvia).

[26] B. Teaca, C.C. Lalescu, I. Petrisor, M. Negrea and D. Carati, *On the transport of charged test particles in two-dimensional turbulent plasma* (to be submitted).

Project BS-14 : **Understanding of the ExB drift nonlinear effects on transport and structure generation in turbulent tokamak plasmas**

Coordinator: Dr. M. Vlad (CS-I)
Plasma Theory Group: F. Spineanu, M. Vlad, D. Nendrean

EFDA Task Agreement: ITM-05-IMP4-T3
EFDA 2008-2009 Work Programme, Task Agreement TGS-02:
- WP08-TGS-02-01 (V-1-1) Studies of core impurity transport in plasma with different dominant core turbulence
- WP08-TGS-02-03 (V-1-3) Turbulence and Transport, particle sources, and impurity influx in the boundary of fusion devices and test particle behaviour in low temperature plasmas.

<u>Summary</u>

The research in the period July-December 2009 was concentrated on the milestone *Turbulent transport of energetic particles*. Work related to the objectives scheduled for 2010 was also performed due to the necessity of responding to the EFDA calls for the Euratom Work Programme in 2010. The topics studied and the main results is presented below.

I.1. Turbulent transport of energetic particles

Starting from our analytical estimation [1], which shows that the turbulent transport coefficient of fast particles can be larger than previously generally accepted, this problem has attracted an increasing interest in the last three years. Numerical simulation were performed in several laboratories, both for given characteristics of the turbulence and in large-scale self-consistent simulations. There are controversial results and it is very important to understand this process. The enhanced transport can appear only as a nonlinear process. We have shown that in these conditions the diffusion coefficients for small energy ions are very sensitive to weak perturbations produced other components of the motion. Thus, the first step for understanding fast ion turbulent transport is to develop the test particle model by taking into account other components of motion. The aim is to find if the enhanced transport persists in the presence of these components of ion motion and how they influence the diffusion coefficients.

The milestone for 2009 is the study of the effect of the parallel motion on the radial diffusion coefficient of energetic particles.

The first stage was the analysis and the improvement of the decorrelation trajectory method for fast particles (introduced in [1]). The gyromotion effect on the Eulerian correlation of the potential was determined and a modified subensemble average velocity was obtained. It was shown that the effects of trapping were overestimated in [1].

The parallel motion was introduced in the model and in the code for determining the diffusion coefficient. The diffusion coefficient was determined as function of the turbulence amplitude and characteristic parameters, geometrical parameters and particle energy. Domains of the parameter space with substantial turbulent diffusion were found.

These studies will be continued by determining the effects of magnetic drifts, collisions and plasma rotation.

I.2. Trapping effect on the evolution of drift type turbulence

Our preliminary studies on test modes on turbulent plasmas suggest a strong connection of ion trajectory trapping or eddying in the structure of the stochastic potential and the strong

nonlinear effects that appear in drift type turbulence. The generation of large correlation lengths (the inverse cascade) is shown to be the consequence of ion trapping, which produce the displacement of the unstable wave number domain toward small k values [2]. The moving potential determines poloidal flows of the ions when the amplitude of the ExB velocity is larger than the effective diamagnetic velocity [3]. The trapped ions move with the potential while the other ions drift in the opposite direction. These opposite (zonal) ion flows compensate such that the average poloidal flux is zero. They determine stabilisation and damping of the drift modes as well as the generation of modes that have zero poloidal wave numbers (zonal modes) and zero frequency.

These preliminary results are the basis of our response to the EFDA Call for the Transport Topical Group, WP10-TRA-01-02 (Role of the multi-scale mechanism in the L-H transition), where we have proposed to participate with the milestone:
"Zonal flow generation and particle trapping in the structure of the turbulent potential"

The results were presented in the Transport Task Group Workshop [C1], in an invited talk at a conferences [C2] and in an article that is in print in AIP Proceedings [L1].

[1] M. Vlad, F. Spineanu, "Larmor radius effects on impurity transport in turbulent plasmas", **Plasma Physics and Controlled Fusion 47** (2005) 281-294.
[2] M. Vlad, F. Spineanu, *"Test particles, test modes and drift turbulence",* AIP Conference Proceedings 1061 (2008), Editors P. K. Shukla, B. Eliasson, L. Steflo, pages 24-33.
[3] M. Vlad, F. Spineanu, *„Trapping, anomalous transport and quasi-coherent structures in magnetically confined plasmas",* **Plasma and Fusion Research 4** (2009) 053**-**1:8.

L1. M. Vlad, F. Spineanu, *"Drift turbulence and structure generation"*, AIP Conference Proceedings, Editors P. K. Shukla, B. Eliasson, L. Steflo, in print.
C1. M. Vlad, *„Test particles, large scale correlations, and zonal flow generation",* 2nd EFDA TTG Workshop, Culham, 16-18 September 2009
C2. M. Vlad, F. Spineanu, *"Drift turbulence and structure generation"*, International Symposium on Cutting Edge Plasma Physics, 24-28 August 2009, invited talk.

1 Turbulent transport of energetic particles

Particle transport determined by a stochastic electric field superposed on a magnetic field was much studied in the guiding center approximation (*drift transport),* which corresponds to Larmor radii smaller than the correlation length of the electric field [1]-[13]. This approximation is not adequate for fusion plasmas for which the ratio of the Larmor radius ρ over the correlation length of the turbulence $\lambda_\perp$, $\overline{\rho} \equiv \rho/\lambda_\perp$, is of the order one for ions and of the order of ten for the fast particles produced in the fusion reaction. We consider here particles with large Larmor radii and study the transport produced by the Lorentz force (*Lorentz transport*). We determine the diffusion coefficient for a very wide range of parameters that describe this stochastic motion.

   A generally accepted idea is that test particle transport in a turbulent magnetized plasma is reduced at large Larmor radius. The reason is that the effective motion of the guiding centers is determined by the average of the stochastic potential over cyclotron gyration, which is smaller than local values. It is expected that the diffusion coefficient continuously decreases with the increase of the Larmor radius ρ and that at very large Larmor radii ($\rho \gg \lambda_\perp$) it becomes negligible compared with D_0, the diffusion coefficient obtained at small Larmor radius. The transport of particles with Larmor radii of the order of the correlation length of the turbulence was studied in a recent paper [14]. It was shown that, in some specified conditions, the reversed effect can appear: the diffusion coefficient of these particles can be sensibly larger than D_0. More precisely the diffusion coefficient increases when Larmor radius increases if the time variation of the turbulence is slow. In the present paper we extend the study [14] from the range of Larmor radius comparable to $\lambda_\perp$ to the range of ρ much larger than $\lambda_\perp$. Our first aim is to find if there is an effect of the turbulence on the transport of the fast ions characterized by $\overline{\rho} \equiv \rho/\lambda_\perp \sim 10$. It is expected that such particles cannot "see" the turbulence since the average of the stochastic potential on the cyclotron gyration is practically zero. We show that this is not always true and that their diffusion coefficient can be much larger than that of slow particles with small Larmor radii, D_0. We determine the conditions in which the transport coefficient is comparable or higher than D_0. Our second aim is to understand this 'anomalous' increase of the diffusion coefficient and to obtain a physical image of this process.

   We consider a constant magnetic field directed along z axis, $\mathbf{B} = B\mathbf{e}_z$ and an electrostatic turbulence represented by an electrostatic potential $\phi'(\mathbf{x}, z, t)$, where $\mathbf{x} \equiv (x_1, x_2)$ are the Cartesian coordinates in the plane perpendicular to $\mathbf{B}$. The potential is considered to be a stationary and homogeneous Gaussian stochastic field, with zero average. Such a stochastic field is completely determined by the two-point Eulerian correlation function, $E(\mathbf{x}, z, t) \equiv \langle \phi'(\mathbf{0}, 0, 0)\, \phi'(\mathbf{x}, z, t) \rangle$, where $\langle ... \rangle$ is the statistical average over the realizations of $\phi(\mathbf{x}, z, t)$. The statistical properties of the drift velocity components $\mathbf{v}^{dr}(\mathbf{x}, z, t) \equiv -\nabla \phi'(\mathbf{x}, z, t) \times \mathbf{e}_z/B$ are determined by those of the potential; they are stationary and homogeneous Gaussian stochastic fields like $\phi'(\mathbf{x}, z, t)$. The two-point Eulerian correlations of the drift velocity components and the potential-velocity correlations are obtained as derivatives of $E(\mathbf{x}, z, t)$. The Eulerian correlation of the drift velocity evidences three parameters:

the amplitude V, the correlation time τ_c, which is the decay time of the Eulerian correlation, and the correlation lengths $\lambda_\perp$, $\lambda_\parallel$ which are the characteristic decay distances perpendicular and respectively parallel to the confining magnetic field.

The motion of an ion with charge q and mass m is determined by the Lorentz force:

$$m\frac{d^2\mathbf{x}(t)}{dt^2} = q\left\{-\boldsymbol{\nabla}\phi'(\mathbf{x}, z, t) + \mathbf{u} \times \mathbf{B}\right\} \tag{1}$$

$$\frac{dz}{dt} = u_\parallel \tag{2}$$

where $\mathbf{x}(t)$, $z(t)$ is the ion trajectory, $\mathbf{u}(t) = d\mathbf{x}(t)/dt$ is its velocity component perpendicular on $\mathbf{B}$, $u_\parallel$ is the velocity along $\mathbf{B}$ and $\boldsymbol{\nabla}$ is the gradient in the (x_1, x_2) plane. The kinetic energy of the particles is much larger that the potential one and the stochastic acceleration along $\mathbf{B}$ is neglected in (2). The initial conditions are

$$\mathbf{x}(0) = \mathbf{0}, \quad z(0) = 0, \quad \mathbf{u}(0) = \mathbf{u}_0. \tag{3}$$

Introducing the instantaneous Larmor radius defined by

$$\rho_i(t) \equiv -\varepsilon_{ij}\frac{u_j(t)}{\Omega}, \tag{4}$$

(where $\Omega = qB/m$ is the cyclotron frequency and $\varepsilon_{12} = -\varepsilon_{21} = 1$, $\varepsilon_{11} = \varepsilon_{22} = 0$), and the guiding center position $\boldsymbol{\xi}(t) \equiv \mathbf{x}(t) - \boldsymbol{\rho}(t)$, the equation of motion (1-2) can be written as the following system of first order equations:

$$\frac{d\xi_i}{dt} = -\varepsilon_{ij}\frac{\partial\phi(\boldsymbol{\xi} + \boldsymbol{\rho}, z, t)}{\partial\xi_j} \tag{5}$$

$$\frac{d\rho_i}{dt} = \varepsilon_{ij}\left[\frac{\partial\phi(\boldsymbol{\xi} + \boldsymbol{\rho}, z, t)}{\partial\xi_j} + \overline{\Omega}\rho_j\right] \tag{6}$$

$$\frac{dz}{dt} = U_\parallel \tag{7}$$

where $\phi = \phi'/B$. We have normalized the time with the average time of flight over $\lambda_\perp$, $\tau_\perp = \lambda_\perp/V$, the distances in the (x_1, x_2) plane with $\lambda_\perp$, the distances along the magnetic field with $\lambda_\parallel$ and the drift velocity with V. The following set of dimensionless parameters determines particle transport in such turbulence:

$$K = \frac{\tau_c}{\tau_\perp}, \quad U_\parallel = \frac{\tau_\perp}{\tau_\parallel}, \quad \overline{\rho} = \frac{|\boldsymbol{\rho}(0)|}{\lambda_\perp}, \quad \overline{\Omega} = \Omega\tau_\perp. \tag{8}$$

The first parameters, the Kubo number, characterizes the stochastic potential. It is the ratio of the correlation time τ_c to the average time of flight of the guiding centers in the (x_1, x_2) plane, and thus it essentially describes the effect of the time variation of the stochastic potential. The second parameter is the ratio of $\tau_\perp$ to the parallel time of flight over $\lambda_\parallel$, $\tau_\parallel = \lambda_\parallel/u_\parallel$. It represents the effect of the parallel motion. The third parameter $\overline{\rho}$ is the initial Larmor radius normalized with the perpendicular correlation length and it appears in the initial condition (3), which is written as

$$\rho_1(0) = \overline{\rho}\cos(\alpha), \quad \rho_2(0) = \overline{\rho}\sin(\alpha), \quad \boldsymbol{\xi}(0) = -\boldsymbol{\rho}(0), \quad z(0) = 0 \tag{9}$$

where α determines the orientation of the initial particle velocity (the angle between the initial velocity $\mathbf{u}_0$ and the x_1 axis is $\pi/2 - \alpha$). $\overline{\rho}$ is related to the initial kinetic energy of the particles since it can be written as $\overline{\rho} = |\mathbf{u}_0| / V\overline{\Omega}$. The forth parameter $\overline{\Omega}$ is the cyclotron frequency normalized with $\tau_\perp$ and describes the relative importance of the cyclotron and drift motion (second and respectively first term in Eq. (6)) in the evolution of the Larmor radius.

The electrostatic potential $\phi(\mathbf{x}, t)$ is a stochastic field and thus Eqs. (5-7) are stochastic equations. The solution consists, in principle, in determining the statistical properties of the ensembles of trajectories, each one obtained by integrating Eqs. (5-7) for a realization of the stochastic potential. The Eulerian correlation of the potential is considered known (from experiments or from a model). We will determine here the mean square displacement and the time dependent diffusion coefficient for the guiding center trajectories $\boldsymbol{\xi}(t)$. These quantities are obtained from the correlation of the Lagrangian drift velocity, defined by:

$$L_{ij}(t) \equiv \left\langle v_i^{dr}\left[\mathbf{x}(0), 0\right]) v_j^{dr}\left[\mathbf{x}(t), t\right]\right\rangle. \tag{10}$$

The mean square displacement of the guiding center and its time dependent diffusion coefficient are integrals of this function:

$$\left\langle \xi_i^2(t)\right\rangle = 2 \int_0^t d\tau \; L_{ii}(\tau) \; (t - \tau), \tag{11}$$

$$D_i(t) = \int_0^t d\tau \; L_{ii}(\tau), \tag{12}$$

provided that the process is stationary [16].

We note that the results of test particle transport directly apply in cases when there is no feedback on the turbulence from the density of the particles. It can be shown that the equation for the average density obtained from the equation of stochastic advection of the (passive) density is, at space and time scales larger than those of the stochastic velocity, the diffusion equation with the diffusion coefficient obtained from test particles (i. e. from the diffusion of the characteristics of the equations for the fluctuating part of the density). In plasma turbulence, particle density cannot be approximated by a passively advected field. However, since test particle calculations are based on the knowledge of the statistical characteristics of the stochastic velocity field (that have to be determined from experiment or from numerical simulation), the self-consistence of the turbulence problem is actually implicitly taken into account. The fields that represent the perturbation of the ion and electron densities can be described in such experiment base analysis by passive field advection processes. Then, taking correctly into account the other elements in the trajectories (parallel motion, average drifts, collisions, etc.) and using the condition of ambipolar turbulent fluxes, it is possible to evaluate the diffusion coefficient for particle density using test particle approach.

This problem of transport determined by the Lorentz force (*Lorentz transport*) in a turbulent magnetized plasma was very recently studied [14] and compared with the guiding center approximation obtained by taking $\boldsymbol{\rho} \rightarrow \mathbf{0}$ (*drift transport*). The range of Larmor radius of the order of the correlation length ($\overline{\rho} \sim 1$) was considered in [14], which applies to impurity and plasma ions. It was shown that the diffusion

coefficient for Lorentz transport is smaller than for the drift transport in the case of a fast time variation of the turbulence corresponding to $K < 1$, but it is larger than in the drift approximation if the time variation of the turbulence is slow ($K > 1$). We extend this analysis to the range of large Larmor radii ($\overline{\rho} \sim 10$) in order to find if such nonlinear process that determines the increase of the diffusion coefficient is still effective. We also introduce the parallel motion that can be important at such large kinetic energies.

The correlation of the Lagrangian drift velocity (10) and the time dependent diffusion coefficient of the guiding centers (12) are determined using the decorrelation trajectory method [21], [13], which was extended to the Lorentz transport in [14]. The following analytical expressions for $D(t)$ and $L(t)$ are derived in [14]:

$$\mathcal{D}(t) \equiv D_B F(t), \tag{13}$$

$$L(t) = V^2 \frac{dF(t)}{dt} \tag{14}$$

with

$$F(t) = \frac{1}{2(2\pi)^{3/2}} \int_{-\infty}^{\infty} d\phi^0 \exp\left(-\frac{(\phi^0)^2}{2}\right) \int_0^{\infty} dv\, v^2 \exp\left(-\frac{v^2}{2}\right) \int_0^{2\pi} d\alpha\, \Xi_1(t; S) \tag{15}$$

where $D_B = \lambda_\perp V$, $v = |\mathbf{v}^0|$ and $\Xi_1(t; S)$ is the $i = 1$ component of the solution of

$$\frac{d\Xi_i}{dt} = -\varepsilon_{ij} \frac{\partial \Phi(\mathbf{\Xi} + \mathbf{\Pi}, Z, t; S)}{\partial \Xi_j}, \tag{16}$$

$$\frac{d\Pi_i}{dt} = \varepsilon_{ij} \left[\frac{\partial \Phi(\mathbf{\Xi} + \mathbf{\Pi}, Z, t; S)}{\partial \Xi_j} + \overline{\Omega}\Pi_j \right], \tag{17}$$

$$\frac{dZ}{dt} = U_\parallel \tag{18}$$

with the initial conditions

$$\Pi_1(0) = \overline{\rho}\cos(\alpha), \quad \Pi_2(0) = \overline{\rho}\sin(\alpha), \quad \Xi_i(0) = -\Pi_i(0). \tag{19}$$

The equations (16-19) determine the decorrelation trajectories. They have the same structure with the equations for particle trajectories (5-7) but the potential $\Phi(\mathbf{\Xi} + \mathbf{\Pi}, Z, t; S)$ is a deterministic function obtained from the Eulerian correlation of the stochastic potential as

$$\Phi(\mathbf{x}, z, t; S) = \phi^0 E(\mathbf{x}, z, t) + v \frac{\partial}{\partial x_2} E(\mathbf{x}, z, t). \tag{20}$$

It is the average potential in a sub-ensemble S of realizations defined by the conditions $\phi(\mathbf{0}, 0, 0) = \phi^0$ and $\mathbf{v}^{dr}(\mathbf{0}, 0, 0) = (v, 0)$. The decorrelation trajectory obtained from equations (16-19) is an approximation of the average trajectory in S. An isotropic stochastic potential with the Eulerian correlation depending $|\mathbf{x}|$ is considered, which leads to a diagonal correlation tensor $L_{ij}(t) = \delta_{ij}L(t)$. Explicit results for $L(t)$ and $D(t)$ are obtained by effectively calculating the decorrelation trajectories in S, solutions of equations (16-19), and the weighted average (15). This

4

procedure appears to be very similar with a direct numerical study of the simulated trajectories. There are however essential differences. The decorrelation trajectories are obtained for a rather smooth and simple potential (20) and the number of such trajectories is much smaller than in the numerical study due to the weighting factor determined analytically. This reduced very much the calculation time, such that it can be performed on PC. A computer code is developed for explicit calculation of $D(t)$ for given values of the parameters K, $U_\parallel$, $\overline{\rho}$, $\overline{\Omega}$ and prescribed Eulerian correlation of the potential.

The results obtain in [14] also show that the asymptotic diffusion coefficient in a time dependent potential is obtained by calculating the function F defined in equation (15) for the static potential with the same space dependence of the Eulerian correlation and by replacing the time t with K

$$D \cong D_B F(K). \tag{21}$$

This equation applies for negligible parallel velocity. The modification determined by $U_\parallel$ is deduced in section 5. As shown in [7], this important property [equation (21)] is a consequence of the shape of the correlation of the Lagrangian drift velocity that accounts for the subdiffusive transport in a static potential.

The Eulerian correlation of the potential is modelled by a function of the type

$$E(\mathbf{x}, z, t) = \mathcal{E}(|\mathbf{x}|) \exp(-t/K) \exp(-z). \tag{22}$$

We note that the nonlinearity of the system (5-7) is essentially determined by the $\mathbf{x}$ dependence of the potential, which is statistically represented by the $\mathbf{x}$ dependence of the Eulerian correlation (by $\mathcal{E}(|\mathbf{x}|)$ in (22)). Consequently, the shape of $\mathcal{E}(|\mathbf{x}|)$ influences the diffusion coefficient (as shown in [13]) while the t and z dependence affects D only through the global parameters τ_c and $\lambda_\parallel$. Thus the exponential functions chosen for simplicity in the Eulerian correlation (22) are not essential and can be replace by other decaying functions without changing sensibly the results. As shown in [13], the general behaviors of the decorrelation trajectories, of $L(t)$ and $D(t)$ are the same for all correlations. $\mathcal{E}(|\mathbf{x}|)$ (more exactly its long distance behavior) determines however the strength of the trapping represented by the exponent β of the scaling $D \sim D_B/K^\beta$. We consider two typical shapes for the $\mathbf{x}$ dependence of the Eulerian correlation:

$$a) \quad \mathcal{E}(|\mathbf{x}|) \quad = \quad \frac{1}{1 + \mathbf{x}^2/2} \tag{23}$$

$$b) \quad \mathcal{E}(|\mathbf{x}|) \quad = \quad \exp\left(-\frac{\mathbf{x}^2}{2}\right). \tag{24}$$

The first one is a simple function that is in agreement with the large distance decay of the measured Eulerian correlation and the second is a localized function that leads to the strongest trapping of the trajectories [13].

The effect of the parallel motion is determined in the gyrokinetic approximation. The solution of equation (7) that represents the parallel component of the decorrelation trajectory, $Z(t) = U_\parallel t$, introduced in the average potential $\Psi(\Xi, Z, t; \overline{\rho}, S)$ obtained with the gyroaveraged correlation, yields a time dependent factor $exp(-|U_\parallel| t)$

in the correlation of the Lagrangian drift velocity. It has a decorrelation effect similar with that produced by the time variation of the stochastic potential, which determines a decaying factor $\exp(-t/K)$. The asymptotic diffusion coefficient is obtained as

$$D(K, U_\parallel) = D_B \, F\left(\frac{K}{1 + KU_\parallel}\right) \tag{25}$$

where F is the function (15) obtained for a static potential with the same space correlation and with $U_\parallel = 0$ (see [15]). In the linear regime one obtains

$$D(K, U_\parallel) \cong D_B \, f(\overline{\rho}) \, \frac{K}{1 + KU_\parallel}. \tag{26}$$

and thus the parallel motion determines the decrease of the diffusion coefficient. The effect is important when $U_\parallel \gtrsim 1/K$. In the trapping regime appearing for $K > K_m$, the parallel motion has an opposite effect: it determines the increase of the diffusion coefficient if $1/K < U_\parallel < 1/K_m$.

The variation of the parallel velocity at constant Larmor radius corresponds to the variation of the kinetic energy of the particles. Physically it is more relevant to consider particles with given kinetic energy and to determine the diffusion coefficient as a function of the orientation of the velocity defined by the pitch angle $tg(\alpha) = u/u_\parallel = \Omega\rho/u_\parallel$. The Larmor radius $\overline{\rho}$ and $U_\parallel$ are functions of the energy $E = mV_{th}^2/2$, where V_{th} is the thermal velocity and of the angle α

$$\overline{\rho} = \frac{1}{\overline{\Omega}} \frac{V_{th}}{V} \sin(\alpha), \quad U_\parallel = \frac{\lambda_\perp}{\lambda_\parallel} \frac{V_{th}}{V} \cos(\alpha). \tag{27}$$

The diffusion coefficient is thus function of the pitch angle. In the linear regime it is obtained by replacing equations (27) in (26) and in the trapping regime it is obtained from Eq.(25). This shows that the transport is dependent on the pitch angle.

These studies have to be continued by taking into account other components that can influence the motion (an average velocity, collisions, etc.) because such components can have strong effects. In the nonlinear stage characterized by trajectory trapping, different perturbations of the ExB drift motion interact in a complicated way producing effects that are completely different of the superposition of thir separate actions. We have shown this property in the case of drift transport and the results presented here suggest that Lorentz transport is similar from this point of view.

2 Trapping effects on the evolution of drift type turbulence

The evolution of turbulence in magnetically confined plasmas is a complex problem that is not yet understood besides the huge amount of work on this topic (see [3] and the references there in). Most of the studies that go beyond the quasilinear

stage are based on numerical simulations. They show the generation of large scale structures and of zonal flows that leads to the nonlinear damping of turbulence.

The aim is to study the nonlinear evolution of the drift turbulence on the basis of test modes on turbulent plasmas. A Lagrangian approach is developed using the results we have obtained in the last decade on the statistics of test particle trajectories.

Semi-analytical statistical methods (the decorrelation trajectory method [21] and the nested subensemble approach [22]) have been developed for the study of test particle stochastic advection. These are the first methods that describe trajectory trapping or eddying that is specific to the $\mathbf{E} \times \mathbf{B}$ drift in turbulent plasmas [6]-[1]. It was shown that trapping determines memory effects, quasi-coherent behavior and non-Gaussian distribution [22]. The trapped trajectories have quasi-coherent behavior and they form structures similar to fluid vortices. The diffusion coefficients decrease due to trapping and their scaling in the parameters of the stochastic field is modified [10]-[30]. Anomalous diffusion regimes [25] and even sub-diffusion or super-diffusion [11] can appear due to trajectory trapping.

Test particle trajectories are strongly related to plasma turbulence. Plasma dynamics basically results from the Vlasov-Maxwell system of equations, which represents the conservation laws for the distribution functions along particle trajectories. Studies of plasma turbulence based on trajectories were initiated by Dupree [31], [32] and developed especially in the years seventies [3]. These methods do not account for trajectory trapping and thus they apply to the quasilinear regime or to unmagnetized plasmas. A very important problem that has to be understood is the effect of the non-standard statistical characteristics of the test particle trajectories on the evolution of the instabilities and of turbulence in magnetized plasmas. We extend the Lagrangian methods of the type of [32], [33], [34] to the nonlinear regime characterized by trapping.

We study linear modes on turbulent plasma with the statistical characteristics of the potential considered known. Analytical expressions are derived, which approximate the growth rates and the frequencies of the test modes as functions of the characteristics of the background turbulence. They lead to a new understanding of important aspects of the physics of drift type turbulence in the non-linear phase: structure generation and zonal flow modes. The main role in these processes is shown to be played by ion trapping.

We consider the drift instability in slab geometry with constant magnetic field. We start from the basic gyrokinetic equations for the distribution of electrons and ions

$$\partial_t f^\alpha - \boldsymbol{\nabla}\phi \times \mathbf{e}_z \cdot \boldsymbol{\nabla} f^\alpha + v_z \partial_z f^\alpha - \frac{e_\alpha}{m_\alpha}\left(\partial_z \phi\right)\partial_{v_z} f^\alpha = 0 \qquad (28)$$

where α represent the species ($\alpha = e, i$), ϕ is the potential, v_z is the velocity along the magnetic field and e_α, m_α are the charge and mass of the particles. The temperatures are considered constant with $T_e = T_i$ and a gradient of density is taken along x direction.

The solution for the potential in the zero Larmor radius limit is

$$\phi(\mathbf{x}, z, t) = \phi_0(\mathbf{x} - \mathbf{V}_* t, z), \qquad (29)$$

where ϕ_0 is the initial condition and $\mathbf{V}_* = T\partial_x[\ln(n_0)]/eB$ is the diamagnetic velocity produced by the gradient of the average density $n_0(x)$. This shows that the potential is not changed but displaced with the diamagnetic velocity. The wave-type solution corresponds to the drift waves that have $\omega = k_y V_*$ and are stable in this limit. The finite Larmor radius effects combined with the non-adiabatic response of the electrons destabilizes the drift waves. The frequency ω and the growth rate γ of the modes are

$$\omega = k_y V_*^{eff}, \tag{30}$$

$$\gamma = \frac{\sqrt{\pi}}{|k_z|\, v_{Te}} \frac{k_y^2 \left(V_* - V_*^{eff}\right) V_*^{eff}}{2 - \Gamma_0}, \tag{31}$$

$$V_*^{eff} = V_* \frac{\Gamma_0}{2 - \Gamma_0}, \tag{32}$$

where $\Gamma_0 = exp(-b)I_0(b)$, $b = k_\perp^2 \rho_L^2/2$ and ρ_L is the ion Larmor radius. The wave number components are k_i, $i = x, y, z$ and $k_\perp = \sqrt{k_x^2 + k_y^2}$. The gyro-average of the potential over the ion orbits produces the decrease of the effective diamagnetic velocity. The growth rate (31) has parabolic dependence on V_*^{eff} and it is positive for $V_*^{eff} \in (0, V_*)$. This conditions is fulfilled by all values of $k_\perp$ and all the modes are unstable. The wave number domain of unstable modes is very large, from values of the order $k_\perp \rho_L \cong 1$ to large values $k_\perp$. These are the characteristics of the linear (universal) drift instability on quiescent plasmas.

2.0.1 Trajectory diffusion and damping of small k modes

We consider a turbulent plasma with given statistical characteristics of the stochastic potential and we study linear test modes. The aim is to determine the effects of trajectory trapping or eddying produced by the $\mathbf{E} \times \mathbf{B}$ drift. The growth rates and the frequencies of the test modes are determined as functions of the statistical characteristics of the background turbulence with potential $\phi(\mathbf{x}, t)$. A wave type perturbation of the potential $\delta\phi(\mathbf{x}, z, t) = \phi_{k,\omega} \exp\left(i\mathbf{k} \cdot \mathbf{x} + ik_z z - i\omega t\right)$ is introduced. It is small $(\delta\phi \ll \phi)$ and thus it has a negligible influence on particle trajectories. Equation (28) is linearized around the turbulent state. The background potential is considered to be Gaussian with known Eulerian correlation or spectrum. The solutions for the perturbations of electron and ion densities are obtained using the characteristics method as integrals along particle trajectories in the background potential of the source terms determined by the density gradientwhere F_M^α is the Maxwell distribution of the velocities. The characteristics $\mathbf{x}^\alpha(\tau), z^\alpha(\tau)$ are the trajectories obtained by integrating the system of equation of motion backwards in time with the condition at time t, $\mathbf{x}^\alpha(t) = \mathbf{x}$, $z^\alpha(t) = z$

$$\frac{d\mathbf{x}^\alpha}{d\tau} = -\boldsymbol{\nabla}\phi(\mathbf{x}^\alpha, z^\alpha, \tau) \times \mathbf{e}_z \tag{33}$$

$$\frac{dz^\alpha}{d\tau} = v_z^\alpha \tag{34}$$

The background turbulence produces two modifications in the response. One consists in the stochastic $\mathbf{E} \times \mathbf{B}$ drift that appears in the trajectories and the other is

the fluctuation of the diamagnetic velocity due to the fluctuations of the density δn in the background turbulence

$$\widetilde{\mathbf{V}}_* = \frac{T}{en_0 B}\mathbf{e}_z \times \nabla \delta n$$

Both effects are important for ions while the response of the electrons is approximately the same as in quiescent plasma. They depend on the parameters of the turbulence.

The perturbed distribution function is averaged over the stochastic trajectories. The dispersion relation (quasi-neutrality condition) of a mode with frequency ω and wave number $\mathbf{k}$ is

$$2 + i\sqrt{\pi}\frac{\omega - k_y V_*}{|k_z|\, v_{Te}} = i\Pi\,\Gamma_0\left[\omega + V_*\left(k_y + ik_i k_j R_{ij}\right)\right]. \tag{35}$$

The background turbulence appears in this equation in the average propagator

$$\Pi = \int_t^{-\infty} d\tau\, \langle \exp\left(-i\mathbf{k}\cdot\mathbf{x}^\alpha(\tau)\right)\rangle \exp\left(i\omega(t-\tau)\right) \tag{36}$$

and in the tensor R_{ij}, which has the dimension of a length and is defined by

$$R_{ji}(\tau, t) \equiv \int_\tau^t d\theta' \int_{-\infty}^{\tau-\theta'} d\theta M_{ji}(|\theta|) \tag{37}$$

where M_{ij} is the Lagrangian correlation

$$M_{ji}(|\theta' - \theta|) \equiv \left\langle v_j\left(\mathbf{x}^i(\theta'), z, \theta'\right)\, \partial_2 v_i\left(\mathbf{x}^i(\theta), z, \theta\right)\right\rangle, \tag{38}$$

and v_j is the $\mathbf{E} \times \mathbf{B}$ drift velocity component. The summation rule over the repeated indices is used in Eq. (35). The average propagator (36) contains the effects of the stochastic trajectories and the tensor R_{ij} yields from the fluctuations of the diamagnetic velocity.

The propagator Π and the tensor R_{ji} are determined using the new statistical methods [22] that are able to describe the effects of trapping. The calculation of the average propagator is performed using simplified models that includes the main characteristics of the probability of displacements. It is so possible to capture the complicated nonlinear effects of strong turbulence in rather simple analytical expressions. The results can easily be improved by taking into account the statistics of test particles obtained with the nested subensemble method. This significantly more complicated approach that relies on numerical calculation of the averages does not changes qualitatively the results. We consider that the simple analytical expressions derived here give a more clear image on the complex nonlinear processes that appear in the drift turbulence evolution beyond the quasi-linear stage. The tensor R_{ji} is more complicated and it was not possible to derive a simplified analytical approximation for him. Moreover, it depends on the non-isotropy of the turbulence that is not taken into account in the present analysis.

The growth rate and the frequency of the drift modes give an image of the turbulence evolution starting from a weak initial perturbation with very broad wave

number spectrum. We show in the next sections that there is a sequence of processes that appear at different stages as transitory effects and that the drift turbulence has an oscillatory (intermittent) evolution.

The effective diamagnetic velocity (32) is a function of k due to finite Larmor radius of the ions. This means that the potential does not translate as in the solution (29) corresponding to $\rho_L = 0$, but it also changes due to k-dependence of the growth rate and of the effective diamagnetic velocity. However, there is an average V_*^{eff}, V_d that is of the order $V_d \lesssim V_*$. The time variation of the potential thus consists of an average translation with the velocity V_d and in the change of its shape. Two characteristic times are associated with this variation: the potential drift time $\tau_* = \lambda_c/V_d$ and the correlation time τ_c. λ_c is the correlation length of the background potential. τ_* is the characteristic time for the potential motion while τ_c accounts for the modification of the shape of the potential. The latter is essentially related to the growth rates of the modes and also depends on the width of the spectrum of the turbulence. As $\gamma \ll \omega$, the drift time is smaller, $\tau_c < \tau_c$. The ordering of the characteristic times for the drift turbulence in the quasilinear stage is

$$\tau_\parallel^e \ll \tau_* \ll \tau_c \ll \tau_{fl} \ll \tau_\parallel^i, \tag{39}$$

where $\tau_\parallel^e, \tau_\parallel^i$ are the parallel decorrelation times for electrons and ions ($\tau_\parallel^{e,i} = \lambda_\parallel/v_{th}^{e,i}$ with $\lambda_\parallel$ the parallel correlation length, and $v_{th}^{e,i}$ the thermal velocity), and $\tau_{fl} = \lambda_c/V$ is the characteristic time of flight of the particles over the perpendicular correlation length with the $\mathbf{E} \times \mathbf{B}$ drift that has the amplitude V (the eddying time). This ordering shows that the dynamics of the electrons is parallel and that the decorrelation of the ions is produced by the drift of the potential. There is no trapping because the time of flight is much larger than the decorrelation time.

The statistics of trajectories is Gaussian for these conditions and the diffusion of trajectories is isotropic. The diffusion coefficient is determined by the amplitude V of the stochastic $\mathbf{E} \times \mathbf{B}$ drift and by the decorrelation time as $D = V^2 \tau_*$. The average propagator (36) is

$$\Pi = -i\frac{1}{\omega + ik_i^2 D}. \tag{40}$$

The average tensor R_{ij} is zero.

The solution of the dispersion relation (35) shows that ω and V_*^{eff} are not changed [Eqs. (30), (32)] and that the growth rate becomes:

$$\gamma = \frac{\sqrt{\pi}}{|k_z|\, v_{Te}} \frac{k_y^2 \left(V_* - V_*^{eff}\right) V_*^{eff}}{2 - \Gamma_0} - k_i^2 D \frac{2}{2 - \Gamma_0}. \tag{41}$$

This is the well known result of Dupree [31], [32] which shows that a stabilizing contribution is produced by the ion diffusion in the background turbulence. This contribution is large for large k modes and can annihilate the first term determining the damping of the large k modes.

The evolution of the potential can be deduced from the growth rate (41). The modes with large k are continuously damped as the amplitude of the potential fluctuations increases. The width of the spectrum slowly decrease leading to a weak increase of τ_c. The maximum of the growth rate appears for $k_2\rho_L$ of a few unit and

10

slowly evolves to smaller values. Thus the amplitude of the potential fluctuations continues to increase while the correlation length remains smaller than ρ_L.

2.0.2 Trajectory structures and large scale correlations

The increase of the amplitude V of the stochastic $\mathbf{E} \times \mathbf{B}$ drift determines the change of the ordering of the characteristic times (39). When V becomes larger than the average velocity of the potential V_d the time of flight is smaller that the decorrelation time τ_*. In these conditions ion trapping or eddying appears. As we have shown this strongly influences the statistics of trajectories. The distribution of the trajectories is not more Gaussian due to trapped trajectories that form quasi-coherent structures. At this stage the trapping is weak in the sense that the fraction of trapped trajectories n_{tr} is much smaller than the fraction n_{fr} of free trajectories.

The probability of displacements $P(\mathbf{x}, t)$ was obtained using the nested subensemble method. It has a pronounced peaked shape compared to the Gaussian probability. The probability of displacements until decorrelation ($t < \tau_*$) is modeled by

$$P(x, y, t) = n_{tr} G(\mathbf{x}; \mathbf{S}) + n_{fr} G(\mathbf{x}; \mathbf{S}') \tag{42}$$

where $G(\mathbf{x}; \mathbf{S})$ is the 2-dimensional Gaussian distribution with dispersion $\mathbf{S} = (S_x, S_y)$. The first term describes the trapped trajectories. We have considered for simplicity their distribution as a Gaussian function but with small (fixed) dispersion that represents the average size of the structures. The shape of this function does not change much these estimations. The free trajectories are described by the secont term in Eq. (42). They have dispersion that grows linearly in time: $S'_i = S_i + 2D_i t$, $i = x, y$. The average propagator is

$$\Pi = -i \frac{1}{\omega + i k_i^2 D_i} \mathcal{F}, \tag{43}$$

where the factor $\mathcal{F}$ is determined by the average size of the trapped trajectory structures

$$\mathcal{F} \equiv \exp\left(-\frac{1}{2} k_i^2 S_i^2\right). \tag{44}$$

The tensor R_{ij} is zero for isotropic turbulence. In the anisotropic case, the non-diagonal component R_{xy} is nonzero and it strongly depends on the non-symmetry of the Eulerian correlation. Its contribution is small and will be neglected at this stage.

The solution of the dispersion relation (35) is

$$V_*^{eff} = V_* \frac{\Gamma_0 \mathcal{F}}{2 - \Gamma_0 \mathcal{F}} \tag{45}$$

$$\omega = k_y V_*^{eff} \tag{46}$$

$$\gamma = \frac{\sqrt{\pi}}{|k_z| v_{Te}} \frac{k_y^2 \left(V_* - V_*^{eff}\right) V_*^{eff}}{2 - \Gamma_0} - k_i^2 D \frac{2}{2 - \Gamma_0}. \tag{47}$$

Thus the effect of trajectory trapping appears in the effective diamagnetic velocity while the growth rate equation is not modified. The decrease of the effective diamagnetic velocity produces the displacement of the position of the maximum of γ

11

toward small k. The factor (44) determined by the size of the trajectory structures has a faster decay than Γ_0 and it leads in connection with the diffusive term to the damping of the modes with $k_y > 1/S_y$. Thus the maximum of γ moves to smaller k values of the order of $1/S_i$ and the size of the unstable k range decreases. The maximum growth rate decreases. The amplitude of the potential fluctuations continues to increase but with slower rate. This leads to the increase of the size of the trajectory structures, which produces the displacement of the unstable k range to smaller values.

In conclusion, the trapping of the ions determines the increase of the correlation length of the potential. The average frequency (proportional with k_2) also decreases. In this nonlinear stage of the turbulence, the evolution becomes slower (the growth rates are much smaller) and leads to ordered states (narrower spectra with maximum at smaller k).

2.0.3   Ion flows and turbulence damping

The evolution of the potential determines the increase of the fraction of trapped ions. This produces another effect on the test modes. The potential continues to move with the average diamagnetic velocity V_d. This determines an average flux of the trapped particles $n_{tr}V_d$. As the $\mathbf{E} \times \mathbf{B}$ drift has zero divergence, the probability of the Lagrangian velocity is time invariant, $i.\ e.$ it is the same with the probability of the Eulerian velocity. The average Eulerian velocity is zero and thus the flux of the trapped ions that move with the potential has to be compensated by a flux of the free particles. These particles have an average motion in the opposite direction with a velocity V_{fr} such that

$$n_{tr}V_d + n_{fr}V_{fr} = 0. \tag{48}$$

The velocity on structures method that we have recently developed shows that the probability of the displacements splits in two components that move in opposite direction. The central peak moves with the velocity of the potential V_d while the marginal part becomes a function that strongly elongates in the y direction and moves in the opposite direction with a velocity that increases with the increase of the fraction of trapped ions. The diffusion coefficients D_x, D_y are strongly different, with $D_y \gg D_x$. Also the distribution of the trapped ions becomes anisotropic with $S_y > S_x$.

Thus, opposite ion flows are generated by the moving potential in the presence of trapping.

The distribution of displacements is approximated as in Eq. (42) by two Gaussian functions but taking into account the ion flows (48)

$$P(x, y, t) = n_{tr}G(x, y - V_d t; S_x, S_y) + n_{fr}G(x, y - V_{fr}t; S'_x, S'_y). \tag{49}$$

The average propagator is

$$\Pi = -i\mathcal{F}\left[\frac{n_{fr}}{\omega + k_y V_{fr} + ik_i^2 D_i} + \frac{n_{tr}}{\omega + k_y V_*}\right]. \tag{50}$$

The solution of the dispersion relation becomes

$$\omega = k_y V_*^{eff}, \tag{51}$$

$$V_*^{eff} = V_* \frac{\Gamma_0 \mathcal{F}(1-n) + 2n}{2 - \Gamma_0 \mathcal{F}}, \tag{52}$$

$$
\begin{aligned}
\gamma &= \frac{\sqrt{\pi}}{|k_z| v_{Te}} \frac{k_y^2 \left(V_* - V_*^{eff}\right)\left(V_*^{eff} - nV_*\right)}{2 - \Gamma_0 \mathcal{F}} \\
&\quad - k_i^2 D_i \frac{2 - \Gamma_0 \mathcal{F} n_{tr}}{2 - \Gamma_0 \mathcal{F}} \\
&\quad + k_i k_j R_{ij} \frac{2V_*}{(2 + n(2 - \Gamma_0 \mathcal{F}))(2 - \Gamma_0 \mathcal{F})}.
\end{aligned}
\tag{53}
$$

The last term in Eq. (53), determined by the fluctuations of the diamagnetic velocity, is analysed in the next section. The effects of the ion flows appear through the fraction of trapped ions n_{tr} that is contained in $n \equiv n_{tr}/n_{fr}$. The ion flows influence both the effective diamagnetic velocity and the growth rate. The drive term of the drift instability (the first term in Eq. (53), γ_1) is still a parabolic function of V_*^{eff} but the range of positive γ_1 is reduced to the interval $(nV_*^{eff},\ V_*^{eff})$. This determines the decrease of the maximum of γ_1. The effective diamagnetic velocity can be written as

$$V_*^{eff}(n) = V_*^{eff}(0) + nV_* \tag{54}$$

which shows that the ion flows determine the increase of V_*^{eff} for all values of k. V_*^{eff} becomes larger that V_* first for small k. This determines the damping of these modes. As n increases modes with larger k are damped and, for $n = 1$, $\gamma_1 < 0$ for any k. The diffusive term also contributes to the damping so that γ becomes negative for smaller values of n.

In conclusion, the ion flows determine the decrease of the correlation length of the potential and a slower increase of its amplitude, and eventually the decay of the drift turbulence. This is the effect of trajectory trapping, which in the previous stage of the evolution has produced the large scale potential cells.

2.0.4 Generation of zonal flow modes

The fluctuations of the density produced by the background turbulence determine the last term in the growth rate (53). This term appears due to the correlation of the nonadiabatic ion response with the perturbation $\delta\phi$ through ion trajectories and is given by Eqs. (37), (38). The component R_{11} is very interesting because it generates modes with $k_2 = 0$ and $\omega = 0$, if this term is positive. This are static oscillations in the direction of the average density gradient, which are known as zonal flow modes and have been intensely studied in the last decade (see [35] and the references therein). The driving term (first term in (53), γ_1) for this modes is zero but they would appear from the dynamics of the drift turbulence. It is thus important to analyze this term and to see if it can generate zonal flow modes.

The average (37) is much more complicated than the propagator and it was not possible to obtain analytical approximation for R_{ij}. It was numerically estimated using the nested subensemble approach for different characteristics of the background turbulence. In the quasilinear turbulence all the components $R_{ij} = 0$. When trapping appears ($V > V_d$, $n_{tr} \ll n_{fr}$), this average is not changed as long as the background turbulence is isotropic. The anisotropy can generate non-diagonal

components of the tensor but they are small compared to the other terms in Eq. (53) for $n \ll 1$. As n increases and the ion flows become important in the effective diamagnetic velocity and in the growth rate γ_1, an anisotropy is generated by the difference in the average velocity of the trapped ions V_d and the average velocity of the free ions $V_{fr} = -nV_d$. This leads to nonzero values of R_{11} components of the tensor. This component is positive and it determines the growth of modes with $k_y = 0$ and $\omega = 0$. The dependence on n of R_{11} shows first an increase followed by the decrease. When $n = 1$, the average velocities of the trapped and free ions are equal and the ion flows are symmetrical. R_{11} is zero in this conditions.

We note that the effects of the fluctuations of the density induced by the background turbulence are rather complex and very sensitive to the details of the turbulence. The present results are first evaluations and a more detailed study in necessary, which has to determine the evolution of the characteristics of the turbulence and especially of the anisotropy. However, a clear connection of the zonal flow modes with the ion flows induced by the moving potential could already be deduced.

In conclusion, we have shown that trajectory trapping has a strong and complex influence on the evolution of the turbulence. Trapping determines the increase of potential cell and the decrease of the spectrum width that forms quasi-coherent structures. The reversed effect appears later in the evolution: ion trapping combined with the motion of the potential with the average diamagnetic velocity destroys the large potential structures and produces the damping of the drift modes. In the same time, the fluctuations of the diamagnetic velocity and the ion flows determine the growth of zonal flows modes.

A different physical perspective on the nonlinear evolution of drift waves is obtained. The main role is played by the trapping of the ions in the stochastic potential that moves with the diamagnetic velocity. We have shown that trapped trajectories form quasi-coherent structures, which determine non-Gaussian distribution of the displacements with a frosen central maximum. Trapping in a moving potential determines flows of the ions when the amplitude of the $\mathbf{E} \times \mathbf{B}$ velocity is larger than the average diamagnetic velocity. The trapped ions move with the potential while the other ions drift in the opposite direction. These opposite (zonal) flows compensate such that the average velocity is zero. The first effect of trapping in the evolution of the turbulence appears when the fraction of trapped ions is small and the ion flows are negligible. The trapped ions determine the evolution of the turbulence toward large wave lengths (the inverse cascade). They also determine a slower increase of the amplitude of the potential fluctuations and also the evolution to more ordered states. The influence of the ion flows produced by the moving potential appears later in the evolution of the turbulence. The ion flows determine the damping of the small k modes, the decay of the growth rate and eventually the damping of the drift modes with any k.The ion flows also seem to determine transitory zonal flow modes (with $k_y = 0$ and $\omega = 0$) in connection with the fluctuation of the diamagnetic velocity due to the background turbulence. Thus, in this perspective, there is no causality connection between the damping of the drift turbulence and the zonal flow modes. Both processes are produced by ion trapping in the moving potential, which determines ion flows. The drift turbulence does not saturate but has an oscillatory evolution.

References

[1] McComb W D 1990 *The Physics of Fluid Turbulence* (Clarendon, Oxford)

[2] Bouchaud J P and George A 1990 *Phys. Reports* **195** 128

[3] Krommes J A 2002 *Phys. Reports* **360** 1

[4] Majda A J and Kramer P R 1999 *Phys. Reports* **314** 237

[5] Falkovich G, Gawedzki K and Vergassola M 2001 *Rev. Mod. Phys.* **73** 913

[6] Kraichnan R H 1970 *Phys. Fluids* **19** 22

[7] Vlad M and Spineanu F 2004 *Phys. Rev. E* **70** 056304

[8] Vlad M, Spineanu F, Misguich J H and Balescu R 1998 *Phys. Rev. E* **58** 7359

[9] Basu R, Jessen T, Naulin V, Rasmunssen J J 2003 *Phys. Plasmas* **10** 2696

[10] Vlad M, Spineanu F, Misguich J H and Balescu R 2000 *Phys. Rev. E* **61** 3023

[11] Vlad M, Spineanu F, Misguich J H and Balescu R 2001 *Phys. Rev. E* **63** 066304

[12] Pommois P, Veltri P. Zimbardo G 2001 *Phys. Rev. E* **63** 066405

[13] Vlad M, Spineanu F, Misguich J H, Reusse J-D, Balescu R, Itoh K and Itoh S-I 2004 *Plasma Phys. Control. Fusion* **46** 1051

[14] Vlad M and Spineanu F 2005 *Plasma Phys. Controlled Fusion* **47** 281

[15] Vlad M, Spineanu F, Misguich J H and Balescu R 2002 *Nuclear Fusion* **42** 157

[16] Taylor G I 1921 *Proc. London Math. Soc.* **20** 196

[17] Littlejohn R G 1982 *J. Math. Phys.* **23** 742

[18] Hahm T S, Lee W W and Brizard A 1988 *Phys. Fluids* **31** 1940.

[19] Pinches S D et al 2004 *Plasma Phys. Control. Fusion* **46** B187

[20] Idomura Y, Wakatani M, Tokuda S 2000 *Phys. Plasmas* **7** 3551

[21] Vlad M., Spineanu F., Misguich J.H., Balescu R., *Phys.Rev.E* **58** (1998) 7359.

[22] Vlad M. and Spineanu F., *Phys. Rev. E* **70** (2004) 056304.

[23] Balescu R., Aspects of Anomalous Transport in Plasmas, Institute of Physics Publishing (IoP), Bristol and Philadelphia, 2005.

[24] Vlad M., Spineanu F., Misguich J. H. and Balescu R., *Nuclear Fusion* **42** (2002) 157.

[25] Vlad M. and Spineanu F., *Physica Scripta* **T107** (2004) 204.

[26] Petrisor I., Negrea M., Weyssow B., *Physica Scripta* **75** (2007) 1.

[27] Vlad M., Spineanu F., Misguich J.H., Balescu R., *Physical Review E* **67** (2003) 026406.

[28] Vlad M., Spineanu F., Benkadda S., *Phys. Rev. Letters* **96** (2006) 085001.

[29] Vlad M., Spineanu F., Benkadda S., *Phys. Plasmas* **15** (2008) 032306.

[30] Vlad M., Spineanu F., Benkadda S., *Plasma Phys. Control. Fusion* **50** (2008) 065007.

[31] Dupree T. H., *Phys. Fluids* **9** (1966) 1773.

[32] Dupree T. H., *Phys. Fluids* **15** (1972) 334.

[33] Spineanu F., Vlad M., *Phys. Letters A* **133** (1988) 319.

[34] Vlad M., Spineanu F., Misguich J.H., *Plasma Phys. Control. Fusion* **36** (1994) 95.

[35] Diamond P. H., Itoh S.-I., Itoh K., Hahm T. S., *Plasma Phys. Control. Fusion* **47** (2005) R35-R161.

BS-4A: Portal ITM

Director Proiect: Vasile Pais

EFDA Task Agreements: ITM-09-ISIP-T10, ITM-09-ISIP-T1, ITM-09-ISIP-T3

1.   Introduction

The aim of the project is to **extend the ITM Web Portal**, by integrating several additional tools, allowing users to manage software projects.

The main objectives envisaged for 2009:
1. *Extending the ITM web portal* (ITM-09-ISIP-T10)
2. *Installation and update of Web Portal related tools (ITM-09-ISIP-T1)*

With respect to these objectives, the work was focused on the following main activities:

i)   Integrating external tools with the existing infrastructure, allowing project management activities;

ii)   Updating the previously installed software;

iii)   Development and implementation of a global access policy for all the portal components.

2. Summary of Results

The main objective for the period June- December 2009 refers to the development and implementation of a global access policy for all the portal components.

A globally unique access policy was required in order to be able to set user rights in a single point of the system and be sure that this setting is respected in all the portal components. Thus, by making the user member of a certain/or several groups, he will gain a series of access rights, reflected in what pages he will be able to access, what portal components he will be able to see and what virtual file system rights he will receive.

3. Scientific progress report

In the context of the ITM task ITM-09-ISIP-T1, software was installed on the ITM Gateway in order to provide software project management. Various versioning systems have been

studied and tested. As a conclusion of these tests, the Subversion versioning system was chosen and installed on the Gateway. Furthermore, the GForge platform was integrated in the Portal and custom modules were written.

In addition, an ITM access policy has been developped and implemented as the basis for software project access.

These roles are described below:

- **itm_member**:
    o RELEASE = RO
    o RELEASE_CANDIDATE = N
    o TRUNK = N
    o BRANCH = N
    o FORUMS = RW
    o Wiki = RO
    o Documents = RO
    o Bugs = RW

- **itm_project_member** (this means member of ISIP, IMP...):
    o RELEASES = RO
    o RELEASE_CANDIDATE = RO
    o TRUNK = N
    o BRANCH = N
    o FORUMS = RW
    o Wiki = RO
    o Documents = RO
    o Bugs = RW

- **software_project_developer** (task_member + others) :
  - RELEASE = RO
  - RELEASE_CANDIDATE = RO
  - TRUNK = RO
  - BRANCH = RW
  - FORUMS = RW
  - Wiki = RW
  - Documents = RW
  - Bugs = RW
- **software_project_admin** (task_coordinator/other):
  - RELEASE = RW
  - RELEASE_CANDIDATE = RW
  - TRUNK = RW
  - BRANCH = RW
  - FORUMS = RW
  - Wiki = RW
  - Documents = RW
  - Bugs = RW
- **support_group** (members of ISIP-T1):
  - RELEASES = RO
  - RELEASE_CANDIDATE = RO
  - TRUNK = N
  - BRANCH = N
  - FORUMS = RW
  - Wiki = RW
  - Documents = RW
  - Bugs = RW

·   **tf_leader**

o   RW to all

This policy has been implemented in GForge and became effective in existing pojects. New projects will start with this policy as the default and the system tries to reinforce it automatically when possible. However, interventions may be required from the project administrator in some cases.

In order to guarantee these access rights, several modules were developed in the form of SVN authentication/authorization hooks and Gforge hooks.

The current architecture of the portal, with its components in place can be summarized in the following diagram:
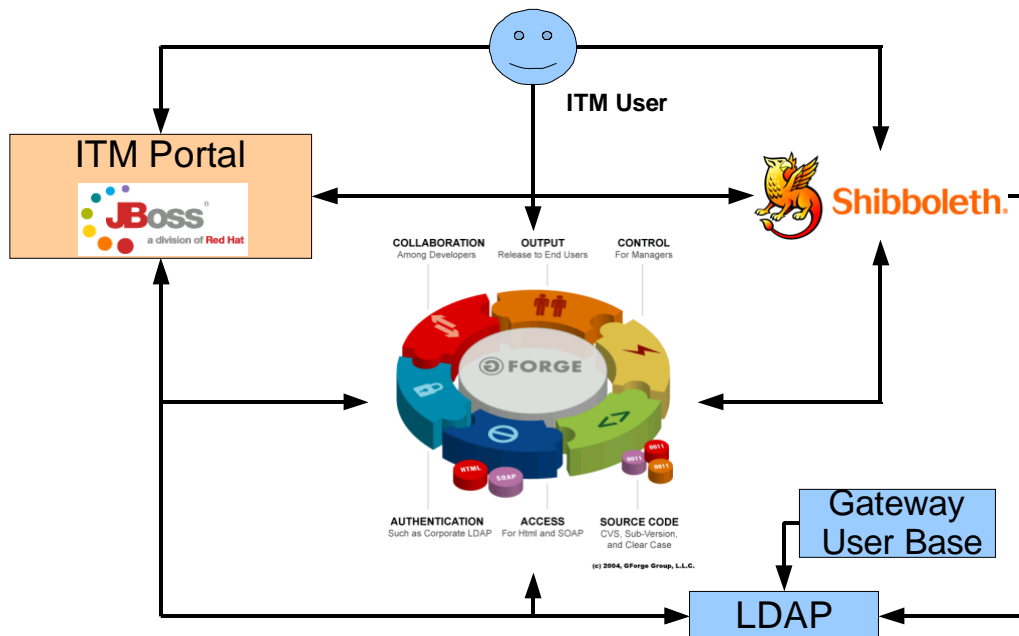
This diagram shows the interactions between the various Portal components. Each interraction must be controlled by the access policy, by checking access rights at each component. Thus, a user may have several access rights at Portal level, but completely different access rights at Gforge level. Therefore, even though it may arrive there from the

Jboss based Portal, the Gforge component must authorize each request based on the specific part of the policy that strictly concerns it.

The implementation of the policy had to take into consideration the various aspects of the objects involved:

- The components are written in different languages:
    - o Jboss portal is a java based application
    - o Gforge is a PHP based application
    - o Subversion is a native application, integrated directly with the Apache web server
- The objects controlled can be manipulated in several ways:
    - o Portal pages can be seen and modified
    - o Software project files, stored in SVN, can support the following operations: read, add new version, add new branch, add new tag

Taking this into consideration, the policy was defined in a system independent way, where possible, or it contains speciffic references to the components involved.

BS-4B: Date atomice pentru ioni cu paturi _d_ incomplete

Director Proiect: Viorica Stancalie

EFDA Task Agreement TFL: ITM-09-TFL2-AMNS-T2, ITM-09-TFL2-AMNS-T3

Introduction

The aim of the project is to **provide atomic data for the open d-shell elements and to contribute to the strategy for implementing an ITM (software) capacity for AMNS data (ITM-09-TFL2-AMNS-T2, ITM-09-TFL2-AMNS-T3)** .

The present work refers to the calculation of atomic data for plasma spectroscopy in strong collaboration with the Atomic Data Analysis Structrure International Project (**ADAS**). As member of **ADAS** consortium, our work contribute to the development of **ADAS database**.

Two main objectives were been envisaged for 2009:

3. *Contribution of data in each of sub groups* (Atomic, molecular, surface, and Nuclear) (January-December 2009)

   WP09-ITM-TFL2-AMNS-T2

4. *Development of modules to provide AMNS data to ITM-TF codes*(January-June 2009):

   WP09-ITM-TFL2-AMNS-T3

With respect to these objectives, our work was focused on the following main activities:

iv)   Atomic data for the iron peak elements which have open *d shells.* The emphases is put on Co^{3+} $1s^22s^22p^63s^23p^63d^6$ (^5D) configuration. Preliminary results on atomic data (energy levels, transition probabilities, line strengths) for this ion have already been obtained in LS coupling. In the present work we describe the salient feature of the theory and computations as they pertain to large-scale Bret Pauli R-matrix Method calculations for this complex atomic system. Identification of fine structure energy is discussed.

v)   To aid to data delivery, a common software interface for the ITM codes will be suggested. This proposal makes use of the existing: ITM Gateway facilities for data storage, Relational databases, MDSplus, HDF5, ADAS, and ITM UAL. This task has been completed in June 2009.

Summary of Results

The main objective for the period June- December 2009 refers to

<u>*Large scale Breit-Pauli R-matrix collision calculations for Co^{3+}.*</u>

Ab initio theoretical calculations are reported for the electric (E1) dipole allowed and intercombination fine structure transitions in Co IV using the Breit–Pauli *R*-matrix (BPRM) method. We restricted our calculation to 136 bound fine structure levels. In addition to the relativistic effects, the intermediate coupling calculations include extensive electron correlation effects that represent the complex configuration interaction (CI). For bound-

bound transitions the BPRM method, based on atomic collision theory, entails the computation of the CI wavefunctions of the atomic system as an (electron+target ion) complex. The target ion Co IV is represented by an eigenfunction expansion of 16 fine structure levels dominated by the spectroscopic configuration $3d^6$, and a number of correlation configurations. Co IV bound levels are obtained with angular and spin symmetries $SL\pi$ and $J\pi$ of the (e + Co V) system such that $2S + 1 = 7,5,3,1$, $L \leq 8$, $J \leq 7$. The bound levels are obtained as solutions of the Breit-Pauli (e + ion) Hamiltonian for each $J\pi$, and are designated according to the 'collision' channel quantum numbers. A major task has been the identification of these large number of bound fine structure levels in terms of standard spectroscopic designations. A new scheme, based on the analysis of quantum defects and channel wavefunctions, has been developed. The identification scheme aims particularly to determine the completeness of the results in terms of all possible bound levels with $n \leq 10$, $l \leq n - 1$, for applications to analysis of experimental measurements and plasma modeling. Preliminary results are presented and the accuracy of the results is discussed. A comparison of the dipole length and velocity oscillator strengths is presented, indicating an uncertainty of 10–20% for most transitions.

The Breit-Pauli R-matrix calculation follows the diagram below:
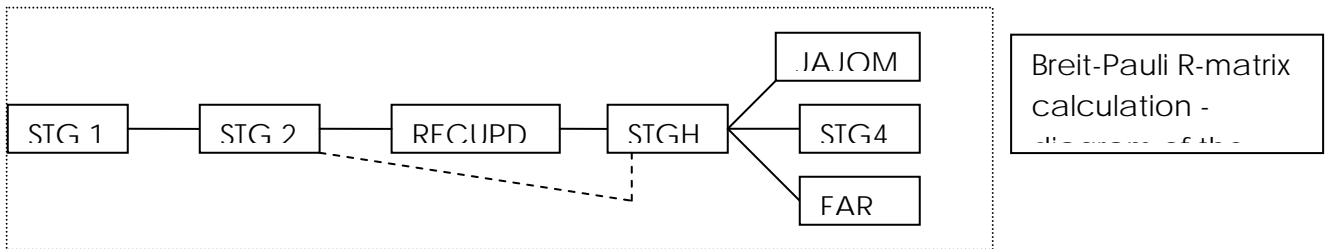
The program modules are run sequentially as outlined in the figure. Calculation can be in LS-coupling, or in intermediate coupling using optional route through RECUPD.

Scientific progress report

   I.   *Briet-Pauli R-matrix Method*

   II. Our aim is to calculate scattering observables from electron collisions with Co^{3+} $1s^2 2s^2 2p^6 3s^2 3p^6 3d^6$ (^5D) configuration (Eq. 1):

$e^- + Co^{3+} (3p^6 3d^6\ ^5D) \rightarrow Co^{2+} *(3p^5\ 3d^8, 3p^5\ 3d^7 4s\ or\ 3p^5\ 3d^7 4p)$

$$\Downarrow \qquad\qquad\qquad\qquad (1)$$

$Co^{3+}(3p^6 3d^6, 3p^6 3d^5 4s\ or\ 3p^6 3d^5 4p) + e^-$
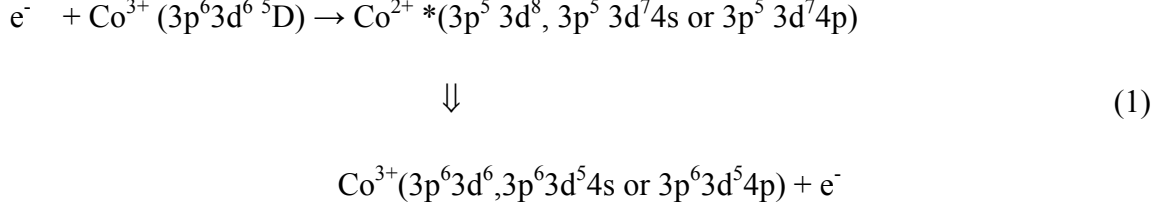
The general theory for the calculation of bound states in the close coupling (CC) approximation of atomic collision theory, using the R-matrix method, is described by Burke and Seaton [1] and Seaton [2]. The relativistic extension of the R-matrix method in the breit-Pauli approximation are discussed by Scott and Taylor [3].

Following standard collision theory nomenclature, we refer to the (e + ion) complex in terms of the ,target' ion, with N bound electrons, and a ,free' electron that may be either bound or continuum. The total energy of the system is either negative or positive; negative eigenvalues of the (N+1)-electron Hamiltonian correspond to bound states of the (e+ion) system. In the coupled channel or close coupling (CC) approximation the wavefunction expansion, $\Psi(E)$, for a total spin and angular symmetry $SL\pi$ or $J\pi$, of the (N+1) electron system is represented in terms of the target ion states as:

$$\Psi_E(e + ion) = A\sum_i \chi_i(ion)\theta_i + \sum_j c_j \Phi_j \qquad (2)$$

where χ_i is the target ion wave function in a specific state $S_i L_i \pi_i$ or level $J_i \pi_i$ and θ_i is the wave function for the (N+1)th electron in a channel labeled as $S_i L_i (J_i)\pi_i k_i^2 l_i (SL\pi)[J\pi]; k_i^2 (= \varepsilon_i)$ is the incident kinetic energy. In the second sum the Φ_j's are correlation wavefunctions of the (N+1) electron system that (a) compensate for the orhogonality conditions between the continuum and the bound orbitals, and (b) represent additional short-range correlation that is often of crucial importance in scattering and radiative CC calculations for each $SL\pi$.

The functions $\Psi(E)$ are given by the R-matrix method in an inner region $r << a$. These are bounded at the origin and contain radial functions that satisfy a logarithmic boundary condition at $r = a$. In the outer region $r > a$ the inner region functions are matched to a set of linearly independent functions that correspond to all possible (e + ion) channels of a

given symmetry $SL\pi$ or $J\pi$. The outer region wavefunctions are computed for all channels, $(C_t\ S_t\ L_t\ \pi_t)$ εl, where C_t is the target configuration, and used to determine the individual channel contributions (called „channel weights').

In the relativistic BPRM calculations the set of $SL\pi$ are recoupled to obtain (e+ion) levels with total $J\pi$, followed by diagonalisation of the (N+1)-electron Hamiltonian,

$$H^{BP}_{N+1}\Psi = E\Psi \tag{3}$$

The BP Hamiltonian is

$$H^{BP}_{N+1} = H_{N+1} + H^{mass}_{N+1} + H^{Dar}_{N+1} + H^{so}_{N+1} \tag{4}$$

where H_{N+1} is the noonrelativistic Hamiltonian,

$$H_{N+1} = \sum_{i=1}^{N+1}\left\{-\nabla^2_i - \frac{2Z}{r_i} + \sum_{j>i}^{N+1}\frac{2}{r_{ij}}\right\} \tag{5}$$

and the additional terms are the one-body terms, the mass correction term, the Darwin term and the spin-orbit term respectively. Spin-orbit interaction, H^{so}_{N+1}, splits the LS terms into fine-structure levels labeled $J\pi$, where J is the total angular momentum. Other terms of the Breit-interaction

$$H^B = \sum_{i>j}\left[g_{ij}(so+so') + g_{ij}(ss')\right] \tag{6}$$

Representing the two-body spin-spin and the spin-other-orbit interactions are not included.

The positive and negative energy states (Eq. 2) define continuum or bound (e + ion) states,

$$
\begin{aligned}
&E = k^2 \rangle 0 \rightarrow continuum \quad (scattering) \quad channel\\
&E = -\frac{z^2}{v^2}\langle 0 \rightarrow \quad bound \quad state
\end{aligned}
\tag{7}
$$

where v is the effective quantum number relative to the core level. If $E < 0$ then all continuum channels are ‚closed' and the solutions represent bound states. Determination of the quantum defect ($\mu(l)$), defined as $v_i = n - \mu(l)$, where v_i is relative to the core level $S_i\ L_i\ \pi_i$, is helpful in estabilshing the l-value associated with a given channel (level).

At E < 0 a scattering channel may represent a bound state at the proper eigenvalue of the Hamiltonian (Eq.3). A large number of channels are considered for the radiative process of Co IV. Each $SL\pi$ or $J\pi$ symmetry is treated independently and corresponds to a large number of channels. Therefore, the overall configuration interaction included in the total (e + ion) wavefunction expansion is quite extensive. This is the main advantage of the CC method in reperesentng electron correlation accurately.

a) Level identification and coupling scheme

The BPRM calculations in intermediate coupling employ the pair-cpoupling representation

$$S_i + L_i \rightarrow J_i$$

$$J_i + l \rightarrow K \tag{8}$$

$$K + s \rightarrow J$$

where the „i" refers to the target ion level and l, s are the orbital angular momentum (partial wave) and spin of the additional electron. According to designations of a collision complex, a channel is fully specified by the quantum numbers

$$\left(S_i L_i J_i\right)\pi_i \varepsilon_i l_i Ks\left[J\pi\right] \tag{9}$$

The main problem in identification of the fine structure levels stems from the fact that the bound levels are initially given only as eigenvalues of the (e + ion) Hamiltonian of a given symmetry $J\pi$. Each level therefore needs to be associated with the quantum numbers characterising a given collision channel. Subsequently, three main parameters are to be determined: (i) the parent or the target ion level, (ii) the orbital, effective and principal quantum numbers (l, ν, n) of the (N+1)th electron, and (iii) the symmetry, $SL\pi$. The task is relatively straightforward for simple few-electron atomic system. However when a number of mixed bound levels fall within a given interval (ν, ν + 1), for the same $J\pi$, the quantum numbers and the magnitude of the components in all associated channels must be analysed. A scheme for identification of level is developed [4] that rests mainly on an analysis of quantum defects of bound levels and their orbital angular momenta, and the percentage of the total wavefunction in all channels of a given $J\pi$.

Following level identification, futher work is needed to enable a direct correspondance with standard spectroscopic designations that follow different coupling schemes, such as between *LS* and *JJ*, appropriate for atomic structure calculations as, for example, in the NIST tables of observed energy levels [5]. The correspondence provides the check for completeness of calculated set of levels or the levels missing. The level identification procedure involves considerable manipulation of the bound level data and, although it has been encoded for general applications, still requires analysis and interpretation of problem cases of highly mixed levels that are difficult to identify.

b)   Oscillator strengths and transition probabilities

The oscillator strength (or potoionization cross section) is proportional to the generalized line strength defined, in either length form or velocity form, by the equations

$$S_L = \left| \left\langle \Psi_f \left| \sum_{j=1}^{N+1} r_j \right| \Psi_i \right\rangle \right|^2 \tag{10}$$

and

$$S_V = \omega^{-2} \left| \left\langle \Psi_f \left| \sum_{j=1}^{N+1} \frac{\partial}{\partial r_j} \right| \Psi_i \right\rangle \right|^2 \tag{11}$$

In these equations ω is the incident photon energy in Rydberg units, and Ψ_i and Ψ_j are the wave functions representing the initial and final states respectively. The boundary conditions satisfied by a bound state with negative energy correspond to exponentially decaying partial waves in all 'closed' channels, whilst those satisfied by a free or continuum state correspond to a plane wave in the direction of the ejected electron momentum $\hat{\underline{k}}$ and igoing waves in all open channels.

Using the energy difference, E_{ji}, between the initial and final states, the oscillator strength, f_{ij}, for the transition can be obtained from *S* as

$$f_{ij} = \frac{E_{ji}}{3g_i} S \tag{12}$$

and the Einstein's A-coefficient, A_{ji}, as

$$A_{ji}(a.u.) = \frac{1}{2}\alpha^3 \frac{g_i}{g_j} E_{ji}^2 f_{ij} \qquad (13)$$

where α is the fine structure constant, and g_i, g_j are the statistical weght factors of the initial and final states, respectively. In terms of c.g.s. unit og time,

$$A_{ji}(s^{-1}) = \frac{A_{ji}(a.u.)}{\tau_0} \qquad (14)$$

where $\iota_0 = 2.4191\ 10^{-17} s$ is the atomic unit of time.

II.   *Computations*

The target wavefunctions of Co IV were obtained from an atomic structure calculation using the CIV3 program. Present work employs optimisation of nine spectroscopic orbitals corresponding to the 136-term LS basis set of $3d^6$. The set of correlation configurations used were $3d^6$, $3d^5 4s$, $3d^5 4p$, $3p^5\ 3d^8$, $3p^5\ 3d^7\ 4s$ and $3p^5\ 3d^7\ 4p$. Table I lists the 136 LS structure energies of Co IV obtained in the first stage of computation (LS coupling).

Table I. The *LS* term energies (in Rydberg), relative to the $3d^6\ {}^5D$ ground state of Co IV, and the comparison with the observed values (NIST, http://www.physics.gov).

Index	*Term*	Calc.	Obs.	Adjust.
1	${}^5D^e$	0.000000	0.000000	0.000000
2	${}^3P^e$	0.232012	0.211109	-0.020903
3	${}^3H^e$	0.254847	0.212702	-0.042144
4	${}^3F^e$	0.258573	0.228077	-0.030496
5	${}^3G^e$	0.302809	0.262573	-0.040236

6	$^1I^e$	0.381807	0.321910	-0.059897
7	$^3D^e$	0.369626	0.326544	-0.043082
8	$^1G^e$	0.359494	0.328659	-0.030835
9	$^1S^e$	0.384711	0.372023	-0.012688
10	$^1D^e$	0.439201	0.380223	-0.058978
11	$^1F^e$	0.526638	0.455752	-0.070887
12	$^3P^e$	0.608396	0.536653	-0.071743
13	$^3F^e$	0.609042	0.539664	-0.069378
14	$^1G^e$	0.701205	0.613190	-0.088015
15	$^7S^e$	0.876278	0.819568	-0.056709
16	$^1D^e$	0.932537	0.825619	-0.106918
17	$^5S^e$	1.032664	0.93092	-0.101744
18	$^5G^e$	1.268811	1.171655	-0.097156
19	$^5P^e$	1.281603	1.204602	-0.077001
20	$^5D^e$	1.337910	1.238279	-0.099631
21	$^3G^e$	1.373155	1.245645	-0.127510
22	$^3P^e$	1.385946	1.278744	-0.107202
23	$^3D^e$	1.442227	1.312401	-0.129825
24	$^3I^e$	1.465373	1.343991	-0.121381
25	$^3D^e$	1.473921	1.370388	-0.103533
26	$^1I^e$	1.517558	1.380534	-0.137024

27	$^5F^e$	1.482440	1.381337	-0.101104
28	$^3F^e$	1.487254	1.393864	-0.093390
20	$^7P^0$	1.469354	1.420613	-0.048741
30	$^1D^e$	1.526041	1.419555	-0.106486
31	$^1F^e$	1.539417	1.429740	-0.109676
32	$^3H^e$	1.548485	1.439397	-0.109088
33	$^3G^e$	1.573892	1.449529	-0.124363
34	$^3F^e$	1.586770	1.455915	-0.130855
35	$^1H^e$	1.600661	1.478729	-0.121932
36	$^1G^e$	1.626130	1.486283	-0.139847
37	$^3F^e$	1.613371	1.487205	-0.126166
38	$^5P^0$	1.583567	1.498706	-0.084861
39	$^1F^e$	1.665542	1.523996	-0.141546
40	$^3S^e$	1.672652	1.541715	-0.130937
41	$^3D^e$	1.742106	1.620272	-0.121834
42	$^1D^e$	1.794380	1.657450	-0.136930
43	$^3G^e$	1.848031	1.708994	-0.139037
44	$^1G^e$	1.900236	1.745875	-0.154361
45	$^5G^0$	1.829206	1.748352	0.080854
46	$^5H^0$	1.856326	1.770026	-0.086300
47	$^5F^0$	1.862659	1.779232	-0.083426

48	$^5D^0$	1.848107	1.785585	-0.062523
49	$^5S^0$	1.845255	1.788173	-0.057082
50	$^3F^0$	1.895127	1.801128	-0.093999
51	$^5P^0$	1.874927	1.803819	-0.071108
52	$^3H^0$	1.911279	1.806143	-0.105136
53	$^3P^0$	1.896513	1.817085	-0.079427
54	$^5F^0$	1.919270	1.829743	-0.089527
55	$^3G^0$	1.961043	1.843162	-0.117881
56	$^5D^0$	1.936416	1.848556	-0.087860
57	$^3D^0$	1.937701	1.850936	-0.086765
58	$^5P^0$	1.946842	1.860584	-0.086258
59	$^3D^0$	1.965757	1.871586	-0.094171
60	$^3F^0$	1.982688	1.879419	-0.103269
61	$^3S^0$	2.001128	1.892639	-0.108488
62	$^3P^0$	2.028364	1.916465	-0.111899
63	$^3I^0$	2.034403	1.931343	-0.103059
64	$^1H^0$	2.041950	1.942073	-0.099877
65	$^3F^0$	2.023999	1.949238	-0.074760
66	$^3H^0$	2.058427	1.949733	-0.108694
67	$^3P^0$	2.063099	1.968548	-0.094552
68	$^3D^e$	2.109511	1.96880	-0.140630

69	$^1G^0$	2.060233	1.969253	-0.090980
70	$^3G^0$	2.066941	1.982587	-0.084354
71	$^5G^0$	2.073433	1.981887	-0.091545
72	$^3D^0$	2.077744	1.980873	-0.096871
73	$^3D^0$	2.080668	1.986431	-0.094238
74	$^1I^0$	2.117976	1.986042	-0.131934
75	$^5F^0$	2.085667	1.990551	-0.095116
76	$^3F^0$	2.086075	1.996376	-0.089700
77	$^3H^0$	2.101476	2.048511	-0.052964
78	$^3H^0$	2.177273	2.022297	-0.154976
79	$^5D^0$	2.095465	2.006568	-0.088896
80	$^1D^e$	2.161682	2.004161	-0.157522
81	$^3G^0$	2.107722	2.008979	-0.098743
82	$^1P^0$	2.108310	2.020451	-0.087859
83	$^3I^0$	2.128323	2.030711	-0.097612
84	$^3G^0$	2.133989	2.027899	-0.106090
85	$^1D^0$	2.023580	2.029976	0.006396
86	$^1F^0$	2.076741	2.035966	-0.040775
87	$^3F^0$	2.153493	2.040702	-0.112791
88	$^1I^0$	2.159699	2.049098	-0.110601
89	$^3D^0$	2.166543	2.050663	-0.115880

90	$^3F^0$	2.171456	2.056117	-0.115339
91	$^3G^0$	2.19033	2.073099	-0.116934
92	$^1G^0$	2.135757	2.076147	-0.059610
93	$^3F^0$	2.205734	2.081641	-0.124093
94	$^1H^0$	2.201721	2.081692	-0.120029
95	$^1F^0$	2.144680	2.084714	-0.059966
96	$^1H^0$	2.218992	2.086492	-0.132500
97	$^1D^0$	2.128420	2.089289	-0.039130
98	$^3G^0$	2.227667	2.111383	-0.116283
99	$^3D^0$	2.225082	2.110669	-0.114414
100	$^3P^0$	2.236155	2.124488	-0.111667
101	$^1F^0$	2.209024	2.147156	-0.061868
102	$^1P^0$	2.277585	2.150332	-0.127253
103	$^3F^0$	2.339860	2.223903	-0.115957
104	$^3D^0$	2.332419	2.228146	-0.104273
105	$^1F^0$	2.296100	2.238975	-0.057125
106	$^3P^0$	2.369491	2.246203	-0.123288
107	$^1P^0$	2.380985	2.257875	-0.123110
108	$^1D^0$	2.197693	2.267477	0.069783
109	$^3H^0$	2.433134	2.306369	-0.126765
110	$^3F^0$	2.429671	2.308263	-0.121408

111	$^3G^0$	2.442527	2.319439	-0.123088
112	$^1H^0$	2.477865	2.338970	-0.138895
113	$^1G^0$	2.191183	2.342534	0.151351
114	$^1F^0$	2.352928	2.352105	0.000177
115	$^3P^0$	2.545808	2.435754	-0.110055
116	$^3D^0$	2.618561	2.482505	-0.136056
117	$^1D^0$	2.392638	2.492199	0.099561
118	$^3S^0$	2.647000	2.505773	-0.141227
119	$^3F^0$	2.706840	2.577992	-0.128848
120	$^3D^0$	2.721454	2.593438	-0.128016
121	$^1D^0$	2.616326	2.599946	-0.016380
122	$^3P^0$	2.753329	2.611894	-0.141435
123	$^1F^0$	2.500079	2.616074	0.115995
124	$^1S^e$	1.175508	-	0.000000
125	$^1S^e$	1.725097	-	0.000000
126	$^1S^0$	2.590005	-	0.000000
127	$^1P^e$	2.089175	-	0.000000
128	$^1P^0$	2.669098	-	0.000000
129	$^1P^0$	2.828917	-	0.000000
130	$^3P^e$	2.037055	-	0.000000
131	$^1D^0$	2.747210	-	0.000000

132	$^1F^0$	2.760551	-	0.000000
133	$^1G^0$	2.261768	-	0.000000
134	$^1G^0$	2.480952	-	0.000000
135	$^1J^0$	2.066176	-	0.000000
136	$^3J^0$	2.039803	-	0.000000

In the BPRM computation, Hamiltonian matrices (and dipole matrices) are first calculated in *LS*-coupling, and then transformed using unitary transformation to pair-coupling. The corresponding Hamiltonian matrix analogous to the non-relativistic case is now much larger, and there are more coupled channels in the external region, requiring a considerable increase in computational effort.

The present calculations are concerned with all possible bound levels giveng rise to the $^4F^e$,(N+1)-electron symmetry (even and odd parities). This symmetry has been selected as it provides the largest contribution to the total collision strength for the transition $3p^63d^6\ ^5D^e \rightarrow 3p^63d^6\ ^3P^e$ (i.e. transition 1-2). The intermediate coupling calculations are carried out on recoupling 136 LS states (belonging to 43 *LS* symmetries) in a pair-coupling representation, Eq. 7, in stage RECUPD. The (e + Co IV) Hamiltonian is diagonalized for each $J\pi$ in STGH.

Table 2. Energy relative to the ground (in Rydbergs) for the first 136 fine-structure levels.

TARGET STATES -
****

INDEX	2J	Parity	ENERGY (RYD)
1	8	0	0.000000
2	6	0	0.006295
3	4	0	0.010694
4	2	0	0.013520
5	0	0	0.014904

6	12	0	0.240698
7	10	0	0.243895
8	8	0	0.246191
9	4	0	0.262571
10	8	0	0.275362
11	6	0	0.278996
12	2	0	0.281126
13	4	0	0.281725
14	0	0	0.288584
15	10	0	0.304026
16	8	0	0.310105
17	6	0	0.312594
18	12	0	0.363430
19	8	0	0.384289
20	4	0	0.393652
21	6	0	0.395464
22	0	0	0.446563
23	4	0	0.477492
24	6	0	0.550697
25	4	0	0.650164
26	8	0	0.650668
27	6	0	0.651393
28	4	0	0.664605
29	8	0	0.735491
30	6	0	0.897494
31	4	0	0.992645
32	4	0	1.049445
33	4	0	1.282180
34	6	0	1.282409
35	8	0	1.282621
36	12	0	1.282640
37	10	0	1.282732
38	6	0	1.336038
39	8	0	1.370296
40	6	0	1.372494
41	10	0	1.383927
42	8	0	1.383937
43	10	0	1.460601
44	12	0	1.460890
45	14	0	1.461432
46	4	0	1.494232
47	6	0	1.499341
48	8	0	1.507130
49	12	0	1.511328
50	10	0	1.526581
51	8	0	1.526961
52	6	0	1.612016

53	4	0	1.616384
54	2	0	1.619177
55	4	0	1.854342
56	6	0	1.854712
57	8	0	1.855332
58	10	0	1.856275
59	12	0	1.857709
60	6	0	1.871025
61	8	0	1.873854
62	10	0	1.876941
63	12	0	1.880116
64	14	0	1.882992
65	10	0	1.893390
66	8	0	1.895454
67	6	0	1.896646
68	4	0	1.897744
69	2	0	1.899153
70	0	0	1.902761
71	2	0	1.905125
72	4	0	1.907733
73	6	0	1.911542
74	4	0	1.915036
75	8	0	1.918990
76	4	0	1.926772
77	6	0	1.928608
78	12	0	1.930135
79	8	0	1.930958
80	10	0	1.932891
81	8	0	1.934632
82	6	0	1.935371
83	4	0	1.940054
84	2	0	1.942035
85	2	0	1.954378
86	4	0	1.956193
87	6	0	1.958975
88	4	0	1.959557
89	8	0	1.962278
90	2	0	1.962718
91	10	0	1.965537
92	6	0	1.983030
93	8	0	1.983952
94	4	0	1.985902
95	6	0	1.988365
96	2	0	1.988733
97	8	0	1.989114
98	10	0	1.989852
99	6	0	1.998572

100	4	0	1.999276
101	6	0	2.003096
102	4	0	2.006807
103	4	0	2.017537
104	6	0	2.019165
105	8	0	2.026395
106	6	0	2.029826
107	12	0	2.031582
108	14	0	2.035284
109	10	0	2.039798
110	12	0	2.046607
111	16	0	2.047177
112	14	0	2.051016
113	10	0	2.064664
114	14	0	2.068264
115	12	0	2.073342
116	10	0	2.078035
117	8	0	2.079088
118	6	0	2.088808
119	8	0	2.098306
120	8	0	2.116419
121	6	0	2.120104
122	6	0	2.121432
123	8	0	2.122510
124	10	0	2.124956
125	12	0	2.125240
126	12	0	2.129758
127	8	0	2.131487
128	10	0	2.132926
129	6	0	2.136373
130	8	0	2.137387
131	8	0	2.138428
132	10	0	2.140837
133	10	0	2.141189
134	12	0	2.148135
135	8	0	2.149986
136	10	0	2.155460

Unlike atomic structure calculations, where the electronic configurations are pre-specified and the levels identified, the bound levels calculated by collision theory methods need to be identified since only the channel quantum numbers are known for the bound states corresponding to the (e + ion) Hamiltonian of a given total angular and spin symmetry $SL\pi$ or $J\pi$. The precise correspondence between the channels of the collision complex, and

the bound levels, must therefore be determined. The problem is non trivial for complex atoms and ions with many highly mixed levels due to configuration interaction. In the Opacity Calculation, carried out in LS coupling, this problem was solved by an analysis based on quantum defects and the numerical components of wavefunctions in the region outside the R-matrix boundary (that envelops the target ion orbitals). In the present work we start the analysis of fine structure levels computed in intermediate coupling. In addistion, considerable effort has been devoted to the determination of the completeness of the set of computed bound levels; preliminary comparison with the expected levels derived from all possible combination of angular and spin quantum numbers reveals the missing levels. This work is in progress.

References

[1] Burke P.G., and Seaton M. J. *Journal Of Physics B* 17, L683 (1984)

[2] Seaton M. J. *Journal Of Physics B* 18, 2111(1985)

[3] Scott N.S and Taylor K.T. *Comput. Phys. Comm.* 25, 347 (1982)

[4] http://www.nist.gov/ads3

[5] Nahar S and Pradhan A., arXiv:physics/0001045v1

PROJECT BS - 5.1: TOKAMAK NEUTRON DIAGNOSTICS BASED ON THE SUPERHEATED FLUID DETECTORS (SHFD's)

Project Leader: Vasile Zoita

EFDA JET Task Agreement: JW8-TA-EXP-04

Specific Objective

Determination of neutron field characteristics for high performance discharges in the JET Campaign C26 (Experiment D-1.5.2)

V. Zoita, T. Craciunescu, M. Gherendi, A. Pantea

National Institute for Laser, Plasma and Radiation Physics

December 2009 milestone: Experimental data processing and analysis obtained during the JET Campaign C26.

1. Introduction

Super-heated fluid detectors (SHFD's or "bubble detectors") are suspensions of metastable droplets which readily vaporise into bubbles when they are nucleated by radiation interactions [1-2]. The active detecting medium is in the form of microscopic (20-50 μm) droplets suspended within an elastic polymer. The phenomenon of neutron detection by a SHFD is a mixture of nuclear interactions (neutron collisions with nuclei of the active medium), thermodynamic behaviour of the detecting medium (the super-heated fluid), and the mechanical response of the elastic polymer. If sufficient energy is transferred from the colliding neutron to the nucleus of one of the elements in the composition of the active medium, the recoil nucleus will initiate the generation of a vapour embryo of sub-micron dimensions. Under proper conditions (that depend on the thermodynamics of the active medium) the vapour embryo will lead to the vaporisation of the super-heated droplet with the subsequent expansion into a macroscopic (0.2 – 0.5 mm) bubble.

The SHFD's have a threshold-type energy response with the threshold energy depending on droplet composition, detector operating temperature, detector operating pressure. For a standard bubble detector like the BD-PND* type, the energy response is approximately flat within the range 0.3-10 MeV.

Using detectors with different energy thresholds, a bubble detector spectrometer (BDS[(*)]) is obtained.

The main aim of the project for 2009 was the determination of the neutron field characteristics in high performance discharges (experiment code D-1.5.2 within the JET Work Programme) during the JET experimental campaign C26 using techniques based on the bubble detectors, indium activation and time of flight [3]. The D-1.5.2 experiments have been scheduled to be carried out as parasitic experiments during the JET campaign C26. The main (host) experiment was chosen that on "Steady-state scenarios at high beta normalised" [4] which employs high neutral beam powers (~20MW) and produces neutron yields in the range (3-5) x10^{16} neutrons. Some other high neutron yield experiments have also been used as the main experiment.

This paper is a report on the data processing and analysis of the neutron energy distribution measurements carried out by means of bubble detectors spectrometer (BDS).

2. Neutron energy distribution measurements

A complex series of neutron measurements have been done by means of the super-heated fluid detectors (SHFD's) during campaign C26 (January - April 2009) within the D-1.5.2 experiment. These included measurements on neutron fluence, neutron energy distribution and time-resolved neutron emission. The bubble detector measurements have been done simultaneously with other two independent techniques: indium activation and time of flight. Only neutron energy distributions measured by means of the bubble detectors (SHFD's) will be reported here.

The SHFD measurements have been done at the end of the KM11 neutron diagnostics

line-of-sight, above the TOFOR neutron time-of-flight spectrometer   (Figure 1). The

distance from the SHFD location to the TOFOR first (start) detector is approximately

---

* All detectors used in this work were manufactured and calibrated by Bubble Technology Industries, Chalk River, Canada

3.5m and the distance to the torus mid-plane is approximately 20m. The SHFD's have

been positioned to cover the "neutron spot" determined in the previous measurements

using (high sensitivity) DEFENDER[(*)]-type bubble detectors [5].
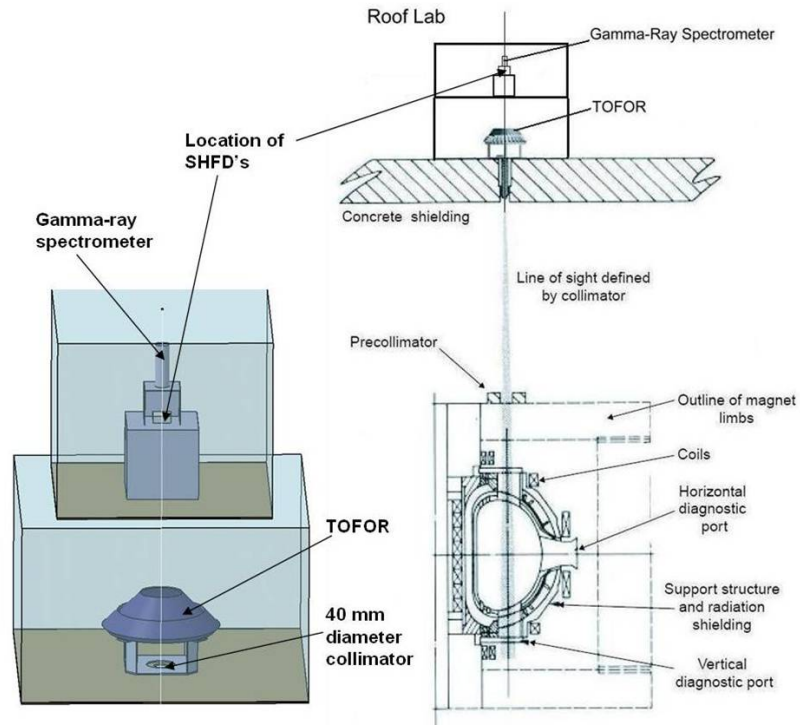
Figure 1. Experimental setup for SHFD neutron measurements along the JET KM11 Line-of-Sight.

The bubble detector spectrometer (BDS) consists of 36 neutron bubble detectors to cover

a broad energy range (0.01 – 20 MeV) and provides six energy thresholds in that range.

Six detectors are used for each of the following energy thresholds: 0.01, 0.1, 0.6, 1.0, 2.5,

10.0 MeV. The neutron energy response is represented in Figure 2. The energy thresholds

define six energy bins as follows:

E1: 10-100 keV

E2: 100-600 keV

E3: 0.6-1.0 MeV

E4: 1.0-2.5 MeV

E5: 2.5-10.0 MeV

E6: 10.0-20.0 MeV

Five different spectrometric sets (BDS type) have been used for neutron energy distribution measurements on forty-one JET pulses.
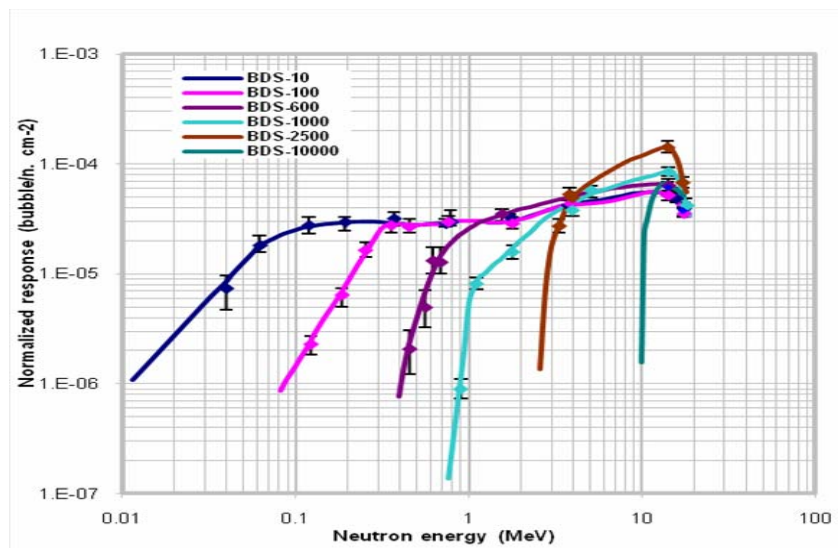
Figure 2. BDS neutron energy response.

3. Data processing and analysis

Three different techniques of increasing complexity have been used for the processing of the neutron energy distribution data obtained by means of the bubble detector spectrometer.

A first method ("Uniform response") is based on the following assumptions:

- All detectors have a constant identical energy response

- All detectors have equal sensitivities

This method allows for a fast qualitative comparison between different measurements.

A second method is based on the "spectral stripping" technique for the de-convolution of the energy distribution. The energy distribution is obtained as a six energy bin histogram. The main assumption is that the fluence per unit energy is constant within one energy bin. The method leads to error accumulation as the "stripping" proceeds from high to low energies.

A third method is based on the "expected energy distribution". The "expected distribution" refers to the energy distribution expected to be obtained for the neutrons produced by thermal deuterium plasma. The main assumptions are:

 -The neutrons have a Gaussian distribution around 2.5 MeV (this is experimentally obtained from the time-of-flight spectrometer TOFOR)

-The energy bin E4 (defined by detectors BDS1000) sees the full TOFOR energy distribution

 -There should be no scattered neutrons with energy above those of the 2.5 MeV Gaussian

 -The scattered neutrons are assumed to be uniformly distributed within lower energy bins

In the analysis of the energy distribution experimental data a "control parameter (CP)" is defined in terms of the number of neutrons in energy bins E4 and E5, as follows: CP = N5/(N4+N5). For a purely Gaussian distribution CP=0.5. A value lower than 0.5 shows the presence of scattered neutrons in the energy distribution. A value higher than 0.5 can be obtained either by a shift of the mean energy distribution to values higher than 2.45 MeV, or by the presence of neutrons generated by other processes than the DD fusion.

Figure 3 shows the "uniform response" distributions for measurements done with three BDS spectrometric sets.
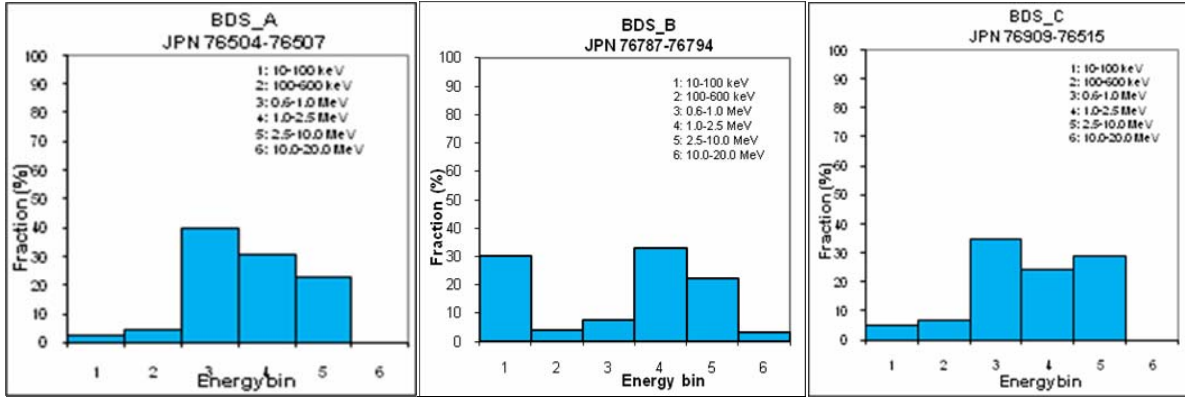
Figure 3. "Uniform response" energy distributions

The control parameter for the three "uniform response" distributions is: 0.42, 0.41 and 0.54, respectively. The distribution measured by the BDS_B spectrometer shows clearly the presence of neutrons with energy above 10 MeV emitted by a deuterium plasma. This confirms the emission of triton burn neutrons (energy 14 MeV) in these high-performance JET discharges. This is also independently confirmed by the Si diode neutron detectors (KM7 14 MeV neutron yield monitors).

For the same measurements the large number of neutrons in the energy bin E1 (10-100 keV) could be explained by non-fusion nuclear reactions such as photo-nuclear reactions induced by high energy electrons generated in the disruption which occurred in one of the measured JET pulses (JPN 76794).

The energy distributions obtained by the "spectral stripping" method are shown in Figure 4.
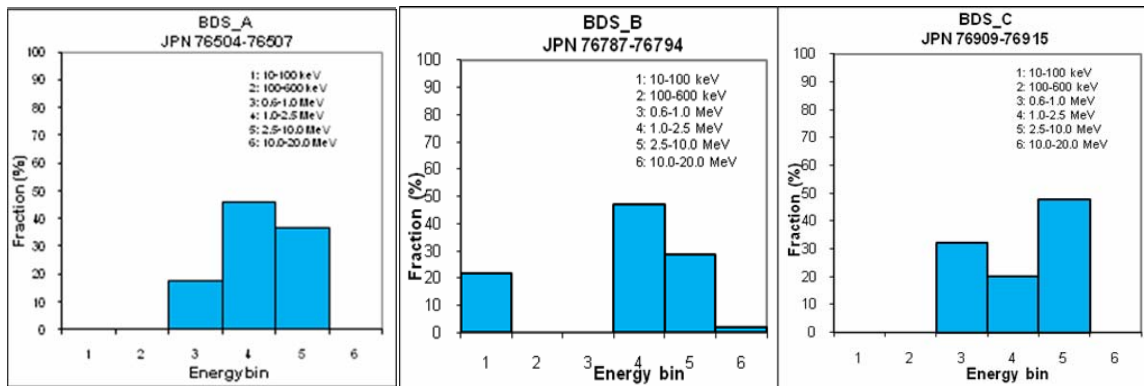
Figure 4. "Spectral stripping" energy distributions

The control parameters for the "spectral stripping" distributions are: 0.443, 0.38 and 0.71, respectively.

The measurement made by means of the BDS_A spectrometer has been processed also by means of the "expected energy distribution" method.

The Gaussian fit to the time-of-flight (TOFOR spectrometer) spectrum integrated over three JET pulses is shown in Figure 5. The Gaussian distribution parameters were: Eo=2.5 MeV and FWHM=0.455 MeV.
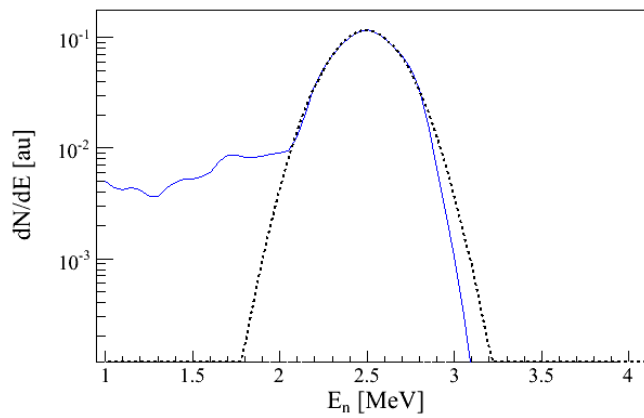
Figure 5. Gaussian fit to the TOFOR neutron spectrum integrated over shots JPN76504,

76506 and 76507.

(Solid blue curve: TOFOR neutron spectrum; Dashed curve: Gaussian fit)

The energy distribution obtained from the BDS_A spectrometer measurement using the "expected energy distribution" is shown in Figure 6.
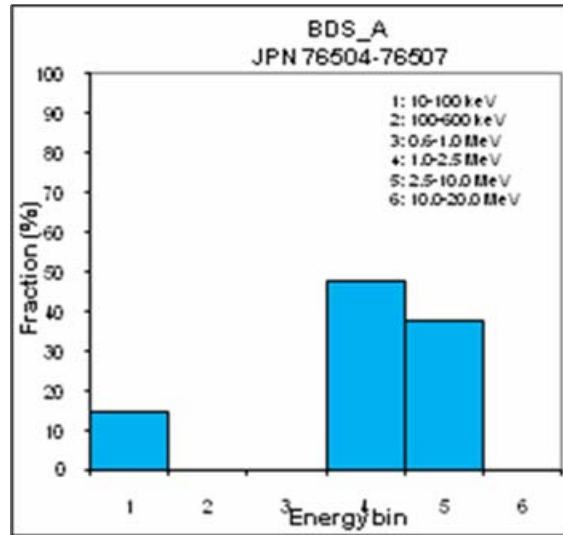
Figure 6. Neutron energy distribution obtained by the "expected (Gaussian) distribution" method.

The control parameter for the "expected (Gaussian) energy distribution" shown in Figure 6 is 0.44. The energy bins 4 and 5 cover the TOFOR neutron spectrum. From the TOFOR energy distribution 88% are fusion neutrons and 12% are "scattered" neutrons. The 15% neutrons seen by the BDS spectrometer at low energies cannot be accounted for by the TOFOR spectrometer.

4. Conclusions

Three different techniques of increasing complexity have been used for the processing of the neutron energy distribution data obtained by means of the bubble detector spectrometer: "uniform response", "spectral stripping" and "expected energy distribution". Using these methods the following main results have been obtained:

-The presence of neutrons emitted from a deuterium plasma with an energy above 10 MeV was clearly shown. This confirms the emission of triton burn neutrons (energy 14 MeV) in high performance JET discharges.

-The fraction of low energy neutrons is, in some discharges, higher than that which could be explained by scattering processes. This could be explained by other neutron emitting reactions from the tokamak machine (such as photonuclear reactions, triggered by high energy electrons generated in a plasma disruption).

Acknowledgements

60

References

[1] M. Gherendi, V. Kiptily, V. Zoita, S. Conroy, T. Edlington, D. Falie, A. Murari, A. Pantea, S. Popovichev, M. Santala, S. Soare "*Super-heated fluid detectors for neutron measurements at JET*", J. Optoelectronics Advanced Mat., 10 (2008) 2092-2094.

[2] V. Zoita, S. Conroy, T. Craciunescu, T. Edlington, M. Gatu Johnson, M. Gherendi, C. Hellesen, S. Jednorog, V. Kiptily, A. Murari, A. Pantea, S. Popovichev, R. Prokopowicz, M. Scholz, *Neutron Fluence Measurements on the JET Tokamak by Means of Super-Heated Fluid Detectors*, 36th International Conference on Plasma Science and 23rd Symposium on Fusion Engineering, May 31 – June 5, 2009, San Diego, California.

[3] V.L. Zoita, T. Craciunescu, M. Gherendi, A. Pantea, T. Edlington, V. Kiptily, S. Popovichev, S. Conroy, M. Gatu Johnson, C. Hellensen, S. Jednorog, R. Prokopowicz, M. Scholz, A. Murari *"Determination of neutron field characteristics for high performance discharges (Experiment D-1.5.2)"*, Presentation to Task Force Diagnostics Meeting, JET, Culham, March 5th, 2009.

[4] J. Mailloux et al., *"Development of a steady-state scenario in JET with dimensionless parameters approaching ITER target values"*, Proceedings of the36[th] EPS Conference on Plasma Physics, 29th June 2009 - 3rd July, 2009, Sofia, Bulgaria.

[5] V. Zoita, D. Falie, M.Gherendi, A. Pantea, S. Soare, V. Kiptily, S. Popovichev, A. Murari, S. Conroy, *"Super-heated fluid detectors ("bubble detectors") for neutron measurements at JET"*, Presentation to Task Force Diagnostics/Task Force Heating Joint Meeting, JET, Culham, January 29th, 2008.

PROJECT BS-6: SHEATH PROPERTIES AND RELATED PHENOMENA OF THE PLASMA WALL INTERACTION IN MAGNETISED PLASMAS. APPLICATION TO ITER

Scientific Report

To the Contract 1EU-3/11.08.2008

For the period 01.07.2009 – 15.12.2009

Project Leader: Claudiu COSTIN, Faculty of Physics, Plasma Physics Laboratory, "Al. I. Cuza" University, Iasi

Authors: C. Agheorghiesei, V. Anita, S. Costea, C. Costin, G. Popa, L. Sirghi, M. L. Solomon

Subject: Plasma diagnostics

Specific Objective: Characterisation of Pilot-PSI plasma beam by electrical methods (different types of probes, electrostatic analysers, etc)

The experiments were performed on Pilot-PSI linear magnetized plasma device at FOM Institute for Plasma Physics "Rijnhuizen", The Netherlands, Association EURATOM/FOM.

Multi-channel analyzer experiments.

One of the main research topics on Pilot-PSI concerns the interaction of magnetized plasma with a solid surface in extreme conditions (particle and energy fluxes), typical for the divertor of a fusion reactor. Our mission in the collaboration with FOM Institute is to develop and use different electrical methods based on probes and electrostatic analyzers to characterize the plasma beam generated by the source of Pilot-PSI device.

During the campaign on November 2009 a multi-channel analyzer (61 collectors) was used to obtain information about the time-space distribution of plasma current and floating potential in front of the target. As in the case of the divertor, electrical diagnosis devices interact with dense plasma and the construction material must be high quality and temperature resistant. Our analyzer was made from machinable aluminum oxide ceramic (MACOR) with tungsten collectors and teflon coated wires. Optionally, a carbon plate can be added in front of the analyzer.

During the experiment it was noticed that copper is sputtered from the source due to the very high density plasma created inside. The sputtered copper deposits both on the vessel's walls and the target. As the multi-channel analyzer was placed in the centre of the target, its surface had to be regularly cleaned (daily).
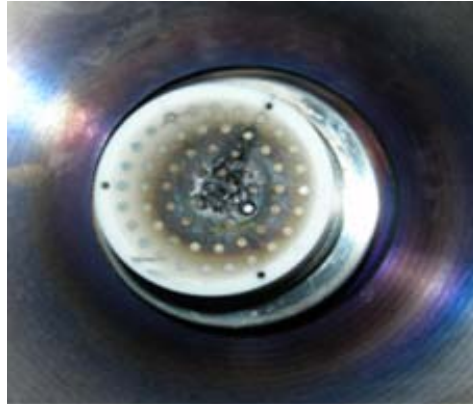
Fig.1. Analyzer surface must be cleaned daily due to Cu deposition

In order to register the current reaching the target, each collector was connected to the ground using a resistor of 0.2 Ω. The voltage drop on each resistor developed during ON-phase of the plasma (which is equivalent to the time interval when the magnetic field is applied) was registered by a high speed data acquisition system with maximum 64 inputs (National Instruments NI PXI 8106). Each measurement generates one digital file containing all 61 signals acquired from the analyzer's channels in time. The currents were registered for different discharge currents (80, 100, 120 and 140 A) and different magnetic fields (0.4, 0.8 and 1.2 T).

Fig.2 shows the current variation measured during ON-phase of the plasma (shortly called 'pulse') on 9 collectors disposed along a diameter of analyzer. Each collector has an identifying number (e.g. *ch 306*), the first figure of this number indicating the radial position of the collector (0 in the centre of the analyzer and 4 the outer radius). Fig.2 reveals the big influence of the magnetic field intensity on currents distribution on the target. In the case of 0.4 T, current intensities are quite equal, with a maximum value of 0.8 A, and the plasma beam covers the entire surface of the analyzer (24 mm in diameter). By increasing the magnetic field to 0.8 T the diameter of the plasma beam decreases, the plasma column is better confined in the centre of the chamber and the central collectors collect the highest current (9 A) while the current on the external collectors is approximately 4 A. It has to be mentioned that the signals plotted in all the figures have been smoothed using the adjacent averaging method by 150 points left and 150 points right. Nevertheless, the relative value of current fluctuations is still large at lower magnetic fields.
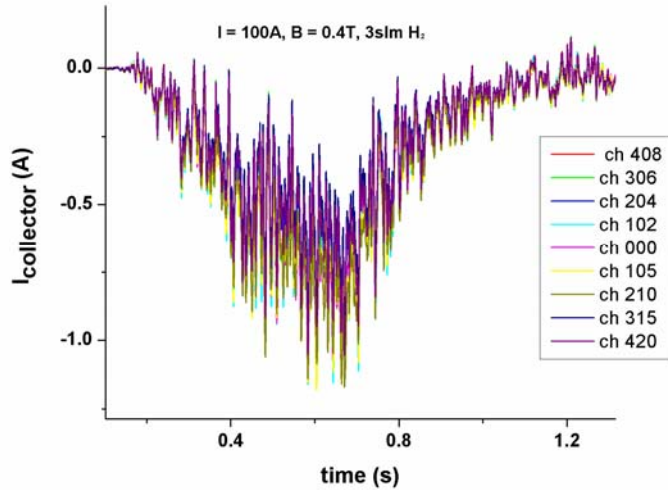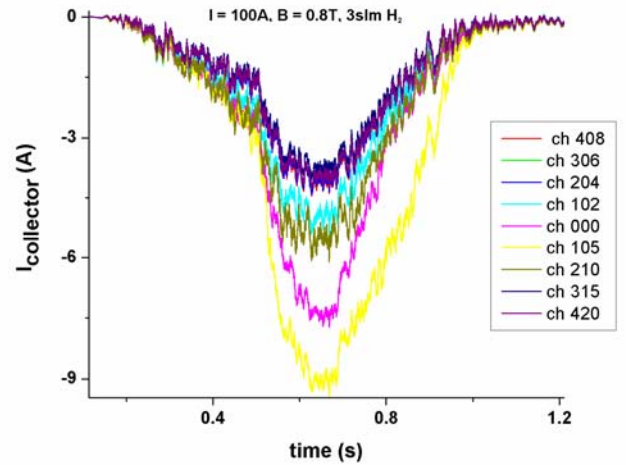
B = 0.4 T   B = 0.8 T

Fig.2. Current variation on 9 collectors during plasma pulse (I = 100 A)

The radial distribution of the current reaching the target is plotted in Fig.3 for two discharge currents, 80 and 100 A. The discharge current is concentrated mainly in the centre of the plasma beam. The increase of the discharge current from 80 to 100 A does not influence this distribution.
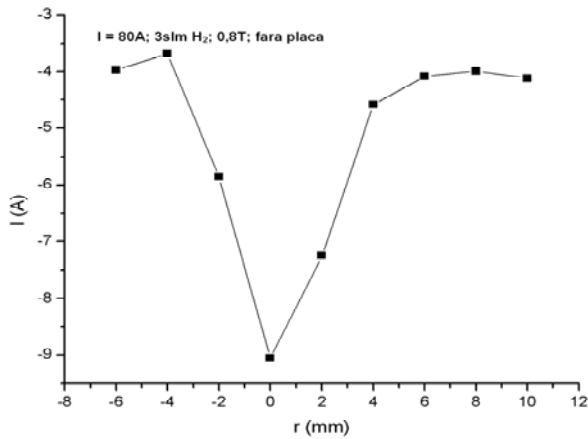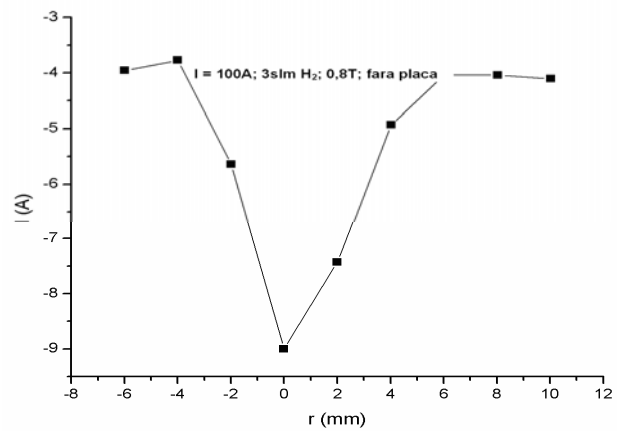
I = 80 A   I = 100 A

Fig.3. Radial distribution of the current at the target (B = 0.8 T)

By using resistive dividers (10 MΩ and 10 kΩ) the floating voltages of the collectors were registered in different experimental conditions. Fig.4 shows the variation of floating voltages during the plasma pulse for a discharge current of 80 and 100 A and a magnetic field of 0.4 T.
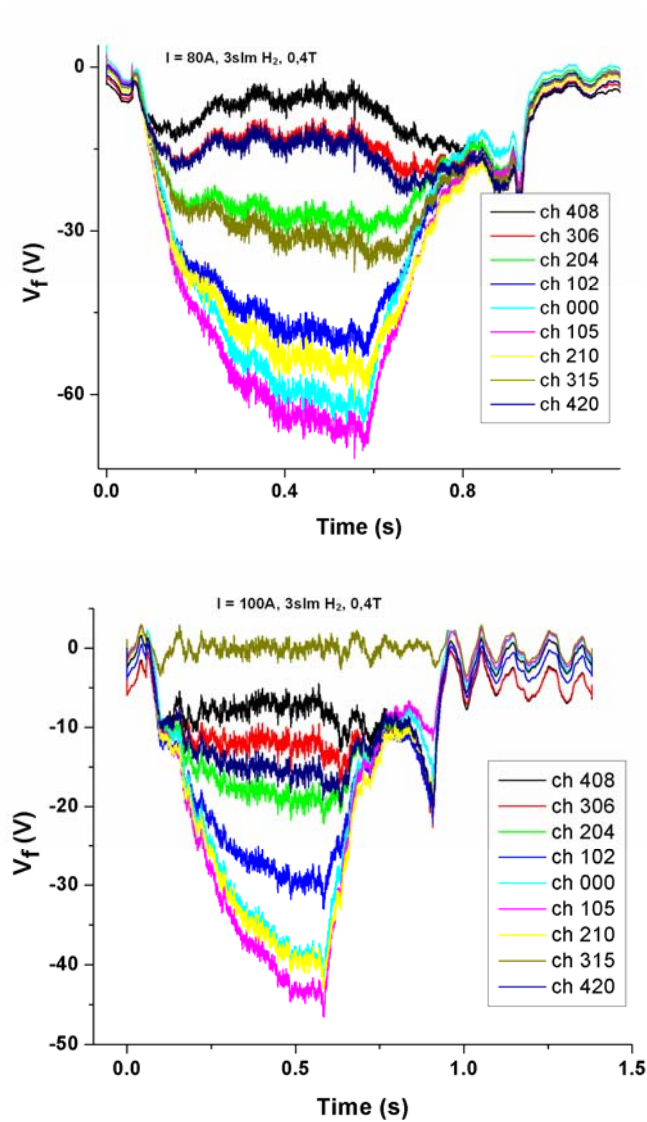
I = 80 A   I = 100 A

Fig.4. Floating voltage variation during plasma pulse (B = 0.4 T)

By increasing the discharge current from 80 to 100 A the floating voltage in front of target decreases as a consequence of the plasma density increase and the decrease of electron

temperature. The time variation of the floating voltage provides information of the plasma source operation. In Fig.5 it is shown the influence of source Cu sputtering on the floating voltages measured at the target.
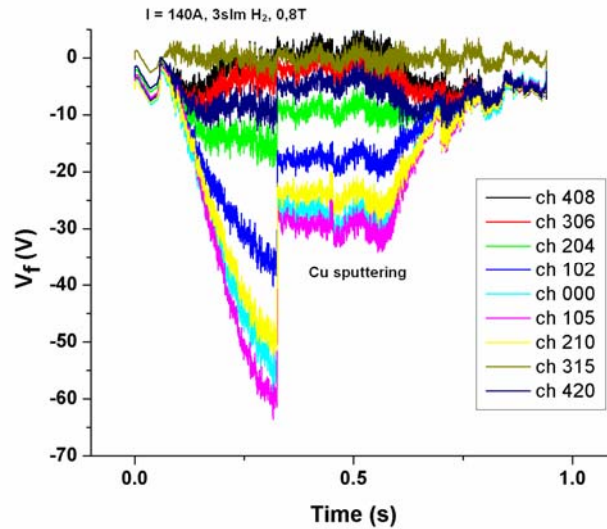
Fig.5. The influence of Cu sputtering on floating voltages

An experiment was imagined to register the currents flowing between different collectors of the analyzer. A Tektronix inductive DC current calibrated probe was used for that. Two collectors were connected together and the rest of the collectors were grounded by 0.2 Ω resistors. Some results are presented in Fig.6. Small currents have between detected between collectors, of the order of mA, currents determined by different local floating voltages in front of collectors. These currents are much smaller than the currents flowing through the grounded electrodes. Nevertheless, the results show that when a metallic surface is in contact with plasma having a non uniform distribution of the floating potential, currents may appear along the metallic surface. More experiments are necessary in order to understand if the net current flowing into the target affects the plasma-surface interaction.
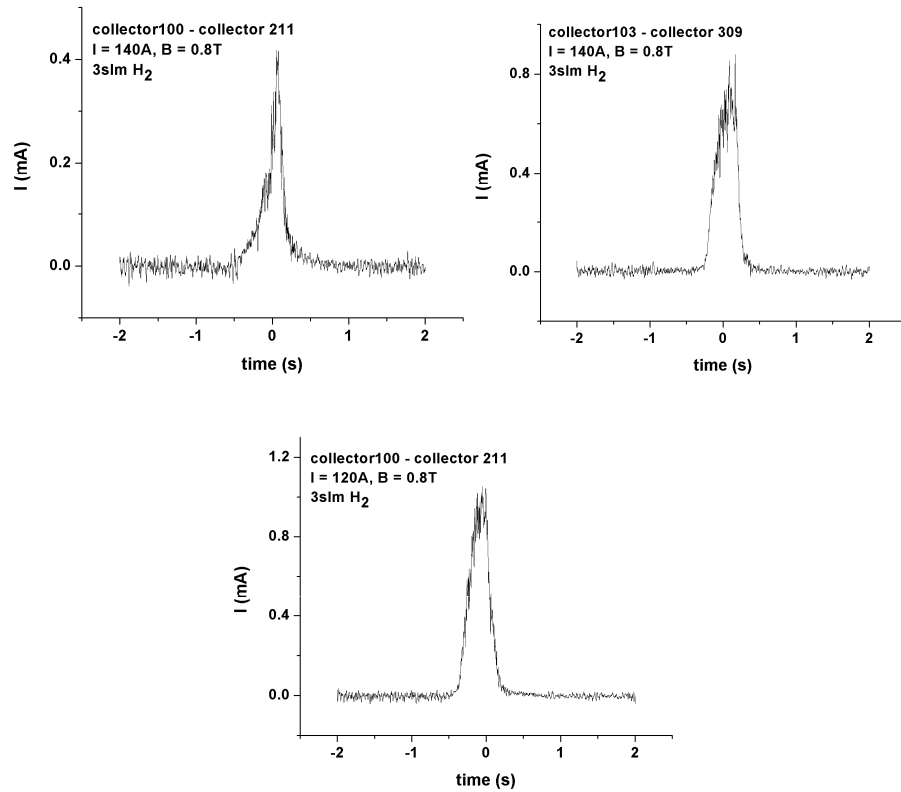
Fig.6. Currents flowing between two collectors during plasma pulse

Previous experiments showed that the target is strongly heated during the plasma pulse. The maximum temperature obtained for tungsten or molybdenum targets is about 1600 K in the centre of the plasma column (Fig.7). Target heating was also evidenced in our experiments, the plasma beam affecting the analyzer surface. The surface made of MACOR was melted while tungsten collectors were not altered (Fig.7).
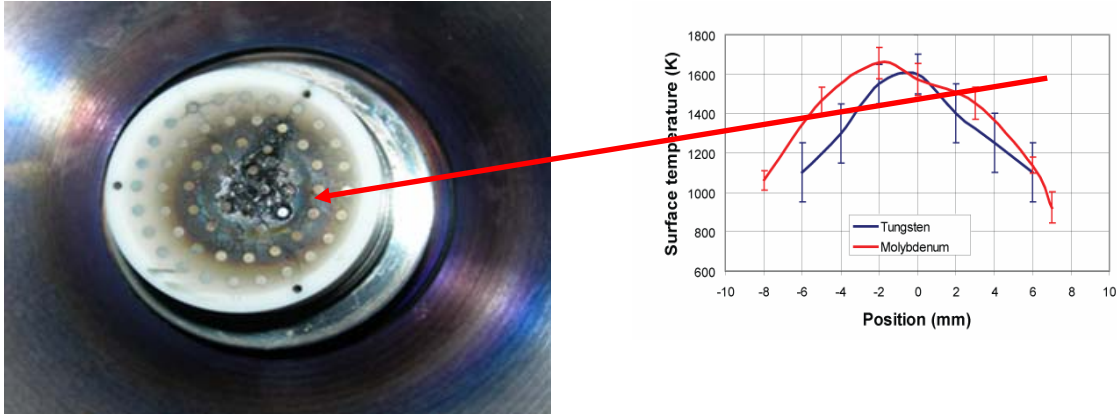
Fig.7. Analyzer surface after the interaction with the plasma beam

Subject: Theory and modelling

Specific objective 1: Development of a 2D fluid model for the simulation of Pilot-PSI device

The two fluid models (2D in argon) previously developed, one for the neutrals flow and the other for the charged particles (electrons and positive ions) were coupled for a complex and realistic description of the plasma produced in Pilot-PSI. Preliminary results were obtained for the radial and axial distributions of plasma parameters, such as plasma potential, charged particle densities and fluxes. However, further investigations have to be done on the stability of the numerical code. In this version, oscillations of the plasma parameters develop at the target surface and propagate into the discharge.

Specific objective 2: Development of a 2D PIC-MCC model for magnetised plasma devices (application to Pilot-PSI)

Milestone: *PLUAIC – alpha release (version December 2009)*
All the modules developed earlier this year together with the module for solving the equation of motion of the charged particles were linked into a test program PLUAIC (alpha release). This release has some limitation due to the testing and bug elimination processes:
1. the total number of charged particle species is 2, electrons and positive ions (Ar^+ or H^+);
2. maximum of total simulation particles in the program is limited to 100.000;
3. evaluation of the electrical potential into a arbitrary spatial point (r,θ,z) is done using the first approximation relative to the spatial mesh;
4. no external electrical circuit is considered in this version;
5. the parallelisation of the code is rewritten using multithreading technique for a rapid and optimization test (PLUAIC program running into 1, 2, 4, 8 threads on a 2 dual-core CPUs machine and on 8 dual-core CPUs machine).

68

Observations:

Module	Issue	Observations
Equation of motion	- leap-frog method	- good results if there is a good time step and mesh spatial grid values. TO DO: use different methods for electrons and ions motion solvers.
Field solving equations	- FFT 2D method for Poisson equation - electrical charge density evaluation	- very fast comparing to direct solver method; - first approximation is used: all the electrical charges from a spatial cell are uniformly distributed to the first neighbour cells. TO DO: interpolation for electrical charge density evaluation.
Mote Carlo Collisions	- random generator - real cross sections for elementary processes	- method inspired from GNU Scientific Library (GSL); - elastic scattering of electrons, ionization, global excitation and resonant charge exchange for ions. TO DO: why there are less elementary processes involved in simulations than expected?
Code parallelisation	- MPI library - multithreading technique	- standard MPICH2 library has been installed and used in the main program function; - for the first release of the program only multithreading technique was used because of the waste of resources in a computing ring. TO DO: eliminate the limitations for the number of species and the total number of particles.
External circuit	- not yet implemented	TO DO: to be implemented.

References

1. D. Tskhakaya and S. Kuhn, Contrib. Plasma Phys. 42 (2–4), 302–308 (2002)
2. XOOPIC plasma simulation http://ptsg.eecs.berkeley.edu/pub/codes/xoopic/
3. GNU Scientific Library (GSL) (http://www.gnu.org/software/gsl/)
4. High Performance Computing facilities http://stoner.phys.uaic.ro/amon/facilities.html

PROJECT BS-9.1: PROFILE RECONSTRUCTION TECHNIQUES FOR THE JET NEUTRON AND GAMMA-RAY CAMERAS

Project Leader: T. Craciunescu

EFDA JET Task Agreement: JW8-TA-EXP-04/JW8-O-MEC-12

Teddy CRACIUNESCU, Ion TISEANU, Cosmin DOBREA, Adrian SIMA, Daniela NENDREAN

EURATOM-MEdC Association, National Institute for Lasers Plasma and Radiation Physics, Bucharest, Romania

1. Introduction

At the JET Tokamak a major goal is the production and measurement of high levels of neutron emission from d-d and d-t fusion reactions. A variety of neutron diagnostics are used independently at JET to measure both fast and thermal ion behavior. The available neutron diagnostics include a neutron profile monitor consisting of a vertical and horizontal camera. The JET neutron cameras, a unique instrument among similar diagnostics available at large fusion research facilities, consist of two concrete shields of which each includes a fan-shaped array of collimators. These collimators define a total of 19 lines of sight, grouped in two cameras (horizontal and vertical). The plasma coverage allows neutron the tomographic reconstruction of neutron emissivity spatial profiles in two dimensions. The reconstructions are useful for the study the thermal and beam-induced sources of neutron emission and to analyze the evolution of fast ion populations. However, due to the existence of only two fairly coarse views of the plasma, the tomographic problem is a highly limited data set one. This restricts the set of tomographic methods which can be used for the reconstruction.

A reconstruction method based on the maximum likelihood (ML) principle was developed for solving the reconstruction problem during the year 2008 [1]. In 2009 several reconstruction methods - maximum entropy (ME), Tikhonov regularization (TR) approach, and a Monte Carlo back-projection algorithm (MCBP) – were improved and adapted for JET tomographic geometry. A comparative study concerning the applicability to JET tomography of these four methods was developed and reported [2]. The methods have been tested on numerically

simulated phantoms with shapes characteristic for this kind of tomography. A both qualitative and quantitative evaluation was performed.

The work on profile reconstruction techniques continued during the second part of the year 2009 with the software package development. The package was used in order to provide support in JET experimental campaigns. This represented a very good opportunity to validate it in a real experimental environment.

2. Software package development and testing

MATLAB was chosen as the appropriate environment for the implementation of the reconstruction methods. It ensures a well balanced compromised between the speed of the calculations and the flexibility of the implementation which can be easily changed in order to include further developed features or to be adapted to specific experimental needs. All the developed methods were implemented. In order to retrieve the tomographic projections the program has to be able to access JET data. The MDSplus software tools [3] were used in order to be able to retrieve neutron/gamma profiles as the MDSPlus server at *mdsplus.jet.efda.org* supports JPF and PPF trees. MDSplus was developed for data acquisition and storage and a methodology for management of complex scientific data. MDSplus allows all data from an experiment or simulation code to be stored into a single, self-descriptive, hierarchical structure. The MDSplus programming interface contains only a few basic commands, simplifying data access even into complex structures. Using the client/server model, data at remote sites can be read or written without file transfers. Due to the existence of only two views and a total number of only nineteen projection rays, the JET tomographic problem is a highly undetermined one. In order to compensate the lack of experimental information a simple but robust smoothing operator was defined (see e.g. Ref. 1). It acts as median filter, walking along the magnetic contour lines. Therefore the software needs to retrieve also the magnetic information specific to each time step of a specific shot. The path to this information is ensured by means of FLUSH (*FLUx Surface Handling*), a collection of FORTRAN routines (also accessible through C, IDL, MATLAB and MDSplus) to assist in reconstructing and post-processing the flux solution of a plasma equilibrium solver. The software package has a user-friendly interface (Fig. 1) and it allows the visualization and storage of the reconstruction and subsequent information.
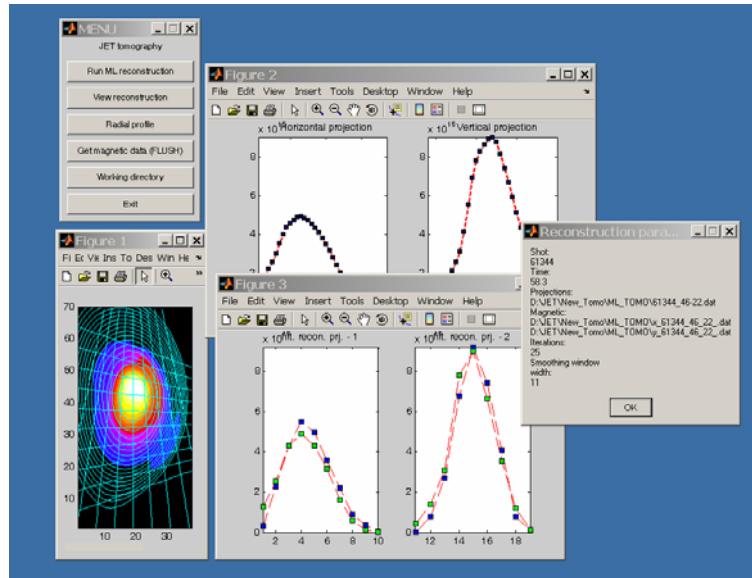
Figure 1 – Tomographic reconstruction software

The software package was tested for both neutron and gamma tomography. In case of neutron tomography we used data from the Trace Tritium Experiment (TTE). It contains several experiments characterized by sophisticated structures of the emissive distribution. This allowed having a complete image of the quality and reliability of the implemented algorithms. A typical example is presented in Fig. 2. The ML method provided the finest results in terms of shapes reconstruction and resolution and produces artefact free images. The profile data is available at fixed 10 ms intervals. The data from adjacent intervals can be summed in order to obtained tomographic projections with lower statistical fluctuations. The price paid for consists in the decrease of the temporal resolution. The ML method proved to be robust enough to ensure a time resolution of 50 ms.
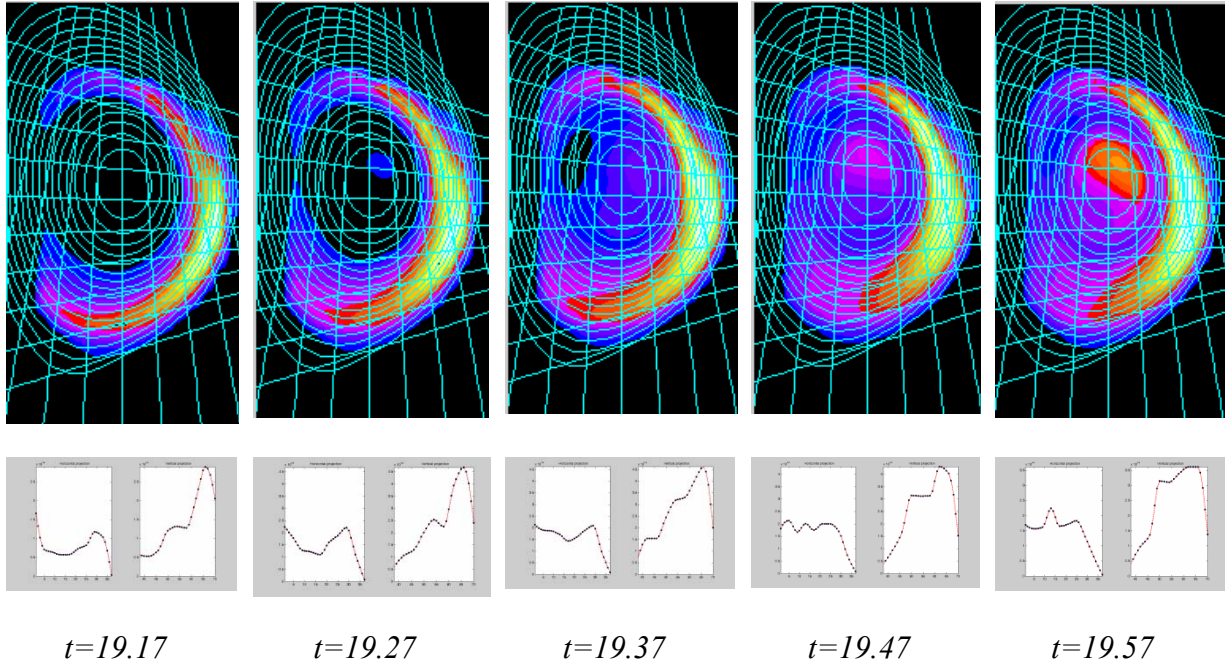
Figure 2 – Temporal evolution of 14 MeV neutron emissivity (ML reconstruction for JET pulse 61138)

The software package was used during the JET experimental campaigns. Diagnostics support, consisting in the reconstruction of the gamma emissivity distribution, was provided for fast ion studies. This was a very good opportunity to test its use in case of inter-shot analysis.

Gamma-rays are emitted in JET plasmas due to nuclear reactions between fast ions and thermal plasma, Be and C impurities. The γ -ray energy spectra uniquely identify the presence of a particular type of fast ions, and such spectra are measured on JET with three independent devices [5], one with a quasi-tangential, and two with vertical lines of sight, through the plasma centre. The γ -ray spectra are continuously recorded during all JET discharges over the energy range 1–28MeV using modern data acquisition system (DAQ) based on a transient recorder at a sampling rate of 25MHz with an amplitude resolution of 14 bit [6]. This DAQ allows avoidance of the pile-up effect and gain instability, which lead to a distortion of γ -ray spectra at high-count rates (up to 1 MHz) with fast rate variations. Spatial profiles of the g-ray emission are reconstructed in the energy range Eg > 1MeV. The data acquisition system accommodates the line-integrated g-ray count-rate measurements in up to four independently adjustable energy windows with a time resolution of less than 100 ms depending on the count-rates. Each window is set to correspond to the γ-ray peak(s) from a

given fast ion population, thus up to four different groups of fast ions giving rise to g-rays of different energies are simultaneously measured with the γ–cameras providing 2D images of these ions. Typical reconstructions obtained JET experimental campaigns are presented in Fig. 3.

| #69432 | #73213 | #73766 | #79168 |
| 56.55 s | 50.50 s | 48.50 s | 53.26 s |
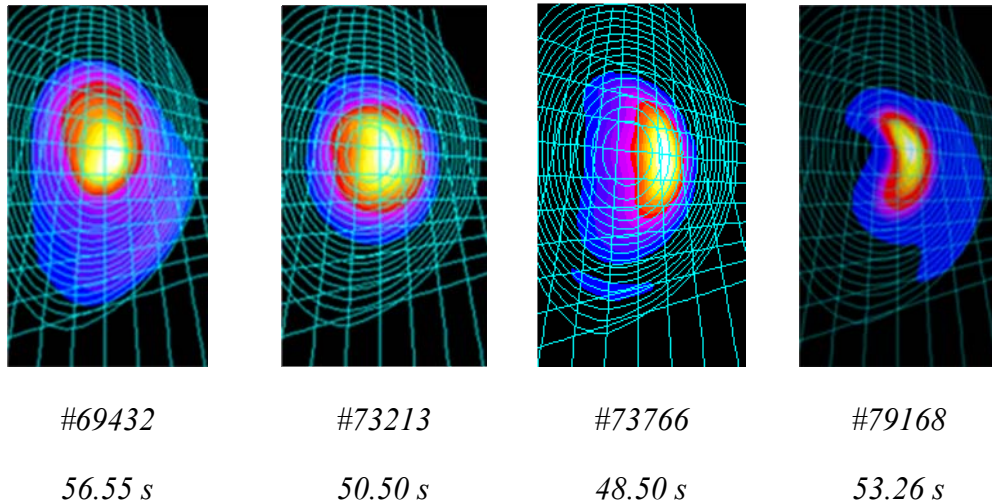
Figure 3 – Typical reconstructions of the gamma emissivity distributions

The reconstruction time becomes a more important parameter in case of gamma tomography due to the existence of several energy windows which multiplies the number of reconstructions which have to be done a limited time (for inter-shot analysis). The typical inter-shot time interval is around 30 minutes. However, in the first 5-7 minutes the data is post-processed and validated; at least 10 minutes must be leaved for human analysis before the next shot. Therefore only 13-15 minutes are available for the tomographic software to run and provide reconstruction of the emissivity distribution. At the present moment the ML method, that provides the best results, needs 3.5 minutes for a reconstruction. It means that 4 images can be retrieved in the available time interval. This proved to allow the retrieval of useful information needed during the experiment. However, a faster computation will allow exploring of the gamma emissivity evolution in all energy channels with finer temporal resolution. In order to reach this objective future work will be dedicated to the implementation of several parallel computing techniques which will allow reducing significantly the computation time. A preliminary evaluation suggests that the improvement

will be characterized by a factor of 5-6. This means that the software will be able to process more than 20 tomograms which will satisfy the needs of the inter-shot analysis.

3. Conclusion

In conclusion we appreciate that the objectives of the present stage of the project were reached. A software package, implementing all the methods developed during the project, was developed and validated. The validation was performed both on neutronic and gamma-ray data. The software package was used in order to provide support in JET experimental campaigns. It allowed the retrieval of useful information needed during the experiment. The results obtained during this phase of the project contributed to two publications [7-8].

The work on profile reconstruction techniques will be continued with the implementation of several parallel computing techniques which will allow reducing significantly the computation time. This will allow the retrieval of the emissivity distribution evolution with finer temporal resolution, for multiple energy channels.

The migration of several numerical techniques, developed during the project, to a new application will constitute also an important objective. The new application will address the image processing of data provided by the JET fast visible camera in order to retrieve the velocity field of moving object inside the plasma. Preliminary tests proven that this technique may lead to a diagnostic method providing information for the study of pellet injection and ablation and of plasma boundary phenomena, able to provide useful information for diagnosis and model development.

References

[1] T. Craciunescu, G. Bonheure, V. Kiptily, A. Murari, S. Soare, I. Tiseanu, V. Zoita, *The Maximum Likelihood Reconstruction Method for JET Neutron Tomography*, Nuclear Inst. and Methods in Physics Research, A, 595, p. 623–630, 2008 (*http://dx.doi.org/10.1016/j.nima.2008.07.145*).

[2] T. Craciunescu, G. Bonheure, V. Kiptily, A. Murari, I. Tiseanu, V. Zoita, *A comparison of four reconstruction methods for JET neutron and gamma tomography*, Nuclear Inst. and Methods in Physics Research, A, 605, pp. 373-384, 2009 (*http://dx.doi.org/10.1016/j.nima.2009.03.224*).

[3] MDSplus – MDSplus developers *http://www.mdsplus.org/index.php/MDSplusDevelopers*, MDSplus documentation library, *http://www.mdsplus.org/*

[4] JET FLUSH library - *http://users.jet.efda.org/pages/data-proc/flush/index.htm*.

[5] V.G. Kiptily, F.E. Cecil, O.N. Jarvis, M.J. Mantsinen, S.E. Sharapov, L. Bertalot, S. Conroy, L.C. Ingesson, T. Johnson, K.D. Lawson, S. Popovichev, *γ-ray diagnostics of energetic ions in JET*, Nucl. Fusion 42(2002) 999-1007

[6] V.G. Kiptily, I.N. Chugunov, D.B. Gin, A.E. Shevelev, P.J.L. Heesterman, A. Murari3, 33rd EPS Conf. on Plasma Physics (Rome, Italy, 19–23 June 2006) vol 30I(ECA) P1.077, *http://epsppd.epfl.ch/Roma/pdf/P1 077.pdf*

[7] V. G. Kiptily, C. P. Perez von Thun, S. D. Pinches, S. E. Sharapov, D. Borba, F. E. Cecil, D. Darrow, V. Goloborod'ko, T. Craciunescu, T. Johnson, F. Nabais, M. Reich, A. Salmi, V. Yavorskij, M. Cecconello, G. Gorini, P. Lomas, A. Murari, V. Parail , S. Popovichev, G. Saibene, R. Sartori, D.B. Syme, M. Tardocchi, P. de Vries, V.L. Zoita. *Recent progress in fast ion studies on JET*. Nuclear Fusion, 49, p. 065030, 2009.

[8] V.G. Kiptily, G. Gorini, I. Proverbio, M. Tardocchi, I.N. Chugunov, D. Gin, M. Nocente, S.D. Pinches, S.E. Sharapov, A.E. Shevelev, T. Craciunescu, F.E. Cecil, M. Gatu Johnson, V. Goloborod'ko, C. Hellesen, T. Johnson, K. Kneupner, A. Murari, P.G. Sanchez, D.B. Syme, P. de Vries, V. Yavorskij, V.L. Zoita. *Doppler Broadening of Gamma Ray Lines and Fast Ion Distribution in JET plasmas*, 11th IAEA Technical Meeting on Energetic Particles in Magnetic Confinement Systems, Kyiv, Ukraine.

PROJECT BS-12: MANUFACTURING AND TESTING OF W-COATED CFC TILES FOR INSTALLATION IN JET FOR THE ITER-LIKE WALL PROJECT

Project Leader : Cristian Ruset

EFDA Task Agreement Code: JW6-TA-EP2-ILC-05

Authors: C.Ruset, E.Grigore, I.Munteanu, N.Budica, D.Nendrean

INFLPR

1. General objective of the project

As it was stated in the previous report, the main objectiv of the project is W coating of particular tiles for the main chamber and divertor tiles for the new JET wall. In total there are approx. 1,800 tiles which have to be coated with layers of 10-15 μm and 20-25 μm.

2. Specific objectives for the period July – December 2009

In the installation process of the JET first wall the divertor tiles are installed first. Consequently the priority concerning W coating of JET tiles has been changed. The specific objectives became as follows:

- qualification of the CMSII technology for divertor tiles (G1 and G8)

- coating about 50 % of the divertor tiles

3. Results and discussion

3.1. Qualification of the CMSII technology for divertor tiles

Qualification of coating technology for a particular type of tile involves the following activities: designing and manufacturing of the jigging device for those tiles, producing of prototype W coating on those tiles and successful testing of prototypes at HHF in GLADIS equipment at IPP Garching, Germany.

The production can only start after successful test in GLADIS.

The W coating technology for G6 and G7 tiles was qualified in June 2009. In July 2009 CMSII technology was qualified for G1 and G8 tiles.

Consequently, the production could be carried out for all divertor tiles. The prototypes for G1, G8 and LBSRP tiles are shown in Fig. 1. In Fig. 2 a batch of G6 and G7 tiles can be seen as well.

(a)

(b)

Fig.1 Prototype W coating for G1, G8 (a) and LBSRP (b) divertor tiles

<div align="center">(a)   (b)</div>
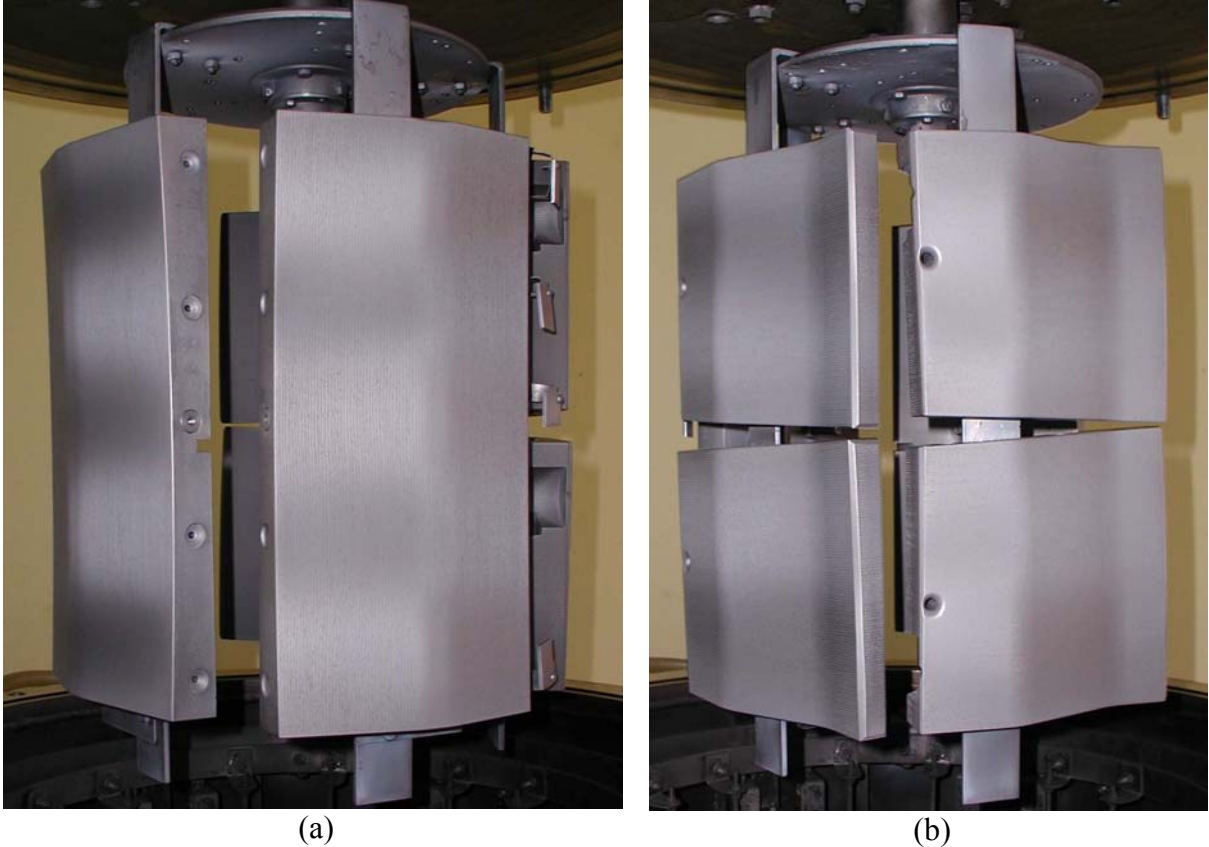
Fig.2 G7 (a) and G6 (b) divertor tiles – series production

3.2. Coating production of divertor tiles

The following tiles have been coated by 15.12.2009.

- Divertor G6 tiles – 98 Off
- Divertor G7 tiles – 49 Off
- Divertor G1 tiles – 102 Off
- Divertor G8 tiles – 101 Off
- Divertor HFGC tiles – 100 Off

Four lots of G6 (10 Off), G7 (6 Off), G1 (7 Off) and G8 (11 Off) have been sent to IPP Garching for HHF tests on production coatings. The tests revealed the good quality of the coatings with "zero" defects.

3.3. Coating production of the main chamber tiles

All the prototypes for the main chamber tiles were coated and successfully tested at IPP with GLADIS ion beam facility.

The following tiles have been coated in the period July – December 2009.

- Tile C– 52 Off
- Divertor C – 52 Off
- Saddle Coil Protection – 2 Off
- Diagnostic covers – Mushroom – 4 Off
- IWGL and IWGL (Be) – 36 Off

The coated tiles were delivered to JET in two consignments.

A synthesis of the coated tiles and delivered to JET is shown below.

- Divertor tiles: 619 (85%)

- Main chamber tiles: 406 (40%)

In accordance with the Milestone M6 of the Task Agreement 75% of the divertor tiles and 25% of the main chamber tiles should be coated and delivered to JET by 31.12.2009.

As it can be seen this milestone was accomplished.

4. Dissemination of results

Although the activity carried out in the framework of this project has mainly a technological character, some results were communicated at the 17th European Fusion Physics Workshop which was held at Velence, Hungary on 7 – 9 December 2009.

[1] C.Ruset, E.Grigore, H.Maier, H.Greuner, R.Neu, M.Mayer and G.Matthews, Status of W coatings techniques.

5. Conclusions

1) „ITER like Wall" project, with a budget of about 40 M€, is very important for both ITER and JET. It will provide information about the plasma-wall interaction under these particular conditions, about the transport of the wall particules through the plasma and about the capacity of these materials to sustain the real thermal loads they are subjected at.

2) EURATOM MEdC Association brings a significant contribution to the project by coating with W all the tiles which have to be coated. This means about 1,800 tiles of different shapes and dimensions. More than a 1000 tiles including 619 divetror tiles were already coated and delivered. This is an impotant milestone which has been accomplished.

Anexa 1-RST

Indicatori de realizare a fazei (conform specificului fiecarui program/proiect)

Denumirea indicatorilor	Numar/ Mii Ron	
	Planificat	**Realizat**
1. Investiții noi in infrastructura CDI	0	0
2. Gradul mediu de utilizare a echipamentelor CDI	80%	80%
3. Număr de entități susținute pentru creșterea capacității de ofertare a serviciilor de experiment		

4.Număr de reviste finanțate, din care
 	
    - Co-editate internațional
 	
    - Indexate ISI
 	
    - Incluse in alte baze de date internaționale recunoscute		

5. Cărți, atlase, dicționare și alte produse cu caracter științific publicate anual, în țară și în străinătate	1 comunicare la conferinta internationala	1 comunicare la conferinta internationala
6.Număr de conferințe organizate, din care internaționale		
7. Număr de expoziții finanțate		
8.Valoarea investiției în infrastructură și servicii de		

comunicaţii		
9.Ponderea cercetătorilor care au acces la resursele de informare on- line	100% *	100%
10.Număr de reviste dedicate popularizării ştiinţei		
11.Număr de proiecte de comunicare ştiinţă-societate		
12.Număr de proiecte de studii prospective		
13.Număr de proiecte de pregătire a unor participări la programe internaţionale		
14.Număr de participări în proiecte internaţionale		
15. Valoarea apelurilor tematice comune lansate		

* Un abonament "on-line" la anumite reviste specifice domeniului fuziunii nucleare ar fi necesar.

PROJECT BS-13: THEORETICAL MODELING OF THE RWM FEEDBACK CONTROL CONSIDERING NEOCLASSICAL TOROIDAL VISCOSITY AND ERROR FIELD PENETRATION

Project Leader : I.G.Miron

EFDA Task Agreement: WP08-MHD-05-01

I.G. Miron

EURATOM-MEdC Association, Romania

National Institute for Lasers, Plasma and Radiation Physics, Bucharest, Romania

Specific Objective II

Determination of the plasma toroidal angular equation of motion

The objective goal is to clearly illustrate the deceleration and finally the toroidal braking of the tokamak plasma toroidal rotation due to non-resonant magnetic error field strength. As a continuation of the first objective, we intend to obtain a plasma coupled analytic toroidal angular equation of motion at the level of each rational surface inside the plasma with respect to the coupling coefficients between neighboring modes.

In a previous theoretical model, starting from the MHD instabilities dispersion relation, the solid increase of the harmonic perturbed flux amplitudes of the modes as the marginal stability is approached has been demonstrated. The error field presence is responsible for the above phenomenon. However the growth rate description type of the instabilities behavior (dispersion relation) is unable to describe the intrinsic influence of the magnetic error field on the plasma neoclassical toroidal viscosity (NTV). The error field augments the NTV destabilizing influence on MHD instabilities. In other words, the electromagnetic torques that develop at the levels of inner plasma inertial layers (at rational surfaces), due to the error field coupling phenomena, increase the destabilizing effect of the NTV torques at the non-ideal MHD layers we have mentioned. Consequently, the non-resonant (i.e. coupled) error field increases the NTV influence that brakes the toroidal plasma rotation locally, at the level of every plasma inner rational surface. To describe the above processes and explicitly illustrate the global braking of

the toroidal plasma rotation a dynamic theoretical model should be built. This model is presented within the frame of this objective.

From the equations that describe the MHD instabilities behavior in vacuum [1], after a laborious calculus we have obtained the following dynamic system of differential equations:

$$\sum_{j,k}\left(\sum_{i=0}^{2} W_{mni}^{jk}\frac{\partial^i}{\partial t^i}\right)\left[u_{ps}^{jk}\frac{\partial\psi^{jk}}{\partial r}+u_{tt}^{jk}\frac{\partial^2\psi^{jk}}{\partial t^2}+\left(\sum_{i=0}^{1} u_{ti}^{jk}\,\Omega_{z0}^i\right)\frac{\partial\psi^{jk}}{\partial t}+\left(\sum_{i=0}^{2} u_{si}^{jk}\,\Omega_{z0}^i\right)\psi^{jk}\right]$$

$$-\sum_{j,k}\left(\sum_{i=0}^{2} A_{mni}^{jk}\frac{\partial^i}{\partial t^i}\right)\psi^{jk}+\sum_{j,k}E_{mn}^{jk}\,\psi_{error}^{jk}$$

The above equations show the interaction of the plasma MHD instabilities with the plasma external structures consisting of a feedback system (a passive and an active shell). Within the assumption of a thin shell approximation, the passive shell consists of two different incomplete and non-overlapping resistive shells (aluminum and stainless steel) disposed in an alternative manner and resistive toroidally uniform. The active system consists of a number of rectangular, radial thin coils and detectors centered at the same local coordinates, the magnetic flux measured by the detector being amplified and fed back into the coils. ψ^{jk} is the perturbed magnetic flux that corresponds to the (j,k) mode perturbation. The parameters W_{mni}^{jk}, u_{ps}^{jk}, u_{tt}^{jk}, u_{ti}^{jk}, u_{si}^{jk}, A_{mni}^{jk} and E_{mn}^{jk} give all the information about the position, disposal, resistive inhomogeneity and amplification amplitude concerning the feedback system that surrounds the plasma column. Ω_{z0} is the plasma toroidal rotation in the MHD regions of the plasma and ψ_{error}^{jk} describes the magnetic error field spectrum.

From the plasma equations that describe the MHD instabilities behavior we have derived the following dynamic system of differential equations:

$$\sum_{j,k}\left[s_{jk4}^{mn}\frac{\partial^4}{\partial t^4}-\left(4ik\Omega_{z0}s_{jk4}^{mn}-s_{jk3}^{mn}\right)\frac{\partial^3}{\partial t^3}-\left(6k^2\Omega_{z0}^2s_{jk4}^{mn}+3ik\Omega_{z0}s_{jk3}^{mn}-s_{jk2}^{mn}\right)\frac{\partial^2}{\partial t^2}+\right.$$

$$+\left(4ik^3\Omega_{z0}^3s_{jk4}^{mn}-3k^2\Omega_{z0}^2s_{jk3}^{mn}-2ik\Omega_{z0}s_{jk2}^{mn}+s_{jk1}^{mn}\right)\frac{\partial}{\partial t}+k^4\Omega_{z0}^4s_{jk4}^{mn}+ik^3\Omega_{z0}^3s_{jk3}^{mn}-$$

$$-k^2\Omega_{z0}^2 s_{jk2}^{mn} - ik\Omega_{z0}s_{jk1}^{mn} + s_{jk0}^{mn}]\psi^{jk} + \sum_{j,k}\{s_{jkl}^{mn} \to t_{jkl}^{mn}, l = \overline{0,4}\}\frac{\partial\psi^{jk}}{\partial t} = 0$$

s_{jkl}^{mn} and t_{jkl}^{mn} are parameters that describe the intrinsic behavior of the plasma, including the viscous stress tensor influence.

To solve the complete system consisting of the above two systems of equations in ψ^{jk} and $\partial\psi^{jk}/\partial r$ the jump of the radial derivative of the magnetic flux perturbation over the inertial layer is needed. Chang et al. [2] derived an analytic formula valid in cylindrical geometry. Adapted for the equilibrium magnetic field structure used here,

$$\frac{\mathbf{B}}{B_{z0}} = \frac{1}{1+\varepsilon\cos\theta}\left(0,\frac{\varepsilon}{q},1\right) + \mathcal{O}(\varepsilon)$$

(where $B_{z0} = B(0,\theta,z)$, q is the safety factor and θ the poloidal angle) the $\partial\psi^{mn}/\partial r$ jump becomes

$$\Delta\Psi_s^{mn} = \frac{\partial\psi_{s+}^{mn}}{\partial r} - \frac{\partial\psi_{s-}^{mn}}{\partial r} = -\frac{m'\pi}{r_s\tan(\pi\sigma_s/2)}\left(\sigma_s\delta_{m'm} + \sum_{m'}\alpha_{m'm}\right)\psi_s^{m'n}$$

The calculated parameters σ_s and $\alpha_{mm'}$ are

$$\sigma_s = -\frac{q_s}{mq'\sqrt{1+\varepsilon^2/q_s^2}}\left[\frac{q_s'}{q_s}\left(3 + \frac{r_s q_s''}{q_s'} - \frac{2r_s q_s'}{q_s}\right)\right.$$
$$\left. + \frac{\varepsilon}{R_0 q_s(1+\varepsilon^2/q_s^2)}\left(2 - \frac{r_s q_s'}{q_s}\right)\left(1 - \frac{r_s q_s'}{q_s}\right)\right]$$

$$\alpha_{m'm} = \frac{q_s(2 - r_s q_s'/q_s)}{m'q_s'R_0\sqrt{1+\varepsilon^2/q_s^2}}\int_0^{2\pi}\frac{\cos\theta\,e^{-i(m'-m)\theta}}{1+\varepsilon\cos\theta}$$

r_s is the minor radius that corresponds to the rational surface where the inertial layer develops, $\varepsilon = r_s/R_0$ and R_0 is the major radius of the plasma ($' \equiv \partial/\partial r$, $'' \equiv \partial^2/\partial r^2$). $\alpha_{m'm}$, i.e. the mode coupling parameter, is the main parameter responsible for error field penetration and NTV torque augmentation.

Using all the relations above we are able to obtain the following Laplace transformed complete system of equations:

$$\sum_{l,k}\left[\left(\sum_{i=0}^{4}\tau^i p_{mnt}^{lk}\right)\overline{\Psi_s^{lk}}+\left(\sum_{i=0}^{4}\tau^i q_{mnt}^{lk}\right)\overline{\Psi_{s+}^{lk'}}\right]=0$$

$$\sum_{l,k}\left[\left(\sum_{i=0}^{4}\tau^i f_{mnt}^{lk}\right)\overline{\Psi_s^{lk}}+\left(\sum_{i=0}^{2}\tau^i g_{mnt}^{lk}\right)\overline{\Psi_{s+}^{lk'}}\right]=\sum_{l,k}\frac{1}{\tau}E_{mn}^{lk}\Psi_{error}^{lk}$$

where $\overline{\Psi_s^{lk}}(r,\tau)=\mathcal{L}\left(\Psi_s^{lk}(r,t)\right)$, p_{mnt}^{lk}, q_{mnt}^{lk} are plasma explicit parameters and f_{mnt}^{lk}, g_{mnt}^{lk} feedback system explicit parameters. Hereinafter we use the Leibniz description of the determinants we have developed in [1] for the above system of equations

$$\Delta_s \equiv \sum_{k=1}^{8L+1}\tau^{k-1}\sum_{\substack{l_1,\dots,l_{2L}=1\\ \text{distinct}}}^{2L}sgn(l_1,\dots,l_{2L})\sum_{\substack{i_1,\dots,i_{2L}=1\\ i_1+\dots+i_{2L}=k+2L-1}}^{5}\prod_{h=1}^{2L}\Gamma_{h i_h}^{l_h}$$

with

$$\Gamma_{h i_h}^{l_h} = p_{h i_h}^{l_h}H(L-l_h)H(L-h) + q_{h i_h}^{l_h}H(l_h-L-1)H(L-h)$$
$$+ f_{h i_h}^{l_h}H(L-l_h)H(h-L-1) + g_{h i_h}^{l_h}H(l_h-L-1)H(h-L-1)H(2-i_h)$$

H is the Heaviside unit step function and $L = (m_2-m_1+1)(n_2-n_1+1)$, where $m_1 \leq m \leq m_2$, $n_1 \leq n \leq n_2$. Within the new index ordering the mode $(m+\alpha,n+\beta)$ becomes the $[(m_2-m_1+1)\beta + \alpha + 1]$ -th mode. Their mutual relations are $l_h = j - m_1 + 1 + (k-n_1)(m_2-m_1+1)$, $h = m - m_1 + 1 + (n-n_1)(m_2-m_1+1)$. Conversely, we have $j = l_h + m_1 - 1 - (m_2-m_1+1)[(l_h-1)/(m_2-m_1+1)]$,

86

$m = h + m_1 - 1 - (m_2 - m_1 + 1)[(h-1)/(m_2 - m_1 + 1)]$, $\qquad$ $k = n_1 + [(l_h - 1)/(m_2 - m_1 + 1)]$ and $n = n_1 + [(h-1)/(m_2 - m_1 + 1)]$, where [ ] denotes the integer part of a number. $sgn(l_1, ..., l_{2L})$ is the sign of the permutations.

The solutions of the Laplace transformed system of equations give the following Laplace transformed magnetic flux perturbations

$$\overline{\Psi^l_s} = \frac{\Delta^l_s}{\tau \Delta_s}$$

for $l = \overline{1, 2L}$ (the index s refers to the rational surface that the inertial layer corresponds). Δ^l_s has the same expression as Δ_s with $\Gamma^{l_h}_{hi_h}$ replaced by the "error field term":

$$\Gamma^{l_h i}_{hi} = p^{l_h}_{hi_h} H(L - l_h) H(L - h)(1 - \delta_{i_h l}) + q^{l_h}_{hi_h} H(l_h - L - 1) H(L - h) +$$

$$+ f^{l_h}_{hi_h} H(L - l_h) H(h - L - 1)(1 - \delta_{i_h l}) + \left(\sum_{i_h = 1}^{2L} E^{l_h}_h \Psi^{l_h}_{error} \right) H(L - l_h) H(h - L - 1) \delta_{i_h l} \delta_{i_h 1}$$

$$+ s^{l_h}_{hi_h} H(l_h - L - 1) H(h - L - 1) H(2 - i_h)$$

Using partial fraction decomposition and the inverse Laplace transform we are finally able to obtain the general expression of the *(m,n)* magnetic flux perturbation at rational surface r_s

$$\Psi^{jk}_s(r, t) = \sum_{j=1}^{L_0} \left[\frac{(\tau - \tau_j) \Delta^{jk}_s}{\tau \Delta_s} \right]_{\tau = \tau_j} (e^{\tau/\varepsilon} - 1)$$

where τ_j are the non-zero roots of the equation $\Delta_s = 0$ and L_0 is the corresponding polynomial degree. Recall that $l = j - m_1 + 1 + (k - n_1)(m_2 - m_1 + 1)$. The marginal stability has been chosen the initial condition, i.e. $\partial^i \Psi^{mn}(r_s, 0)/\partial t^i \approx 0$ for any $i \geq 0$. However, due to the low

values of the error field, the solution did not essentially change if the following initial conditions are chosen: $\partial^i \Psi^{mn}(r_s, 0)/\partial r^i \approx 0$ for any $i \geq 1$ and $\Psi^{mn}(r_s, 0) \approx \Psi^{mn}_{error}(r_s)$.

Following the Braginskii [3] description of the viscous stress tensor into parallel (η_0), perpendicular (η_1 and η_2) and gyroviscous (η_3 and η_4) components, the tensor elements are:

$$\Pi_{ij} = -\eta_0 W_{0ij} - \eta_1 W_{1ij} - \eta_2 W_{2ij} + \eta_3 W_{3ij} + \eta_4 W_{4ij}$$

where $W_{0ij} = (3/2)(n_i n_j - \delta_{ij}/3)(n_k n_l - \delta_{kl}/3)W_{kl}$, $W_{1ij} = [(\delta_{ik} - n_i n_k)(\delta_{jl} - n_j n_l) + (\delta_{ij} - n_i n_j)n_k n_l/2]W_{kl}$, $W_{2ij} = [(\delta_{ik} - n_i n_k)n_j n_l + (\delta_{jl} - n_j n_l)n_i n_k]W_{kl}$, $W_{3ij} = (1/2)[(\delta_{ik} - n_i n_k)\varepsilon_{jml} + (\delta_{jl} - n_j n_l)\varepsilon_{imk}]n_m W_{kl}$, $W_{4ij} = (n_i n_k \varepsilon_{jml} + n_j n_l \varepsilon_{imk})n_m W_{kl}$ and $W_{kl} = \partial v_k/\partial x_l + \partial v_l/\partial x_k - (2/3)\delta_{kl}\nabla \cdot \mathbf{v}$. $\mathbf{n} = \mathbf{B}/B$ where $\mathbf{B}$ is the equilibrium magnetic field and $\mathbf{v}$ is the fluid velocity. After the space integration of the inertial plasma layer toroidal equation of motion, within the cylindrical approximation and negligible poloidal rotation (compared to the the toroidal rotation), the only significant viscous coefficient that matters is the perpendicular coefficient η_2.

The toroidal angular equation of motion of the inertial layer is:

$$\rho \frac{\partial \Omega_z}{\partial t} = -\frac{\eta_2}{r_s^2 c_s^2}\Omega_z + \frac{1}{2\mu_0 r_s^2 R_0 c_s}\sum_{m,n} n\, \mathrm{Im}(\Delta\Psi_s^{mn}\Psi_s^{mn*})$$

ρ is the layer mass density, Im is the imaginary part and * denotes the complex conjugate of a number. $c_s = \delta_s/r_s$ where δ_s is the layer width. δ_s has been chosen as a fixed parameter, although magnetic islands width theory exhibits an explicit perturbed magnetic flux dependence on the former. The mentioned dependence is not relevant for our purpose and is beyond the scope of the present work. The first term on the left-hand side of the equation corresponds to the NTV torque that acts on the inertial layer whereas the second term defines the error field electromagnetic torque that finally increases the destabilizing influence of the NTV.

Finally, after a straightforward calculus we have obtained the following analytic solution of the above equation

$$\Omega_z(t) = \Omega_{z0}e^{-\frac{\eta_a}{\rho r_z^2 c_s^2}t} - \frac{\pi c_s}{2\mu_0 R_0^2}\sum_{\substack{m,\,m',\,n \\ m \ne m'}}\frac{m'n}{\tan(\pi\alpha_s/2)}\times$$

$$\times\sum_{j,k=1}^{L_p}\text{Im}\left\{\frac{\alpha_{m'm}\,\beta_j^{m'n}\beta_k^{mn*}}{\tau_j\tau_k^*}\left[\frac{e^{(\tau_j+\tau_k^*)c}}{\eta_a+\rho(\tau_j+\tau_k^*)r_z^2 c_s^2}-\frac{e^{\tau_j c}}{\eta_a+\rho\tau_j r_z^2 c_s^2}-\frac{e^{\tau_k^* c}}{\eta_a+\rho\tau_k^* r_z^2 c_s^2}+1\right]\right\}$$

where $\beta_j^{mn} = \lim_{\tau\to\tau_j}\left[(\tau-\tau_j)\Delta_s^{mn}/\Delta_s\right]$. A few observations can be made. First, the presence of the magnetic error field changes the NTV dependence of the toroidal plasma rotation. Secondly, all the spectrum of the non-resonant error field contributes to the toroidal deceleration of a certain plasma inertial layer but only due to the mode coupling process. Consequently, it seems that the dynamic theoretical model of the single mode theory is unable to explain the error field penetration and NTV non-resonant magnetic braking effects phenomena, starting from marginal stability.

To prove the above final relation correctness, for the well known Wesson profiles of plasma current and safety factor with $q_0 = 1.01$, $q_a = 2.95$ (the safety factors on the magnetic axis and plasma boundary, respectively), $m_1 = 1$, $m_2 = 3$, the dependencies below have been drawn. The figures clearly show the plasma deceleration and rotation braking under error field penetration and NTV destabilizing influence.
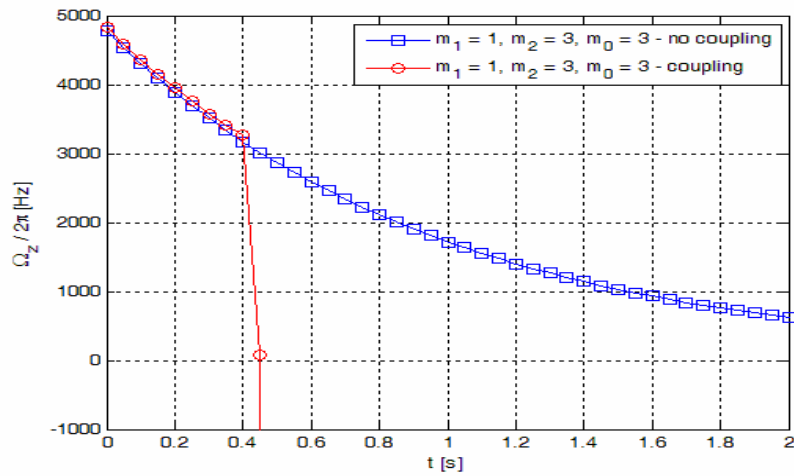
Figure 1: (3,1) inertial layer toroidal rotation rate (t is the

normalized time, $q_z = m_0/n_0$)

Figure 1 presents the *(3,1)* inertial layer toroidal rotation rate (the plasma boundary layer that theoretically explains the appearance and behavior of the external kink modes) under error field action (round symbols) and in the absence of the error field mode coupling (square symbols). The abrupt toroidal rotation braking caused by the highly increased NTV influence under error field penetration process compared to the normal decreasing behavior of the rotation rate under weak feedback stabilizing conditions can be clearly observed.
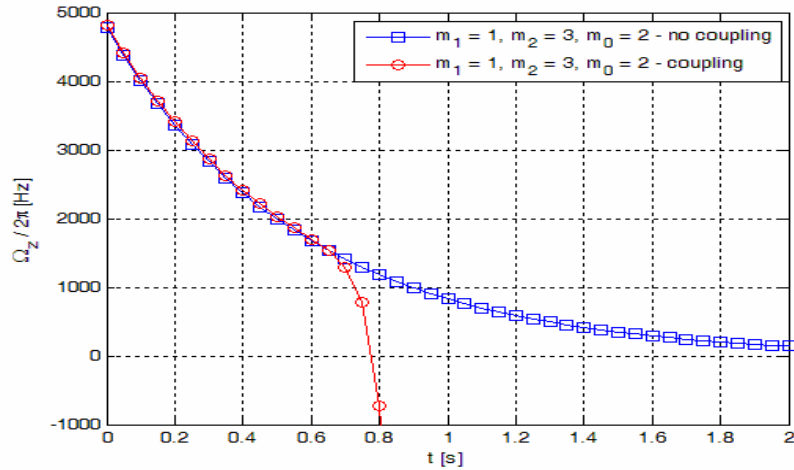
Figure 2: (2,1) inertial layer toroidal rotation rate (t is the

normalized time, $q_s = m_0/n_0$)

Figure 2 shows the above dependency for the inner plasma *(2,1)* inertial layer. The same abrupt deceleration of the plasma layer under the error field influence and NTV amplification effect is showed.

Conclusions

A full analytic dynamic description of the error field penetration and neoclassical toroidal viscosity non-resonant magnetic braking effects has been built. The analytic solutions for the components of the perturbed magnetic flux function have been found. The plasma toroidal angular equation of motion has been solved, an explicit analytic time-dependent solution being

provided. We have showed that the error field penetration process is responsible for the increased destabilizing influence of the neoclassical toroidal viscosity on external and internal magnetohydrodynamic perturbations, caused by the global deceleration of the toroidal rotation of the plasma. The full spectrum of the non-resonant error field contributes to the damping of the rotation of every rational surface corresponding inertial layer due to the mode coupling phenomenon. The clear and explicit analytic obtained solution makes it possible to find the optimal less destabilizing error field spectrum as well as the optimal choice for the feedback parameters in order to provide stability.

[1] I.G. Miron, *Plasma Phys. Control. Fusion* 50 (2008) 095003

[2] Z. Chang et al., *Phys. Plasmas*, 5 (1998) 1076

[3] S.I. Braginskii, *Rev. Plasma Phys.*, 1 (1965) 205.

PROJECT AS-2, BS-2: STUDY OF THE SUBSTRATE TEMPERATURE INFLUENCE DURING FILM DEPOSITION FORMATION OF THE STABLE ALLOYS Be/C, Be/W

Project Leader : C. Lungu

Task Agreement WP09-PWI-07-01

1. Introduction

The current design of ITER involves the use of beryllium (Be), carbon fiber composite (CFC) and tungsten (W) as plasma facing materials. It is expected that Be eroded from the first wall and ionized in the *scrape-off-layer* (SOL) plasma will be mainly re-deposited at divertor surfaces leading to the formation of mixed materials films and corresponding changes of the original material properties of W and C. The in-vessel fuel retention inventory is one of the key issues affected by the mixed material systems. Its and the development of control strategies require a detailed knowledge of both retention and release behaviour of such mixed systems.

After the Be/W ratio was determined by MeV ion beam analysis the films were exposed to a deuterium ion beam using the IPP Garching High Current Ion Source. The energy of the D ion beam was 600 eV D_3^+ (i.e. 200 eV/D) with implantation performed at normal incidence to the target surface at different target temperatures (room temperature, 200 ºC and 350 ºC). Deuterium retention was measured also as function of deuterium fluence in the range of 10^{21} to 10^{23} D/m^2 for each sample. After deuterium implantation, the near surface (up to a depth of 1 μm) amount of D retained in the films was determined by Nuclear Reaction Analysis (NRA) using the $^3He(D,^4He)p$ reaction. As expected, the retention behavior of the films varies as a function of Be/W ratio from that of a pure Be-like behavior at low W concentration, to that of polycrystalline W-like behaviour at high W concentration.

The deuterium release behavior of the films was investigated by Thermal Desorption Spectrometry using the TESS facility at IPP Garching. It turned out that by increasing the W concentration, the low temperature D_2 release peak characteristic to pure Be (present at ≈ 200 ºC [2]) becomes broader and decreases. The experimental results will be interpreted in terms of the

underlying fundamental processes and their effect not only from D fluency and implantation temperature, but also from the morphology and the structure of the films which was determined by Atomic Force Microscopy (AFM), Scanning Electron Microscopy (SEM) and Transmission Electron Microscopy (TEM).

2. Coatings using TVA method

Tungsten and beryllium multilayers were coated on W, graphite and silicon substrates at substrates temperatures of 100; 300 si 500 ^{O}C. The experiments were carried out in a stainless steel vacuum chamber using thermionic vacuum arc (TVA) method developed at NILRP. The evaporation ensemble consists of a beryllium or tungsten anode and a grounded electron source – the cathode. The electron source is made of a loop filament of W wire externally heated with electrical currents of 60 to 120 A (see Fig. 1).

For metals with low vapour pressure (less than 10^{-1}torr) at their melting temperature, ignition of the TVA plasma can only be obtained if the metal is melted in a crucible. For the other metals with high melting points like tungsten, the anode is a rod which is evaporated from the top, like a candle; no crucible is needed. Tungsten rods are only available as sintered material. As such materials contain high amounts of impurities with different vapour pressures at a certain temperature, unwanted sparks appear and ignition of the TVA plasma is not possible using such an anode. A specially designed anode allowed ignition of very stable plasma in W vapours. The W anode consisted of a bunch of thin W wire (0.2 mm) which allowed thorough melting of the material upon electron heating, as can be seen in Fig. 1.[1]
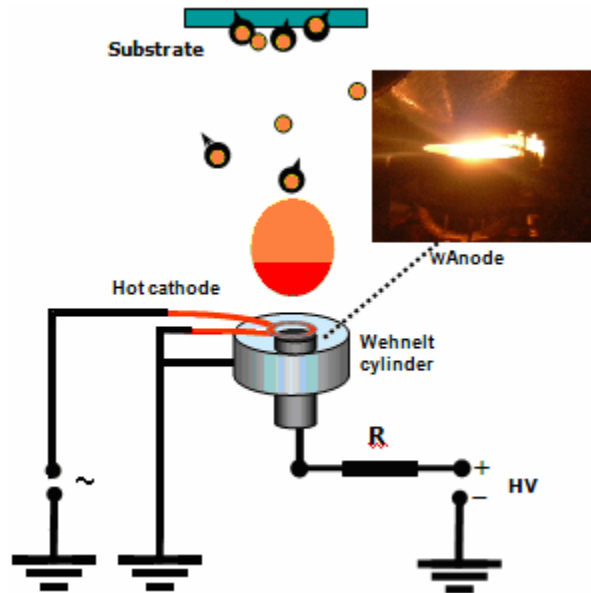
Fig. 1. Experimental setup of Thermionic Vacuum Arc method for W deposition. Inset image: anode made of W wires.

Beryllium was also deposited using a beryllium rod in order to produce pure Be films without impurities that can be generated by the crucible [1]. As the TVA plasma is localized at the anode and does not fill the vacuum chamber, ions and neutrals escape from the plasma and travel without collisions (negligible phenomenon) towards the chamber walls. The ions escape from the plasma due to the potential difference between the plasma and the grounded chamber walls. A bias negative potential was applied on the samples in order to increase the kinetic energy of W or Be ions to produce compact, dense layers.

Were prepared multilayers on W, Si and C (graphite) substrates in the following sequence: Be films of 300-500nm + W films of 20-10nm. Were prepared also mixed layers of Be-C and Be-W in order to determine the fuel retention, in cooperation with specialists of IPP Garching, Germany.

The process parameters are shown below, as collected form the operating process journal:

Be, W deposition (substrate at 100°C)

Sample arrangement:

Samp.	Si1	C2	Si3		C4	Si 5	C6		C7	Si 8	C9	C10	Si 11	C12	Si 13
Pos (cm)	-4.5	-3.5	-3		1	2	3.5		10	11.5	12.5	16.5	18	19.5	22.5

Anode   Anode

W   Be

Deposition parameters:

$P_{initial} = 8.2*10^{-6}$ torr

For Tungsten: For Beryllium:

$U_{a-W} = 1400V$ $U_{a-Be} = 830V$

$I_{a-W} = 1200mA$ $I_{a-Be} = 500mA$

$rata_W = 0,02nm/s$ $rata_{Be} = 0,2nm/s, dar$ initial $0.6nm/s$

$I_{f-W} = 55A$ $I_{f-Be} = 42.8A$

Substrates temperature reached $260\,^{0}C$ at the end of the process.

Deposited layer above each anode: Be: 414nm

W: 31nm

Be, W deposition (substrate heated at $300\,^{0}C$)

Sample arrangement:

Samp.	Si	C	Si		C	Si		C	Si 7	C	Si	C		C	Si	C

	1	2	3		4	5		6		8	9	10	Si 11	12	13	14
Pos (cm)	-3.5	-2.5	-1.5		2.5	3.5		8		10.5	12.5	13.5	17.5	20	21.5	23	25

<center>Anode   Anode</center>

<center>W   Be</center>

Deposition parameters:

$P_{initial} = 2.3*10^{-5}$ torr

For Tungsten:

For Beryllium:

$U_{a-W} = 800 - 900V$

$U_{a-Be} = 1000V$

$I_{a-W} = 2300 - 2500mA$

$I_{a-Be} = 450mA$

$rata_W = 0,08nm/s - constanta$

$rata_{Be} = 0,15nm/s - constanta$

$I_{f-W} = 50A$

$I_{f-Be} = 43A$

Substrates temperature reached $310\,^{0}C$ at the end of the process.

Deposited layer above each anode: Be: 269nm

                                       W: 131.7nm

Note: Very shiny samples and color gradient from W to Be

Be-W co-deposition (substrate heated at $500\,^{0}C$)

Sample arrangement:

Samp.	Si 1	C 2	Si 3		Si 4	C 5	Si 6		Si 7	C 8	Si 9	Si 10	Si 11	Si 12	Si 13	Si 14
Pos	-	-	-		1.5	2.8	4.5		6.5	8	9.5	13	14.5	17.5	20	21.5

(cm)	4.5	3	1.5											

<div align="center">

Anode   Anode

W   Be

</div>
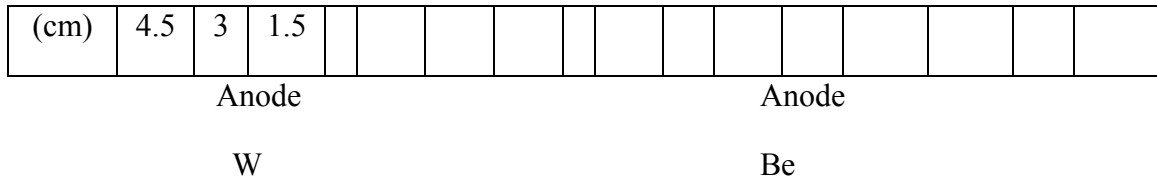
Deposition parameters:

$P_{initial} = 9.5*10^{-6}$ torr

For Tungsten: For Beryllium:

$U_{a-W} = 750V$ $U_{a-Be} = 1000V$

$I_{a-W} = 2800mA$ $I_{a-Be} = 550mA$

$rata_W = 0,08nm/s - constanta$ $rata_{Be} = 0,1nm/s - constanta$

$I_{f-W} = 57A$ $I_{f-Be} = 46A$

Substrates temperature reached $360\,^{0}C$ at the end of the process.

Deposited layer above each anode: Be   -250nm

                                       W   -153nm

Note: Very shiny samples and color gradient from W to Be

3. SEM analyses

The morphology of the substrates and the deposited films was analyzed using a scanning electron microscope Philips ESEM XL 30 TMP operating at 20-30kV. The scanning electron microscope ESEM has all characteristics of and usual SEM microscope, but it can operate in the low vacuum mode, allowing analysis of nonconductive samples, for example.

The microscope has an EDS (Energy Dispersive Spectrometer) device, able to determine the compositional, qualitative and quantitative distribution of an element, as well the surface elemental mapping of a certain sample.

Were obtained secondary electron images and compositional analyses bulletins.
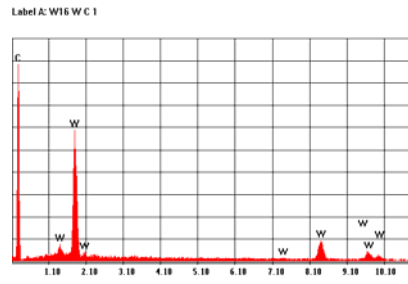
Element	Wt %	At %
C K	70.72	97.37
W L	29.28	2.63
Total	100.000	100.000

W/C 1   W/C 1   W/C 1
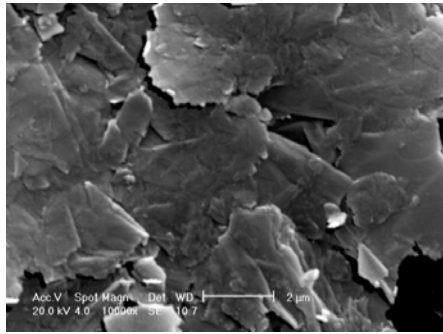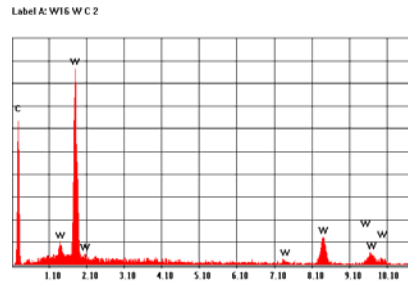
Element	Wt %	At %
C K	61.18	96.02
W L	38.82	3.98
Total	100.000	100.000

W/C 2   W/C 2   W/C 2
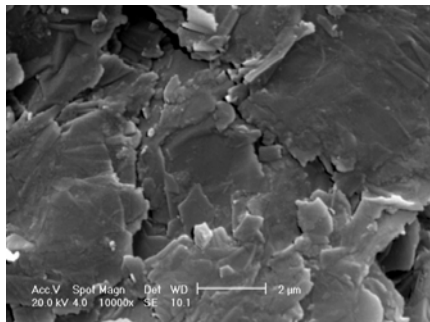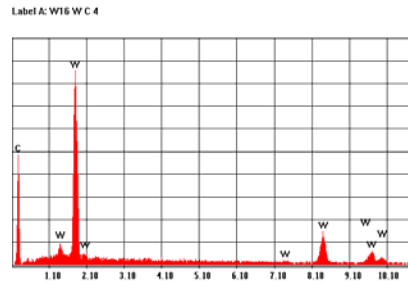
Element	Wt %	At %
C K	54.06	94.74
W L	45.94	5.26
Total	100.000	100.000

W/C 4   W/C 4   W/C 4

Fig. 2. SEM secondary electron images and compositional analyses bulletins of the W films deposited on C substrates. (W films of 20 nm (W/C 1), 40 nm (W/C 2) and 60 nm (W/C 4),
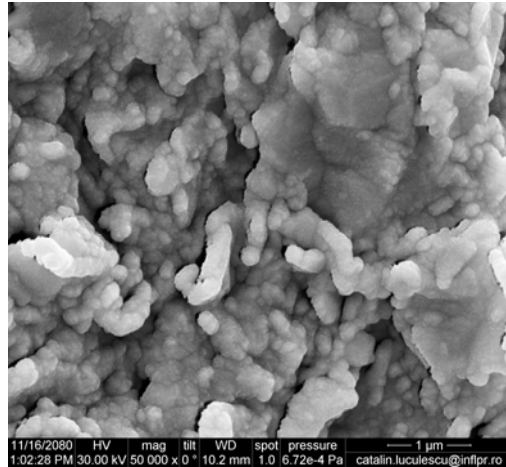
Fig. 3. SEM image of a 300 nm W film coated on C(graphite) substrate
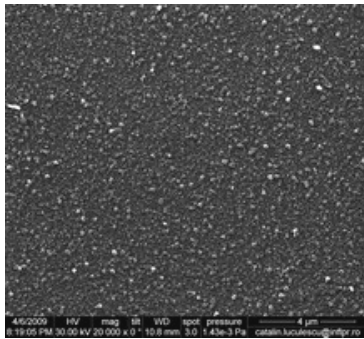
Fig. 4 Be-W at 100°C; Be: 60.55%; O:36.21 %; W:3.25 %
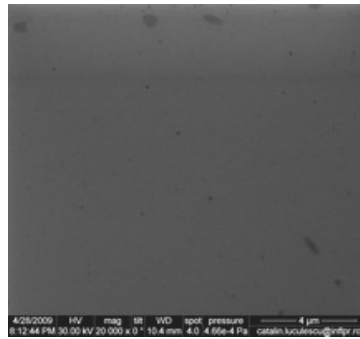
Fig. 5. Be-W at 300°C; Be: 12.52 %; O: 22.98 %; W: 64.48 %
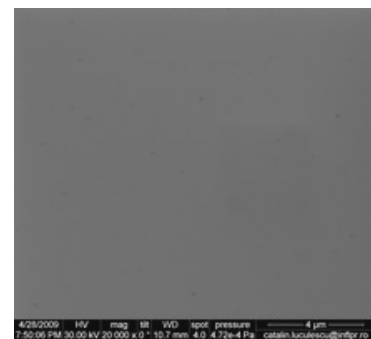
Fig. 6. Be-W at 500°C; Be: 11.83 %, O: 18.09 %; W: 70.06 %

4. AFM analysis

The atomic force microscopy (AFM) data were recorded in non-contact operating mode using a Park XE-100 equipment (silicon tip with conical shape). We used the horizontally line by line flattening as planarization method. The topographical AFM images in combination with a subsequent statistical data analysis, including the calculation of the root mean square roughness and power spectral density (PSD) analysis gave detailed information about the surface

morphology. A typically AFM image of a Be/W film shows a smooth film surface with a step of 100 nm between the coated and uncoated area of a silicon substrate. (Fig.7)
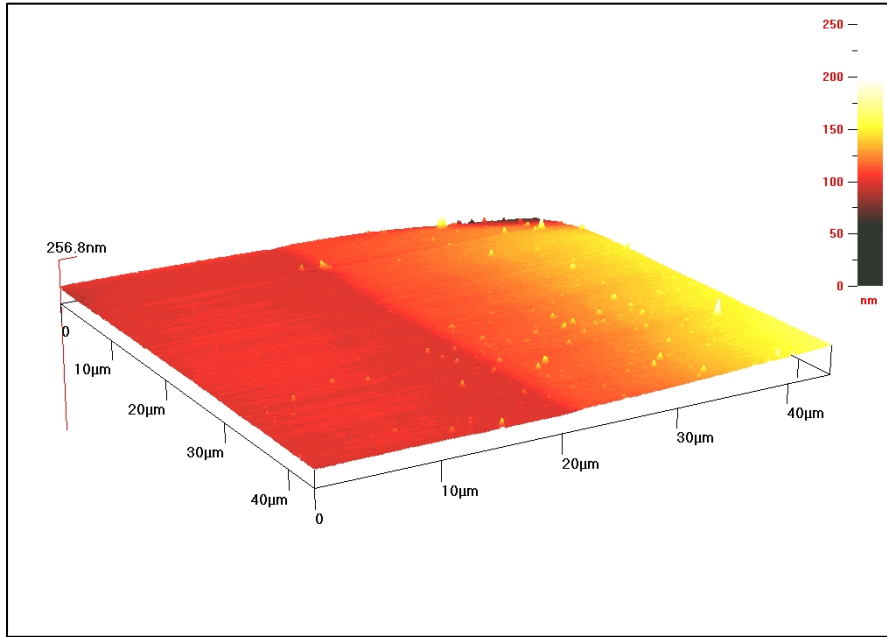
Fig. 7. AFM image of a 100 mm Befilm coated with 50 nm W coated on Si substrat.

5. SIMS analysis

SIMS (Secondary Ion Mass Spectrometry) analyses were performed at VTT Institute in Helsinki, Finland, using following measurement parameters: VG IX70S double focussing magnetic sector SIMS; O_2^+ (5keV) primary ions, ion current 250nA, sputtered area 300 x 220 μm^2 ; Sputter rates: 0.56nm/s (Be/W): Be/W on silicon samples 17Si, 18Si and 19Si contain carbon, iron, nickel, copper and molybdenium in the W/Be interface.

Sample 19Si has some hydrogen at the Be/Si interface. There is some carbon in the Be/Si interface. Be has a peak in the W/Be interface and this could be due to matrix effects; secondary ion yield may change at the interface which changes the signal intensity even though the Be amount may be constant. Another possibility is that W and Be react at the interface. Be-oxide signal seems to be more stable than beryllium. BeO/Be signal ratio varies as a function of substrate temperature; it is highest for sample 19Si (100^oC) and smallest for 17Si (500^oC).

It has to be pointed out that the Be-oxide signal is not real oxide signal because samples were bombarded with oxygen beam and thus oxygen signal is at least partly due to the primary beam. The tail of W signal seems to broaden as a function of the substrate temperature. The long tail in the beryllium and beryllium oxide signals in the silicon substrate can be due to SIMS parameters.

Iron (56) and nickel (58) signals in the Si substrate are not real iron and nickel signals; they are due to silicon molecular signals $^{28}Si_2$ and $^{29}Si_2$.

Thicknesses of the layers are given in Table 1.Depth profiles of Be/W coatings are presented in Figs. 8-10.

Table 1. Thickness of Be/W samples, as determined by SIMS analysis

Sample	Thickness of W layer (nm)	Thickness of Be layer (nm)
17Si Be/W at 100°C	65	340
18Si Be/W at 300°C	58	385
19Si Be/W at 500°C	64	365

Fig.8 SIMS depth profile of the Be/W sample deposited at 100°C
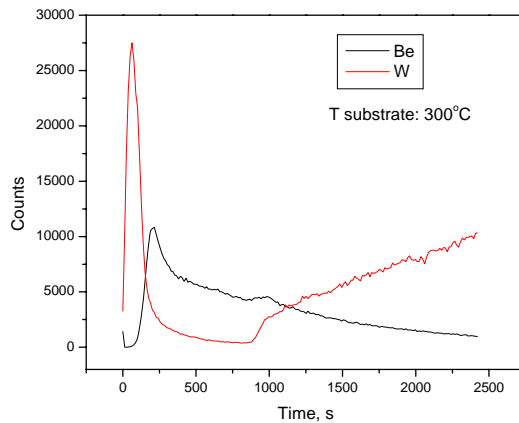
Fig. 9 SIMS depth profile of the Be/W sample deposited at 300°C

101
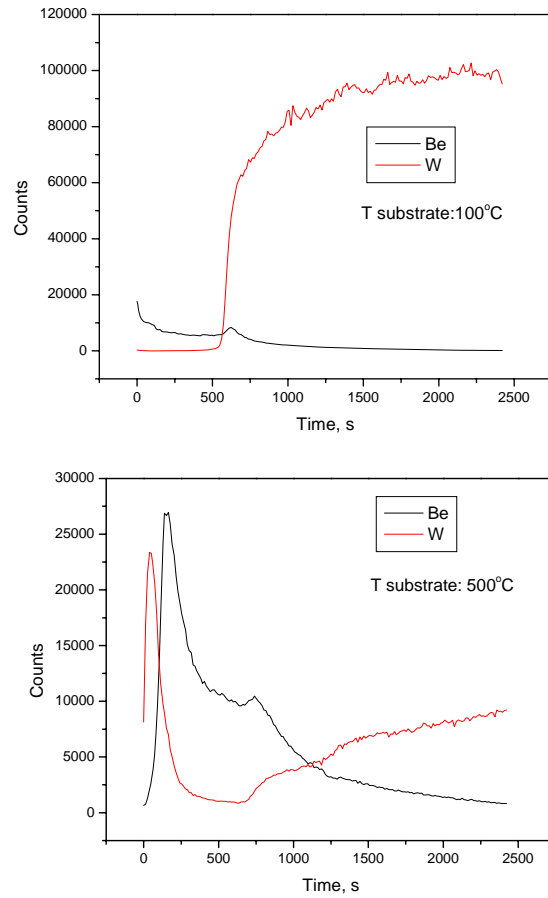
Fig. 10 SIMS depth profile of the Be/W sample deposited at 500°C

6. RBS analysis

From RBS measurements it was revealed that no impurities except oxygen were present in the film. Fig. 11 presents the RBS spectrum obtained using a 2.6 MeV ^{4}He ion beam. From it, one can see that the tungsten is not uniformly distributed into the film; on the top surface of the film the tungsten concentration is lower than near the film substrate interface. Also, the presence of the oxygen at the film-substrate interface and on top surface is observed.
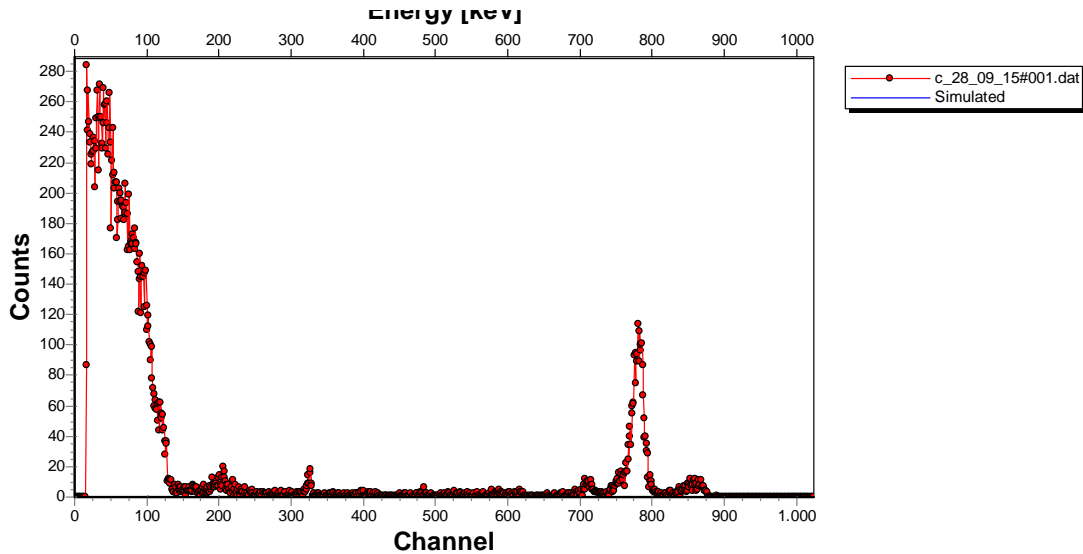
Figure 11. Experimental RBS spectra of a Be-W mixed film deposited on graphite

In order to study the fuel retention in this Be-W mixed films, deuterium implantation was performed at IPP Garching in the High Current Ion Source. The energy of D ion beam was 600 eV D_3^+ (meaning 200 eV/D) at an incident direction normal to the target surface at room temperature. The fluence was 5 x 10^{22} D/m^2 for each sample. After the implantation, the amount of D retained in the films was determined by Nuclear Reaction Analysis (NRA) using ^3He ion beam. Thermal Desorption Spectrometry (TDS) was also performed in TESS facility of IPP Garching. The temperature ramp was 15K/min the same as for pure Be films. The TDS measurements revealed the presence of a sharp low temperature desorption peak at ~ 200º C, characteristic to pure Be, where almost all the deuterium is desorbed from the sample. Also, a broad peak centered around 300º C was observed. According to the literature, this peak, which is characteristic to pure tungsten, can be attributed to the tungsten presence in the film. For exemplification, in Fig.12 and Fig.13, the TDS spectra obtained for pure Be film as well as for Be-W mixed film are presented.
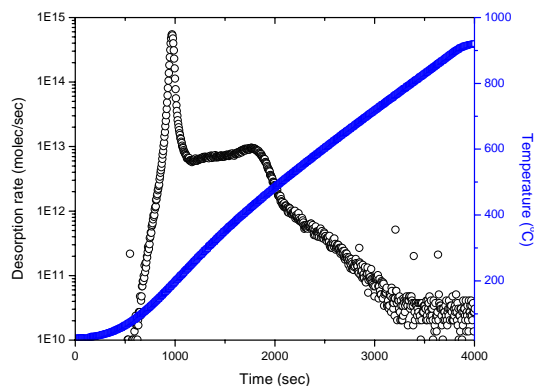
Fig. 11. TDS spectra of a pure Be film deposited on graphite
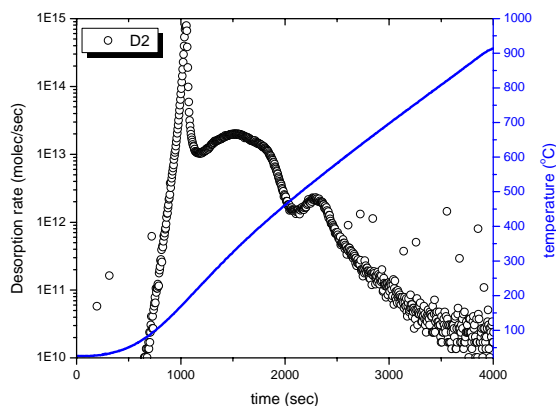
Fig. 12. TDS spectra of a Be-W mixed film deposited on graphite

7. Retention and desorption studies on composite films.

Deuterium implantation was performed in the High Current Ion Source at IPP Garching, Germany. The energy of D ion beam was 600 eV D_3^+ (200 eV/D), and the incident direction was normal to the target surface. The implantation was carried out at a room temperature with the flux of ~ 3 x 10^{19} D/m^2s. After certain continuum implantation (1.39 x 10^{22} D/m^2), the amount of D retention was determined by nuclear reaction analysis with using ^{3}He (d, p) α reaction.

The total amount of Deuterium retained as a function of the tungsten concentration is shown in Fig.13.

Total amount of deuterium in samples after implantation with 200eV/D at RT
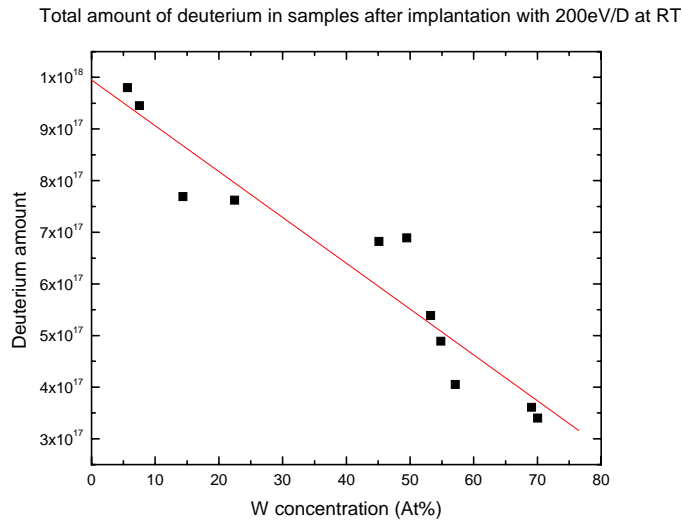
Fig. 13 The total amount of deuterium retained as a function of the tungsten concentration

It is observed that the deuterium retained in the samples depends highly on the Be/W relative concentration. In TESS facility at IPP Garching, thermal desorption spectroscopy (TDS) experiment was performed for the implanted samples. The experiment consists in heating the sample with 15K/min ramp, up to 1000K followed by a 20 minutes hold, and the cooling by it self, measuring the amount of deuterium ejected from the samples. The temperature was measured on the oven, and by having a good calibration previously made (Fig.14), it is possible to correlate the real sample temperature with the deuterium emission.
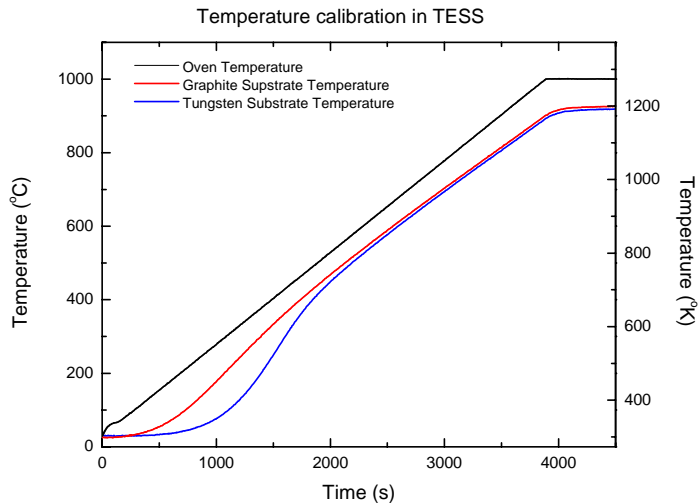
Fig. 14 Substrate temperature calibration in TESS facility

The TDS spectra obtained measuring samples with increased W content are shown in Fig.15. Clearly can be observed the large amount of D2 retained in the samples with low W content.
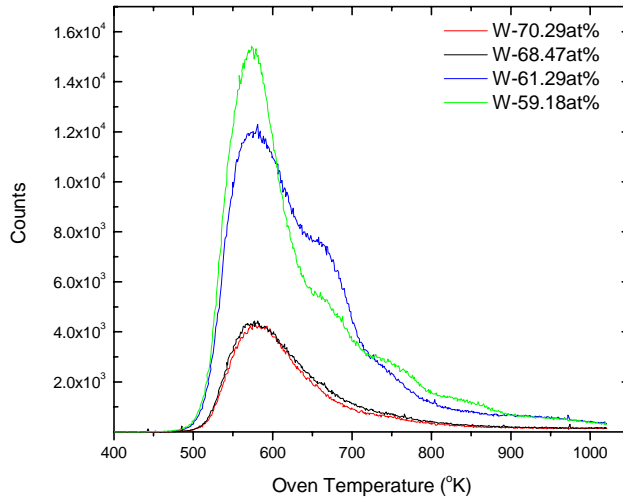
Fig. 15 TDS D_2 spectra of the Be-W films

The Deuterium retained in the samples was measured using NRA method. The results were in good correspondence with the TDS measurements, as shown in Fig. 16. Here is a plot of the amount of deuterium retained inside the sample as a function of the tungsten concentration. As it is shown, the deuterium retained in the sample does have a trend of decreasing with the relative increase of the W concentration.
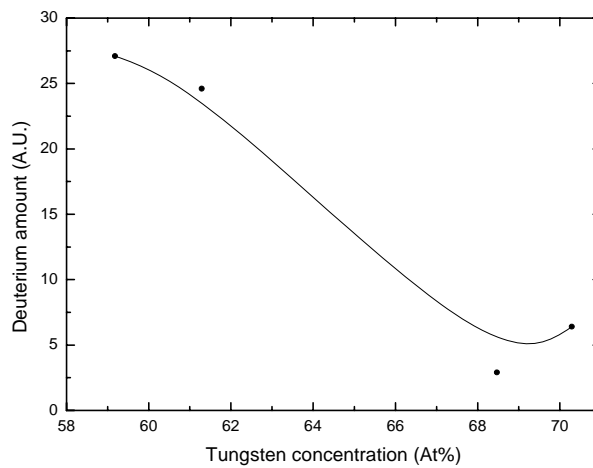
Fig. 16 The deuterium retained in the Be-W samples after TDS

Analyzing the obtained results we can conclude that W presence into the prepared Be/W composite films leads to almost linear decrease of the fuel retention as function of the W concentration.

8. Conclusions

Were obtained relevant data from the experiments concerning Be, C and W in multistrat as well as binary composite structures prepared using therionic vacuum arc method, at NILPRP.

The influence of the substrate temperature during sample preparation was inffered by SEM, AFM, RBS, NRA and SIMS analyses.

Increased tungsten concentration into the Be-W composite films was found to linerly decrease the fuel retention is such films. The TDS spectra proved that different behavior is caused by different trapping sites for each of these elements.

References

[1] R. Vladoiu, V. Ciupina, C. P. Lungu, V. Bursikova, G. Musa, Thermoionic vacuum arc (TVA) deposited tungsten thin film characterization, Journal of Optoelectronics and Advanced Materials Vol. 8, No. 1, February 2006, p. 71—73.

[2] C. P. Lungu, I. Mustata, V. Zaroschi, A. M. Lungu, A. Anghel, P. Chiru, M. Rubel, P. Coad G. F. Matthews and JET-EFDA contributors, Beryllium Coatings on Metals: Development of Process and Characterizations of Layers, Phys. Scr. T128 (2007) 157–161.

[3] Anghel, I. Mustata, C. Porosnicu, C. P. Lungu,   Influence of the bias voltage on the formation of beryllium films by a thermionic vacuum arc method, *Journal of Nuclear Materials*, *Volume 385, Issue 2, 31 March 2009, Pages 242-245*

[4] Anghel, C. Porosnicu, C. P. Lungu, I. Mustata, K. Krieger, Influence of thermal treatment of Beryllium thin films deposited on graphite on the Be – C mixture formation, PFMC 12 International Conference, Julich May 2009

[5] A. Anghel, C. Porosnicu, M. Badulescu, I. Mustata, C.P. Lungu, K. Sugiyama, S. Lindig, K. Krieger, J. Roth, A. Nastuta, G. Rusu, G. Popa, Surface morphology influence on deuterium retention in beryllium films prepared by thermionic vacuum arc method, Nuclear Instruments and Methods in Physics Research Section B: Beam Interactions with Materials and Atoms, Volume 267, Issue 2, January 2009, Pages 426-429.

Publications connected to the project

1. C.P.Lungu, Nanostructured film preparation by thermionic vacuum arc, 19 pagini, contributie in cartea: New applications of micro- and nanotechnologies/ Editors: Maria Zaharescu, Liviu Giurgiu, Dan Dascalu, Editura Academiei Romane, 2009, ISBN 978-973-27-1803-2, pp.67-96.

2. C. P. Lungu, I. Mustata, V. Zaroschi, A.M. Lungu, P. Chiru, A. Anghel, C. Porosnicu, I. Jepu, V. Bailescu, G. Burcea, G. Dinuta, F. Din, N. Balan, G. Serban and JET-EFDA Contributors, Comparison of the beryllium films prepared by thermionic vacuum arc and thermal evaporation methods, Proc of. ISPC 19, International Symposium on Plasma Chemistry, Bochum, Germany, July 27-31, 2009

3. Cristian P. LUNGU, Ion MUSTATA, Alexandu ANGHEL Corneliu POROSNICU, Ionut JEPU, Catalin TICOS Ana M. LUNGU, Mihai GANCIU, Arcadie SOBETKII Gheorghe HONCIUC and Patrick CHAPON Preparation and Characterization of Multifunctional, Nanostructured Coatings Using Thermionic Vacuum Arc Method, Symposyum Kobe, March 2-4 2009, *Frontier of Applied Plasma Technology (Edited by Osaka University, Japan),* Vol.2 July 2009, pp1-6.

4. K. Sugiyama, K. Krieger, C.P. Lungu, J. Roth, Hydrogen retention in ITER relevant mixed material layers *Journal of Nuclear Materials*, *Volumes 390-391*, *15 June 2009*, *Pages 659-662*

5. Cristian P. LUNGU, Alexandru ANGHEL, Corneliu C. POROSNICU, , Ion MUSTATA, Ana M. LUNGU, Petrica CHIRU, Valer ZAROSCHI, Dorin DUDU, Ion VATA, Florin MICULESCU, Victor ANDREI, Rodica VLADOIU and Victor CIUPINA Study of the substrate temperature influence on Be-C, Be-W stable alloy formation, 10th International Balkan Workshop on Applied Physics, July 6-8th, 2009, Constanta, Romania

Indicatori de realizare a fazei (conform specificului fiecarui program/proiect)

Denumirea indicatorilor	Numar/ Mii Ron	
	Planificat	**Realizat**
1. Investiții noi in infrastructura CDI	20	20
2. Gradul mediu de utilizare a echipamentelor CDI	90%	90%
3. Număr de entități susținute pentru creşterea capacității de ofertare a serviciilor de experiment		

4.Număr de reviste finanțate, din care
 	
    - Co-editate internațional
 	
    - Indexate ISI
 	
    - Incluse in alte baze de date internaționale recunoscute		

5. Cărți, atlase, dicționare şi alte produse cu caracter ştiințific publicate anual, în țară şi în străinătate		
6.Număr de conferințe organizate, din care internaționale		
7. Număr de expoziții finanțate		
8.Valoarea investiției în infrastructură şi servicii de comunicații		

9.Ponderea cercetătorilor care au acces la resursele de informare on-line	100%	100%
10.Număr de reviste dedicate popularizării științei		
11.Număr de proiecte de comunicare știință-societate		
12.Număr de proiecte de studii prospective		
13.Număr de proiecte de pregătire a unor participări la programe internaționale	1	1
14.Număr de participări în proiecte internaționale	4	4
15. Valoarea apelurilor tematice comune lansate		

Anexa la Raportul Științific și Tehnic- RST

Indicatori de realizare a fazei (conform specificului fiecarui proiect)

Nr. crt.	Indicatori	UM
1.	Număr de publicați în reviste: Co-editate internațional - Indexate ISI - Incluse în alte baze de date internaționale recunoscute	Nr. 1 1

2.	Articole publicate în cărți, atlase, dicționare și alte produse cu caracter științific publicate anual (în țară și în străinătate)	Nr. 1
3.	Participări la conferințe organizate, dintre care internaționale	Nr. 3/3
4.	Evenimente organizate dintre care internaționale	Nr.
5.	Pliante, broșuri, postere pentru diseminare de informații	Nr.
6.	Proiecte de comunicare științifică	Nr.
7.	Proiecte de studii prospective	Nr.
8.	Proiecte / participanți în proiecte internaționale finanțate	Nr. 4/7

6. C.P.Lungu, Nanostructured film preparation by thermionic vacuum arc, 19 pagini, contributie in cartea: New applications of micro- and nanotechnologies/ Editors: Maria Zaharescu, Liviu Giurgiu, Dan Dascalu, Editura Academiei Romane, 2009, ISBN 978-973-27-1803-2, pp.67-96.

7. C. P. Lungu, I. Mustata, V. Zaroschi, A.M. Lungu, P. Chiru, A. Anghel, C. Porosnicu, I. Jepu, V. Bailescu, G. Burcea, G. Dinuta, F. Din, N. Balan, G. Serban and JET-EFDA Contributors, Comparison of the beryllium films prepared by thermionic vacuum arc and thermal evaporation methods, Proc of. ISPC 19, International Symposium on Plasma Chemistry, Bochum, Germany, July 27-31, 2009

8. Cristian P. LUNGU, Ion MUSTATA, Alexandu ANGHEL Corneliu POROSNICU, Ionut JEPU, Catalin TICOS Ana M. LUNGU, Mihai GANCIU, Arcadie SOBETKII Gheorghe HONCIUC and Patrick CHAPON Preparation and Characterization of Multifunctional, Nanostructured Coatings Using Thermionic Vacuum Arc Method, ISAPS Symposyum Kobe, March 2-4 2009, Frontier of Applied Plasma Technology (Edited by Osaka University, Japan), Vol.2 July 2009, pp1-6.

9. K. Sugiyama, K. Krieger, C.P. Lungu, J. Roth, Hydrogen retention in ITER relevant mixed material layers Journal of Nuclear Materials, Volumes 390-391, 15 June 2009, Pages 659-662

10. Cristian P. LUNGU, Alexandru ANGHEL, Corneliu C. POROSNICU, , Ion MUSTATA, Ana M. LUNGU, Petrica CHIRU, Valer ZAROSCHI, Dorin DUDU, Ion VATA, Florin MICULESCU, Victor ANDREI, Rodica VLADOIU and Victor CIUPINA Study of the substrate temperature influence on Be-C, Be-W stable alloy formation, 10th International Balkan Workshop on Applied Physics, July 6-8th, 2009, Constanta, Romania.

STUDY OF THE TERNARY SYSTEM FORMATION Be-C-W USING THERMIONIC VACUUM ARC METHOD; INFLUENCE OF OXYGEN ON THE PROCESS

1. Introduction

Mixed materials thin film depositions are used in order to obtain structures that they have the same characteristics as the films that are deposited in different fusion reactor's areas. This type of films can be generated under working conditions of the thermonuclear reactors, where some of the walls are made of beryllium tiles, or beryllium coated inconel tiles, and other reactor regions are made of carbon and tungsten. The high energy plasma determine the migration and mixture of these elements in unwanted places.

As it is well known, within the thermonuclear reactor there is the probability that the heat, ion and especially neutron flux damaging the wall by cracks, material sputtering and transport inside the reactor, superficial film erosion, chemical composition change of the walls, etc.. Tritium and deuterium plasma inside the ITER fusion reactor, which will be in operational use by 2018, reaches a temperature higher than 100 million degrees, and stopping the wall material plasma contamination trough the above mentioned mechanisms is the main issue of operating it.

The inner wall is one of the main components of ITER and must be designed so that to be able to remove the plasma's caloric flux, to reduce the nuclear effects inside the vacuum chamber and to protect the superconductive coils against overheating and the radiation damage. The generated fusion power is around 1500MW with a medium neutron flux near the wall of $1MW/m^2$. The inner wall must also endure the plasma disruption heat and electromagnetic loads.

The beryllium-tungsten-carbon combination was never tested inside the tokamak, both materials being of high interest for this purpose. Although tungsten is high temperature resistant (melting point: 3695^0C) and has a very high atomic number, it ionizes very easy, so that the tungsten atoms that reach inside the plasma cause a high energy absorption from the deuterium and tritium ions.

Theoretical analysis using simulations were performed regarding sputtering and erosion combined with plasma evaporated particles transport and their later deposition in other parts of the reactor but the obtained results need to be confirmed through several experiments that use layers containing different tungsten-beryllium-carbon mixtures and their high energy plasma and ion flux interaction behavior is met to determine the most suited for the tokamak parts that interact with the fusion plasma.

2. Experimental Set-up

The obtained mixed materials films using the deposition method suggested by the research group from NILPRP will be investigated using experimental conditions similar to the ITER operational/ working conditions (high flux ions, electrons and neutrons bombardment, etc).

The Thermionic Vacuum Arc (TVA) method was used to prepare pure and mixed materials layers to be studied as point of view of morphological, structural and fuel retention properties. The evaporation was performed at a temperature lower than the material's melting point and the deposition process may be obtained using neutral atoms from the material's surface, but also by generating metal vapor plasma, the substrate being bombarded with metallic neutrals as well as ions. The plasma generated ions may be accelerated towards the substrate by applying a bias voltage on the substrates.

In order to obtain a variable Be-C-We relative concentrations with different oxygen content into the prepared layers, a setup as in Fig.1 was developed. The distance between the anodes was 20cm and the sample holder-anodes distances were around 25 cm, as the particle flux depends on the distance and the incident angle. The two anodes (one made of pure Be rod and another made by a graphite rod surrounded by 1 mm in diameter tungsten wires) and the substrates were positioned so that a different particle flux was present for each sample in a deposition batch.
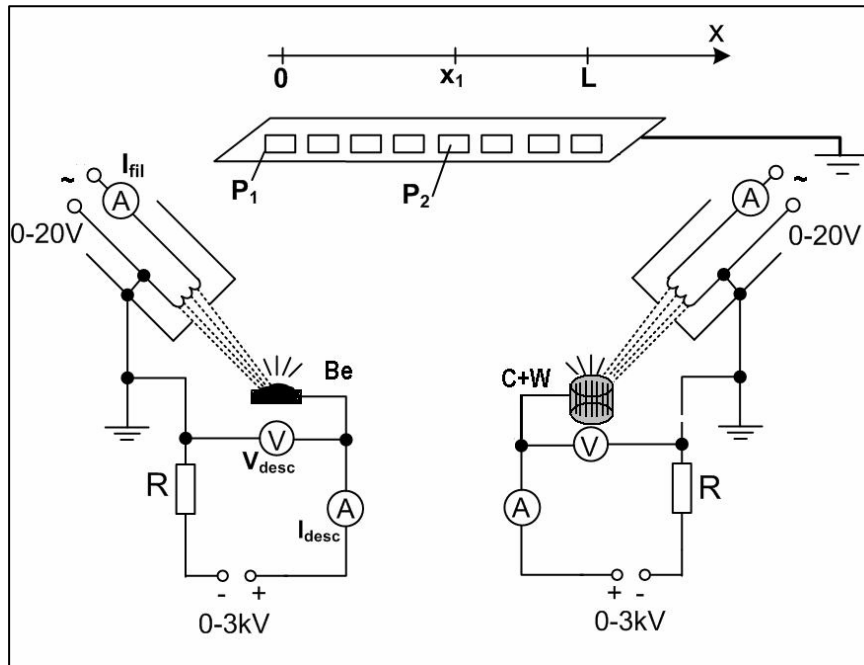
Fig.1. Schematic representation of the deposition system and the electrical conections used to obtain mixed Be-C-W layers.

If several samples are placed at diferent distances to the two evapotaion sources (as shown in figure 1), it is possible to obtain almost continuum concentration variation.

The electron beams evaporate both the Be and the C-W used as anodes, by applying high voltages (1-5kV) between cathodes and respectively anodes. Bright plasmas in pure beryllium and carbon-tungsten atoms are ignited simultaneously. The plasmas are independently controlled by the electron beams (thermo-electrons) emitted by the heated cathodes and the applied voltage on the anodes, in order to obtain the desired concentrations. The oxygen was introduced into the layers adjusting the evaporation rates, allowing the residual gas from the reaction chamber to enter the layers just during their formation. In order to increase the oxygen content, the residual gas pressure was controlled by adding additional oxygen gas. The depositions were performed usually at $5*10^{-6}$ tor, residual air, and at $5*10^{-5}$ torr in residual atmosphere of oxygen.

2.1 Substrates and deposition conditions

For each batch, carbon and silicon substrates were used. The carbon substrates were mirror polished fine grain graphite. The substrates were 12 by 15 mm rectangular shape. In the

114

first two batches, the films were deposited at room temperature, while for the next two, an oven was used to heat them at 350, and 500C respectively. This way, the atoms and the ions from the plasma, reach the substrate without causing thermal shocks and the lack of thermal shocks decreases the possibility of getting defects caused by mechanical stress.

The substrates were placed on a holder that was mounted inside the deposition camber, and put in thermal contact with the oven.

For a better systematization and to improve further calculus, the samples were given coordinates. Doing so, x=0 on the sample holder is exactly above the beryllium anode. The samples were indexed according to the deposition date and their position relative to the anodes. The sample position, index and substrate type are presented in Tables 1-3. Table 4 presents the TVA processing parameters.

Table 1. Substrate's positions at room temperature deposition

Samp.	Si	C	Si	C	Si	C	C	Si	C	C	Si	C	Si
Index	P01	P02	P03	P04	P05	P06	P07	P08	P09	P10	P11	P12	P13
x(cm)	-4.5	-3.5	-3	1	2	3.5	10	11.5	12.5	16.5	18	19.5	22.5

Table 2. Substrate's positions at 350°C temperature deposition

Samp.	Si	C	Si	C	Si	C	Si	C	Si	C	Si	C	Si	C
Index	P01	P02	P03	P04	P05	P06	P07	P08	P09	P10	P11	P12	P13	P14
x(cm)	-3.5	-2.5	-1.5	2.5	3.5	8	10.5	12.5	13.5	17.5	20	21.5	23	25

Table3. Substrate's positions at 500°C temperature deposition

Samp.	Si	C	Si	Si	C	Si	Si	C	Si	Si	Si	Si	Si	Si

Index	P01	P02	P03	P04	P05	P06	P07	P08	P09	P10	P11	P12	P13	P14
x(cm)	-4.5	-3	-1.5	1.5	2.8	4.5	6.5	8	9.5	13	14.5	17.5	20	21.5

Table 4. The parameters for the depositions performed

T_{sub} str^o C	I_{fW} (A)	I_{aW} (mA)	U_{aW} (V)	Dep.rate for W (nm/s)	Deposited W (μm)	I_{fBe} (A)	I_{aBe} (mA)	U_{aBe} (V)	Dep. Rate for Be (nm/s)	Deposited Be (nm)	Total thickness (nm)
R.T	55	1200	1400	0.02	31	42.5	500	830	0.2-0.6	414	445
350	50	2400	900	0.08	131.7	43	450	1000	0.15	269	400.7
500	57	2800	750	0.08	153	46	550	1000	0.1	250	403

3. RBS depth profile analysis

RBS measurements were performed to investigate the films compositions, the position of the oxygen and to see if there is a mixture of the three elements. For this it had been used a 4He energy beam of 2.6 MeV. The beams energy value was chosen taking into account the interaction cross section of ^{4}He and Be to avoid the non-Rutherford interaction that may cause errors in the data interpretation. The fitting of the experimental data was done using SIMNRA code, developed at IPP Garching. Fig. 2 shows the RBS experimental and SIMNRA code simulated spectra of the Be-C-W film deposited on graphite substrate at room temperature and Fig. 3 shows the elemental concentration depth profile of the same film obtained by processing the RBS spectra.
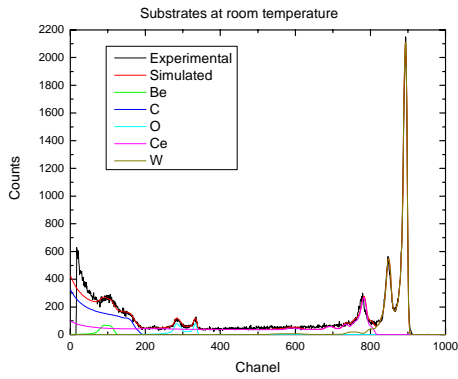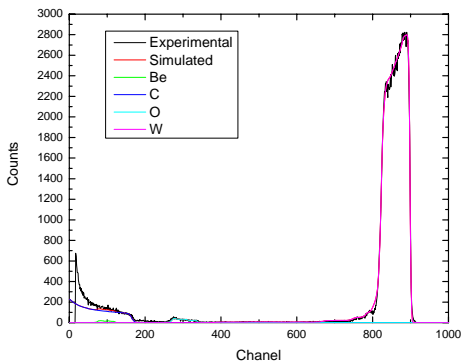
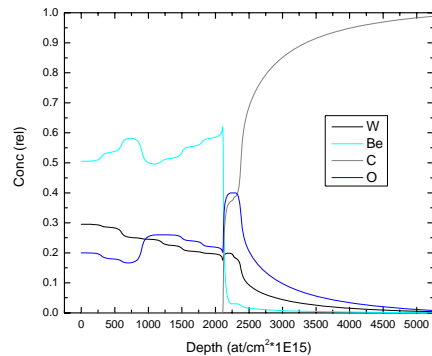Fig. 2 RBS experimental and SIMNRA code simulated spectra of the Be-W film deposited on graphite substrate at room temperature.
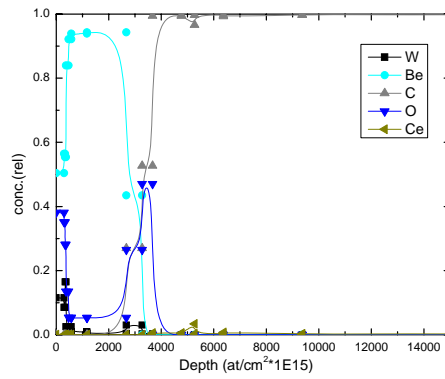
Fig. 3 The depth profile of elemental concentration obtained by processing RBS spectra of the Be-W film deposited on graphite substrate at room temperature.

Fig. 4 shows the RBS experimental and SIMNRA code simulated spectra of the Be-W film deposited on graphite substrate at 500°C and Fig.5 shows the elemental concentration depth profile of the same film obtained by processing the RBS spectra

Fig. 4 RBS experimental and SIMNRA code simulated spectra of the Be-W film deposited on graphite substrate at 500°C.

Fig. 5 The depth profile of elemental concentration obtained by processing RBS spectra of the Be-W film deposited on graphite substrate at 500°C

The main aspect underlined by RBS measurements is that for the room temperature substrates the film was oxidized only at the surface and at the interface, while for the heated substrates the oxygen present at the surface, and diffuses into the material, oxidizing the beryllium and the tungsten in the whole film. In addition, the interface oxygen begins to migrate into the substrate as the temperature is increased.

As in RBS method the elements peak shifts with the depth where the material is found in the film, and considering that the thickness of the film cannot be determined with enough precision to know exactly where the interface is, other analysis was needed to check the composition. Although EDS does not give information about the depth profile because it integrates the signal of the distorted electrons, it can give accurate information about the composition. Using the EDS results, we concluded that at the substrate-film interface was identified cerium, material used in graphite substrate polishing.

4. XPS analysis

The films deposited using two anodes (one Beryllium and the other made of tungsten wires inside a carbon rod) XPS analysis was performed.

For the beryllium inside the film high oxidation occurred. We can argue that this happened during and after the deposition. The ratio also changes as we go inside the film as shown in figures 6 and 7.

| (a) at the surface | (b) inside the film | (c) at the interface |
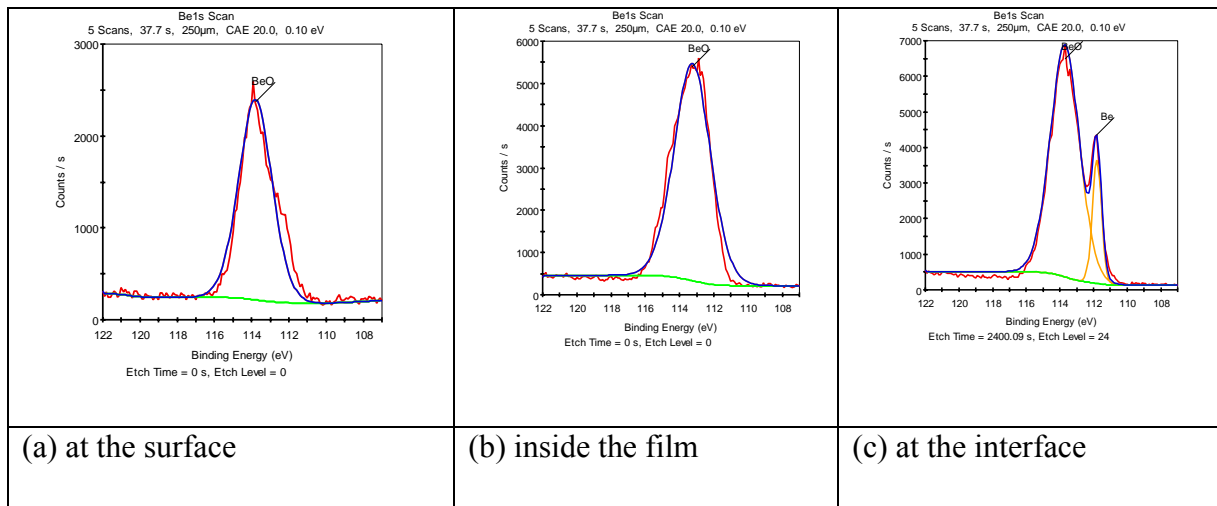
Figure 6 B1s peak at the surface (a), inside the film (b) and at the interface (c)

Fig. 7 The depth evolution of the B1S peak
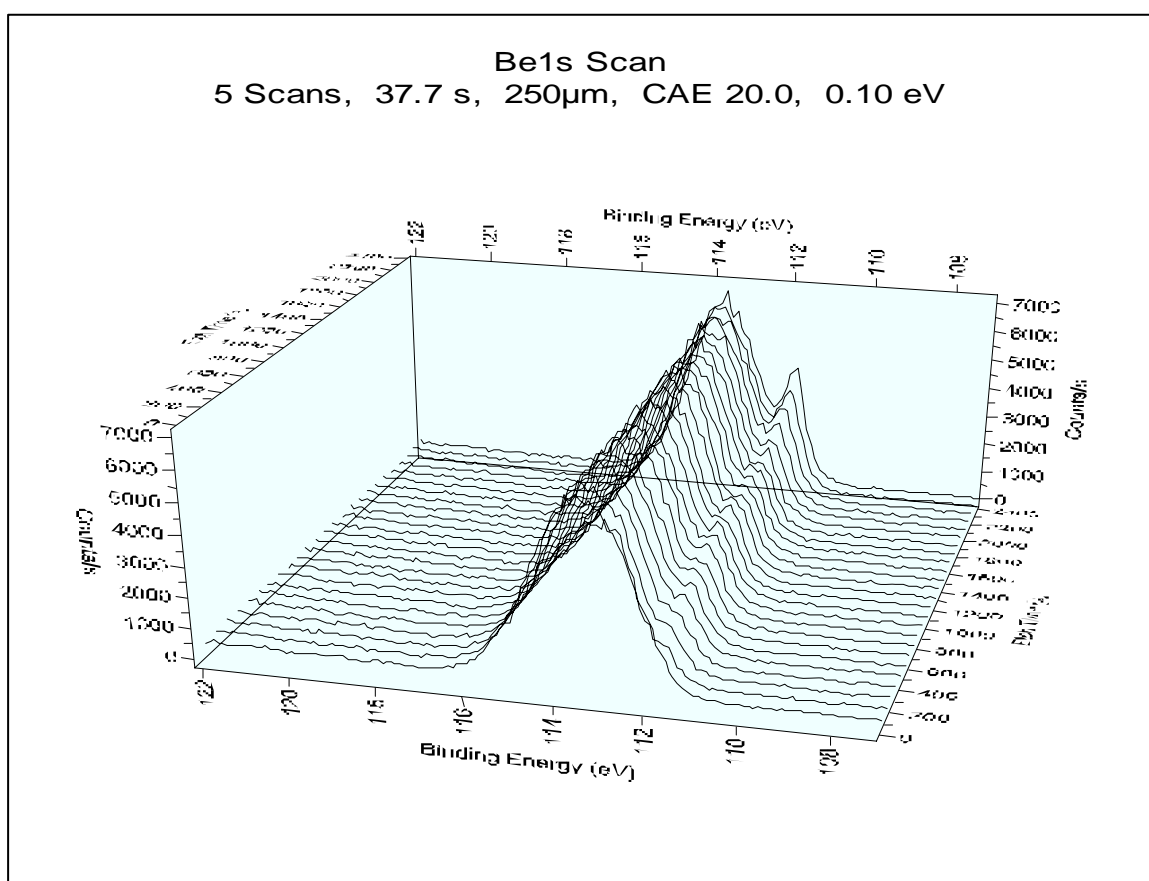

Be1s Scan
5 Scans, 37.7 s, 250µm, CAE 20.0, 0.10 eV

Fig. 8 shows the evolution of the Be/BeO ratio using the sputtered XPS technique. This way it is proven the fact that the oxidation is higher at the surface and the elemental beryllium is more present inside the film. This fact is proven also by Fig. 9
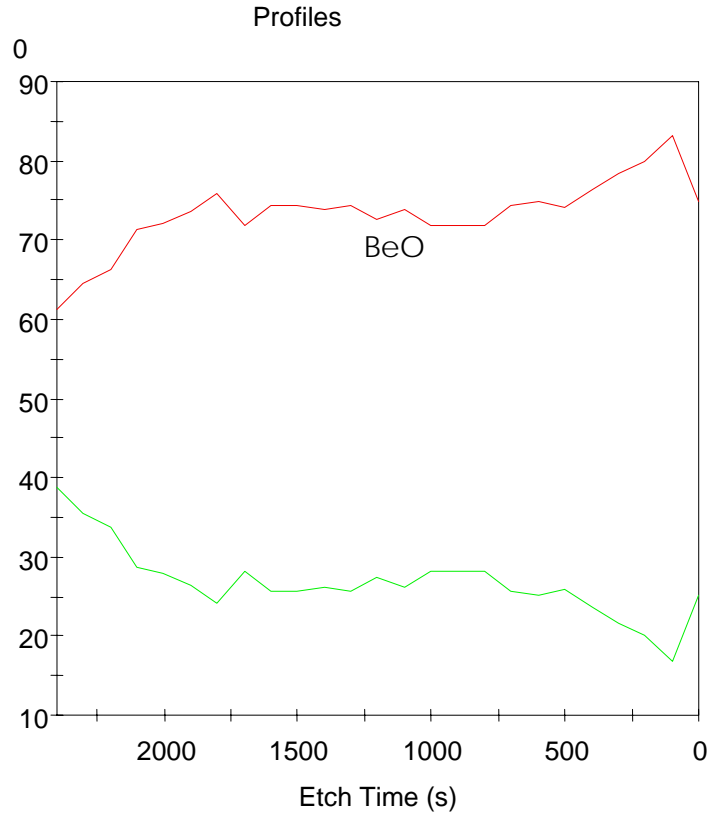

Fig 8 . BeO/Be relative concentrations depth profile
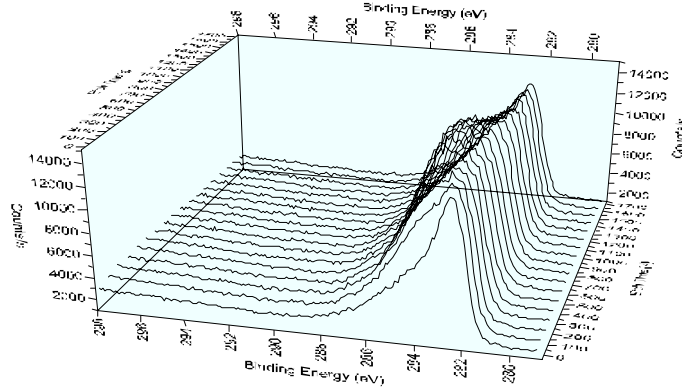
Fig. 9 The depth evolution of the C1s peak

(a) at the surface		(b) inside the film		(c) at the interface	
Element	at%	Element	at%	Element	at%
Be$_2$C	49.53	Be$_2$C	47.69	Be$_2$C	52.46
C	50.47	C	52.31	C	25.59
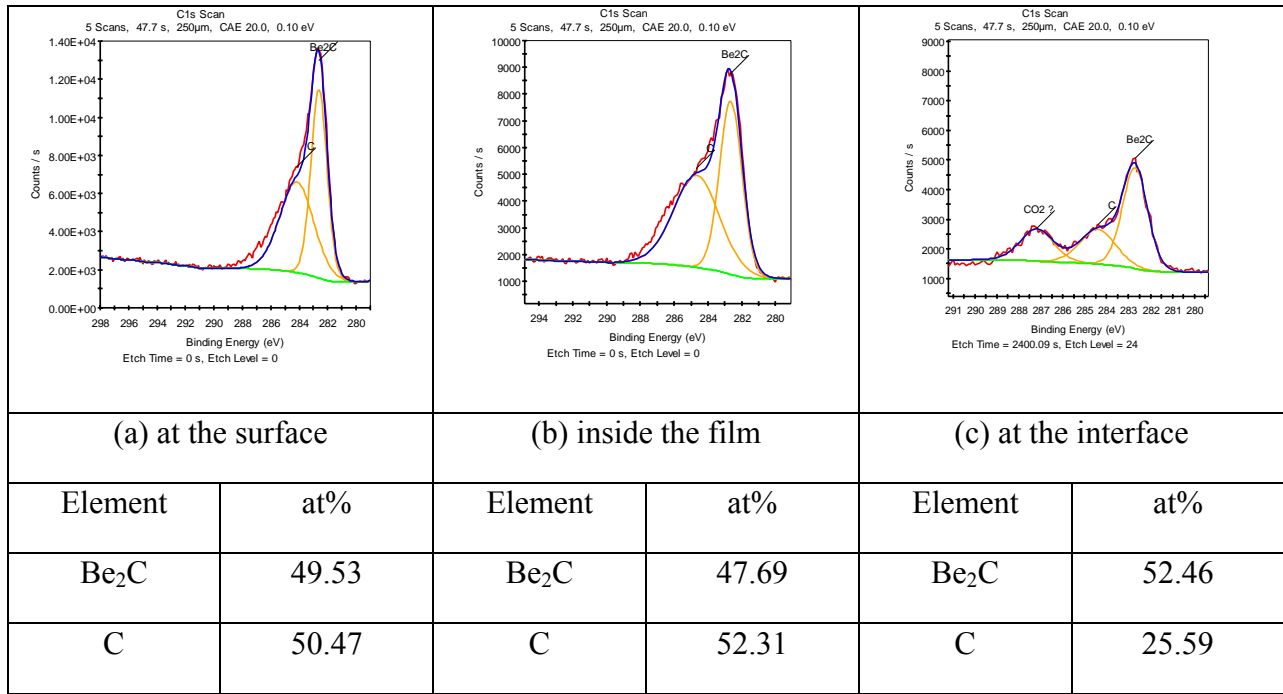
Fig.10 C1s peak at the surface (a), inside the film (b) and at the interface (c) as well as the Be$_2$C/C ratios

Carbon C1s peak also changes as with the depth as shown in figure 10. The carbon concentration is very high at the surface but it decreases up to 25 % close to the films interface.

For Be-C composite, Fig. 11 that shows for high atomic carbon concentration Be_2C is present in all the film up to 30%.

Peak to Peak Normalised Height Profile
5 Scans, 0.25 s, 250µm, CAE 20.0, CAE 20.0
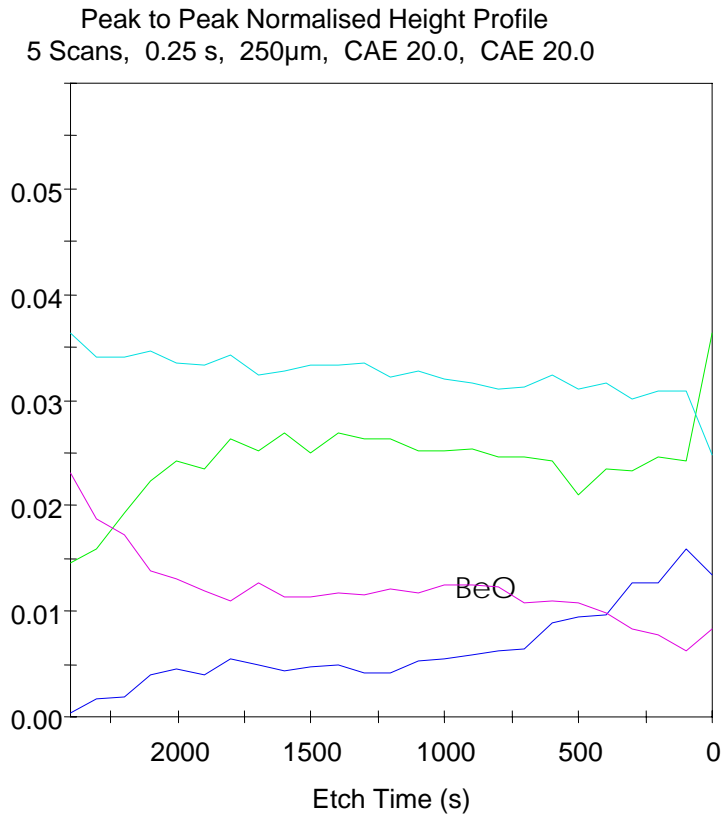
Fig.11 XPS depth profile of a Be-C-W sample deposited at 500^oC

The XPS spectrum obtained for the W4f peak at the level "0" (layer not sputtered) is shown in Fig.12, while the same peak after 200 s sputtering (the level 4) is shown in Fig.13.
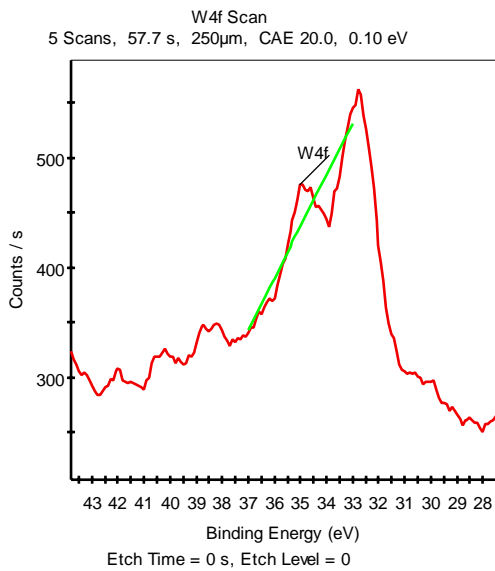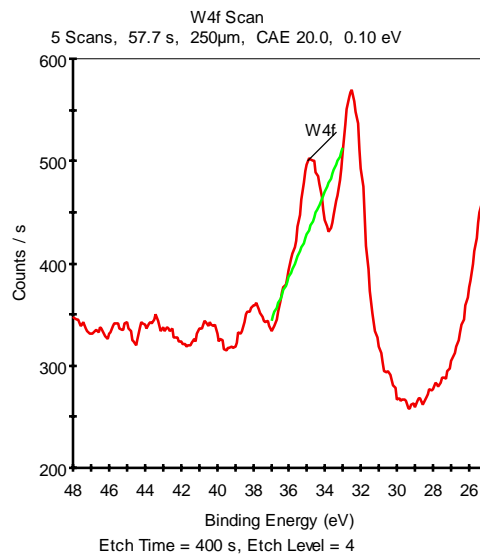
Fig.12 W4f peak, level "0"

Fig.13 W4f peak, level "4"

3D representation of the XPS W4f peak shown in Fig.14 reveal the W oxidation at the top of the layer and possible formation of the Be_xW_y chemical compound.
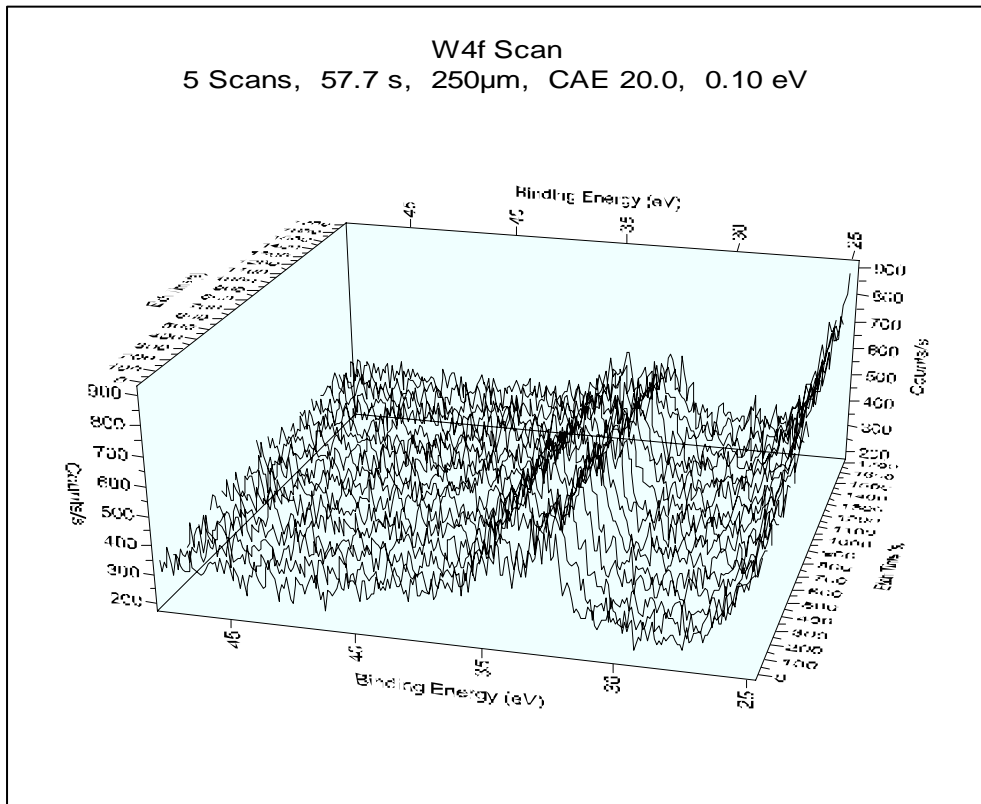
Fig.14. 3D representation of the XPS W4f

5. Oxygen migration:

Fig. 15 presents the RBS depth profile of the 100nmW/200nmBe films coated on the gaphite substrate. By the RBS analysis the oxygen concentration is inferred to be higher at the W-Be and Be-C interfaces. After e-beam irradiation using a TVA electron gun, the oxygen concentration from the Be-C interface decreased, and drastically increased at the Be-W interface. The W layers acts at a barrier of the oxygen present at Be-C interface, as well into the whole deposited film. (Fig.16).
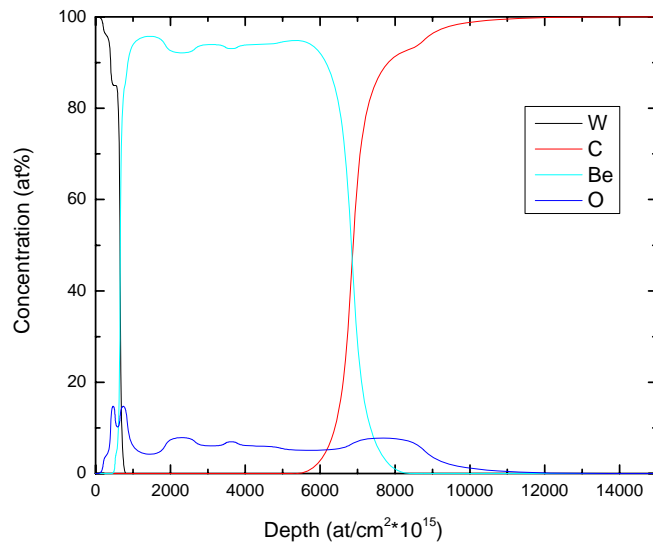
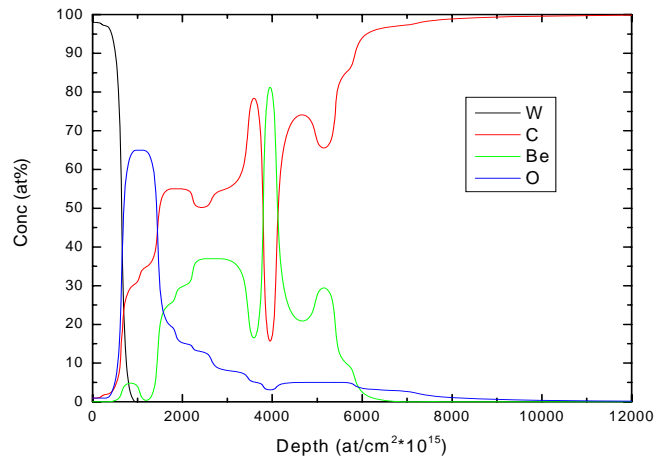Fig.15. The depth profile of the 100nmW/200nmBe films coated on the gaphite substrate.

Fig.16. The depth profile of the 100nmW/200nmBe films coated on the gaphite substrate after E-Beam irradiation/annealing at 900°C using a TVA electron gun.

Analyzing By XPS a 200 nm Be film deposited on graphite substrate, was identified oxygen at the Be-C interface, as shown in Fig.17. After a thermal annealing at 750°C in vacuum, was observed the migration of the BeO compound toward the surface as shown in Fig.18
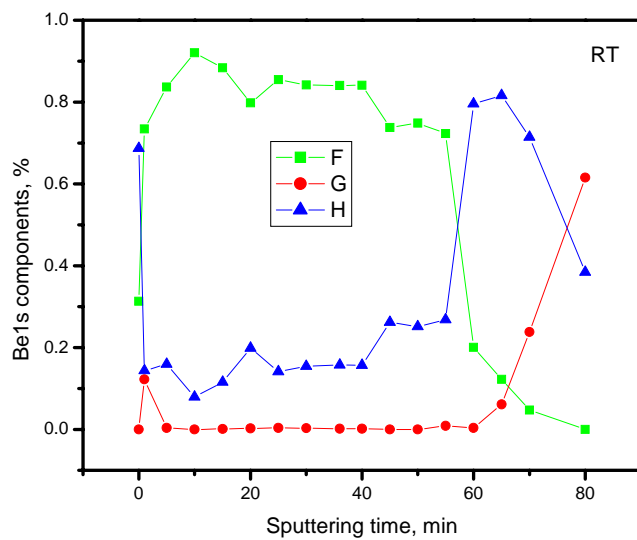

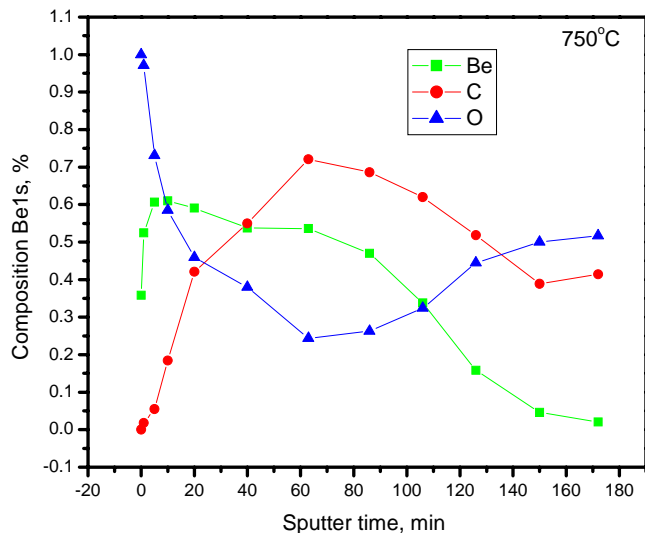Fig.17. The depth profile of the 200nm Be films coated on the gaphite substrate.

Fig.18. The depth profile of the 200nm Be films coated on the gaphite substrate after annealing at 750^oC in vacuum.

Fig. 19 presents the RBS depth profile of the 200nmBe films coated on the gaphite substrate. By the RBS analysis the oxygen concentration was evidentiated the presence of the oxygen gas at Be-C interfaces. After the annealing in vacuum at 750^oC, the oxygen concentration from the Be-C interface decreased, and drastically increased at the Be surface.. (Fig.20)
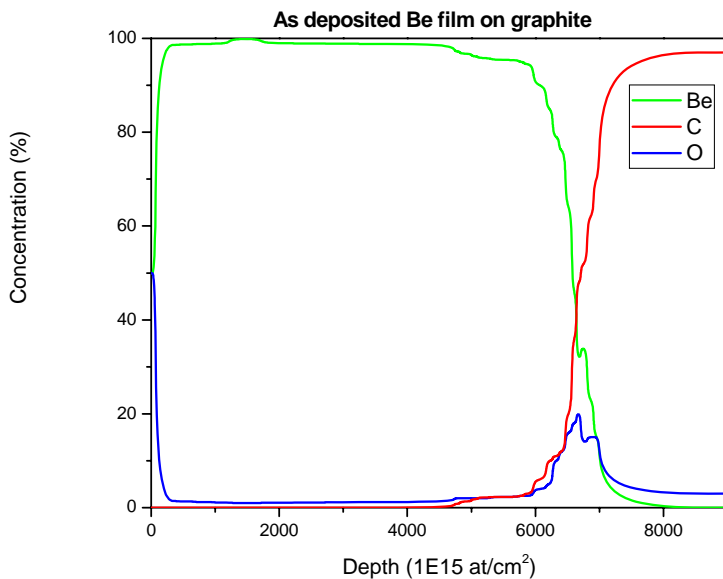
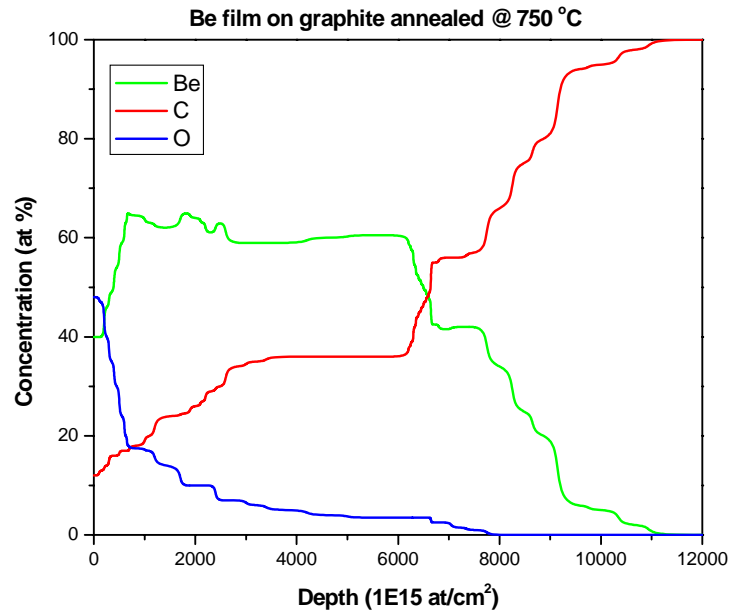Fig.19. RBS depth profile of the 200nmBe film coated on the gaphite substrate.

Fig.20. The RBS depth profile of the 200nmBe films coated on the gaphite substrate after annealing at 750°C in vacuum.

6. SIMS analysis

SIMS (Secondary Ion Mass Spectrometry) analyses were performed at VTT Institute in Helsinki, Finland, using following measurement parameters: VG IX70S double focussing magnetic sector SIMS; O_2^+ (5keV) primary ions, ion current 250nA, sputtered area 300 x 220 μm^2 ; Sputter rates: 0.56nm/s (Be/W).
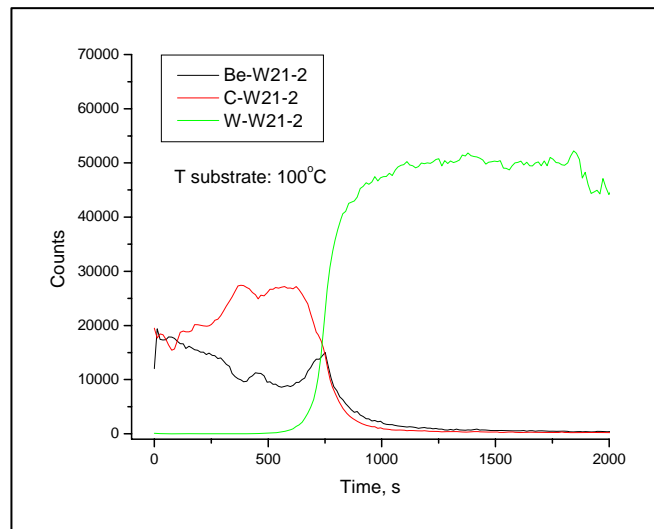
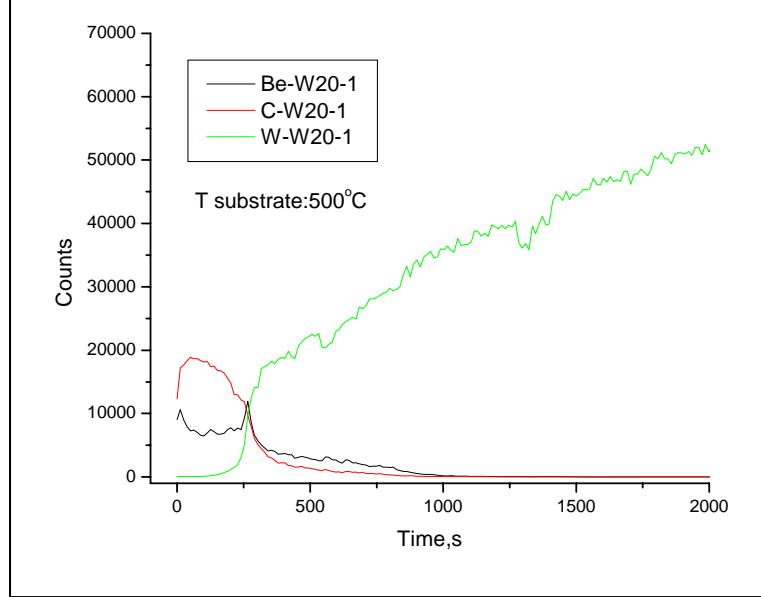Fig.21 SIMS analysis of a Be-C-W mixed layer deposited at $100^{\circ}C$ (equivalent to RT)

Fig.22 SIMS analysis of a Be-C-W mixed layer deposited at $500^{\circ}C$.

Both Be-C-W samples prepared at $100^{\circ}C$ (sample name 20W, deposited at $100^{\circ}C$, equivalent to RT) and $500^{\circ}C$ (sample name 21W) were analyzed. The thicknesses of the coatings are: 200nm (20W) and 560nm (21W). Be has a peak at the W/coating and the top of the mixed layer. The interface peak is broader on sample W21 ($100^{\circ}C$) than on sample W20 ($500^{\circ}C$) which could be due to higher substrate temperature. The interface peaks may indicate a reaction between W and Be.

7. Conclusions

The original Thermionic Vacuum Arc method (TVA) developed by our team, was used for preparation of Be-C-W mixed layers with different oxygen content into the prepared films. The oxygen was introduced into the layers adjusting the evaporation rates, allowing the residual gas from the reaction chamber to enter the layers just during their formation. The residual gas pressure was controlled by adding additional oxygen gas. The depositions were performed at $5*10^{-6}$ torr, residual air, and at $5*10^{-5}$ torr in residual atmosphere of oxygen.

XPS and SIMS analyses proved the formation of Be/W, BeO compounds at film-substrate interfaces and BeO, CO, compounds at the top of the prepared coatings.

The main aspect underlined by RBS measurements is that for the room temperature substrates the film was oxidized only at the surface and at the interface, while for the heated substrates the oxygen was present at the surface, and diffuses into the material, oxidizing the beryllium and the tungsten in the whole film. In addition, the interface oxygen begins to migrate into the substrate as the temperature increased.

References:

[6] G. Piazza, G.F. Matthews, J. Pamela, H. Altmann, J.P. Coad, T. Hirai, A. Lioure, H. Maier, Ph. Mertens, V. Philipps, V. Riccardo, M. Rubel, E. Villedieu and Collaborators of the JET ITER-like Project, R&D on tungsten plasma facing components for the JET ITER-like wall project, *Journal of Nuclear Materials*, *Volumes 367-370, Part 2, 1 August 2007*, *Pages 1438-1443*

[7] Ch. Linsmeier, K. Ertl, J. Roth, A. Wiltner, K. Schmid, F. Kost, S.R. Bhattacharyya, M. Baldwin, R.P. Doerner, Binary beryllium–tungsten mixed materials Journal of Nuclear Materials, Volumes 363-365, 15 June 2007, Pages 1129-1137

[8] C. P. Lungu, I. Mustata, V. Zaroschi, A. M. Lungu, A. Anghel, P. Chiru, M. Rubel, P. Coad G. F. Matthews and JET-EFDA contributors, Beryllium Coatings on Metals: Development of Process and Characterizations of Layers, Phys. Scr. T128 (March 2007) 157–161

[9] Cristian P. LUNGU, Ion MUSTATA, Alexandu ANGHEL Corneliu POROSNICU, Ionut JEPU, Catalin TICOS Ana M. LUNGU, Mihai GANCIU, Arcadie SOBETKII Gheorghe HONCIUC and Patrick CHAPON Preparation and Characterization of Multifunctional, Nanostructured Coatings Using Thermionic Vacuum Arc Method, Symposyum Kobe, March 2-4 2009, *Frontier of Applied Plasma Technology,* Vol.2 July 2009, pp1-6

[10] C. Porosnicu, C. P. Lungu, A. Anghel, K. Sugiyama, K. Krieger, J. Roth, and V. Andrei, Substrate Temperature Influence in Formation of Stable Be-W Composite Films Prepared by Thermionic Vacuum Arc Method, PFMC, Julich May 2009

[11]   C. Porosnicu, A. Anghel, C. P. Lungu, I. Mustata, V. Zaroschi, Morphological and Compositional Study on Be-C/Be-W Composite Films Prepared By Thermoinic Vacuum Arc Method, E-MRS, Strasbourg, France, 7-9 June 2009.

Publications connected to the project

11. C.P.Lungu, Nanostructured film preparation by thermionic vacuum arc, 19 pagini, contributie in cartea: New applications of micro- and nanotechnologies/ Editors: Maria Zaharescu, Liviu Giurgiu, Dan Dascalu, Editura Academiei Romane, 2009, ISBN 978-973-27-1803-2, pp.67-96.
12. C. P. Lungu, I. Mustata, V. Zaroschi, A.M. Lungu, P. Chiru, A. Anghel, C. Porosnicu, I. Jepu, V. Bailescu, G. Burcea, G. Dinuta, F. Din, N. Balan, G. Serban and JET-EFDA Contributors, Comparison of the beryllium films prepared by thermionic vacuum arc and thermal evaporation methods, Proc of. ISPC 19, International Symposium on Plasma Chemistry, Bochum, Germany, July 27-31, 2009
13. Cristian P. LUNGU, Ion MUSTATA, Alexandu ANGHEL Corneliu POROSNICU, Ionut JEPU, Catalin TICOS Ana M. LUNGU, Mihai GANCIU, Arcadie SOBETKII Gheorghe HONCIUC and Patrick CHAPON Preparation and Characterization of Multifunctional, Nanostructured Coatings Using Thermionic Vacuum Arc Method, IAPS Symposyum Kobe, Japan, March 2-4 2009, *Frontier of Applied Plasma Technology (Edited by Osaka University, Japan),* Vol.2 July 2009, pp1-6.
14. K. Sugiyama, K. Krieger, C.P. Lungu, J. Roth, Hydrogen retention in ITER relevant mixed material layers. *Journal of Nuclear Materials*, *Volumes 390-391*, *15 June 2009*, *Pages 659-662*
15. Cristian P. LUNGU, Corneliu C. POROSNICU, Alexandru ANGHEL, Catalin LUCULESCU, Ion MUSTATA, Ana M. LUNGU, Petrica CHIRU, Valer ZAROSCHI, Dorin DUDU, Ion VATA and Victor ANDREI, TERNARY Be-C-W SYSTEM FORMATION USING THERMIONIC VACUUM ARC METHOD, 10th International Balkan Workshop on Applied Physics, July 6-8th, 2009, Constanta, Romania.

Anexa 1-RST

Indicatori de realizare a fazei (conform specificului fiecarui program/proiect)

Denumirea indicatorilor	Numar/ Mii Ron	
	Planificat	**Realizat**
1. Investiții noi in infrastructura CDI	20	20
2. Gradul mediu de utilizare a echipamentelor CDI	90%	90%
3. Număr de entități susținute pentru creşterea capacității de ofertare a serviciilor de experiment		
4.Număr de reviste finanțate, din care - Co-editate internațional - Indexate ISI - Incluse in alte baze de date internaționale recunoscute		
5. Cărți, atlase, dicționare şi alte produse cu caracter ştiințific publicate anual, în țară şi în străinătate	-	1
6.Număr de conferințe organizate, din care internaționale		
7. Număr de expoziții finanțate		

8.Valoarea investiției în infrastructură şi servicii de comunicații	20	20
9.Ponderea cercetătorilor care au acces la resursele de informare on-line	100%	100%
10.Număr de reviste dedicate popularizării ştiinţei		
11.Număr de proiecte de comunicare ştiinţă-societate		
12.Număr de proiecte de studii prospective		
13.Număr de proiecte de pregătire a unor participări la programe internaţionale		
14.Număr de participări în proiecte internaţionale	2	4
15. Valoarea apelurilor tematice comune lansate		

Anexa la Raportul Ştiinţific şi Tehnic- RST

Indicatori de realizare a fazei (conform specificului fiecarui proiect)

Nr. crt.	Indicatori	UM
9.	Număr de publicați în reviste: Co-editate internațional - Indexate ISI - Incluse în alte baze de date internaționale recunoscute	Nr. 1 1
10.	Articole publicate în cărți, atlase, dicționare şi alte produse cu caracter ştiinţific publicate anual (în ţară şi în străinătate)	Nr. 1
11.	Participări la conferinţe organizate, dintre care internaţionale	Nr. 3/3
12.	Evenimente organizate dintre care internaţionale	Nr.
13.	Pliante, broşuri, postere pentru diseminare de informaţii	Nr.
14.	Proiecte de comunicare ştiinţifică	Nr.
15.	Proiecte de studii prospective	Nr.
16.	Proiecte / participanţi în proiecte internaţionale finanţate	Nr. 4

1. C.P.Lungu, Nanostructured film preparation by thermionic vacuum arc, 19 pagini, contributie in cartea: New applications of micro- and nanotechnologies/ Editors: Maria

Zaharescu, Liviu Giurgiu, Dan Dascalu, Editura Academiei Romane, 2009, ISBN 978-973-27-1803-2, pp.67-96.

2. C. P. Lungu, I. Mustata, V. Zaroschi, A.M. Lungu, P. Chiru, A. Anghel, C. Porosnicu, I. Jepu, V. Bailescu, G. Burcea, G. Dinuta, F. Din, N. Balan, G. Serban and JET-EFDA Contributors, Comparison of the beryllium films prepared by thermionic vacuum arc and thermal evaporation methods, Proc of. ISPC 19, International Symposium on Plasma Chemistry, Bochum, Germany, July 27-31, 2009

3. Cristian P. LUNGU, Ion MUSTATA, Alexandu ANGHEL Corneliu POROSNICU, Ionut JEPU, Catalin TICOS Ana M. LUNGU, Mihai GANCIU, Arcadie SOBETKII Gheorghe HONCIUC and Patrick CHAPON Preparation and Characterization of Multifunctional, Nanostructured Coatings Using Thermionic Vacuum Arc Method, IAPS Symposyum Kobe, Japan, March 2-4 2009, *Frontier of Applied Plasma Technology (Edited by Osaka University, Japan),* Vol.2 July 2009, pp1-6.

4. K. Sugiyama, K. Krieger, C.P. Lungu, J. Roth, Hydrogen retention in ITER relevant mixed material layers. *Journal of Nuclear Materials*, *Volumes 390-391*, *15 June 2009*, *Pages 659-662*

5. Cristian P. LUNGU, Corneliu C. POROSNICU, Alexandru ANGHEL, Catalin LUCULESCU, Ion MUSTATA, Ana M. LUNGU, Petrica CHIRU, Valer ZAROSCHI, Dorin DUDU, Ion VATA and Victor ANDREI, TERNARY Be-C-W SYSTEM FORMATION USING THERMIONIC VACUUM ARC METHOD, 10th International Balkan Workshop on Applied Physics, July 6-8th, 2009, Constanta, Romania.

PROJECT AS-5: ANOMALOUS TRANSPORT IN PLASMA

Project Leader: G. Steinbrecher

Task Agreement WP08-TGS-01b/06/MedC/PS

Universitatea din Craiov

- **General objectives**

 For the year 2009 the objectives are

General objective: Characterization of long-range correlations and multi-scale physics in L-mode plasmas and during edge improved confinement regimes.

- **Specific Objectives**

In the stage of the project, July-December 2009 we have attained the following specific objectives from the previous mentioned objectives:

Objective 1: Long range correlations, reduced stochastic models.

- **Resume of the stage**

Objective 1: *Long range correlations, reduced stochastic models.*

In the framework of the second objective two reduced stochastic models of the edge plasma turbulence were elaborated: low and high dimesional models. New arguments for the validity of the low dimesional models are give by the results of the higher dimensional reuced models. The main results are the following

a. It is possible to correlate the two important effects observed on large tokamaks: the L-H transition and the occurence of the intermittent ELM modes, by a very simple reduced stochastic one dimensional model having minimal assumptions.

b. The new one dimensional model predicts an increased intermittency , together with the improvement of the confinement

c. A large class of analytically treatable higher dimensional linear stochasti models were elaborated. New mathematical phenomena that explains the occurence of streamers, inverse cascade was discovered

- **Scientific description**

Specific Objective I-b

Long range correlations, reduced stochastic models.
Coordinator: Dr. György Steinbrecher.

By using the results from the refs. [1], the main result concerning the long-range correlations from ref [2] was generalized in ref. [3-4]. These results from ref. [3-4] give a sound mathematical and physical foundation for the results from [5], were the conditions of the validity of the analytic result concerning the effect of the long range temporal correlation on the asymptotic behavior of the stationary probability density function of the random linear dynamical system studied previously in ref. [2], was extended . By this extension the previous limitations of our model of long-range interactions in the edge plasma turbulence, was removed. In the work [5] a new mechanism, based purely on stochasticity, of the L/H transitions are proposed. This new model with minimal assumptions, give a mathematical explanation for the occurrence of the intermittent ELMs in the H mode plasmas.

The main shortcoming of this class of the models is the reduced number of components.

Consequently we begin the study of a new class of stochastic models [6,7]: Discrete Random Linear Partial Differential Equations (DRLPDE). These models appear in the stochastic version of the linear instability studies. This category of DRLPDE also describes the effect of the small spatial and temporal scale turbulence to the large-scale evolution of the physical system. The mathematical difficulties related to the analytic study of this class of stochastic equations were overcome by adapting (at least to the particular case studied, see later) of the new, powerful mathematical methods discovered in the study of the Anderson localization the framework of tight binding Anderson model the Schrödinger equation with random potential. [8]. By this class

of methods we studied This higher dimensional Discrete Random Linear Partial Differential Equations (DRLPDE) are interesting also because they relate the local, disordered random fluctuations to the global statistical characteristics of the physical system, they models the multi scale physics. We studied a simplified model: classical Hamiltonian linear hyperbolic equations with random potential term ("Klein-Gordon Equation with random " mass" term"). The main motivation was that exactly the Hamiltonian systems in higher dimensions are most exposed to destabilization by random perturbation. The main results are:

1.   For a stochastic system with N components, it is possible to obtain a closed set of soluble linear deterministic differential equations for the moments of order p.

2.   The k=0 mode is always destabilized

3.   In dimension 1 and 2 all of the modes are destabilized, but the modes with high k has a smaller positive Liapunov exponent

4.   In 3 dimensions, for low noise intensity, the modes with sufficient high k remain stable. This is a mechanism for the occurrence of the long-range spatial correlations, generated by a completely disordered noise. It is an interesting multi-scale physics effect. This is also an interesting linear stochastic model that gives at least a qualitative description of the inverse cascade, formation of the streamers.

5.   The results concerning the increased stability under perturbations of the short wavelength modes give a **new strong support** for the previous one component model of the edge plasma turbulence from ref. [2].

Conclusions.

Long range correlations, reduced stochastic models.

    On component model that predicts the increase of the intermittency in H mode was elaborated. The model is remarkable by its minimal assumptions and by the use of stochastic mechanism.

 The second model proposed for the study of multi scale physics, linear stochastic stability, by the study of the random linear partial differential equations by using the methods from condensed matter physics, will be continued. The stochastic model obtained give an interesting alternative to explain the inverse cascade in turbulence, streamers in the edge plasma turbulence. The method works in linear approximation, when the noise is a spatial and temporal white noise. In order to obtain analytic results local homogeneity is required. The method computes only the

time evolution of the moments, not of the probability density functions. The removal part of these problems will be the subject of further works

Our results give a shortcut to intensive direct numerical simulations in the case of frozen turbulence. It also gives a benchmark for transport codes that simulates large tokamaks, like ITER, JET.

References

[1] **G. Steinbrecher, W. T. Shaw**. "*Quantile Mechanics*", European Journal of Applied Mathematics, **19**, 87, (2008). http://en.wikipedia.org/wiki/Quantile_function. **http://functions.wolfram.com/GammaBetaErf/InverseErf/06/01/02/0004/**

[2] **G. Steinbrecher, B. Weyssow**, "Generalized Randomly Amplified Linear System Driven by Gaussian Noise: Extreme Heavy Tail and Algebraic Correlation Decay in the Plasma Turbulence", Phys. Rev. Lett. 92, 125003-1, 2004.

[3] **G. Steinbrecher, X. Garbet, B. Weyssow**, " *Weak Convergence to Stationary Distributions in Heavy Tail Models*", sent to Journal of Differential Equations.

[4] **G. Steinbrecher, X. Garbet, B. Weyssow**, "*Stochastic version of the linear instability analysis*", Annals of the Univ. Craiova "Physics AUC", 19, 107-123, (2009). http://cis01.central.ucv.ro/pauc/

[5] **X. Garbet, G. Steinbrecher**, "*On-Off Intermittency of Bifurcating Systems and Heavy Tail Exponent in Random Multiplicative Processes.*", to be published.

[6] **G. Steinbrecher, X. Garbet**, "*Stochastic Linear Instability Analysis*", International Workshop on "*Hamiltonian Approaches to ITER Physics*", CIRM, Marseille, 2-6 November 2009.

http://www.cirm.univ-mrs.fr/web.ang/liste_rencontre/programmes/AbstractsProgRenc395.pdf

[7] **G. Steinbrecher, X. Garbet**, "*Stochastic Linear Instability Analysis of the Hamiltonian Systems*" to be published

[8] **V. N. Kuzovkov, W. von Niessen, V. Kascheyevs**, O. Hein, J. Phys. Condens. Matter 14, 1377 (2002).

PROJECT AS-6: X-RAY MICRO-TOMOGRAPHY STUDIES ON GRAPHITE AND CFC SAMPLES FOR POROSITY NETWORK CHARACTERIZATION

Project Leader: Ion Tiseanu

Task Agreement WP09-PWI-01

Ion Tiseanu, Teddy Craciunescu, Cosmin Dobrea, Adrian Sima

National Institute for Lasers, Plasma and Radiation Physics, Bucharest, Romania

1. Introduction and objectives

The CFC monoblocks of the ITER divertor vertical target must sustain high heat fluxes of 10 MW/m^{2}during 400 s (normal operation) and up to 20MW/m^2 during 10 s (off-normal event). Carbon–carbon fibre composites (CFCs) have a unique combination of high conductivity, low Z and resistance to damage due to high heat loads. Given the demanding environmental requirements in the ITER divertor, specially developed CFCs are required as plasma facing components (PFC) materials.

The problem of fuel retention in carbon material is a major concern because tritium is radioactive, and the amount allowed within the ITER installation is an essential safety issue.

There are two main fuel retention mechanisms: i) carbon eroded from PFCs can be re-deposited in form of amorphous layers, containing significant fraction of fuel of up to H/C~1, ii) H isotopes from plasma can be implanted into carbon PFCs and diffuse into the material bulk [1,2].

From earlier investigations the retention in the material bulk was considered to be less critical than the retention in co-deposited layers. Recent gas balance experiments in Tore Supra [3,4] indicated, however, that significant fractions of fuel can be stored in CFC materials via this mechanism. It was attributed to a higher effective diffusion of H in the bulk of CFC due to a relatively high porosity of these materials of ≈10-15%.

Hence, the accurate 3D porosity description of the CFC materials would provide an essential input for the quantization of the fuel retention in material bulk. In this project we address the

problem of quantitative characterization of the porosity structure of the carbon reinforced fiber (CFC) materials by high resolution X-ray tomography. This topic is included in the EFDA 2009 Work Programme, Task Agreement TA-1 "Fuel retention as a function of wall materials foreseen for ITER" organized under the Special Expert Working Group (SEWG) "Gas balance and fuel retention".

In 2009 the main **objectives** of this project are the following:

- Establish an working environment for high resolution X-ray tomography (μCT) on miniaturized graphite and CFC samples;
- Determination of microtomography scanning parameters for optimum space and density resolution;
- Quantitative evaluation of the sample porosity factor.

During the reporting period (July-December 2009) we have carried out the following research activities: i) optimized tomography measurement of the 3D model of relevant volumes of CFC materials and ii) development and validation of an image processing technique for volume analysis in terms of absolute porosity factor.

2. Results and discussion

Most experiments were carried out at our newly upgraded X-ray tomography facility NanoCT (see http://tomography.inflpr.ro for the NanoCT system description and its overall parameters). A limited series of experiments were performed on a high end tomography facility which uses an advanced transmission X-ray tube with a high power diamond target and a 16 bits flat panel detection system.

Tomography measurements were performed on relatively large volumes of two type of CFC samples (former ITER reference CFC NB31, JET CFC DMS780 and for reference on a porosity free fine-grain graphite EK98.

Moderate resolution measurements of CFC rods of 5x5x5 mm^3 at voxel resolution of approx. 14 μm with an estimated minimum detectable feature of cca. 15-20 μm have been reported in the semiannual report of January-June 2009. These measurements were devoted to the optimization of the X-ray source working parameters (high voltage and current) as well as the detection parameters (pitch size and integration time).

Once the optimum parameters determined one has proceeded to high resolution measurements (2.5 μm/voxel) on same CFC samples by the "offset tomography" technique [7].

Figure 1 shows representative tomographic images with 14, 5 and 2.5 μm per voxel of CFC of type Nb31. The images with 5 μm and 2.5 μm were obtained with the newly implemented "offset tomography" scanning method. A set of up to 1440 of radiographies at equidistant angles have been used for high resolution fully 3D tomography. Offset tomography is a powerful technique to almost double the magnification factor (accordingly doubling the space resolution) for a given

detector size. Same high resolution (2.5 μm) tomography cross-sections for the CFC DMS780 sample are also measured and reported elsewhere.

While the maximum resolution of 2.5 μm per voxel on a relatively large sample is a remarkable performance the images noise might be not sufficient for accurate porosity factor evaluation. In order to reduce the image noise we have carried out following steps: i) reduction of reconstruction artefacts like "ring artefacts" and "beam hardening artefacts" and ii) repeat the measurements on a high-end tomography facility which uses an advanced transmission X-ray tube with a high power diamond target and a 16 bits flat panel detection system. Both the high power target and the upgraded digital output of the detector are instrumental in the noise reduction on the tomographic images. The diamond target provides a significantly higher X-ray output and the 16 bits flat panel detector is able to display the X-ray transmission factors on a broader gray values scale.
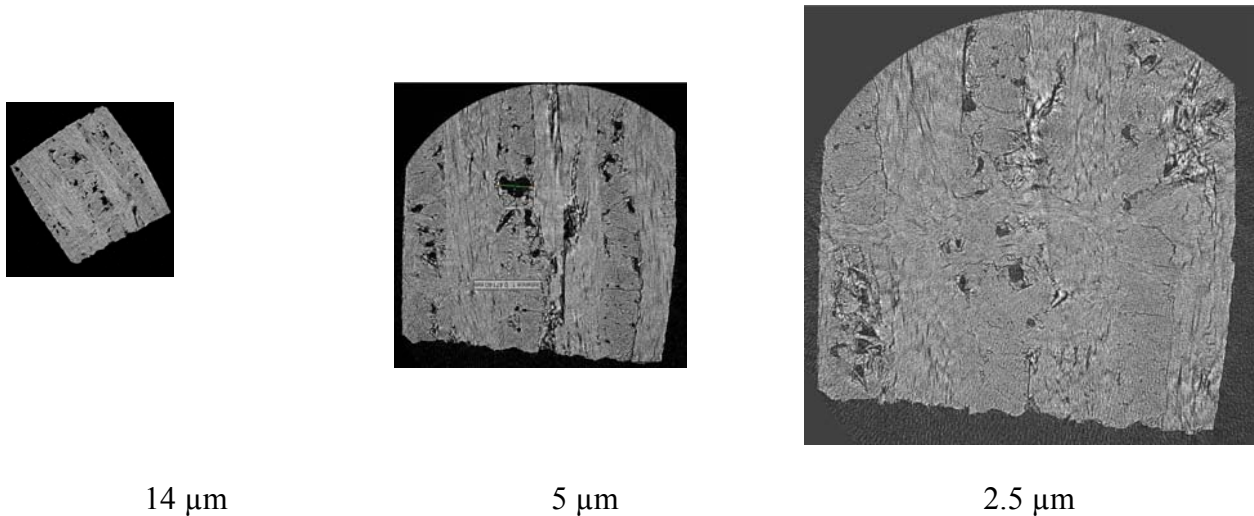

| 14 μm | 5 μm | 2.5 μm |

Figure 1 - CFC Nb31 - representative images of tomographic reconstructions with 14 , 5 and 2.5 μm per voxel. The images with 5 μm and 2.5 μm were obtained with the newly implemented "offset tomography" scanning method.

Images shown in Figure 2 are representative for the results of high resolution tomography measurements on a CT facility with high power diamond target and 16 bits flat panel detector.
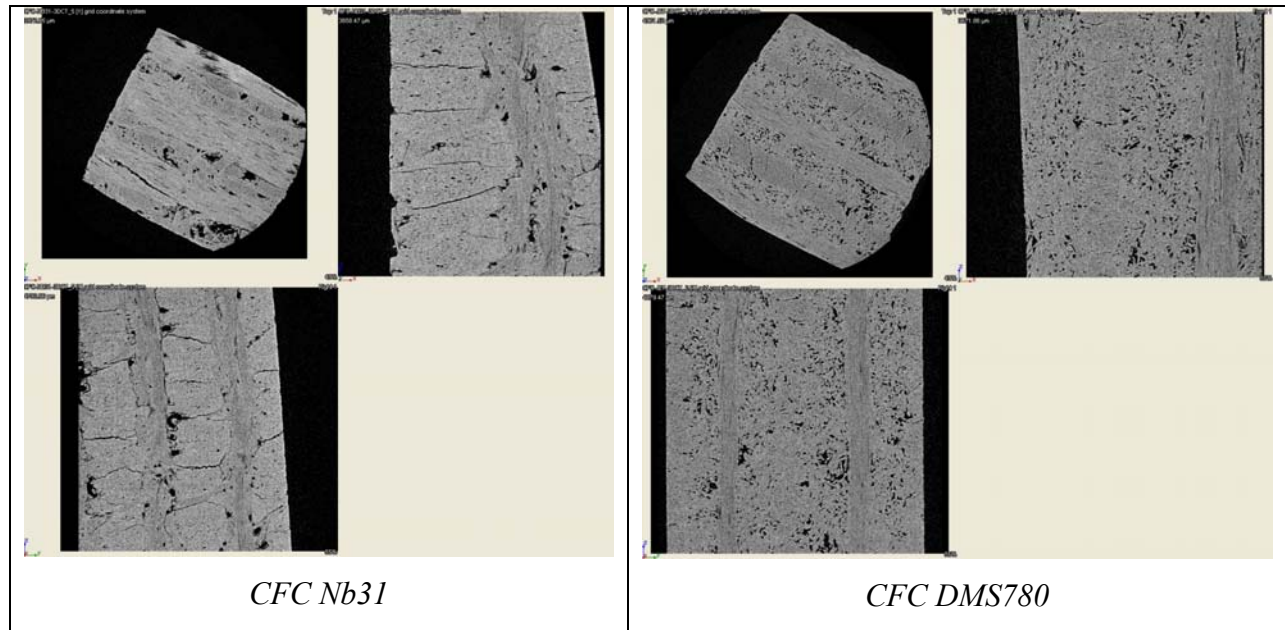
| CFC Nb31 | CFC DMS780 |

Figure 2 - CFC Nb31and CFC DMS780 high resolution tomography on a CT facility with high power diamond target and 16 bits flat panel detector. Sample size: ≥ 4x4x4 mm^3 ; voxel resolution: 6 μm.

Already from the visual inspection on can note the high quality of these images which a totally free of *ring* and *beam hardening* artefacts. The ring artefacts reduction was performed by a special scanning method in which the sample and/or the detector were randomly shifted. The beam hardening artifacts were mitigated by a linearization of the CFC transmission curve with the help of lookup tables obtained for calibration CFC materials.

Quantitative evaluation of the sample porosity factor

The 3D reconstructed volumes can be processed in order to determine the main CFC network porosity characteristics. For the quantitative analysis of the porosity structure in terms of total void fraction, network connectivity, wall thicknesses we used a powerful 3-D visualization and measurement software VG Studio MAX of Volume Graphics GmbH, Germany. In Figure 3 we introduce some of the data post-processing steps. The first one is to find an optimal choice for the threshold level, in order to create a correct border between CFC and porous regions. A detailed inspection of this demarcation is performed while navigating through the reconstructed volume along transversal, longitudinal and sagital cross-sections. After validation, the reconstructed volume is segmented and the porous structure is extracted as an independent object which can be represented also as a 3D structure. With the volume analysis module we determined the absolute value of porosity factor. The defect analysis tool can be used to determine the voids volume/size/projected area distribution.

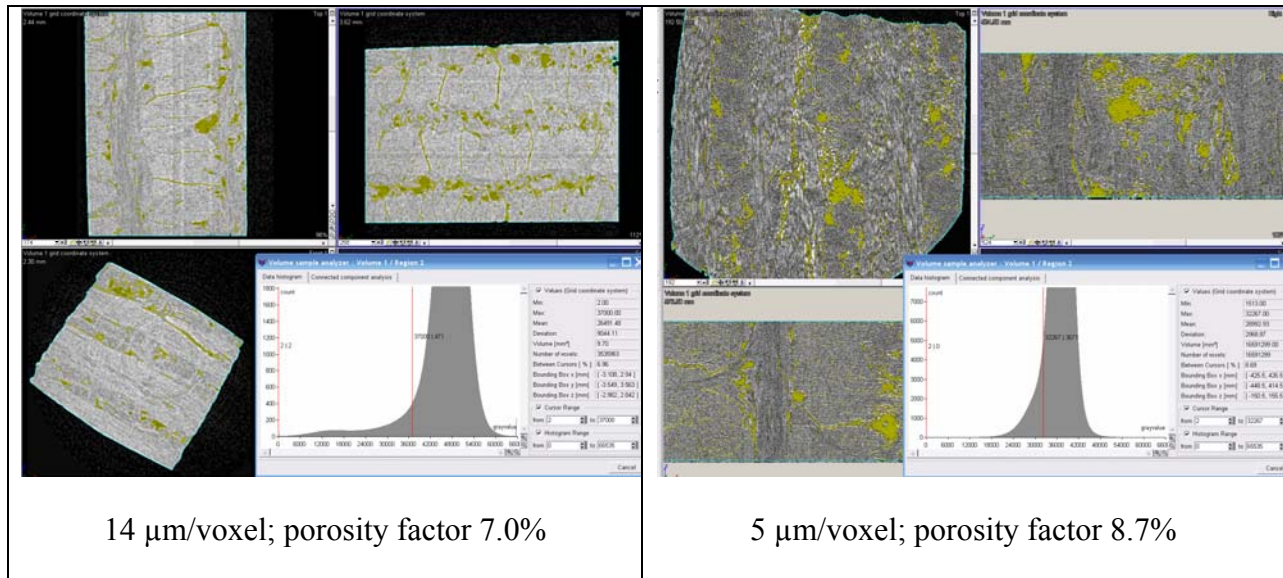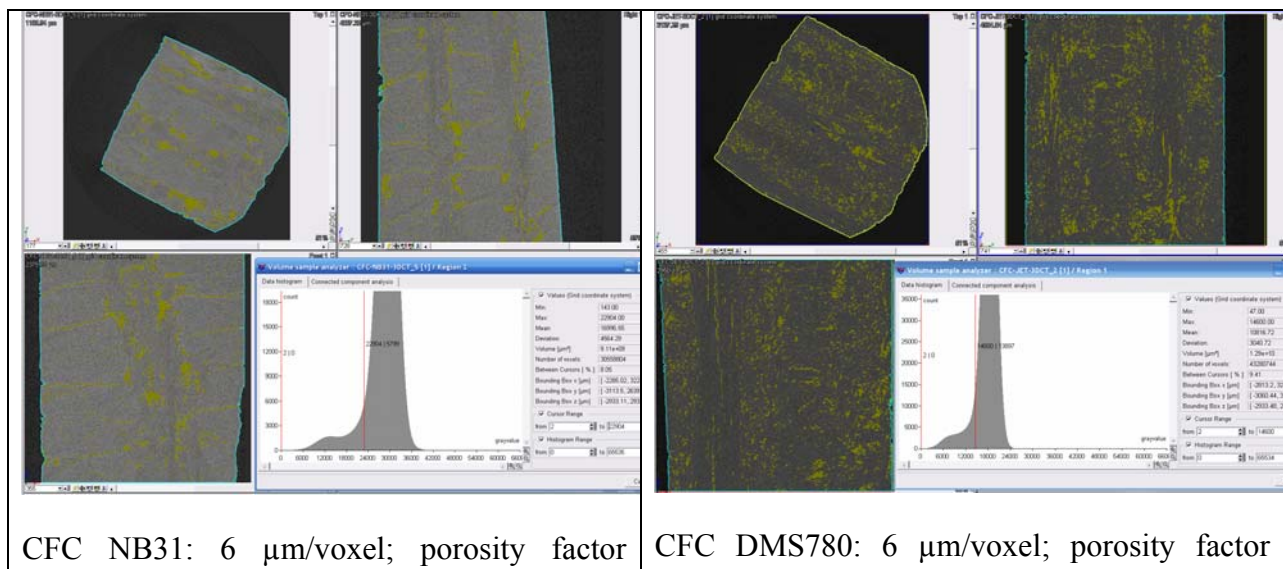| 14 µm/voxel; porosity factor 7.0% | 5 µm/voxel; porosity factor 8.7% |

Figure 3: Post-processing steps of the reconstructed volume data in order to obtain the CFC NB31 porosity factor: the differentiation between CFC materials and porous regions is determined by the threshold levels.

From Figure 3 one note that the moderate resolution of 14 µm/voxel coupled with the relatively intense "ring artefacts" could be the possible cause of the underestimation of the porosity factor. The much higher resolution achieved in the reconstruction images depicted in the right panel could better provide the absolute porosity factor.

Finally, the porosity factors calculation procedures for the two types of fusion technology relevant CFC samples are illustrated in Figure 4. As input data we used the reconstructed volumes delivered by the high end tomography facility. The porosity factors values are in good agreement with the manufacturer nominal specifications.

| CFC NB31: 6 µm/voxel; porosity factor | CFC DMS780: 6 µm/voxel; porosity factor |

8.05%	9.41%

Figure 4: Post-processing steps of the reconstructed volume data in order to obtain the CFC NB31and DMS780 porosity factors. The input data were obtained at a high end CT facility with diamond target and 16 bits flat panel detection system.

The radical improvement of the images quality has convinced us to purchase and install a diamond high power target on the NanoCT facility from INFLPR.

3. Conclusion and future work

High resolution cone beam tomography has been optimized for CFC samples. One important result was understanding the dependence of the porosity evaluation accuracy on the space resolution and the amount of tomography images noise.

A procedure for the quantitative evaluation of the sample porosity factor has been introduced and tested. For example for CFC NB31 we obtained porosity factors of around 8% and for CFC DMS780 of around 9.4% in very good agreement with the manufacturer nominal values.

We believed that the main goal of the project was reached and that are fully equipped to participate at the Deuterium Inventory in Tore Supra (DITS) post mortem analysis by providing high resolution tomography measurements on CFC samples. Our current 3D micro-tomography reconstructions for relatively large samples of CFC (NB31 and DMS780) could be considered a good basis for the characterization of the initial porosity of the new CFC ITER reference material NB41.

Preliminary results on the "X-ray micro-tomography studies on graphite and CFC for porosity network characterization" were presented at the Annual meeting of Special Expert Working Groups (SEWG) on «Fuel retention » organized at CEA-Cadarache. Recently, our results were also presented at The Annual General Meeting for the EU PWI Task Force which took place in Warsaw 4-6 November 2009.

4. Acknowledgement

5. References

[1] A Kreter et al, Deuterium retention in different carbon materials exposed in TEXTOR, Journal of Physics: Conference Series 100 (2008) 062024

[2] A T Peacock, M Merola, M A Pick and R Tivey, Status of CFC development in Europe for ITER, Phys. Scr. T128 (2007) 23–28

[3] E. Tsitrone, D. Reiter, T. Loarer, C. Brosset, J. Bucalossi, L. Begrambekov, C. Grisolia, A. Grosman, J. Gunn, J. Hogan, R. Mitteau, B. Pérourié, P. Ghendrih, R. Reichle and P. Roubin, Role of wall implantation of charge exchange neutrals in the deuterium retention for Tore Supra long discharges, J. Nucl. Mater. 337–339 (2005), p. 539.

[4] J. Bucalossi, C. Brosset, B. Pégourié, E. Tsitrone, E. Dufour, A. Eckedahl, A. Geraud, M. Goniche, J. Gunn, T. Loarer, P. Monier-Garbet, J.C. Vallet, S. Vartanian, Deuterium in-vessel retention characterisation through the use of particle balance on Tore Supra, J. Nucl. Mater. 363–365 (2007), p. 759.

[5] VGStudio MAX, Release 2.0, Volume Graphics, http://www.volumegraphics.com

[6] I. Tiseanu , T. Craciunescu, C. Dobrea, A. Sima, Advanced X-ray imaging techniques for non-destructive analysis of fusion materials, Romanian Conference on Advanced Materials ROCAM 2009, August 25-28th, 2009, Brasov, Romania

PROJECT AS-7: QUALIFICATION OF THE X-RAY MICRO-BEAM ABSORPTION/ FLUORESCENCE METHOD FOR EROSION ANALYSIS

Project Leader: Ion Tiseanu

Task Agreement WP09-PWI-04

Ion Tiseanu, Teddy Craciunescu, Cosmin Dobrea, Adrian Sima

National Institute for Lasers, Plasma and Radiation Physics, Bucharest, Romania

1. Introduction

Currently, the primary materials choice for ITER (International Thermonuclear Experimental Reactor) is a full beryllium main wall with CFC at the strike points and tungsten at divertor baffles and dome. Since this combination has never been tested in a tokamak, ITER-like Wall project has been launched at JET, consisting of 10 μm W coating of approx. 1,000 CFC tiles.

In connection with this task, the main objectives of our project consist in developing of a non-destructive technique for the evaluation of the W coating uniformity as well as a quantitative mapping of the multilayer compositions and thicknesses.

In the first part of the year 2009, a combined X-ray absorption/fluorescence method for erosion analysis was evaluated. Preliminary tests proved that the method is able to provide information about the uniformity of the CFC coating and can be used to determine its thickness. The preliminary experiments proved also that the lateral resolution is ~30 μm and the in-depth resolution is ~ 3% of the layer thickness. The work was continued by establishing a well defined and reliable experimental setup and by validating the technique on real-life samples from ASDEX-Upgrade.

2. Methods and results

The method for erosion analysis was implemented using the Tomo-Analytic system, which we developed especially for fusion materials analysis. Tomo-Analytic is a combined X-ray fluorescence (XRF) and cone-beam tomography (3DCT) system for the noninvasive 3-D morphology and composition mapping. With its high space resolution, delivered by X-ray focalization with a policapillary lens, the XRF method permits the characterization of complex structures with lateral resolution of around 20 μm. The implementation of a confocal geometry realized with the attachment of a polycapillary conic collimator to the X-ray detector further

allows the extension of capabilities of the instrument up to fluorescence tomography (3-D composition mapping). The XRF analysis with Fundamental Parameters (FP) converts elemental peak intensities to elemental concentrations and/or film thicknesses. The 3DCT component is configured to take highly resolved (48 µm) radiographic views of the object in order to build a 3-D model of its internal structure. 2-D slices through this volume can be viewed as images, or the 3-D volume may be rendered, sliced, and measured directly. For the NDT inspection of miniaturized samples the microtomography analysis is guaranteed for feature recognition better as 15 µm. 3-D tomographic reconstructions are obtained by a proprietary highly optimized computer code based on a modified Feldkamp algorithm.

For the case of the assessment of the thickness uniformity of graphite/CFC with metallic coatings for a large number of samples, we found that an X-ray transmission technique is more pragmatic solution in comparison with the tomographic analysis. As the Tomo-Analityc system is a configurable and versatile measuring tool, we modified the geometry of the system (Fig. 1). The X-ray source has a direction of emission perpendicular to the flat panel detector. The X-rays are detected after passing through the investigated sample where they are attenuated accordingly with the composition and thickness of the materials.
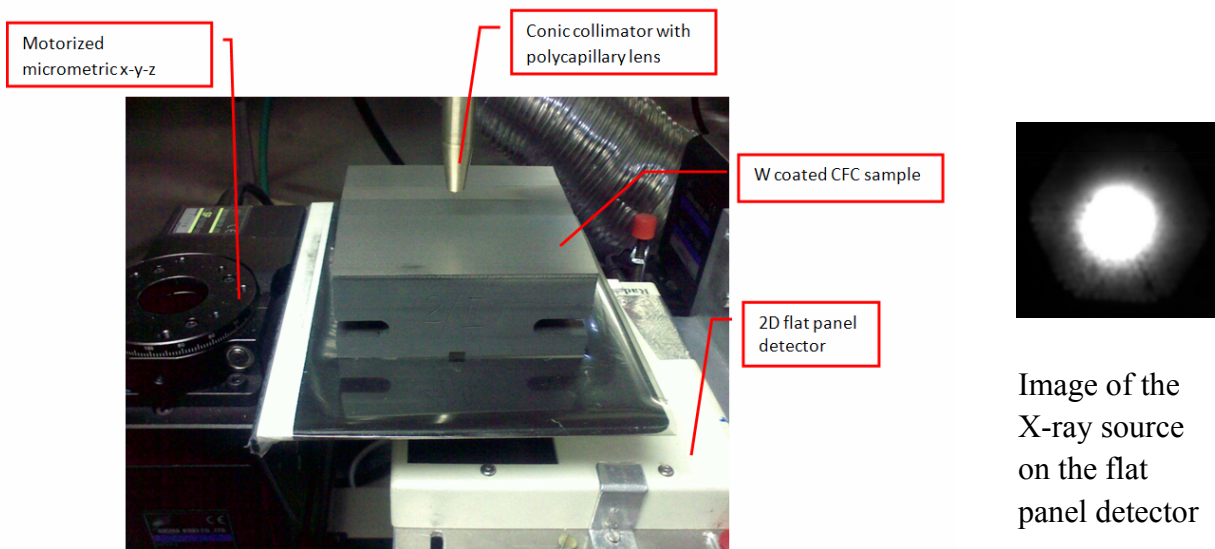

Image of the X-ray source on the flat panel detector

Figure 1 – View of the X-ray transmission geometry

The optimal measurement configuration and irradiation parameters were obtained by MCNP-5 Monte Carlo simulations [1].

A special attention was necessary to be paid on the dependence of X-ray intensity, provided by the X-ray sources (Oxford Instruments), with their temperature. The test (see Fig. 2) showed that a warm-up period is necessary before starting the measurements. The X-ray intensity becomes stable when a threshold of approximately 31° is reached (after a period of ~ 20 min). The explanation of this effect consists in the different time scales of the temperature accommodation of the internal components of the tube and the polycapillary lens.
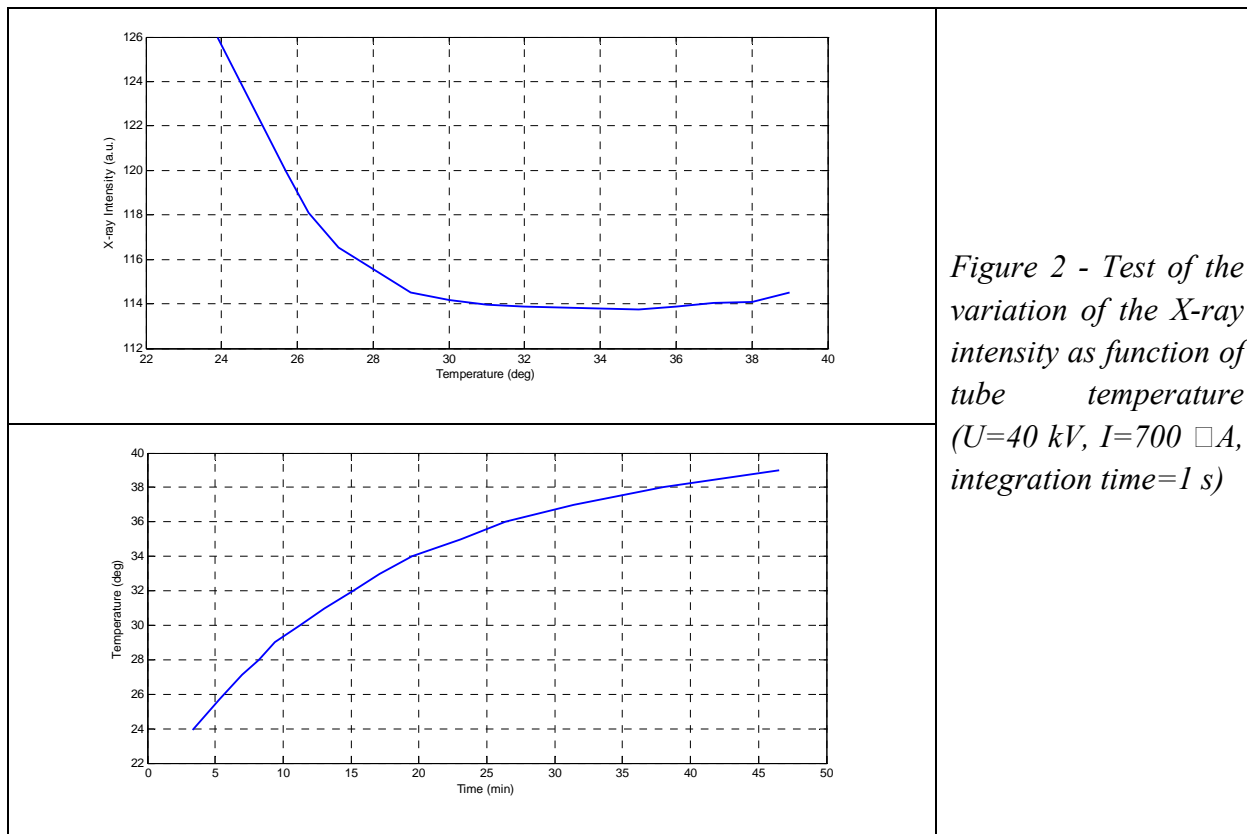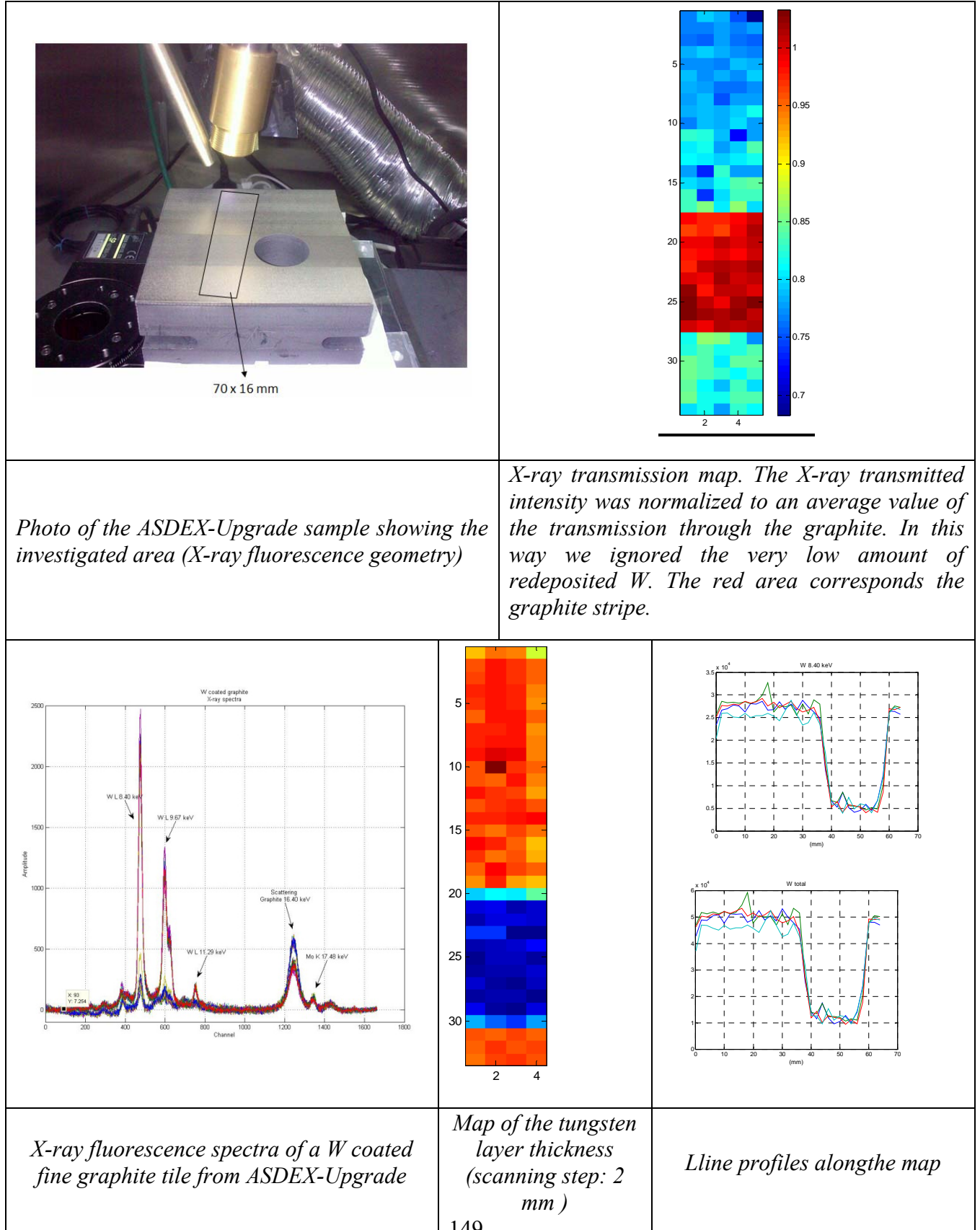
Figure 2 - Test of the variation of the X-ray intensity as function of tube temperature (U=40 kV, I=700 A, integration time=1 s)

The problem of evaluating the thickness uniformity of graphite/CFC with metallic coatings for a large number of samples was addressed also in case of the X-ray fluorescence analysis. In order to reduce the measuring time we replaced the multichannel analyzer (MCA) of the Tomo-Analytic system - Amptek MCA8000A - with a new one FAST MCA-3Series. The new MCA ensures a much fast and flexible data transfer of spectral data to the PC and allows an improved control of the acquisition process. The MCA-3 Series is a family of PC-based; software controlled PCI-bus Multichannel Analyzers. The design is capable of converting incoming signals at up-to 10^6 events/s or collect data at rates of up-to 5 Megaevents/s. The on board ultra fast pulse height analyzing 8k ADC is characterized by a 500 ns conversion time for Pulse-Height Analysis. No dead-time between channels, no end-of-sweep dead-time are also extremely valuable characteristics of the MCA. The dwell time extends from 100 ns to 50s (200ns to 50s using two inputs). The large data memory can be segmented to enable to accumulate successive measurements. Spectra accumulated in sequential PHA mode can be displayed in a two-dimensional array. The operating software allows the integration in the Tomo-Analytic application which is developed on a combined Labview/C++ platform. The implementation is in progress.

Figure 3 - Post-mortem analysis of W coated fine graphite tiles from the divertor of ASDEX-Upgrade

Photo of the ASDEX-Upgrade sample showing the investigated area (X-ray fluorescence geometry)	*X-ray transmission map. The X-ray transmitted intensity was normalized to an average value of the transmission through the graphite. In this way we ignored the very low amount of redeposited W. The red area corresponds the graphite stripe.*

X-ray fluorescence spectra of a W coated fine graphite tile from ASDEX-Upgrade	*Map of the tungsten layer thickness (scanning step: 2 mm)*	*Lline profiles alongthe map*

149

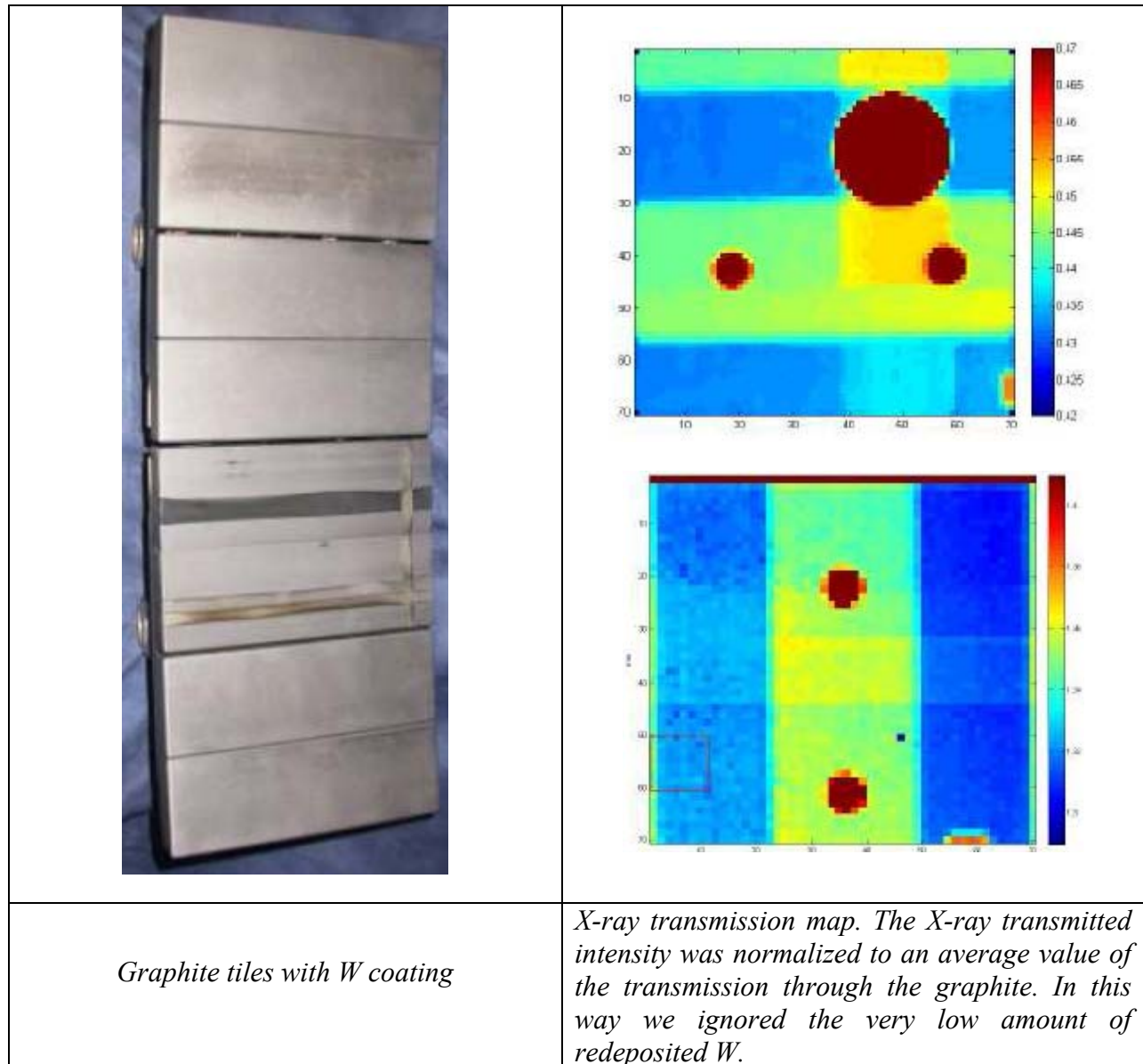|	X-ray transmission map. The X-ray transmitted intensity was normalized to an average value of the transmission through the graphite. In this way we ignored the very low amount of redeposited W.
Graphite tiles with W coating	

Figure 4 – High resolution post-mortem analysis of W coated fine graphite tiles from the divertor of ASDEX-Upgrade

A typical result of the combined X-ray transmission and X-ray fluorescence analysis is presented in Fig. 3. The X-ray transmission map can be used for the determination of the absolute value of the thickness of the W coating layer. In order to remove the influence of the fine graphite layer a calibration sample must be used. The calibration sample is multi-step one with regions with different thickness of fine graphite. As the real tiles contain several cutting up profiles, the CAD model of the tile must be also taken into account. The X-ray transmission ensures fast and high resolution analysis. The images presented in Fig. 4 are obtained for a scanning time of approximately four hours. The 70 x70 pixels images are obtained for a resolution of 1.0

mm/pixel. The main advantages of the X-ray fluorescence method are: i) it do not need a calibration sample for the determination of the thickness of the coating layer and ii) it can detect the composition and thickness of possible deposited layers of intrusions. However the time needed for the inspection of the sample in considerably larger: approximately 60-90 s are needed for the acquisition of a spectrum. Therefore a spatial resolution equal with that one obtained in the case of the X-ray transmission method becomes prohibitive in what it concerns the acquisition time needed. Also, due to the attenuation of the low energy of the emitted X-ray lines, the fluorescence method is limited to thin coating layers (up to ~10 m) depending on the coating material. However the combined use of X-ray transmission and X-ray fluorescence methods represent a unique instrument for the post-mortem analysis of the coatings.

3. Conclusion

An evaluation of the combined X-ray absorption/fluorescence method for erosion analysis was performed. As individuals each method has its own advantages/disadvantages, but the combined use of X-ray transmission and X-ray fluorescence methods represent a unique instrument for the post-mortem analysis of the coatings. It can provide fast analysis, high spatial resolution and detection of deposited layers and intrusions. The combined method was validated on W coated fine graphite tiles from the divertor of ASDEX-Upgrade. The results were presented at two international conferences [2-3] and it will be published.

The work will continue with X-ray fluorescence and tomography coating evaluation for a set of ASDEX-Upgrade tiles and of ITER-like CFC tiles. Marker probes of Al C Ni W will be also measured. A comparison with previous quantitative analysis with EPMA, RBS and NRA techniques will be carried out. Finally a technical concept for a compact/low cost instrument based on X-ray micro-fluorescence to be used in high productivity coating analysis will be elaborated.

4. Acknowledgement

5. References

[1] MCNP-5 - Los Alamos National Laboratory, 2005. MCNP – A General Monte Carlo N-Particle Transport Code, Version 5, vols. I–II, LA-UR-03-1987 and LA-CP-03-0245

[2] I. Tiseanu, T. Craciunescu, C. Dobrea, A. Sima, Tomo-Analytic - a combined fully 3D X-Ray microtomography and microbeam fluorescence system, PRORA 2009 - Fachtagung Prozessnahe Röntgenanalytik, 26-27 Nov. 2009, Berlin, Germany.

[3] I. Tiseanu , T. Craciunescu, C. Dobrea, A. Sima, Advanced X-ray imaging techniques for non-destructive analysis of fusion materials, Romanian Conference on Advanced Materials ROCAM 2009, August 25-28th, 2009, Brasov, Romania

PROJECT AS-8: TRITIUM TECHNOLOGIES FOR THE FUSION FUEL CYCLE

Project Leader: S. Brad

Task Agreement: WP08-GOT-TRI_TOFFY

MEdC/ICIT Trainee in TRI-TOFFY network - Work package No. 5, Experimental Pilot Plant for Tritium and Deuterium Separation, such planned just for ICIT training period:

- Introductory/accompanying training at ICIT

  (duration: 5 months in total)

This scheduled objective has been already achieved in accordance with *the Individual Development Plan and communicated into the last report to MEdC/EUROATOM*

Training Period at ICIT (22 months)
- First Training Period (5 months)
- Completed Training Period (6 months)
- Still to Complete (11 months)

23% Complete

27% Complete

50% Still to complete

- Research training at ICIT

  (duration: 17 months)

TOTAL: 22 months
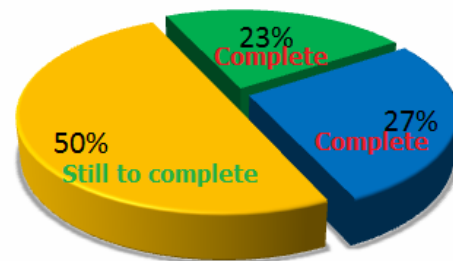
1.1 Tritium extraction systems and the Tritium Removal Facility (TRF) from ICIT Ramnicu Valcea

For a better understanding of the design and the functionality of tritium extraction systems I had to study some published papers that comment this issues.

Tritium(^{3}H or T) is the only radioactive isotope of hydrogen - which is disintegrating trough very weak radiation emission, giving birth of stable isotope 3He. Regardless of origin, tritium is incorporated mainly in the molecules of HT, HTO and sometimes CH$_3$T types. Based on the sources of tritium production two types of are identified:

- natural sources

- artificial sources.

This regenerative presence of tritium(figure 1) like natural source and the possibilities to produce some in artificial processes like thermonuclear

Figure 1. Tritium

explosions and activities of nuclear power confers the possibilities for obtaining an inexhaustible fusion fuel source for a total green technology, without release of greenhouse gases and hazardous waste in the nature. The largest suppliers of tritium are the nuclear power plants that use fusion reaction of deuterium and fission reactors like Light Water Reactors (LWR), Heavy Water Reactors (HWR). To obtain tritium like a fusion fuel, first of all it must be extracted and stored properly.
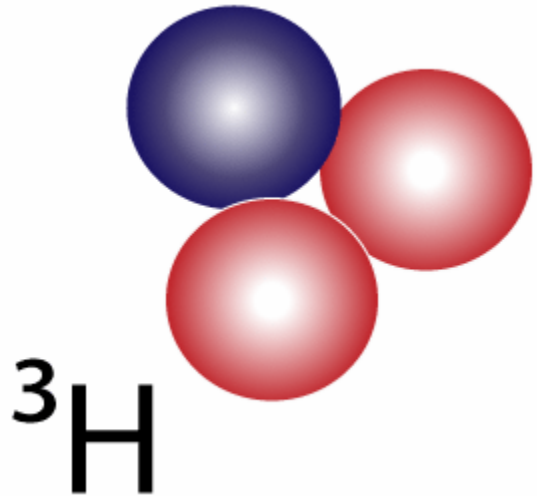
The raise of tritium level concentration in heavy water determines some problems in operation of nuclear reactor and also for the environment. Therefore it is very important to decrease the tritium level in heavy water and in this way most owners of CANDU reactors are doing researches to develop technologies for tritium removal from heavy water. As it is well known after several years of working the radioactive level in the moderator attained such a value that imposes tritium removal.

In conclusion in all studied lectures tritium extraction plants have been developed as an environmental protection method against tritium which is also considered as fuel for fusion reactors (in future activities).

This technology is based on isotopic catalytic exchange between water and hydrogen gas both carrying various isotopes of hydrogen: normal hydrogen, deuterium, tritium and mixed species. This isotopic exchange is followed by cryogenic distillation separating the various isotopes of the hydrogen gas. Available technologies are:

- LPCE columns
  - Many countries have developed exchange catalysts
  - Well demonstrated technology
- Electrolysis Cells
  - Tritium compatible cells built in the world
  - No long-term demonstration in tritium service
- Cryogenic Distillation

154

– Well demonstrated – common industrial process

Detritiation in Romania starts with tritium related activities in ICSI Rm. Valcea – TRF:

• Test and experiments for isotopic separation – starting from heavy water separation it was developed a new technology for hydrogen/ deuterium/ tritium separation, with new catalysts, packings or other specific materials.

• **Cryogenic Distillation (CD) systems:** The technology was developed in ICSI also for isotopes separation, with new package or other specific materials and experience for equipment design at low temperatures. The objective of CD system is to recover the entire amount of tritium from the hydrogen mixture. This system can work at temperatures between 21 and 26K, depending on the mixture concentration in heavier isotopes.

• Improving the pilot plant in order to meet the nuclear safety requirements and licensing process up to commissioning (present stage of the plant).

The design basis for TRF from ICSI Rm. Valcea (figure 2) is:

- • maximum activity for tritium in heavy water: 30 Ci/kg
- • detritiation factor of 3
- • maximum tritium inventory: 300,000 Ci
- • annual quantity of heavy water: 2000 kg
- • minimum D_2O feed isotopic: 99.8 %
- • water feed rate: 4-8 kg/h
- • tritium inventory in CD: 200,000 Ci (60,000 Ci for commissioning)
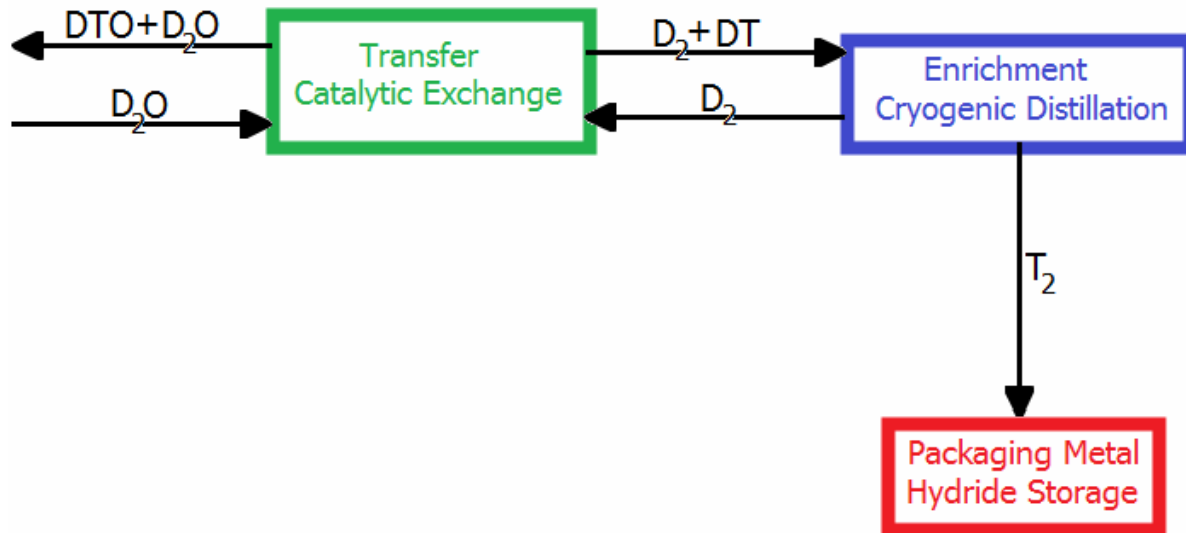- • design service life: 30 years

Figure 2. *Block diagram of the detritiation plant from ICIT*

Process Description

- Front-end transfer to gas
  - LPCE
  DTO + D2 ⇔ D2O + DT (catalytic process)

- Enrichment to pure T2
  - Cryogenic distillation
- Long-term storage
  - Titanium metal at room temperature (metal hydride)
- Process control & monitoring from the control room through DCS (Digital Control System) and Plant Control System (PDS)
- In addition independent safety instrumentation with credit in the safety analysis:
  - Safety Instrumented System (SIS)

  - Automated protection system

    - Emergency shutdown
    - Safety interlocks
- D2O handled in D2O Feed System, LPCE System and D2O Product System
- D2/DT gas from LPCE system pumped through adsorbent bed dryer system to removes moisture
- Tritium is concentrated in distillation column
- Tritium drawn off periodically to gas-handling system
  - Assayed

- Immobilized
- Removed for long-term storage

From my study I realized that tritium control and management will be one of the difficult issues for fusion energy development, both from the technical challenge and "public acceptance" points of view. This problems are caused by unprecedented amounts of highly mobile, radioactive, elemental tritium that is used as fuel in DT fusion systems (from JET Culham experience and future calculation for ITER) resulting:

- ~0.5 kg/day must be bred and extracted from solid/liquid breeder blankets
- ~5-10 kg/day or more must be fueled to, recovered and processed from the plasma
- Uncertain amounts of trapped inventory can exist in Blanket/PFC components and tritium processing systems
- Extremely small release limits (~10 Ci/day), mobilization limits, and the desire to recover and utilize valuable tritium fuel require extremely small loss rates and high accountability

Some critical issues of tritium extraction systems in the fusion reactor have the following reasons:

- Fusion plasma is likely to have low tritium burn fraction (a few percent) requiring large fueling rates and processing rates
- Most fusion blankets have high tritium partial pressure: He purge gas in solid breeders ~ 0.6 Pa
- The temperature of the blanket coolants and purges are high (500–700ºC)
- Surface area of heat exchanger is high, with thin walls
- Tritium is in elementary form. These are perfect conditions for tritium permeation.

I have identified some sophisticated design principles and analytic databases that positive influence the T-flows in the fuel cycle systems/components, that are very importing in obtaining a high efficiency in tritium extraction process, like:

- complexities from geometric factors,
- temperature dependent properties,
- concentration/impurity dependent properties,
- convection effects

One of the important characteristics from safety point of view is accountability. Accountability must ensure tritium is not a threat to workers, the public and the environment, and that the tritium has not be diverted from the facility. Accountability measurements generally is performed by in-bed calorimeters or off-line P-V-T methods. Processing times are long and accuracies are limited.

For future studies I intend to make some investigation in domains like:

- Tritium fundamental behavior (solubility, diffusivity) in the many materials of blanket, coolants, processing systems
- Effects of multiple processes (transport, dissociation, diffusion, trapping, etc.); multiple materials, coolants and interfaces; and the synergistic effects of radiation characterization

2. Experimental activities

2.1 Involvement in hydrophobic catalysts temporally tests database

I continued my research regarding on getting high mechanical characteristics and large active area for catalyst used in experiments. Also the exchange factor and the separation factor must be high, for the proper process of isotopic catalytic exchange to take part. Past studies regarding catalysts components, heat sintering treatment tests and thermo-mechanical process of pressing, mechanical and physical characteristics tests, gave me the opportunity to prepare a table with results (figure 3), showing so far that the catalysts sintered in He atmosphere at a constant pressure of 1,5 bar(g), and temperature of 60˚ C and kept for 15 minutes has the maximum specific surface and a good mechanical behavior.

Date of Analysis	Test Name	Specific Surface (m²/g)	Cumulative Surface (m²/g)	Maximum Volume of Pores (cm³/g)
27/07/2009	Cat 100 C 20 min N2 1 bar A1X	105,43	320,29	0,096
28/07/2009	Cat 100 C 20 min N2 1 bar A1	100,64	306,14	0,091
29/07/2009	Cat 350 C 6 min vid B1	83,090	247,46	0,078
30/07/2009	Cat 350 C 3 min vid B1	85,87	257,30	0,078
31/07/2009	Cat 350 C 6 min N2 1bar B1	94,64	280,46	0,085
03/08/2009	Cat 350 C 6 min N2 1bar B2	86,67	265,40	0,082
04/08/2009	Cat 350 C 5 min He 2bar F1	95,50	281,36	0,086
05/08/2009	Cat 350 C 6 min He 2 bar	86,67	265,40	0,082

Figure 3: *Experimental catalyst database*

This database for catalysts test was completed after BET surface measurements, resulting that treatment at a higher temperature leads to a lower BET surface, but in the same time at a significant increase of the mechanical properties. For further investigation in the obtaining of high surface and mechanical characteristics I've also tried to modify the catalyst composition structure by replacing the quantity of the "support material", in our case *POLITETRAFLUORETILEN* (Teflon) with alumina and palladium mixture (Al_2O_3 + Pd), after proper determination of added mixture characteristics and theoretical influence over the isotopic catalytic exchange efficiency process rate.

During this process I had the opportunity to become familiar with the process itself of catalysts fabrication and treatment, the new composition showing remarkable mechanical characteristics compared with the base used catalyst. The continuity of the created catalytic tests database, involves BET surface measurements and further mechanical and physical characteristics tests.

Research in this direction is in progress testing obtained catalysts under previously specified conditions.

2.2 Participation to the assembly of an oxidation rig after the design activities

After designing a 3D model of a catalytic oxidation rig I had the opportunity to participate to the physical assembly of it (figure 4).

Further investigations aim to describe the results and the functionality of this part of an extraction system from a cryogenic distillation (CD) column. Theoretically functioning of such rig is relatively simple described: the hydrogen (tritium) stream is passed through a catalyst bed consisting of CuO or Cu_2O. The process of oxidation (catalytic burning) takes place on the surface of the catalyst at a temperature of around 450°C. After passing the catalyst, the hydrogen is in the form of water vapours which are condensed in a water cooled condenser. In this way tritiated water is obtained that can be measured or sent to storage.

In the picture below one can see the main components of the rig in design mode (figure 4) and below also you can observe the assembled system (figure 5) :
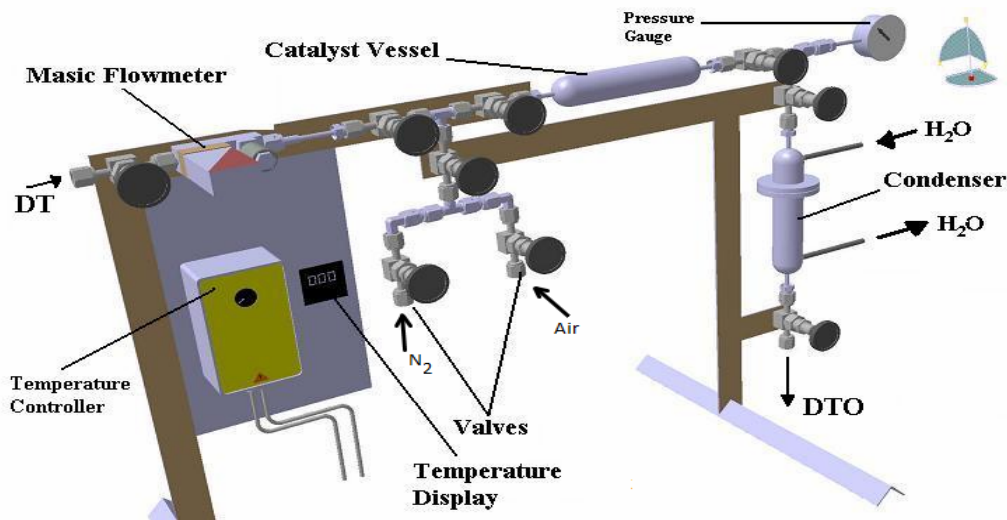

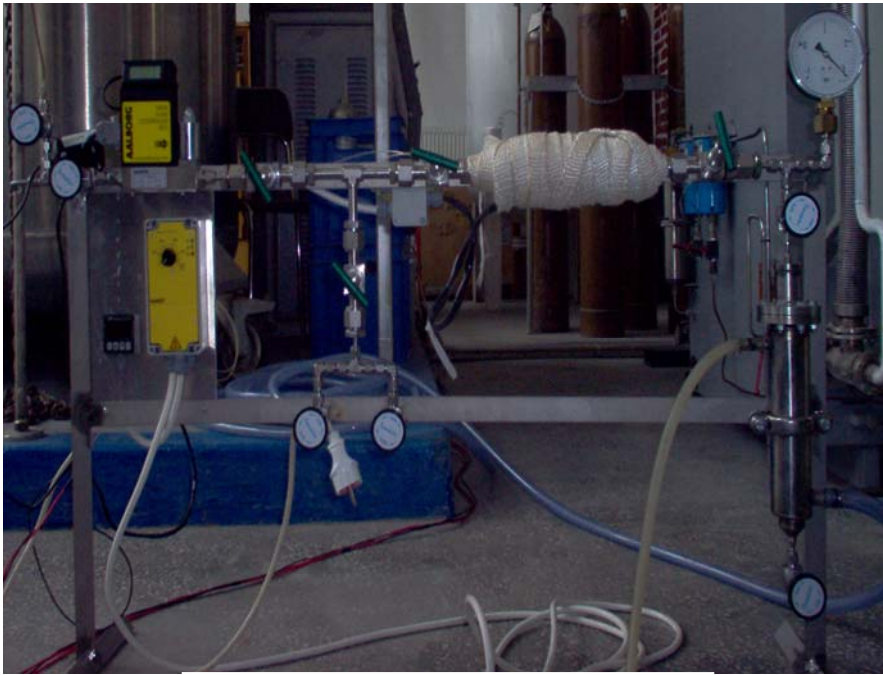
Figure 4: *The 3D model of the catalytic*

The construction of the 3D model has been made respecting all the details and using all the parts represented in the design:

- Masic flow meter;

- Catalyst vessel;

- Pressure Gauge;

- Condenser;

- Temperature display;

Figure 5: *Assembly realisation*   Temperature controller;

3. Design activities:

Using again CATIA, I designed another 3D model of a rig with absorber for the testing of tritium permeation trough different types of membrane materials (figure 6).

The main components of the rig are:

- clamping device for metal membrane subjected to experiment
- catalytic burner (catalyst vessel) for permeation gas water burning.
- calibrated vessel for hydrogen
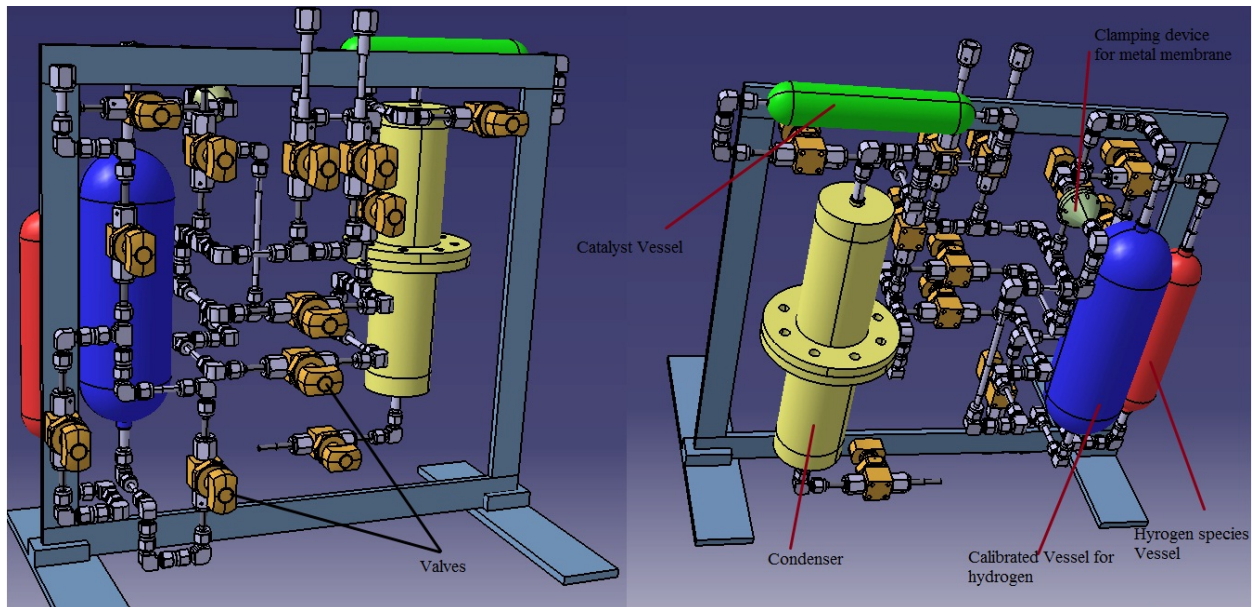
- vessel for hydrogen species and a condenser

Figure 6: The 3D model of the testing rig with absorber

The burner is filled with catalyst based on copper oxide. The water vapours thus obtained are condensed and the collected water is analysis by LSC, in order to measure the quantity of permeated tritium. The experiments will be done with very low tritium concentration and the parameters that will be modify in order to see the influence on the permeation process will be the partial pressure and temperature. copper oxide (regeneration), a process that occurs at a temperature of 400° C.

4. Participation to courses:

- Introductory course on vacuum technology:
  - definition of vacuum and a description of the physical conditions existing in a vacuum environment;
  - phenomena of gas flow though vacuum systems;
  - materials compatible with the vacuum environment;
  - vacuum leak detection methods and the far-reaching applications of vacuum technology today.

- 3rd Karlsruhe International School on Fusion Technologies
  - introduction to fusion;
  - introduction to plasma physics;
  - materials development for fusion reactors;

- divertors;
- safety analysis.

- Fundamentals of International Project Management:
  "Management of Intellectual Property Rights and Contract Management"

  - confidentiality and intellectual property rights;
  - market strategy and business environment;
  - patents ,trademarks and logos;
  - negotiation strategies and contracts management;
  - legal risk management.

5. Presentations sustained and papers published

- So far I had the opportunity this presentations:

1. Title of the presentation: "2nd Periodic Report" in the framework of TRI-TOFFY

   network

   Location: JET facility Culham, U.K. Fuel Cycle / TRI-TOFFY
network meeting

   Sustained at: 25.10.2009

2. Title of the presentation: "Nuclear fusion: technology development and achievements"

   Location: Ramnicu Valcea at "The 15th National Conference
   with International Participation *"PROGRESS IN
   CRYOGENICS AND ISOTOPES SEPARATION*"

   Sustained at: 28-30.10.2009

3. Title of the presentation: ""Fuel Cycle" and "TRI-TOFFY" training networks"

   Location: Bucuresti at EURATOM-MEdC Association Days 2009

Sustained at: 26.11.2009

- So far I had the opportunity to publish this papers:

1. G. Ana, S. Brad, Gh. Popescu, **I. Spiridon**, "Tritium measurement systems used in the Detritiation Experimental Pilot Plant from Rm. Valcea" to be published ;

2. **I. Spiridon**, „Nuclear Fusion: Technology development and achievements", proceedings of Progress in Cryogenics And Isotopes Separation, 21, 2009;

6. Bibliography and references

1. Timmerhaus Klaus D., Flynn T.M. – "Cryogenics Process Engineering", Plenum Press, New York, 1989

2. Bailey C.A. – "Advanced Cryogenics", Plenum Press, New York, 1971

3. McClintock Michael – "Cryogenics", Reinhold Publishing Corporation, New York, 1964

4. Whalley, P.B. –"Boiling, Condensation and Gas-Liquid Flow', Oxford Science Publications, Clarendon Press, 1987

5. Souers, P. Clark – "Hydrogen Properties for Fusion Energy", University of California Press

6. J.H.Rolston, J.dem Hartog and J.P.Butler – "The Deuterium Isotope Separation Factor between Hydrogen and Liquid Water". In: J.Phys. Chem., 80(10), 1064-1067 (1976)

7. J.H.Rolston and K.L.Gale: "Deuterium-protium Isotopic Fractionation between Liquid Water and Gaseous Hydrogen". In: J.Phys.Chem., 86(13), 2494-2498 (1982)

8. ITER Technical Basis Document

9. JET Plant Integration Document

PROJECT TT 19 5.1b: PRODUCEREA ACOPERIRILOR DE BERILIU PENTRU PLACILE MARKER PENTRU PROIECTUL „PERETE DE TIP ITER")

Project Leader: C. Lungu

Activitate I

Ni and Be coatings on marker tiles provided by JET

1. Introduction

The deposition methods by vacuum evaporation have the advantage of no buffer gas inside the deposition chamber, which makes the gas inclusions in the structure of the thin film to be practically absent. The method used in obtaining the Ni and Be films is the thermionic vacuum arc, which is an anodic arc. The principle of this method is the ignition of the plasma in pure vapors of the material. The energy introduced in the system for the ignition of the plasma is given simultaneous by an electronic gun and a high voltage source. Producing the vapors is obtained by heating the anode material using accelerated electrons between the electrodes. By this electronic bombardment the material is easily evaporated.

For the reason that of the high adherence degree, high density on purity of the thin films, the thermionic vacuum arc method is highly efficient. Another advantage of this method consists in the high degree maneuverability of the ions energy and in the same time of the plasma parameters. This is because the TVA plasma is localized and the ions are moving in a straight line in vacuum up till the walls/substrates connected to the ground. The energy is given by the plasma potential, easy to control by the arcs current, filament current and the anodic voltage.

There is no need of a gas-tampon or a catalytic one, ensuring the high purity of the thin films. Due to the high vacuum, the are no particles that could transmit the heat, the substrates being only by the ions collision with the surface.

The experimental setup of the thermionic vacuum arc consists in a ground cathode with a tungsten filament, with a Wehnelt cylinder to focus the electrons and the crucible that has inside the material for deposition, which is the anode.

The electrons emitted by the filament are directed through the Wehnelt cylinder towards the anode. By applying a positive voltage on the anode, the electrons are accelerated which makes the heating of the anodes' material. After a short period of time the first vapors appear. A prospecting increase of the voltage accelerates the electrons, the result being more vapors. For a specific value of the applied voltage on the anode, the ignition in pure vapors arc plasma appears. The thermionic vacuum arc plasma is localized. The ions created inside the plasma are accelerated also on the chambers walls due to the potential difference between the plasma and the ground connected walls. The neutral atoms move outside the plasma because of the pressure gradient. The film is formed of both ions and neutral atoms. For the rejection of the electrons which are going toward the target, the substrate is negatively polarized by applying a bias voltage. The interest parameters which must be monitored and controlled during the deposition are:

➢ I_f – the current value of the filament;
➢ I_a – arc current during the deposition;
➢ I_b – BIAS current value during the deposition;
➢ U_a – arc voltage during the deposition;
➢ U_b – BIAS voltage value applied on the substrate;
➢ Deposition rate;
➢ The thickness of the thin film.

The beryllium has been evaporated without a special crucible, being heated by an electronic bombardment at the surface. The anode was a cooled stainless steel one, where the cylinder of the beryllium had been put. In this case, the evaporation of the material takes place only at the superior face, the inferior face remaining a solid state. The evaporation of this kind of anode reduces to zero, the contamination of the growing. The deposition rate had values of 6-7 nm/s. For the deposition of nickel the evaporation has been made using a TiB_2 crucible. The ions generated inside the plasma have been accelerated using a bias voltage source having a value of 700V and 10-15 mA the bias current. For both deposition of nickel and beryllium it had been used an experimental setup like in Fig.1
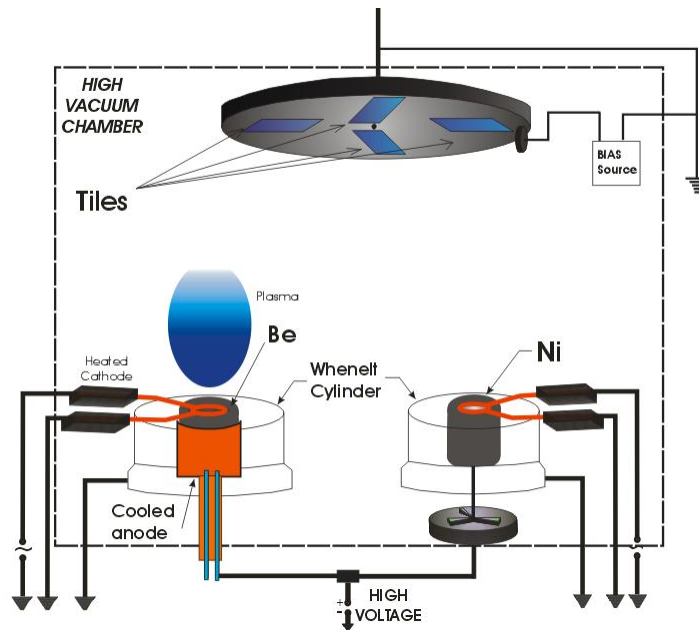
Fig.1 *Nickel and Beryllium deposition experimental setup*

Evaporation process

The process consisted in five steps:

I.   First step was of obtaining a low pressure inside the discharge chamber, about $4\text{-}6*10^{-6}$ torr. Inside the vacuum chamber there was an oven that could be controlled to obtain a specific temperature. One of the oven purposes is to obtain a good value of the vacuum. The other purpose is to increase the tiles temperature up till $250^0\text{-}300^0C$. This first process lasted between 3 and 4 hours, depending on the size of the tiles that were being coated. The tiles with a higher volume needed an extended period of time to reach the desired temperature, those with a lower volume needed a short period of time to reach the same value of the temperature.

II.   The second step consists in an Argon gas glow discharge that was made to ensure a proper cleaning of the tiles. The pressure of argon gas inside the vacuum chamber was set to $2\text{-}3*10^{-2}$ torr. By applying a negative bias voltage on the tiles, a glow discharge localized on the area of the tiles appeared. This process took 15 - 20 minutes, depending on the values of the voltage and the current. The bias voltage applied on the tiles was 700 V, with an electrical current of 50 mA. After the end of this step, a period of time of about 10-15 min was necessary to obtain again values of 10^{-6} torr for the vacuum inside the chamber.

III. Step no.3 consisted in Ni coating of the tiles. The filament heating current was of 45-50A, depending on the distance between the cathode and the anode. This distance vary in time because of the Ni evaporation, so that it is needed a constant increase of the input power. On the anode a high voltage potential had been applied, of about 1.5kV. The electrons from the cathode were accelerated by this high voltage potential. Firstly, nickel started to melt locally up till the point of ignition. The plasma was created in pure nickel vapors. The thickness of the film was of 2μm. After obtaining the desired thickness, the process of nickel coating stopped, the whole coating experiment going forward with step number 4.

IV. Fourth step was Beryllium coating of the tiles. The beryllium block was placed in a cooled stainless steel anode, so that the melting point occurred only at the surface. A filament heating current of 50A-55A was used. The electrons from the heated filament have been accelerated by a dropping voltage at the anode of 1.7-1.9kV. Beryllium first melted at the surface, and by increasing the input power the ignition of the pure vapors occurred. The thickness of the beryllium film was of 7 μm.

V. Final step consisted in the cooling down of the installation. The coated tiles have been taken out when its temperature was under 50^0C.

In all period of the coating, a negative bias voltage was applied on the tiles, with a value of 700V and a bias current of 5-15 mA, which insured a better coating by rejecting the electrons from the electronic gun, and an acceleration of the plasma ions.

Pre-production run

Before the real tiles to be coated, an experimental pre-production run was made using three Be blocks, to make some test of adherence, thickness and process procedures. Using the same experimental setup described before, and as well the five steps of the deposition process, an experimental pre-run was made. The positioning of the tiles is shown in Fig.2
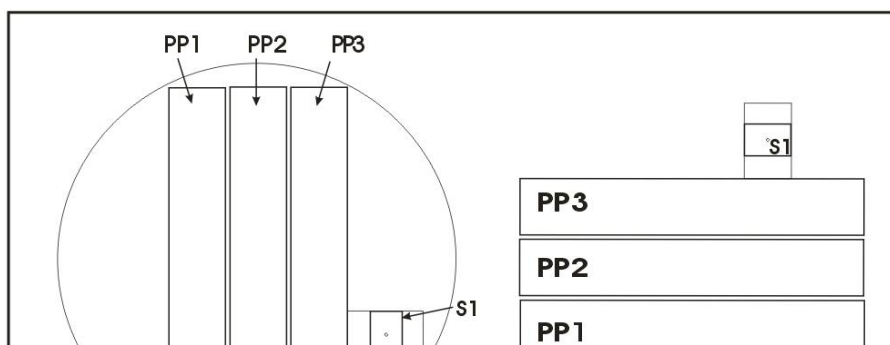
Fig.2 *Be tile positioning in the pre-production run process*

Figs. 3 and 4 show the tiles before and after the Ni+Be coating process, in the pre-run experiment.

Fig.3 *Be tiles BEFORE Ni+Be deposition*

Fig.4 *Be tiles AFTER Ni+Be deposition*

Adherence test on some of the test Be tiles have been made. The tests showed up that the Ni+Be coating is very adherent to the Be tiles use as substrates. Figure 5 presents the scratching of one of the tiles. One can be observed no delamination or pell-of of the prepared films.
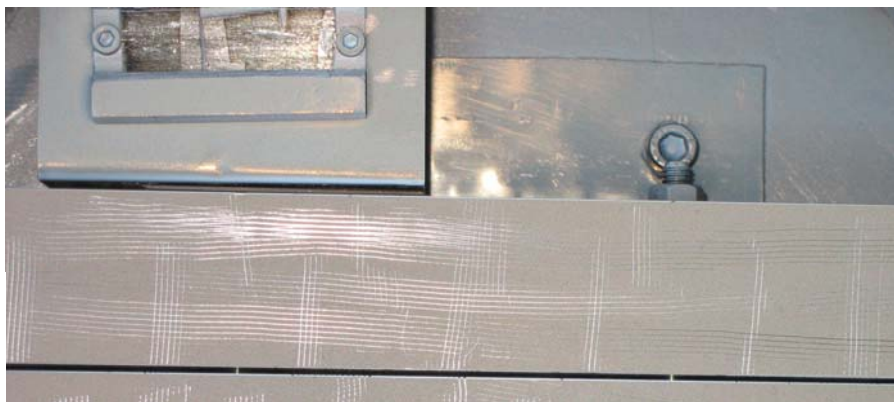
Fig.5 *Scratching of the Be test tiles after the adherence test.*

Production run

The parameters used in an actual deposition of Ni+Be process for the Be tiles is being presented in the Technological record, an official document, accompanying every deposition batch. The tiles used for coating **P F70100061, P F70100107** tiles**,** where the **WP-1, WP-2, WP-3** were some witness probes. The positioning of the tiles inside the vacuum chambers are presented in Fig.6
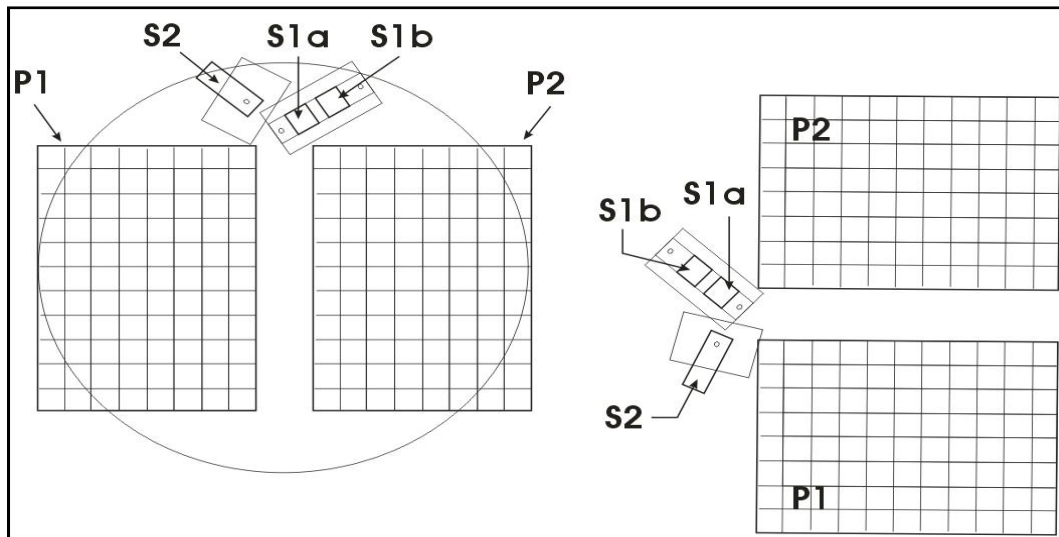

Fig.6 *Tile positioning inside the vacuum chamber*

TECHNOLOGICAL PARAMETERS used in the process of Ni+Be coating:

Technological Record

Loading of the Be tiles				
Tile reference number~	**P F70100061**	**P F70100107**		
Tile Position reference~	**P1**	**P2**		
Witness sample reference numbers~	**W P-1**	**W P-2**	**W P-3**	
Sample Position reference ~	**S1a**	**S1b**	**S2**	
Loaded holder, Photograph~	Jpeg No. IMG_2288/3623			

Outgassing

Oven temperature set to 450deg C

Target chamber pressure less than $5*10^{-5}$torr

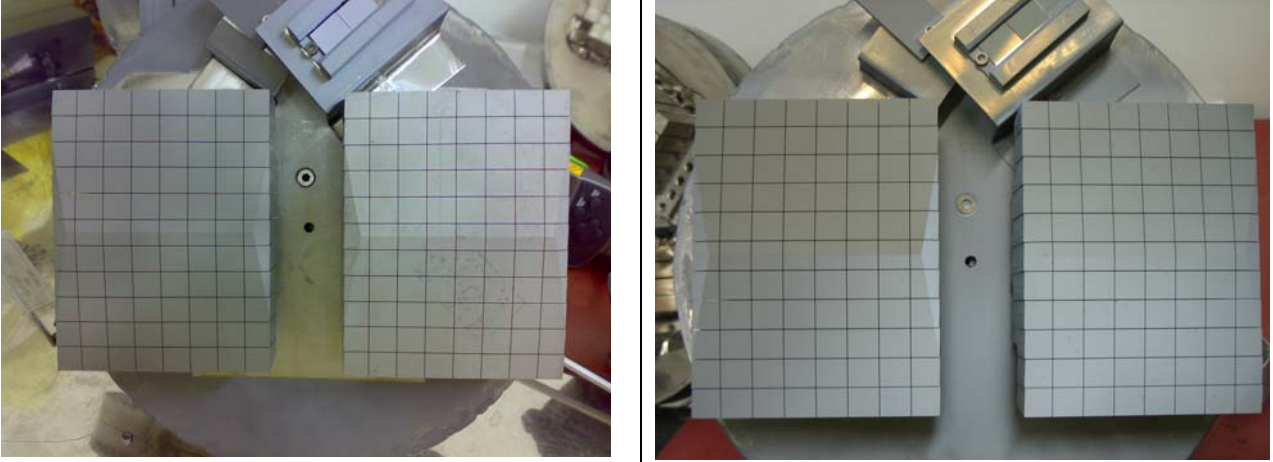| Time (mins)	Oven temperature deg C	Tile temperature		Pressure (x 10^{-6} torr)
		reading	deg C	
0	**20**		**20**	**4**
30	**427**		**102**	**4.6**
49	**444**		**151**	**4**
88	**447**		**200**	**3.4**
118	**447**		**223**	**3.2**
152	**446**		**245**	**3**
179	**445**		**262**	**2.9**
197	**445**		**266**	**2.8**

Glow Discharge Cleaning

DC Supply ~ Vdc=900V, Idc=50 mA

Time (mins)	Oven temperature	Tile temperature		Pressure (x 10^{-2} torr)
		reading	deg C	
0	**440**		**270**	**4**
5	**317**		**243**	**2.1**
10	**236**		**228**	**1.9**
15	**225**		**222**	**2**

Substrate heating turned off.		
6	**Nickel Coating**	
	Cathode filament heating. Vac __**50**__ A	
6(a)	Oven pressure (target <5 x 10^{-5}) ~ start **5.5**x 10^{-6} Torr, end **4.8** x 10^{-6} Torr	
6(b)	Tile surface temperature ~ start **253** deg C, end **398** deg C	
6(c)	DC discharge Supply ~ Vdc= **1500V**, Idc= **1.33A**	
6(d)	DC bias Supply ~ Vdc= **700V** , Idc= **15mA**	
6(e)	Length of time for Ni Coating~ (Target 120mins) **40** mins 14:20→15:00	
6(f)	Thickness reading on QMB (Target 2000=2μ) ~ **1.719~2 μm**	

7	**Beryllium Coating**
	Cathode filament heating. _____Vac **53.4** A
7(a)	Oven pressure (target <5 x 10-5) ~ start **3.8x 10^{-6}** Torr, end **3.6x 10^{-6}** Torr
7(b)	Tile surface temperature ~ start **370** deg C, end **380** deg C
7(c)	DC discharge Supply ~ Vdc= **1350 V**, **Idc= 870 mA**
7(d)	DC bias Supply ~ Vdc= **700 V**, Idc= **10 mA**
7(e)	Length of time for Be Coating~ **40** mins 15:10→15:50
7(f)	Thickness reading on QMB (Target 7000=7μm) ~ **6.110~7.5 μm**
8	**Stopping the deposition process**
8(a)	Tile temperature when exposed to air Target 50 deg C) **53** deg C

IMG_2288 (**Before** Ni+Be deposition)	IMG_3623 (**After** Ni+Be deposition)
PRODUCTION-Run 1/22.10.2009	

This way, the 22 beryllium tiles were coated with 2-3 μm Ni and 7-9 μm Be. After coatings, the tiles were double heat sealed, packed in carton crates and put together in a wooden box. The plastic bag surfaces, carton crates and wooden box were smeard and the smear products (25 mm paper filters) were sent to NFC-Pitesti in order to analyze the be contamination.

Conclusions

Thermionic vacuum arc method was used to obtain thin film layers of 2-3 μm Ni and 7-9 μm Be for coating on a number of 22 marker tiles, part of the ITER fusion reactor inside wall.

The technique used was of coating from two different sources, on one hand the Nickel and on the other hand Beryllium, without opening the vacuum chamber between these two depositions. Having inside both systems for producing plasma in pure vapors of Nickel and Beryllium contributed to the compactness, adherence and purity of the thin films. The purity of the thin films was also able to be obtained because of the absence of a buffer gas inside the vacuum chamber. The control of the ion energy and of the electron flux by handling the exterior plasma parameters is another advantage of using the thermionic vacuum arc method. By controlling the exterior plasma parameters like the heating current filament, the dropping voltage on the anode, the distance between electrodes, the deposition rate was also controlled. Because the films thickness on the tiles was very important, the control of the deposition rate made possible the process stopping to a precise thickness.

References

[1] C. P. Lungu, I. Mustata, V. Zaroschi, A. M. Lungu, A. Anghel, P. Chiru, M. Rubel, P. Coad G. F. Matthews and JET-EFDA contributors, Beryllium Coatings on Metals: Development of Process and Characterizations of Layers, Phys. Scr. T128 (March 2007) 157–161

[2] C. P. Lungu, I. Mustata, V. Zaroschi, A. M. Lungu, P. Chiru, A. Anghel, G. Burcea, V. Bailescu, G. Dinuta, F. Din, Spectroscopic study of beryllium plasma produced by thermionic vaccum arc Vol. 9, Iss. 4, 2007, J Optoelectron Adv M, Vol. 9, No. 4, 2007, 884-886.

[3] T. Hirai, J. Linke, M. Rubel, J.P. Coad, J. Likonen, C.P. Lungu, G.F. Matthews, V. Philipps, E. Wessel and JET-EFDA contributors, Thermal load testing of erosion-monitoring beryllium marker tile for the ITER-LikeWall Project at JET, Fusion Engineering and Design, Fusion Engineering and Design, Volume 83, Issues 7-9, December 2008, Pages 1072-1076.

[4] Cristian P. LUNGU, Ion MUSTATA, Alexandu ANGHEL Corneliu POROSNICU, Ionut JEPU, Catalin TICOS Ana M. LUNGU, Mihai GANCIU, Arcadie SOBETKII Gheorghe

HONCIUC and Patrick CHAPON Preparation and Characterization of Multifunctional, Nanostructured Coatings Using Thermionic Vacuum Arc Method, Symposyum Kobe, March 2-4 2009, Frontier of Applied Plasma Technology (Edited by Osaka University, Japan), Vol.2 July 2009, pp1-6.

[5] K. Sugiyama, K. Krieger, C.P. Lungu, J. Roth, Hydrogen retention in ITER relevant mixed material layers Journal of Nuclear Materials, Volumes 390-391, 15 June 2009, Pages 659-662

[6] A. Anghel, C. Porosnicu, M. Badulescu, I. Mustata, C.P. Lungu, K. Sugiyama, S. Lindig, K. Krieger, J. Roth, A. Nastuta, G. Rusu, G. Popa, Surface morphology influence on deuterium retention in beryllium films prepared by thermionic vacuum arc method, Nuclear Instruments and Methods in Physics Research Section B: Beam Interactions with Materials and Atoms, Volume 267, Issue 2, January 2009, Pages 426-429.

[7] Anghel, I. Mustata, C. Porosnicu, C. P. Lungu, Influence of the bias voltage on the formation of beryllium films by a thermionic vacuum arc method, Journal of Nuclear Materials, Volume 385, Issue 2, 31 March 2009, Pages 242-245